Different evolutionary stages in massive star formation

Centimeter continuum and H₂O maser emission with ATCA

Á. Sánchez-Monge[1], M. T. Beltrán[1], R. Cesaroni[1], F. Fontani[1], J. Brand[2], S. Molinari[3], L. Testi[4,1], and M. Burton[5]

[1] Osservatorio Astrofisico di Arcetri, INAF, Largo Enrico Fermi 5, I-50125, Firenze, Italy
[2] Istituto di Radioastronomia & Italian ALMA Regional Centre, via P. Gobetti 101, I-40129, Bologna, Italy
[3] Istituto di Fisica dello Spazio Interplanetario, INAF, Area di Recerca di Tor Vergata, Via Fosso Cavaliere 100, I-00133 Roma, Italy
[4] ESO, Karl Schwarzschild str. 2, 85748 Garching bei Munchen, Germany
[5] School of Physics, University of New South Wales, NSW 2052, Australia

ABSTRACT

Aims. We present ATCA observations of the H₂O maser line and radio continuum at 18.0 GHz and 22.8 GHz, toward a sample of 192 massive star forming regions containing several clumps already imaged at 1.2 mm. The main aim of this study is to investigate the water maser and centimeter continuum emission (likely tracing thermal free-free emission) in sources at different evolutionary stages, using the evolutionary classifications proposed by Palla et al. (1991) and Molinari et al. (2008).

Methods. We used the recently comissioned CABB backend at ATCA obtaining images with ∼20″ resolution in the 1.3 cm continuum and H₂O maser emission, in all targets. For the evolutionary analysis of the sources we used the millimeter continuum emission from Beltrán et al. (2006) and the infrared emission from the MSX Point Source Catalogue.

Results. We detect centimeter continuum emission in 88% of the observed fields with a typical rms noise level of 0.45 mJy beam^{-1}. Most of the fields show a single radio continuum source, while in 20% of them we identify multiple components. A total of 214 centimeter continuum sources have been identified, likely tracing optically thin H II regions, with physical parameters typical of both extended and compact H II regions. Water maser emission was detected in 41% of the regions, resulting in a total of 85 distinct components. The low angular (∼20″) and spectral (∼14 km s^{-1}) resolutions do not allow a proper analysis of the water maser emission, but suffice to investigate its association with the continuum sources. We have also studied the detection rate of H II regions in the two types of IRAS sources defined by Palla et al. (1991) on the basis of the IRAS colours: High and Low. No significant differences are found, with large detection rates (>90%) for both High and Low sources.

Conclusions. We classify the millimeter and infrared sources in our fields in three evolutionary stages following the scheme presented by Molinari et al. (2008): (type 1) millimeter-only sources, (type 2) millimeter plus infrared sources, (type 3) infrared-only sources. We find that H II regions are mainly associated with type 2 and 3 objects, confirming that these are more evolved than type 1 sources. The H II regions associated with type 3 sources are slightly less dense and larger in size than those associated with type 2 sources, as expected if the H II region expands as it evolves, and type 3 objects are older than type 2 ones. Regarding the maser emission, it is mostly found associated with type 1 and 2 sources, with a higher detection rate toward type 2, consistent with the results of Breen et al. (2010). Finally, our results on H II region and H₂O maser association with different evolutionary types confirm the evolutionary classification proposed by Molinari et al. (2008).

Key words. stars: formation – stars: massive – ISM: HII regions – radio continuum: ISM – masers

1. Introduction

The problem of massive star formation (O & B stars with masses ≳8 $M_\odot$) still represents a challenge from both a theoretical and observational point of view. Such stars reach the zero-age main sequence (ZAMS) still undergoing heavy accretion, and their powerful radiation pressure should halt the infalling material, thus inhibiting growth of the stellar mass beyond ∼8 $M_\odot$ (e. g., Palla & Stahler 1993). Recently, various studies have proposed a solution to this problem based on non-spherical accretion and high accretion rates (e. g., McKee & Tan 2003; Bonnell et al. 2004; Krumholz et al. 2009; Kuiper et al. 2010). Together with the theoretical efforts, the comprehension of the massive star formation process requires good observational knowledge of the star-forming environment and of the evolutionary steps through which OB star formation occurs.

In 1991, we started a thorough investigation of a sample of luminous IRAS sources, selected on the basis of their far-infrared colours and with the additional constraint of δ>−30° (Palla et al. 1991, 1993). The hypothesis that this sample could contain high-mass young stellar objects (YSOs) in different evolutionary phases has been supported by a large number of observations that we have performed both at low- and high-angular resolution (Molinari et al. 1996, 1998a, 1998b, 2000, 2002; Brand et al. 2001; Fontani et al. 2004a, 2004b, 2006; Zhang et al. 2001, 2005). We started a similar study in the southern hemisphere, which represents an excellent testbed for these studies, thanks to the large number of (massive) star forming regions that are observable. For this reason, we used the SEST telescope to search for CS-line and 1.2 mm continuum emission in a sample of sources with δ<−30° (Fontani et al. 2005; Beltrán et al. 2006). Along the same line, other authors (e. g., Bronfman et al. 1989; Sridharan et al. 2002; Beuther et al. 2002; Fáundez et al. 2004; Hill et al. 2005) have also studied large samples of mas-
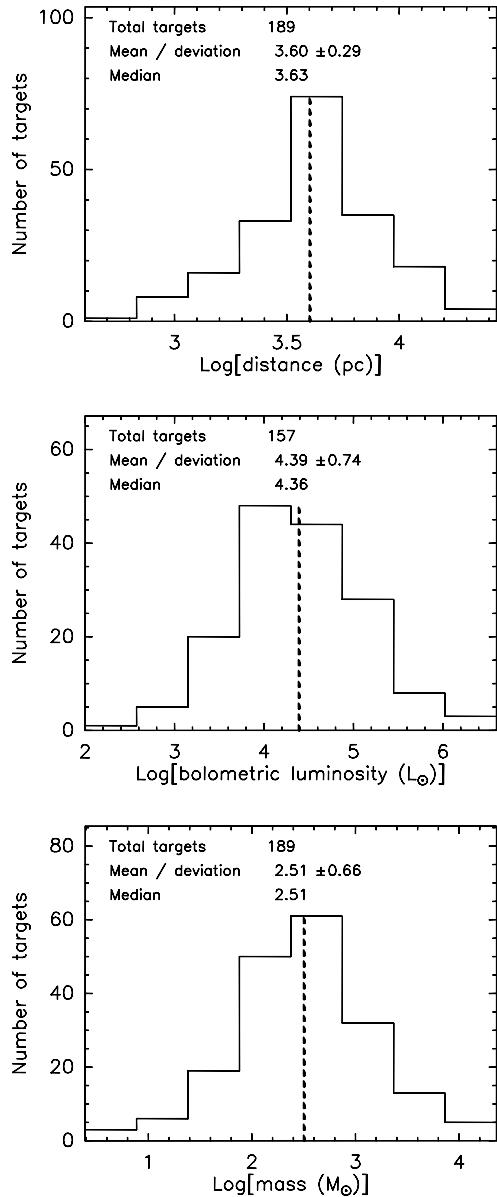
Fig. 1: **Top**: Distribution of kinematic distances for the observed fields (see Table 1 for references). **Middle:** Distribution of bolometric luminosities for the fields centered on an IRAS source. **Bottom:** Distribution of the sum of the masses of the millimeter sources within the observed fields (from Beltrán et al. 2006). At the top of each panel we indicate the total number of sources used in the histogram, the mean, the standard deviation, and the median. The vertical dashed lines indicate the median values.

sive young stellar objects in the millimeter continuum and line emission.

To study a possible evolutionary sequence of the objects, Molinari et al. (2008) performed a detailed analysis of a small sub-set of our samples from millimeter down to mid-infrared wavelengths. According to these authors, the sources can be divided into three types, in order of increasing age: MM (and MM-S; hereafter *Type 1*) with dominant millimeter emission and possibly close to an infrared MSX source, but not coincident with it; IR-P (hereafter *Type 2*) with both millimeter and infrared emission; and IR-S1/S2 (hereafter *Type 3*) with only infrared

emission but located near a millimeter source. Using a simple model, Molinari et al. (2008) could relate the infrared and millimeter emission to the physical state of the core and explain the distribution of these source types in a mass-luminosity plot in terms of evolution. As illustrated in Fig. 9 of Molinari et al. (2008), *Type 1* would correspond to high-mass protostars embedded in dusty clumps, possibly surrounded by infrared emission that could originate from more evolved, nearby lower-mass stars (see Faustini et al. 2009), *Type 2* would be deeply embedded ZAMS OB stars, still undergoing accretion, and *Type 3* would be ZAMS OB stars surrounded only by remnants of their parental clumps.

In this paper, we aim to extend the analysis performed by Molinari et al. (2008) to a larger sample of sources, and add the information of the centimeter continuum emission (likely tracing H II regions: see e. g., Kurtz et al. 1994, Sánchez-Monge et al. 2008) and H_2O masers (being signposts of the presence of outflows/shocks associated with protostars: e. g., Felli et al. 2007; Moscadelli et al. 2011) to set constraints on the evolutionary scheme. In Sections 2 and 3 we describe the sample and observations. In Section 4 we present the centimeter continuum and maser line results of the ATCA observations. An analysis of the centimeter continuum sources is presented in Section 5, and the evolutionary scenario is discussed in Section 6. We end in Section 7 with the main conclusions of this work.

2. Sample

The first step to extend the search for massive YSOs towards the southern hemisphere was to select a sample of possible candidates from the IRAS Point Source Catalogue following the Palla et al. (1991, 1993) criteria: $F_{60\,\mu m} \geq 100$ Jy and colours satisfying the criteria established by Richards et al. (1987) for compact molecular cores. The sources were divided into two sub-samples based on the IRAS colors: sources with [25–12]>0.57 and [60–12]>1.3 were named *High* (with colors characteristic of sources associated with ultracompact H II regions; Wood & Churchwell 1989), the others were named *Low*. A sample of 235 IRAS sources, containing 142 *Low* and 93 *High* sources, was observed by Beltrán et al. (2006) at 1.2 mm with the SEST, resulting in a total of 667 millimeter clumps detected. In this paper we present observations carried out with the Australia Telescope Compact Array (ATCA; see Sect. 3) toward a large sub-sample of these millimeter sources. In total, we observed 192 distinct fields (defined by the full width at half maximum primary beam of ATCA of ~2'.5; see Sect. 3), containing 315 millimeter sources. Out of the total 192 fields, 160 were centered on an IRAS source (81 *Low* and 79 *High* IRAS sources), while the remaining 32 fields were centered on millimeter clumps (detected with the SEST) located >150″ from an IRAS source.

In Fig. 1 we show the distributions of kinematic distances, bolometric luminosities and masses of the sources observed with ATCA. Note that we only have distance determinations for 189 of the 192 observed fields, most of them obtained from CS-line observations (Fontani et al. 2005; Beltrán et al. 2006; see Table 1). For 96 of these fields there is an ambiguity between near and far distances (see Beltrán et al. 2006). Searching the literature we have been able to solve the ambiguity for 36 fields (using H I line observations; see references in Table 1), for the remaining fields we have considered the near distance for further analysis[1]. The bolometric luminosities have been derived

---

[1] Most of the distance estimates are obtained from spectral line observations pointing toward an IRAS source. We have assumed that the
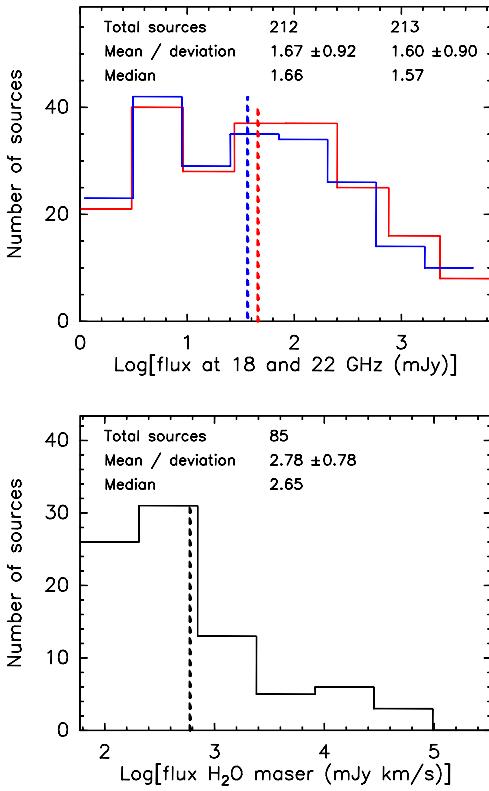
Fig. 2: **Top**: Distributions of the flux density of the centimeter continuum sources detected at 18.0 GHz (blue, 212 sources) and 22.8 GHz (red, 213 sources). Note that the number of sources detected at both wavelengths is different, since one source is detected only at 18.0 GHz and two sources are detected only at 22.8 GHz (see Table 3). **Bottom**: Distribution of the integrated flux of the H_2O maser emission. The numbers at the top of each panel correspond to the total number of sources, the mean, the standard deviation, and the median values.

only for the 157 fields centered on an IRAS source with distance determination (see middle panel of Fig. 1). Finally, we have considered the sum of the masses of the millimeter sources within our observed fields, and constructed the distribution of masses. The median values of 4.3 kpc, 2×10^4 $L_\odot$, and 300 $M_\odot$, and the distributions are similar to those obtained for all the sources in Beltrán et al. (2006), confirming that our source selection is representative of the whole sample.

3. Observations and data reduction

The 192 selected fields were observed with the Australia Telescope Compact Array (ATCA) interferometer at Narrabri (Australia) on the 25th and 26th of July 2009, and 9th and 10th of October 2009 (project C1804). In Table 1, we list the observed fields. Column 1 gives the field name, Col. 2 the source type of the IRAS source (*High* or *Low*), Col. 3 the kinematic distance adopted, Cols. 4 to 7 give the coordinates of the phase center[2] (both in equatorial and galactic systems), Cols. 8 to 13

---

millimeter sources detected in the SEST fields surrounding an IRAS source (although not coincident) are located at the same kinematic distance (following the analysis carried out by Beltrán et al. 2006).

[2] Note that in Beltrán et al. (2006) the coordinates of the phase centers reported in their Table 1 for two sources were slightly wrong.

Table 2: Summary of centimeter continuum detections

	192 observed ATCA fields			
	centered on IRAS[a]		centered on mm[a]	
no cm source	8	(–)	15	(–)
single cm source	118	(118)	13	(13)
multiple cm sources	34	(74)	4	(9)
all	160	(192)	32	(22)

[a] The first number corresponds to the number of fields, while the second number (in parentheses) corresponds to the number of centimeter sources detected in the corresponding fields.

give the synthesized beams, position angles, and rms noise levels at 18.0 GHz and 22.8 GHz, and Col. 14 indicates the day of observation of the field. Observations were conducted using the recently commissioned Compact Array Broadband Backend (CABB; Wilson et al. 2011) providing a total bandwidth of 4 GHz divided in two sidebands: 2 GHz in the lower sideband (LSB) centered at a frequency of 18.0 GHz, and 2 GHz in the upper sideband (USB) centered at a frequency of 22.8 GHz, covering the H_2O (6_{15}–5_{23}) maser transition at 22.235 GHz (although with low spectral resolution: channel width of 1 MHz, corresponding to $\sim$13.5 km s^{-1}). The array was in the H75 configuration for the four observing runs, resulting in a synthesized beam of $\sim$25″ at 18.0 GHz and $\sim$20″ at 22.8 GHz.

Observations were conducted in snapshot mode. The typical strategy was to observe each target field for 10 minutes. This total on-source time was broken up into a series of 3-minute snapshots in order to get a better coverage of the *uv*-plane. A gain calibrator was observed every 15-minutes to correct for the phase variations. A total of 14 gain calibrators[3] were used for the 192 target observed fields. The absolute flux scale was calibrated daily using PKS B1934−638 as a primary calibrator for all the 4 observing runs. The flux of PKS B1934−638 was assumed to be 1.03 Jy at 20 GHz. Daily bandpass calibration was achieved by observing 0537−441 (with a flux of 8.35 Jy).

The data reduction was done using the MIRIAD software package (Sault et al. 1995). In all cases, data from the antenna located at 6 km from the main array (antenna CA06) were not included in the data reduction, to avoid an increase in the rms noise of the final images. Images of each target field were produced using the CLEAN algorithm with natural weighting. Fields with water maser emission at 22 GHz were self-calibrated. The self-calibration process consisted in identifying the channel with the strongest maser component, self-calibrate it (using the task SELFCAL), and apply the gain solutions to the continuum at 22.8 GHz and 18.0 GHz if both continuum maps improved with the new gain solutions. The mean rms noise is 0.45 mJy beam^{-1} at 18.0 GHz and 0.40 mJy beam^{-1} at 22.8 GHz (see Table 1 for the noise in individual fields).

For correct coordinates for the SEST observations were α=16:12:42.7, δ=−51:45:11 for 16085−5138; and α=17:25:42.0, δ=−36:21:57 for 17221−3619.

[3] The gain calibrators were 0826−373, 1004−50, 1045−62, 1059−63, 1129−58, J1326−5256, 1352−63, 1511−55, 1613−586, 1646−5, 1710−269, 1714−336, 1830−210 and 1923+210.

3

4. Results

4.1. Centimeter continuum emission

In Fig. B.1, we present a panel for each field showing the centimeter continuum emission at 18.0 GHz (color scale) and 22.8 GHz (contours). In Fig. B.2, we present three panels (in a row) for each field showing all possible comparisons between maps of the radio continuum emission, the 1.2 mm continuum from SEST (Beltrán et al. 2006) and the 21.8 μm emission from the MSX (Midcourse Space Experiment; Price et al. 1999). We detect centimeter continuum emission above the 5σ level in 169 out of 192 fields, corresponding to a detection rate of 88%. In most of the maps, the centimeter continuum emission comes from a single object, and only a few of them show extended complex emission with multiple peaks. In order to identify the centimeter sources and derive their properties, we use the following criterion: if the contour at half-maximum of the intensity peak (over 5σ) is closed, we consider it as an independent source. With this method we identified a total of 214 centimeter continuum sources. There are multiple sources in 38 fields, and a single detection (with an angular resolution of $\sim20''$) in 131 fields. Therefore, in 12% of the 192 observed fields no centimeter continuum emission is detected, in 68% we find a single component, and in 20% of the targets there are multiple sources. In Table 2 we list a summary of the detections in the observed fields, distinguishing between fields centered or not on IRAS sources. We can see that most of the fields with no continuum detection (65%) correspond to fields centered on a millimeter source located far from the IRAS source.

In Table 3, we list all the sources detected and, for completeness, the 23 fields with no centimeter emission indicating 5σ upper limits. We give the name of the region (Col. 1), the number of each centimeter continuum source detected in a field (Col. 2), the coordinates of the 22.8 GHz detection[4] (except where otherwise indicated for which the coordinates of the 18.0 GHz source are reported; Cols. 3 and 4), the peak intensity, integrated flux, observed size and deconvolved size at 18.0 GHz (Cols. 5 to 8) and at 22.8 GHz (Cols. 9 to 12), and the association of a water maser with the centimeter source (Col. 12). The angular diameter, θ_S, has been calculated assuming the sources are Gaussians from the expression

$$\theta_S = \sqrt{\text{FWHP}^2 - \text{HPBW}^2}$$

with FWHP$=2\sqrt{A/\pi}$, where A is the area inside the polygon corresponding to the contour at half maximum, and HPBW is the synthesized beam listed in Table 1. For unresolved sources, we have considered an upper limit on the angular diameter of $7''$, i. e., 1/3 of the synthesized beam.

In the top panel of Fig. 2, we show the distribution of flux densities for the detected sources. The mean and median values are 47 and 46 mJy at 18.0 GHz, and 40 and 37 mJy at 22.8 GHz. Thus, we are typically measuring fluxes at 22.8 GHz lower than at 18.0 GHz. This can be due either to the flux density decreases with frequency for the detected sources (as expected in optically thin H II regions), or to some part of the centimeter emission is being filtered out at shorter wavelengths (as seen by comparing the images in sources like 10184−5748 and 13106−6050).

---

[4] The peak separation in the images at the two frequencies (18.0 GHz and 22.8 GHz) is typically $\lesssim5''$, smaller than the synthesized beam.

4.2. Water maser emission

Although the main goal of our observations was the study of the centimeter continuum emission, we also observed the H$_2$O maser line at 22.235 GHz. In Table 4, we list the properties of the detected masers: the name of the region, the coordinates, the integrated intensity and the velocity of the peak of the emission. Due to the poor spectral resolution (~13.5 km s^{-1}), the maser emission was typically detected in a single channel. Only in few cases we detected emission in more than one channel: two channels for 16573−4214 2, three for 15579−5303 0 and 16344−4605 0. The integrated intensity was calculated as the sum of the channel intensities multiplied by the corresponding width (13.5 km s^{-1}). Out of the 192 observed fields, 78 show water maser emission (detection rate of 41%), and only four fields show multiple (spatial) components (see Table 4). Assuming a typical linewidth of ≈0.5 km s^{-1} for the water masers (e. g., Gwinn 1994), the dilution factor due to our poor spectral resolution would be ~0.037. Thus, taking into account the mean rms noise level of 18 mJy beam^{-1} per channel, we are only sensitive to strong ($\gtrsim2$ Jy; assuming 5σ detections) water maser single components. In the bottom panel of Fig. 2, we show the distribution of H$_2$O maser integrated flux densities. In Figures B.1 and B.2, the masers are shown as white stars.

5. Analysis

5.1. Physical parameters of H II regions

Assuming that the centimeter continuum emission detected comes from homogeneous optically thin H II regions, we calculated the physical parameters (using the formalism of Mezger & Henderson 1967 and Rubin 1968) and list them in Table 5. The linear radius of the H II region (Col. 5) was determined from the deconvolved size listed in Table 3. We calculated the source-averaged brightness temperature (T_B; Col. 6) using

$$T_B = \frac{S_\nu\, c^2}{2\nu^2\, k_B\, \Omega_S},$$

where S_ν is the integrated flux density, Ω_S is the solid angle of the source, c the speed of light, k_B the Boltzmann constant and ν the observing frequency. The emission measure (EM; Col. 8) and the electron density (n_e; Col. 7) were calculated from

$$\left[\frac{EM}{\text{cm}^{-6}\ \text{pc}}\right] = 1.7 \times 10^7 \left[\frac{S_\nu}{\text{Jy}}\right]\left[\frac{\nu}{\text{GHz}}\right]^{0.1}\left[\frac{T_e}{\text{K}}\right]^{0.35}\left[\frac{\theta_S}{''}\right]^{-2},$$

$$\left[\frac{n_e}{\text{cm}^{-3}}\right] = 2.3 \times 10^6 \left[\frac{S_\nu}{\text{Jy}}\right]^{0.5}\left[\frac{\nu}{\text{GHz}}\right]^{0.05}\left[\frac{T_e}{\text{K}}\right]^{0.175}\left[\frac{d}{\text{pc}}\right]^{-0.5}\left[\frac{\theta_S}{''}\right]^{-1.5},$$

where T_e is the electron temperature assumed to be 10^4 K, θ_S is the angular diameter of the source, and d is the distance. The mass of ionized gas (M_i; Col. 9) was calculated assuming a spherical homogeneous distribution as

$$\left[\frac{M_i}{M_\odot}\right] = 3.5 \times 10^{-12} \left[\frac{S_\nu}{\text{Jy}}\right]^{0.5}\left[\frac{\nu}{\text{GHz}}\right]^{0.05}\left[\frac{T_e}{\text{K}}\right]^{0.175}\left[\frac{d}{\text{pc}}\right]^{2.5}\left[\frac{\theta_S}{''}\right]^{1.5}.$$

The number of Lyman-continuum photons per second (N_{Ly}; Col. 10; hereafter Lyman continuum for simplicity) was calculated from the flux density and kinematic distance as

$$\left[\frac{N_{Ly}}{\text{s}^{-1}}\right] = 8.9 \times 10^{40} \left[\frac{S_\nu}{\text{Jy}}\right]\left[\frac{\nu}{\text{GHz}}\right]^{0.1}\left[\frac{T_e}{10^4\text{K}}\right]^{-0.45}\left[\frac{d}{\text{pc}}\right]^2.$$
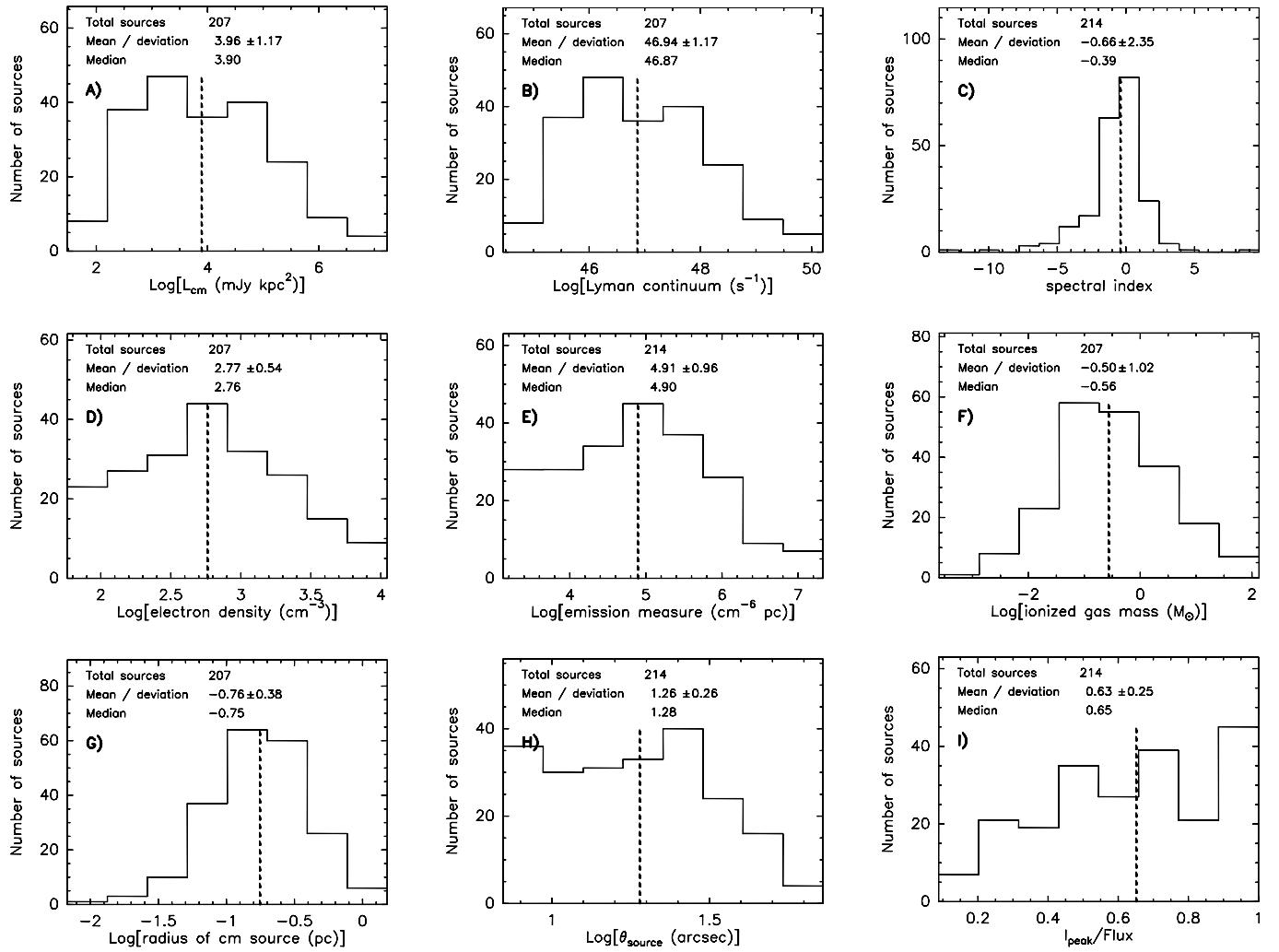
Fig. 3: Distributions of **a)** centimeter luminosity; **b)** Lyman continuum; **c)** spectral index; **d)** electron density; **e)** emission measure; **f)** ionized gas mass; **g)** linear radius of the centimeter source; **h)** deconvolved angular diameter, θ_S; and **i)** peak intensity to flux density ratio, for the centimeter sources detected with ATCA. The numbers at the top of each panel indicate the total number of sources used in the histogram (in some cases we only can use 207 sources, those with distance determination), and the mean, standard deviation and median values. The vertical dashed line indicates the median value.

From the estimated N_{Ly}, using the tables of Panagia (1973) and Thompson (1984) and assuming that a single ZAMS star is the source of the ionizing photons, we computed the spectral type of the ionizing source (Col. 11). Similar results (with variations of at most one subtype) are obtained when using the more recent calculations of Vacca et al. (1996), Diaz-Miller et al. (1998) or Martins et al. (2005).

Assuming an uncertainty of 10% on the flux density and angular diameter, one finds that this implies uncertainties of 30% for the emission measure, 20% for the electron density, 20% for the ionized gas mass, and 10% for the Lyman continuum. Note that for extended sources the measured flux density could be a lower limit should the interferometer be filtering extended emission, and the measured size could be underestimated by up to 50% if the source is not Gaussian (see Panagia & Walmsley 1978).

In Column 12 of Table 5 we give the spectral index (α; $S_\nu \propto \nu^\alpha$) estimated from the 18.0 GHz and 22.8 GHz fluxes. However, these values must be taken with caution due to the large uncertainties involved, mainly because the two frequencies

are very close and hence the error on α is large. In addition, the 22.8 GHz images could be more affected than the 18.0 GHz images by filtering of extended structures.

In Fig. 3, we show the distribution of the main physical parameters of the centimeter continuum sources. The mean, standard deviation, and median values of each histogram are shown at the top of each panel. In Table 6, we list the median values of these parameters for the whole sample (Col. 3), and for the various classes of objects considered in this paper (Cols. 4–8; see next Sections). The median diameters (~0.36 pc), electron densities (~580 cm^{-3}) and emission measures (~7.9×10^4 cm^{-6} pc) are in agreement with typical values of compact H ɪɪ regions (Kurtz 2005), with the observed parameters ranging between those of classical and ultracompact H ɪɪ regions.

5.2. Lyman continuum

In Fig. 4 we compare the Lyman continuum, N_{Ly}, obtained from the measured radio flux with the bolometric luminosity, L_{bol}, estimated from the IRAS fluxes (Fontani et al. 2005). We have

Table 6: Median values of main physical parameters of the centimeter sources

Parameter (1)	Units (2)	all sources (3)	Low[a] (4)	High[a] (5)	Type 1[b] (6)	Type 2[b] (7)	Type 3[b] (8)
number of sources	-	214	75	74	15	99	55
flux$_{18.0\ GHz}$	mJy	46	37	125	13	107	48
flux$_{22.8\ GHz}$	mJy	37	33	102	10	120	43
spectral index	-	−0.4	−0.3	−0.3	−0.8	−0.2	−0.2
L_{cm}	mJy kpc^2	7900	5700	37100	1100	15100	15800
I_{peak}/S_{flux}	mJy beam^{-1}/mJy	0.65	0.62	0.71	0.52	0.70	0.59
angular size	arcsec	19	22	14	27	15	21
radius	pc	0.18	0.18	0.17	0.36	0.14	0.25
n_e	10^3 cm^{-3}	0.58	0.46	1.12	0.13	1.23	0.46
EM	10^6 cm^{-6} pc	0.79	0.60	3.09	0.13	2.82	0.71
M_i	$M_\odot$	0.28	0.26	0.46	0.28	0.28	0.60
N_{Ly}	log(s^{-1})	46.9	46.7	47.6	46.0	47.2	47.2
H_2O integrated flux	mJy	400	447	490	355	575	310

[a] Classification (*Low* and *High*) by Palla et al. (1991).
[b] Classification (*type 1*, *type 2* and *type 3*) by Molinari et al. (2008) and this work.

considered that a centimeter continuum source is associated with the IRAS source if their separation is ≤60″ (corresponding to the HPBW of the IRAS satellite at 25 μm). We stress, as explained in Sect. 2, that for those sources for which it was not possible to discriminate between the near and far kinematic distances, the near estimate was arbitrarily assumed.

The red solid curve in Fig. 4 corresponds to the relationship between N_{Ly} and L_{bol} expected for an O-B type star. This has been computed by various authors (e.g., Panagia 1973; Thompson 1984; Vacca et al. 1996; Schaerer & de Koter 1997; Díaz-Miller et al. 1998), resulting in a maximum discrepancy ≲30% among different calculations. While most points in Fig. 4 fall below the red curve, a significant fraction of the sources happen to lie above it. This is surprising, as the Lyman continuum from a single star is the maximum value obtainable for a given bolometric luminosity, as illustrated by the dashed area in the figure, which corresponds to the expected N_{Ly} if L_{bol} is due to a stellar cluster. This result has been obtained by generating a large collection (10^6) of clusters with sizes ranging from 5 to 500000 stars each. The clusters are assembled randomly from a cluster membership distribution which describes the number of clusters (N_{cl}) composed by a given number of stars (N_{st}) of the form: $dN_{cl}/dN_{st} \propto N_{st}^\alpha$ with α=−2. Each cluster was populated assuming a randomly sampled Chabrier (2005) initial mass function with stellar masses in the range 0.1–120 $M_\odot$. For each cluster we computed the total mass, bolometric luminosity, maximum stellar mass and integrated Lyman continuum. The shaded area in Fig. 4 was produced by plotting at each bolometric luminosity the range that includes 90% of the simulated clusters.

How can one explain the presence of so many objects in the "forbidden region" above the red curve in Fig. 4? A priori several explanations are possible and we discuss them in the following:

 – The radio flux (from which N_{Ly} is computed) could be overestimated. In practice, one cannot think of any reason why this should be the case. On the one hand, if the H II regions were optically thick, density bound, or dusty, the free-free emission would be reduced and the estimated N_{Ly} would be a *lower* limit. On the other hand, interferometric observations tend to resolve extended emission and rather *decrease* the measured flux density (and hence the estimated value of N_{Ly}). Finally, uncertainties in the flux calibration may reach a few 10%, much less than the observed excess with respect
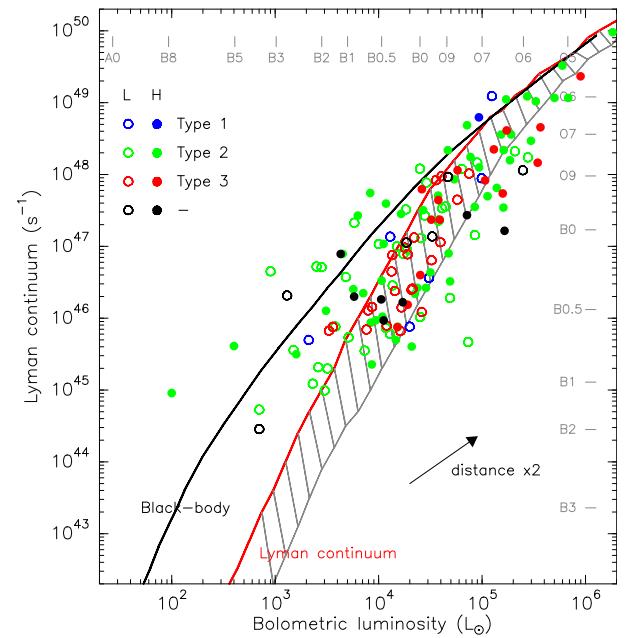
Fig. 4: Lyman continuum, N_{Ly} (from Table 5), as a function of the bolometric luminosity, L_{bol}. Open and filled symbols denote *Low* and *High* sources, respectively. The different colors indicate the *types 1* (blue), *2* (green) and *3* (red), while the black symbols correspond to those centimeter sources not classified in any of the three types (see Sect. 6). The red solid line corresponds to the Lyman continuum of a ZAMS star of a given bolometric luminosity, while the dashed region indicates the expected N_{Ly} if L_{bol} is due to a cluster (see Sect. 5.2 for details). The black solid line corresponds to the Lyman continuum expected from a blackbody with the same radius and temperature of a ZAMS star. At the top and right axes we list the spectral type corresponding to a given Lyman continuum and a given bolometric luminosity. The arrow indicates how much a point should be shifted if its distance is doubled.

to the single-star curve in Fig. 4 (up to almost 3 orders of magnitude).

- The bolometric luminosity could be underestimated. Since we have derived L_{bol} from the flux densities reported in the IRAS Point Source Catalogue, this explanation is very unlikely. The IRAS HPBW ranges from 0.''5 to 2' and thus encompasses an area even larger than that of the observed H II regions. Consequently, the IRAS fluxes are more likely overestimating the emission from the relevant sources and the estimated L_{bol} is rather an upper limit.

- The sources in the "forbidden region" could be Planetary Nebulae (PNe) instead of H II regions. In this case the value of N_{Ly} would be much greater than for a ZAMS star, for the same L_{bol}. We note that most of the objects above the red curve in Fig. 4 belong to *type 1* and *2* (see Sect. 6) and are thus associated with molecular clumps, which appears quite unlikely for an evolved star such as those powering PNe.

- The source of N_{Ly} could be other than a ZAMS star. For example, it has been proposed that UV photons from shocks could be ionizing thermal jets (e. g., Anglada 1996). However, the expected free-free emission at 1.3 cm from such a jet is on the order of 0.1 mJy kpc^2, much less than the measured radio luminosities of the objects in the "forbidden region" – typically 10–10^6 mJy kpc^2. Another possibility is that the UV photons are originating from shocks in the accretion flow onto the protostar/disk system. Although intriguing, this hypothesis is yet to be investigated theoretically and thus must be regarded as purely speculative at present.

- The distances could be wrong. Indeed, a relatively small error on our distance estimates could significantly affect the position of the corresponding points in Fig. 4. The arrow in this figure indicates how much a point should be shifted if its distance is doubled. In fact, for many sources we have arbitrarily assumed the near kinematic distance, while replacing this with the far distance would certainly move the corresponding points to the right of the red curve. However, even if for all sources above the solid red line the far distance were assumed, still ~50% of them would lie in the "forbidden region".

In conclusion, we believe that the observed excess of Lyman continuum cannot be trivially explained by any of the above hypotheses. It is worth pointing out, though, that almost all of the sources in the "forbidden region" fall very close to or below the Lyman continuum expected from a black-body with the same radius and effective temperature as a ZAMS star (black solid line in Fig. 4). Although not conclusive, this fact suggests that some B-type stars could emit in the UV range much more than predicted by standard models of stellar atmospheres. Given that ~70% of the HII regions lying above the red curve belong to *types 1* and *2*, one may further speculate that such an excess in N_{Ly} occurs preferentially during the earliest evolutionary stages of a high-mass star. Further investigation is needed to confirm our findings and shed light on this intriguing issue, which, to our knowledge, has not been reported previously. Previous interferometric large surveys of H II regions (e. g., Wood & Churchwell 1989, Kurtz et al. 1994) were carried out with angular resolutions ≤1'', which could be filtering out a large fraction of the extended centimeter continuum emission that we can image with our ~20'' observations, thus obtaining lower values of N_{Ly}.

5.3. Source size and electron density relationship

It is interesting to investigate the relationship between density and size in our sample of H II regions. This is illustrated in Fig. 5, which shows a plot of the electron density, n_e, versus the diam-

eter of the H II region, D_{HII}, for all of our objects. Note that for a given Lyman continuum, the relationship between the radius and the electron density of a Strömgren H II region is fixed. The solid lines drawn in the figure correspond to such a relationship for ZAMS stars of spectral types ranging from B3 to O4. As expected, all points lie in the region spanned by these spectral types.

The result in Fig. 5 is similar to that obtained by other authors (see e.g. Garay & Lizano 1999 and Martín-Hernández et al. 2003), who noted that the distribution of the points in the plot appears to be consistent with a steeper relationship than that expected for a simple Strömgren sphere ($n_e \propto D_{HII}^{-3/2}$). However, before drawing such a conclusion, one should take into account any possible observational bias that could affect the observed distribution of points in that plot. For example, the largest H II regions may be resolved out by the interferometric observations, while the smallest could fall below our sensitivity limit. To take these and other effects into account, we have attempted a more quantitative approach. This consists in comparing the distribution in Fig. 5 with that obtained assuming that O-B type stars are distributed in the Galaxy as established by Mottram et al. (2011). The details of our procedure are given in Appendix A. Here we only stress that with respect to Mottram et al. we have introduced the additional assumption that the number of H II regions with electron density n_e is given by a function of the type $\frac{dN}{dLog n_e} \propto n_e{}^\alpha$. In practice, our model depends only on the exponent α and the total number of H II regions in the Galaxy, N_{HII}. As shown in Appendix A, we can fit the observed electron density function $\frac{dN}{dLog n_e}$ and thus obtain the values of the two free parameters, $N_{HII}=15000^{+2000}_{-1300}$ and $\alpha=-0.15 \pm 0.1$. With this model one can also estimate the expected distribution of points in the plot of Fig. 5. This is shown as a colour scale, indicating the number of detectable H II regions per pixel. Clearly, the expected distribution is far from homogeneous, and consistent with the distribution of the observed points. The agreement between model and data can be better appreciated in Figs. A.1 and A.3 where the best-fit density ($\frac{dN}{dLog n_e}$) and diameter ($\frac{dN}{dLog D_{HII}}$) functions are compared to those obtained from our data.

Although the fit is quite satisfactory, a word of caution is in order. Our findings refer to a sample of objects which is not the result of an unbiased search across the Galactic plane, because our observations were performed towards a limited number of targets selected mostly on the basis of their IRAS colours. However, the adopted selection criteria on the IRAS colours (see Sect. 2) are expected to identify most Galactic H II regions (and their precursors). It is also worth noting that the number of H II regions estimated by us ($N_{HII}=15000$) is significantly larger than that obtained by other authors. For instance, Wood & Churchwell (1989) estimate ~1600 embedded O-type stars in the Galaxy, while from the results of Mottram et al. (2011) one may obtain ~8200 Galactic massive young stellar objects and compact H II regions. However, the former estimate refers only to stars above ~30000 $L_\odot$ and the latter does not consider extended H II regions, which can be detected with our observations.

5.4. Background source contamination

Most of the sources in our sample are located in the fourth galactic quadrant, covering the range $254°<l<360°$, with a few at $l≈10°$. Regarding the galactic latitudes, our sources are confined to the galactic disk with $|b|<3°$, with most of them (85%) restricted to $|b|<1°$. Note that most of these sources are included in the range of galactic coordinates covered by recent in-
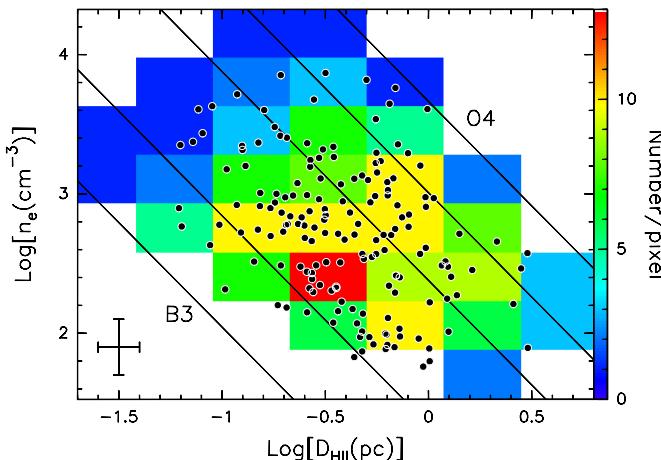
Fig. 5: Electron density of the H II regions detected in our survey versus the corresponding linear diameter. The points denoting the data (listed in Table 5) are overlayed on an image whose intensity (colour scale) gives the number of H II regions expected in each pixel on the basis of the model described in Appendix A. The solid lines correspond to ZAMS stars of spectral types B3, B1, B0, O7 and O4. The cross indicates the 20% error in the electron density and the 10% error in the source size (see Sect. 5.1).

frared and submillimeter unbiased surveys (e. g., GLIMPSE and MIPSGAL with *Spitzer*; Hi-GAL with *Herschel*; ATLASGAL with APEX) that can be used to construct the spectral energy distributions from infrared to millimeter wavelengths. This will be the subject of a forthcoming paper (Sánchez-Monge et al., in prep). The location of our sources within the galactic disk is consistent with them being associated with star-forming regions, with the centimeter continuum emission coming from H II regions (as shown in the previous section). However, we cannot exclude the possibility that some of the radio continuum sources are in fact extragalactic sources. Following the Appendix of Anglada et al. (1998), and considering our ATCA observations at a frequency of 20.4 GHz, we can estimate the number of expected background sources as

$$< N > = 0.041 \left[1 - \exp^{-0.109 \, \theta_{\mathrm{FOV}}^2} \right] \left(\frac{S_0}{\mathrm{mJy}} \right)^{-0.75},$$

with θ_{FOV} the field of view in arcmin, and S_0 the detectable flux density threshold at the center of the field that we will consider to be 5σ (~2 mJy). For a field of view of $2'.5$, and considering that we have 192 distinct fields, we expect to detect $< N > \simeq$ 3 background sources. Since we have detected a total of 214 centimeter continuum sources, only ~2% of them could be in fact extragalactic sources.

There are 8 sources with large negative spectral indices (<-5) that could be extragalactic non-thermal sources: 10184−5748 0, 10317−5936 0, 13106−6050 0, 13592−6153 0, 14214−6017 0, 15015−5720 0, 16363−4645 0, 17242−3513 (see Table 5). However, visual inspection of the radio continuum maps reveals that these sources are associated with strong millimeter condensations or infrared sources, and some of them are coincident with or close to H_2O masers, suggesting a galactic origin. Also, the spectral indices are too negative even for synchrotron emission from jets found in star-forming regions (e. g., Reid et al. 1995, Carrasco-González et al. 2010). Therefore, such

spectral indices are probably the result of filtering out more emission at 22.8 GHz than at 18.0 GHz. Thus, these regions are probably extended and more evolved H II regions, rather than extragalactic sources. In fact, it is interesting to note that the 8 sources with large negative spectral indices correspond to sources located in regions with multiple centimeter sources, suggesting that confusion in combination with the poor *uv*-coverage of our snapshot observations could complicate the estimate of the flux, eventually resulting in unreliable spectral indices.

5.5. Low versus High: centimeter continuum properties

The two groups (*High* and *Low*) defined by Palla et al. (1991) to classify the IRAS sources associated with massive star-forming regions, have been proposed to include sources in different evolutionary stages, with the *High* sources being more evolved and more likely associated with UC H II regions. Several works have studied the molecular and dust content in these two groups of sources. Brand et al. (2001) compared the molecular properties of two samples containing *Low* and *High* sources, and reported that molecular clumps associated with *Low* sources have larger sizes, are less massive, cooler and less turbulent than *High* sources. More recently, Fontani et al. (2005) observed different transitions of CS and $C^{17}O$ tracing the dense gas associated with a larger (130) sample of *Low* sources. They found that the temperatures and linewidths estimated for the *Low* sources were similar to those found toward different samples of *High* sources (Bronfman et al. 1989; Sridharan et al. 2002; Beuther et al. 2002), with only slightly narrower lines for the *Low* sources, suggesting that the gas could be more perturbed in *High* sources, due to the presence of H II regions. Beltrán et al. (2006) studied the dust properties by observing the 1.2 mm continuum emission toward a large (235) sample of *Low* and *High* sources. The sizes of the clumps, masses, surface densities and H_2 volume densities were similar between the two groups of sources, with only small variations found in the size and mass (slightly larger for *High* sources). Thus, it seems that there are no clear differences in the molecular and dust properties between *High* and *Low* sources.

In this section, we compare the properties of the centimeter emission (likely tracing H II regions) associated with the two different groups of sources. In our sample — 79 IRAS *High* sources and 81 IRAS *Low* sources — the detection rate of centimeter continuum emission is 94% and 93% for *High* and *Low* sources, respectively. Thus, there are no differences between both groups regarding the presence of H II regions. Is there any difference in the physical properties of the H II regions associated with the *High* and *Low* sources? In Fig. 6, we show the distribution of the main physical parameters of the centimeter continuum sources for both groups. The physical properties of the H II regions in both groups seem to be similar, with values of the electron density, emission measure, flux density and Lyman continuum slightly higher for *High* sources (see also the median values listed in the Columns 4 and 5 of Table 6). Moreover, the plot of the Lyman continuum as a function of the bolometric luminosity (see Fig. 4) does not show large differences between the distribution of *High* (solid symbols) and that of *Low* (open symbols) sources. It is worth noting that our detection rates (>90%) seem to contradict those obtained by Molinari et al. (1998a): 43% and 24% for *High* and *Low* sources, respectively. However, their higher angular resolution observations (~10 times better) could be filtering out the extended H II regions (still observable in our ATCA observations), which results in a decrease of their detection rates. It is worth noting that Molinari et al. (1996) suggest that *Low* sources could be contaminated by evolved (and more
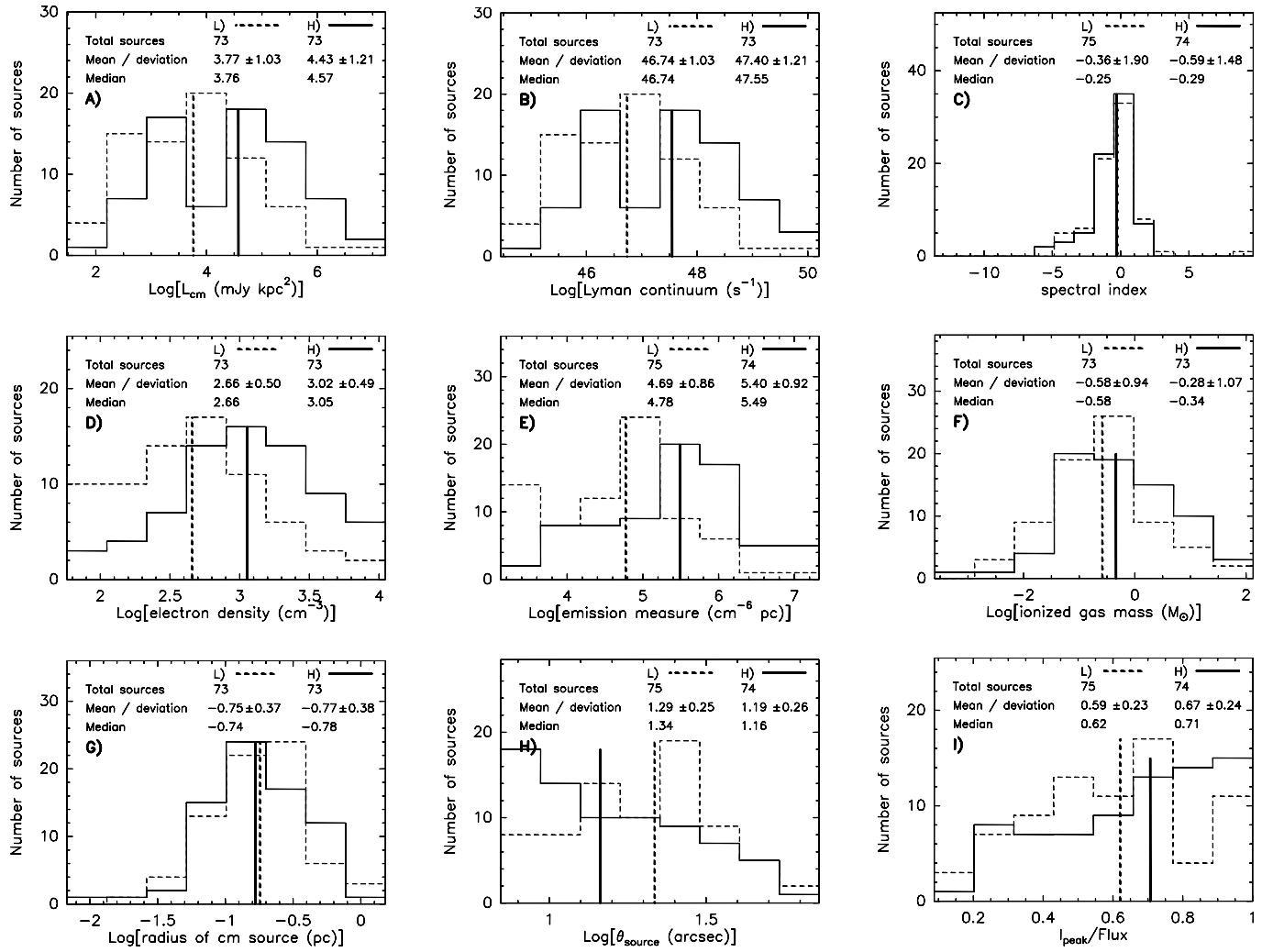
Fig. 6: Distributions of **a)** centimeter luminosity; **b)** Lyman continuum; **c)** spectral index; **d)** electron density; **e)** emission measure; **f)** ionized gas mass; **g)** linear radius of the centimeter source; **h)** deconvolved angular diameter, θ_S; and **i)** peak intensity to flux density ratio, for the centimeter sources associated with *Low* (dashed line) and *High* (solid line) regions. The numbers at the top of each panel are as in Fig. 3. The vertical thick lines indicate the median values.

extended) H ɪɪ regions. Regarding the water maser association, Palla et al. (1991) find that the detection rate for *High* sources (26%) is almost 3 times larger than that of *Low* sources (9%). In our sample, we obtain a water maser detection rate of 46% and 33% for the *High* and *Low* sources, respectively. A direct comparison of the detection rates between the two works is difficult since the observing conditions (sensitivity and spectral resolution) differ considerably between our observations and Palla et al. (1991).

In summary, it seems that the presence of H ɪɪ regions or water masers, as well as the properties of the millimeter and dense gas emission, are similar for both groups, suggesting that there may exist more effective criteria to make an evolutionary classification rather than the infrared colors of *Low* and *High* sources. This will be discussed in the next section.

6. Evolutionary sequence

6.1. Millimeter and infrared counterparts

In this section, we discuss the association between millimeter and infrared sources, with the aim of establishing a classification of the objects based on their emission in the two wavelength regimes. For the millimeter sources, we used the sample of 210 regions, containing 667 millimeter clumps, studied by Beltrán et al. (2006) with the SEST telescope at 1.2 mm. For the infrared sources, we used the MSX Point Source Catalogue (Price et al. 1999), providing information between 8 μm and 21 μm (mid-IR) with an angular resolution (20″) similar to that of the SEST (24″) and ATCA (20–25″) maps . We considered only the MSX sources detected at 21 μm satisfying one of two additional criteria: (a) quality factor $\geq$3 in the E-band (21.3 μm), i. e., well detected; (b) quality factor 1 or 2 in the E-band, and quality factor $\geq$3 in at least one of the other bands (A: 8.3 μm, C: 12.1 μm, D: 14.7 μm). We used the MSX data, instead of other more sensitive and recent surveys (e. g., MIPSGAL at 24 μm) for four reasons: the existence of a point source catalogue for the MSX data, not yet available for other surveys; the saturation of many regions in

9

Fig. 8: 21 μm-to-1.2 mm flux ratio versus the normalized angular separation between millimeter and infrared sources. Blue open circles correspond to *type 1* sources (only millimeter emission), green filled circles correspond to *type 2* sources (association between millimeter and infrared emission); and red stars correspond to *type 3* sources (only infrared emission). Blue symbols (millimeter-only sources) are upper limits in which we have considered an upper limit of 4 times the rms noise in the MSX image. Red symbols (infrared-only sources) are lower limits in which we have considered an upper limit of 4 times the rms noise in the SEST image.

Fig. 7: **Top**: 21 μm-to-1.2 mm flux ratio versus the normalized angular separation between millimeter and infrared sources (see Sect. 6.1 for details). The flux at 21 μm flux has been obtained from the MSX catalogue, and the flux at 1.2 mm has been obtained from Beltrán et al. (2006). **Bottom**: standard deviation in the 21 μm-to-1.2 mm flux ratio versus the normalized angular separation (black dots). The dashed horizontal blue line correspond to the standard deviation ($\simeq 0.57$) for data with $\Delta_n > 0.7$. The grey histogram indicates the probability that the distribution of data within one bin is the same as the global distribution with $\Delta_n > 1$, using the Kolmogorov-Smirnov statistical test. The red vertical line indicates the normalized angular separation that differentiates between millimeter and infrared associated and non-associated sources (see Section 6.1).

our sample in the MIPSGAL images; the similar resolution with our millimeter and centimeter images; and consistency with the method used by Molinari et al. (2008; see next sections).

In order to determine the association between millimeter and infrared sources, we performed the following analysis. We calculated the angular separation between millimeter and infrared sources, and searched for the closest companion of each millimeter source. In the top panel of Fig. 7, we plot the 21 μm-to-1.2 mm flux ratio (hereafter $S_{21\mu m}/S_{1.2mm}$) versus the angular separation for each pair of millimeter and infrared sources (hereafter Δ_n). Note that we use a normalized angular separation (to get rid of the dependence on distance), computed by dividing the angular separation by the sum of the angular radii of the millimeter and infrared sources. The angular radius is equal to half the angular diameter reported in Beltrán et al. (2006) for the millimeter sources, and is assumed to be half the 20″ HPBW for the MSX sources. Our expectation is that $S_{21\mu m}/S_{1.2mm}$ could take any value if the millimeter and infrared fluxes come from two

different (unrelated) objects, whereas it should span a narrow range of values if the two fluxes belong to the same object (as young stellar objects have roughly similar spectral energy distributions). We expect that the probability that the MSX source is the real counterpart of the mm source decreases with such a separation. This expectation is confirmed by the fact that the flux ratio spans a larger range of values for increasing separation, thus confirming that the MSX source is really associated with the mm source only for sufficiently small Δ_n. This can be seen in the bottom panel of Fig. 7 (black dots), where the dispersion σ_r of $S_{21\mu m}/S_{1.2mm}$ appears to decrease below $\Delta_n \simeq 0.7$, marked by the vertical line in the figure. This normalized separation corresponds approximately to an angular separation between the millimeter and infrared sources of ~15″ (taking into account the typical sizes of the millimeter sources: ~20–40″; Beltrán et al. 2006). For a range of distances between 1 and 7 kpc, the resulting spatial separation is ~0.07–0.5 pc.

In addition, we used the Kolmogorov-Smirnov statistical test to compare the $S_{21\mu m}/S_{1.2mm}$ distribution in different bins with the global distribution containing data with $\Delta_n > 1$. The result is shown by the grey histogram in the bottom panel of Fig. 7, and demonstrates that the distributions for almost all bins with $\Delta_n \lesssim 1$ are statistically different with respect to the global distribution: the test shows that the probability of the distribution in each bin being the same of the global distribution becomes very low ($P \lesssim 0.3$) for $\Delta_n \lesssim 1$. Furthermore, the comparison of the distributions with $\Delta_n < 1$ and $\Delta_n > 1$ results in a minimum probability of $P \simeq 0.05$. The results of the Kolmogorov-Smirnov statistical tests, together with the decrease in the dispersion for $\Delta_n \lesssim 0.7$, are strong evidence of a different behavior between IR-mm associations with respect to the normalized angular separation. We thus conclude that only an IR counterpart satisfying the condition $\Delta_n < 0.7$ (as a conservative value from the range 0.7–1, corresponding to a spatial separation of 0.07–
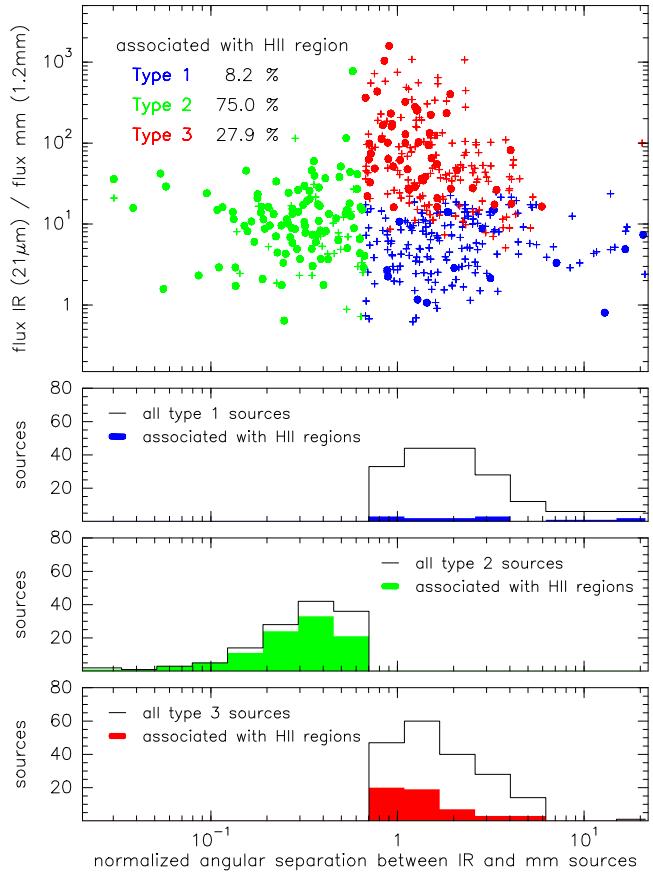
Fig. 9: Associations with H II regions. **Top**: 21 μm-to-1.2 mm flux ratio versus the normalized angular separation between millimeter and infrared sources as in Fig. 8. Blue symbols correspond to *type 1* sources (only millimeter emission), green symbols correspond to *type 2* sources (association between millimeter and infrared emission); and red symbols correspond to *type 3* sources (only infrared emission). Colored filled dots show those objects associated with H II regions detected with ATCA (see Table 3). The numbers at the top of the panel indicate the percentage of association of H II regions in each of three groups. **Bottom**: Histograms of the normalized angular separation for the different groups. The solid black lines correspond to all the sources of each group, and the colored filled histograms correspond those objects associated with H II regions.

0.5 pc; see above) is physically associated with the corresponding mm source.

6.2. Source classification

The analysis presented in the previous section allows us to identify three types of YSOs: millimeter sources associated with infrared counterparts, millimeter sources not associated with an infrared source, and infrared sources lying relatively close to millimeter sources (and therefore likely associated with star forming regions) but not associated with them. Note that while the millimeter continuum emission probably comes from dust envelopes around YSOs, we cannot be sure that the same is true for the infrared emission, which could be produced by more evolved objects or background/foreground stars. With the aim of selecting only YSO candidates we applied the following restric-
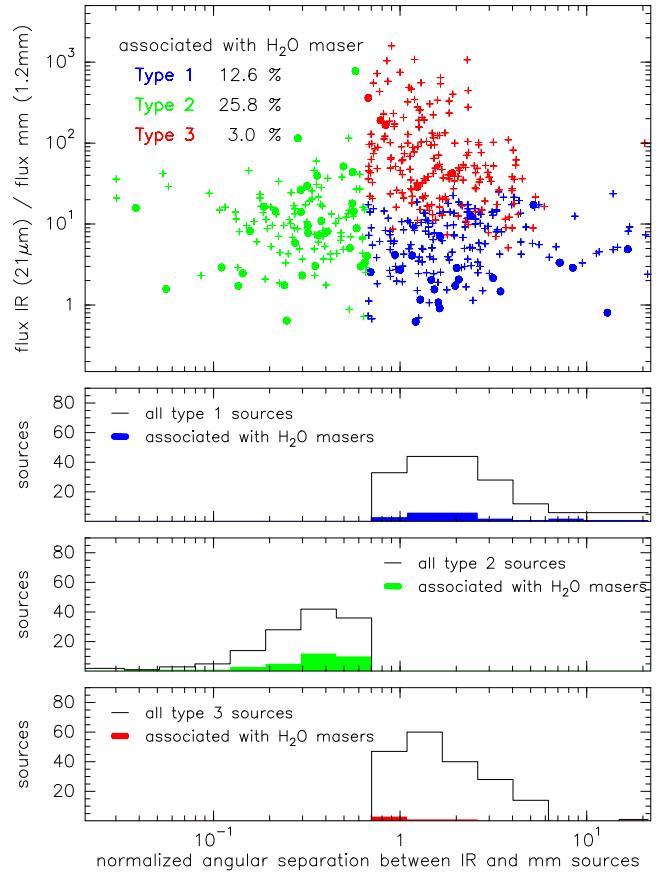
Fig. 10: Associations with H$_2$O masers. **Top**: 21 μm-to-1.2 mm flux ratio versus the normalized angular separation between millimeter and infrared sources as in Fig. 9. Colored filled dots show those objects associated with H$_2$O masers detected with ATCA (see Table 4). The numbers at the top of the panel indicate the percentage of association of H$_2$O masers in each of three groups. **Bottom**: Histograms of the normalized angular separation for the different groups. The solid black lines correspond to all the sources of each group, and the colored filled histograms correspond those objects associated with H$_2$O masers.

tion to our catalogue of infrared-only sources: $F_{21\,\mu m} \geq F_{15\,\mu m}$ and $F_{21\,\mu m} \geq F_{12\,\mu m}$ in the MSX bands, to ensure an increasing spectral energy distribution at infrared wavelengths typical of YSOs[5]. In Fig. 8 we plot the ratio $S_{21\mu m}/S_{1.2mm}$ versus the normalized angular separation, taking into account the previous restriction, and considering the sources within the ATCA fields. For those millimeter sources with no infrared counterpart we assumed a flux at 21 μm equal to an upper limit 4 times the rms noise level of the MSX map, and, similarly, for sources only detected at infrared wavelengths we assumed the flux at 1.2 mm to be an upper limit equal to 4 times the rms noise level of the millimeter map. The resulting plot shows the three different groups of sources: *type 1* only millimeter continuum sources (blue circles), *type 2* millimeter continuum sources associated with an infrared counterpart (green dots), and *type 3* infrared sources located far from a millimeter source (red stars).

---

[5] These selection criteria based on the MSX fluxes are similar to those used for the Red MSX Source (RMS) survey (e. g., Hoare et al. 2004; Urquhart et al. 2008): $F_{21\,\mu m} \geq 2.7$ Jy, $F_{21\,\mu m} \geq 2\,F_{8\,\mu m}$, and $F_{21\,\mu m} \geq F_{15\,\mu m} \geq F_{8\,\mu m}$
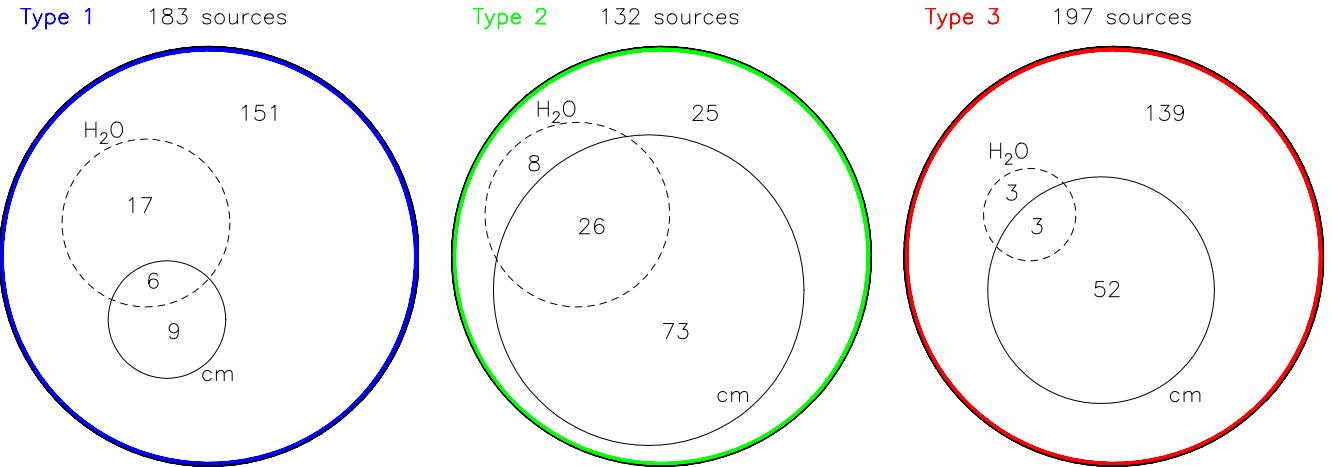
Fig. 11: Sketch showing the number of sources in each of the three types of sources. We indicate the number of sources associated with only H II regions, only water maser emission, and both H II regions and water masers.

Table 10: Number (and percentage) of sources associated with H II regions and water masers for types 1, 2 and 3.

	type 1		type 2		type 3	
H II region	15	8%	99	75%	55	28%
H_2O maser	23	13%	34	26%	6	3%
all	183	100%	132	100%	197	100%

These three groups of sources correspond to the classification proposed by Molinari et al. (2008) from a study of the infrared and millimeter properties of a sample of 42 regions. Molinari et al. (2008) checked by eye the infrared and millimeter emission, and by fitting different spectral energy distributions, identified associations between infrared and millimeter sources. A simple model allowed the authors to establish an evolutionary sequence, in order of increasing age going from *type 1* to *type 3* objects. In the sample studied by Molinari et al. (2008) there are 33 millimeter sources taken from Beltrán et al. (2006) and thus included in our analysis. Taking into account our method for determining associations between infrared and millimeter sources, and comparing it with the results of Molinari et al. (2008), we conclude that ~80% of the 33 sources agree with respect to the source classification in type 1, 2 or 3. Thus, our more automatic classification method, used for the classification in different evolutionary stages of our sources, agrees with the Molinari et al. method, and will be used for further analysis. In Tables 7 to 9, we list the millimeter and/or infrared sources classified in the three evolutionary stages.

At this point, we can compare the evolutionary classification derived from the IR–mm analysis with the *High–Low* classification obtained from the IRAS colors. If we consider the millimeter (SEST) and infrared (MSX) sources located within an IRAS beam (~2′), we find that an IRAS source with *Low* colors contains 42%, 27% and 31% of *type 1*, *2* and *3* sources, respectively; while within the beam of a *High* IRAS source we can find 23%, 37% and 40% of *type 1*, *2* and *3* sources, respectively. This result agrees with the analysis done by Molinari et al. (2008) in a much smaller sample, and suggests that less evolved sources (*type 1*) are typically found closer to a *Low* IRAS source than more evolved sources (*type 2* and *3*). However, evolved objects can also be found associated with *Low* IRAS sources, as shown by distinct studies (e. g., Molinari et al. 1998a, 2000), and as ex-
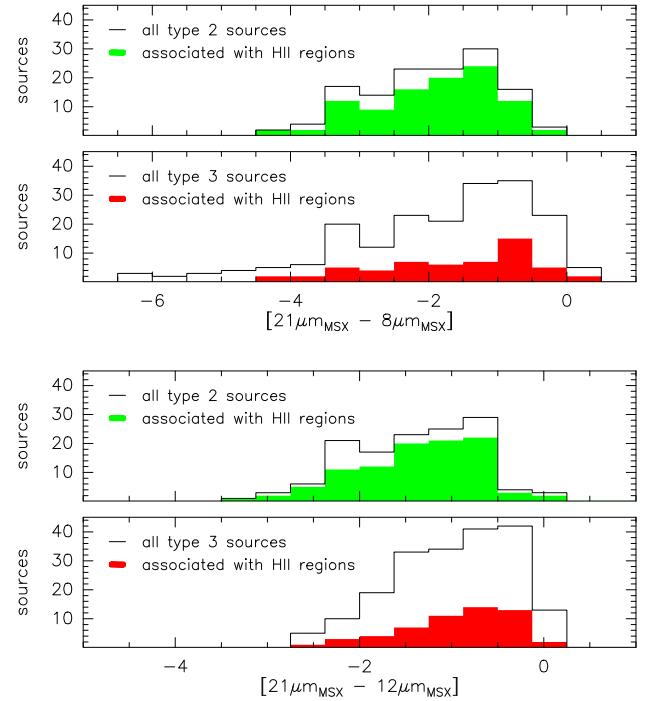
Fig. 12: Distributions of the MSX colors [21 μm–8 μm] (two top panels) and [21 μm–12 μm] (two bottom panels) for *type 2* (green histograms) and *type 3* (red histograms) sources. The solid black lines show the total number of sources of each group, and the colored filled histograms show those sources associated with H II regions.

pected by the large detection rate of H II regions found associated with *Low* sources (see Section 5.5).

6.3. H II *regions and* H_2O *masers*

In this section, we investigate the presence of H II regions and water masers in the three evolutionary stages (see Figures 9 and 10). We use the same criteria to establish if an H II region or a water maser is associated with a millimeter or infrared source, i. e.,
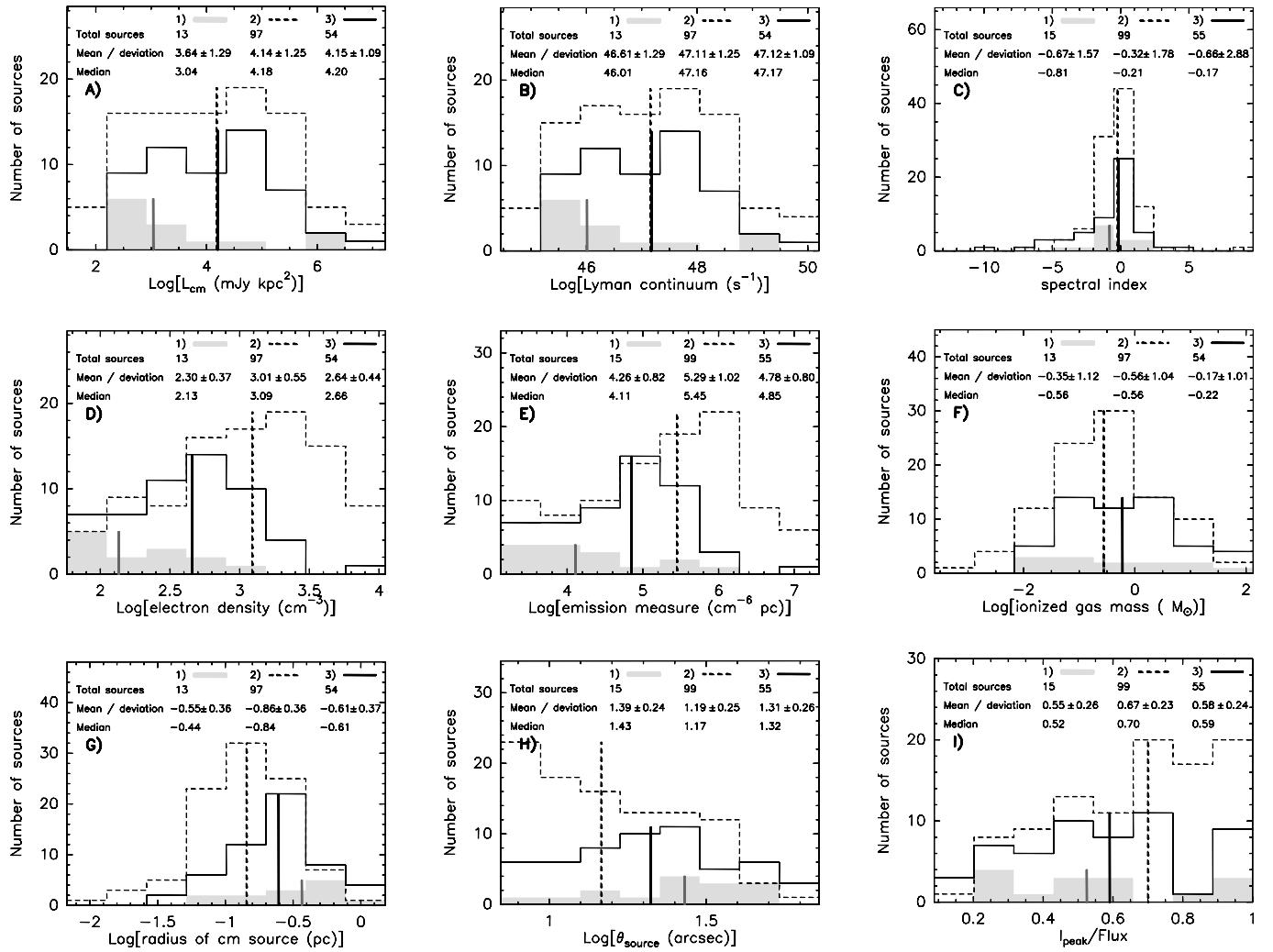
Fig. 13: Distributions of **a)** centimeter luminosity; **b)** Lyman continuum; **c)** spectral index; **d)** electron density; **e)** emission measure; **f)** ionized gas mass; **g)** linear radius of the centimeter source; **h)** deconvolved angular diameter, θ_S; and **i)** peak intensity to flux density ratio, for the centimeter sources in the evolutionary stages *type 1* (grey filled), *type 2* (dashed line) and *type 3* (solid line). The numbers at the top of each panel are as in Fig. 3. The vertical thick lines indicate the median values.

the normalized distance must be <0.7, using the size listed in Table 3 for the H ɪɪ regions, and the HPBW at 22 GHz for the water maser (the water maser emission is unresolved in our observations). In Fig. 11, we show a simple sketch indicating the associations with H ɪɪ regions and water masers for the three source types, and in Table 10, we summarize the number of sources and percentages of associations with H ɪɪ regions and water masers in the *type 1*, *2* and *3* sources.

Regarding the H ɪɪ regions, most of the centimeter continuum sources appear associated with *type 2* and *3* objects (corresponding to 72% of all detected sources), and only a low percentage (7%) are associated with *type 1* objects. The remaining 21% corresponds to H ɪɪ regions not associated with millimeter nor infrared sources. These results indicate on the one hand that for the first evolutionary stage (*type 1*) the H ɪɪ region has not developed yet (only an 8% of *type 1* sources are associated with H ɪɪ regions; see Fig. 9), and that the massive protostar begins to ionize the surrounding gas when the millimeter core is detectable at infrared wavelengths (75% of *type 2* sources are associated with H ɪɪ regions). On the other hand, in the last stages when the infrared source dominates the emission and most of the dusty

clump has been destroyed (i. e., *type 3*), one would expect that the association of H ɪɪ regions with infrared sources was higher than for *type 2* objects. In contrast, we observe a decrease in the percentage of associations (from 75% down to 28%). We investigated if there was a contamination of infrared sources not associated with star formation in our sample of *type 3* objects. From MSX color-color diagrams we do not detect a differentiation between infrared sources associated with H ɪɪ regions and infrared sources not associated. In Fig. 12, we show two MSX-color histograms for *type 2* and *type 3* objects. We can see that for each type the distribution of sources associated with H ɪɪ regions is similar to the total distribution, and thus we conclude that no significant contamination of not associated sources should affect the *type 3* sample.

In Fig. 13, we show the distribution of the physical parameters of the H ɪɪ regions associated with the three types of objects. It seems that the continuum flux and Lyman continuum is greater in more evolved objects (*type 2* and *3*) than in the regions associated with only millimeter emission (see last three columns of Table 6). Focusing on the two more evolved types, we can see that the electron density and the emission measure decrease from

type 2 to *type 3*, while the size increases, as expected if the H ɪɪ regions associated with type 3 objects are more evolved. Taking this into account, the relatively low percentage of association for *type 3* objects could be understood in terms of the properties of their H ɪɪ regions: if the H ɪɪ region is larger and has a lower density, our snapshot observations would be inadequate to detect these H ɪɪ regions, and thus the percentage of associations would appear reduced in comparison with *type 2* objects, the latter being associated with more compact and dense H ɪɪ regions, more easily detectable in our interferometric observations. The small number of H ɪɪ regions associated with *type 1* objects, makes it difficult to derive typical values for these H ɪɪ regions. However, it is worth noting that the sizes of these centimeter continuum sources are larger than those of *type 2* and *3* objects, contrary to what is expected if the H ɪɪ regions of *type 1* objects are less evolved. Similarly, low values of the density and emission measure, due to the large sizes, are also unexpected for less evolved H ɪɪ regions. An inspection of the maps for these sources reveals that most of these centimeter continuum sources are faint, which results in a bad estimation of the size, and in other cases a faint MSX infrared emission appears at the position of the H ɪɪ region, suggesting that there could be some contamination of *type 2* objects. This would imply, that the detection rate of H ɪɪ regions in the *type 1* group would be lower, as expected if these sources are younger.

In Fig. 14, we report the distribution of normalized distances between the millimeter source and the nearest centimeter continuum source. The distribution for *type 2* objects peaks at smaller normalized distances than for millimeter-only *type 1* objects. In massive YSOs the association with centimeter continuum emission typically indicates the developing of an H ɪɪ region, and thus, objects that have reached the ZAMS. The results shown in Fig. 14 agree with the tentative result shown by Molinari et al. (2008) in a smaller sample.

Regarding the water maser emission (see Fig. 10), we find that most of the water masers are associated with the earliest stages (67% for *type 1* and *2*), and only few of them (7%) are associated with *type 3* objects. The evolution might begin with millimeter-only objects (*type 1*) with only some of them associated with water maser emission. As the object evolves and becomes visible in the infrared (*type 2*), the number of masers associated with these objects increases by a factor of 2, most of them being associated with H ɪɪ regions. Finally, as the object evolves and becomes less embedded, the association with masers also decreases.

The sketch shown in Fig. 11 summarizes the results found in this work: while the H ɪɪ region phase is dominant in the *type 2* and *type 3* objects, the water masers are most likely associated with the first stages. These results confirm the evolutionary classification proposed by Molinari et al. (2008), in which *type 1* sources would be high-mass protostars embedded in dust clumps with maser emission but still not developing an H ɪɪ region, *type 2* sources would correspond to ZAMS OB stars with developed H ɪɪ regions, but still embedded in dust condensations and associated with maser emission, and *type 3* sources would be more evolved ZAMS OB stars surrounded only by remnants of their parental clouds and with more extended and less dense H ɪɪ regions. This scenario is consistent with the evolutionary schemes presented by Ellingsen et al. (2007) and Breen et al. (2010), in which water masers appear first in the evolution of a massive protostar, coexist with the H ɪɪ regions, and disappear while the H ɪɪ regions are still detectable. Similarly, the evolutionary stages proposed by Molinari et al. (2008) and this work compare well with the evolutionary classifications described by Beuther et al.
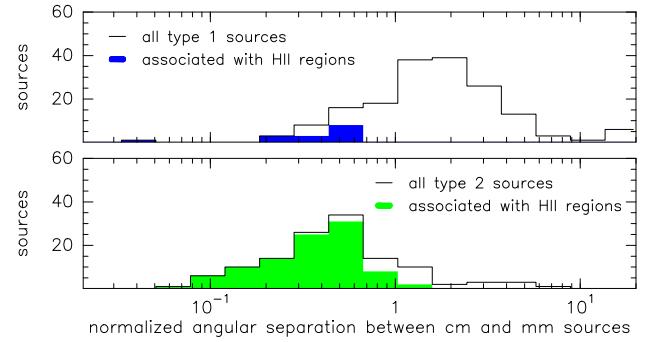
Fig. 14: Histograms of the normalized angular separation between the millimeter continuum source and the nearest H ɪɪ region for *type 1* (top panel) and *type 2* (bottom panel) sources.

(2007) or Zinnecker & Yorke (2007): *type 1* sources would correspond to High-Mass Starless Cores (HMSCs) or young High-Mass Protostellar Objects (HMPOs) likely associated with infrared dark clouds (IRDCs) and hot molecular cores (HMCs), *type 2* sources would be mainly evolved HMPOs or final stars associated with ultracompact H ɪɪ regions, and *type 3* objects would be final stars associated with compact or classical H ɪɪ regions.

7. Summary

We have carried out ATCA observations of the H_2O maser line and radio continuum emission at 18.0 GHz and 22.8 GHz, toward a sample of 192 southern ($\delta < -30°$) massive star forming regions containing several clumps already imaged at 1.2 mm (Beltrán et al. 2006). The sample consisted of 160 fields centered on an IRAS source plus 32 fields centered on a millimeter clump located $>150''$ from an IRAS source. In total we observed 79 *High* IRAS sources and 81 *Low* IRAS sources (according to the criteria of Palla et al. 1991). The main findings obtained in this work are:

– We detected centimeter continuum emission in 169 out of 192 fields, corresponding to a detection rate of 88%. In total, 12% of the fields do not show centimeter continuum emission (up to a level of ∼2 mJy), in 68% we find a single component (with an angular resolution of ∼20″), and in 20% we find multiple components.

– For the water maser emission, we have detected 85 distinct components in 78 fields, corresponding to a detection rate of 41%. Due to the poor spectral resolution (12.5 km s^{-1}), we are probably detecting only relatively strong ($\gtrsim$1 Jy) water masers.

– Assuming that the centimeter continuum emission comes from optically thin H ɪɪ regions, we have derived the physical parameters obtaining values in agreement with compact H ɪɪ regions (diameters ∼0.36 pc, electron densities ∼580 cm^{-3}, emission measures ∼7.9×10^5 cm^{-6} pc). The derived number of Lyman continuum photons spans a range between 10^{44} s^{-1} and 10^{50} s^{-1}, corresponding to spectral types B5 to O5.

– No large differences are found when studying the association or physical parameters of the H ɪɪ regions in the *High* and *Low* groups of sources. We found an H ɪɪ region detection rate of 94% and 93% for *High* and *Low* sources, respectively, with the electron density and emission measure slightly higher for *High* sources. For the water maser emission, we found a detection rate of 46% and 33% for *High* and

Low sources. These detection rates differ from previous results (e. g., Palla et al. 1991; Molinari et al. 1998a) probably due to the different observing conditions (sensitivity, angular resolution and spectral resolution).

– We have compared the Lyman continuum obtained from the measured radio flux with the bolometric luminosity estimated from the IRAS fluxes. Several sources (preferentially associated with the earliest evolutionary stages, and with B-type stars) show an excess of Lyman continuum that cannot be trivially explained. If the distances, which are the main source of uncertainty in this comparison, are confirmed (or more accurately estimated), and the excess of Lyman continuum is still appreciable, we should consider that B-stars could emit in the UV range much more than predicted by standard models of stellar atmospheres or that there exists another source of Lyman continuum in addition to the ZAMS star.

– We have investigated the relation of the electron density and size of the H II regions, and compared our distribution with that obtained assuming that O-B type stars are distributed in the Galaxy as proposed by Mottram et al. (2011). From this analysis, we estimate the number of compact and extended H II regions in the Galaxy to be ∼15000.

We have used the SEST millimeter survey by Beltrán et al. (2006) and the MSX Point Source Catalogue (Price et al. 1999), to investigate the presence and association of millimeter and infrared sources, with the aim of establishing an evolutionary classification. Following the work of Molinari et al. (2008), we have established three different groups of sources, in order of increasing age: (*type 1*) only millimeter continuum sources, (*type 2*) millimeter continuum sources associated with an infrared counterpart, and (*type 3*) infrared sources without millimeter continuum emission. The main findings for the H II region and water maser properties in this evolutionary classification are:

– H II regions are mainly associated (72%) with *type 2* and *3* sources, while only 7% are associated with *type 1* objects. Water masers are mainly associated with *type 1* and *2* objects: 67% compared to the 7% association with *type 3* sources.

– H II regions associated with *type 3* sources are larger in size and less dense than those associated with *type 2* sources, as expected if the H II region expands as it evolves.

– The detailed analysis of each group results in an evolutionary trend for the association of H II regions (8% for *type 1*, 75% for *type 2*, and 28% for *type 3*) and water masers (13% for *type 1*, 26% for *type 2*, and 3% for *type 3*). This scenario is consistent with the evolutionary schemes presented by Ellingsen et al. (2007) and Breen et al. (2010), in which water masers appear first in the evolution of a massive protostar, coexist with the H II regions, and disappear while the H II regions are still detectable. Our results of H II regions and H$_2$O maser associations with different evolutionary types, confirm the evolutionary classification proposed by Molinari et al. (2008), which compares well with the evolutionary classifications described by Beuther et al. (2007) and Zinnecker & Yorke (2007). Thus, *Type 1* sources, associated with the earliest stages in our evolutionary scheme, appear to be good candidates to discriminate between the different theoretical models of massive star formation.

References

Anglada, G. 1996, Radio Emission from the Stars and the Sun, 93, 3
Anglada, G., Villuendas, E., Estalella, R., et al. 1998, AJ, 116, 2953
Beltrán, M. T., Brand, J., Cesaroni, R., et al. 2006, A&A, 447, 221
Beuther, H., Schilke, P., Menten, K. M., et al. 2002, ApJ, 566, 945
Beuther, H., Churchwell, E. B., McKee, C. F., & Tan, J. C. 2007, Protostars and Planets V, 165
Bonnell, I. A., Vine, S. G., & Bate, M. R. 2004, MNRAS, 349, 735
Brand, J., Cesaroni, R., Palla, F., & Molinari, S. 2001, A&A, 370, 230
Breen, S. L., Caswell, J. L., Ellingsen, S. P., & Phillips, C. J. 2010, MNRAS, 406, 1487
Bronfman, L., Alvarez, H., Cohen, R. S., & Thaddeus, P. 1989, ApJS, 71, 481
Carrasco-González, C., Rodríguez, L. F., Anglada, G., et al. 2010, Science, 330, 1209
Chabrier, G. 2005, The Initial Mass Function 50 Years Later, 327, 41
Diaz-Miller, R. I., Franco, J., & Shore, S. N. 1998, ApJ, 501, 192
Ellingsen, S. P., Voronkov, M. A., Cragg, D. M., et al. 2007, IAU Symposium, 242, 213
Faúndez, S., Bronfman, L., Garay, G., et al. 2004, A&A, 426, 97
Faustini, F., Molinari, S., Testi, L., & Brand, J. 2009, A&A, 503, 801
Felli, M., Brand, J., Cesaroni, R., et al. 2007, A&A, 476, 373
Fontani, F., Cesaroni, R., Testi, L., et al. 2004a, A&A, 414, 299
Fontani, F., Cesaroni, R., Testi, L., et al. 2004b, A&A, 424, 179
Fontani, F., Beltrán, M. T., Brand, J., et al. 2005, A&A, 432, 921
Fontani, F., Caselli, P., Crapsi, A., et al. 2006, A&A, 460, 709
Garay, G., & Lizano, S. 1999, PASP, 111, 1049
Grave, J. M. C., & Kumar, M. S. N. 2009, A&A, 498, 147
Green, J. A., & McClure-Griffiths, N. M. 2011, MNRAS, 417, 2500
Gwinn, C. R. 1994, ApJ, 429, 253
Hill, T., Burton, M. G., Minier, V., et al. 2005, MNRAS, 363, 405
Hoare, M. G., Lumsden, S. L., Oudmaijer, R. D., et al. 2006, Milky Way Surveys: The Structure and Evolution of our Galaxy, 317, 156
Krumholz, M. R., Klein, R. I., McKee, C. F., Offner, S. S. R., & Cunningham, A. J. 2009, Science, 323, 754
Kuiper, R., Klahr, H., Beuther, H., & Henning, T. 2010, ApJ, 722, 1556
Kurtz, S., Churchwell, E., & Wood, D. O. S. 1994, ApJS, 91, 659
Kurtz, S. 2005, in IAU Symp. 227, Massive Star Birth: A Crossroads of Astrophysics, ed. R. Cesaroni, M. Felli, E. Churchwell, & M. Walmsley (Cambridge: Cambridge Univ. Press), 111
Lampton, M., Margon, B., & Bowyer, S. 1976, ApJ, 208, 177
McKee, C. F., & Tan, J. C. 2003, ApJ, 585, 850
Martins, F., Schaerer, D., & Hillier, D. J. 2005, A&A, 436, 1049
Martín-Hernández, N. L., van der Hulst, J. M., & Tielens, A. G. G. M. 2003, A&A, 407, 957
Mezger, P. G., & Henderson, A. P. 1967, ApJ, 147, 471
Moscadelli, L., Cesaroni, R., Rioja, M. J., Dodson, R., & Reid, M. J. 2011, A&A, 526, A66
Molinari, S., Brand, J., Cesaroni, R., & Palla, F. 1996, A&A, 308, 573
Molinari, S., Brand, J., Cesaroni, R., Palla, F., & Palumbo, G. G. C. 1998a, A&A, 336, 339
Molinari, S., Testi, L., Brand, J., Cesaroni, R., & Palla, F. 1998b, ApJ, 505, L39
Molinari, S., Brand, J., Cesaroni, R., & Palla, F. 2000, A&A, 355, 617
Molinari, S., Testi, L., Rodríguez, L. F., & Zhang, Q. 2002, ApJ, 570, 758
Molinari, S., Pezzuto, S., Cesaroni, R., et al. 2008, A&A, 481, 345
Mottram, J. C., Hoare, M. G., Davies, B., et al. 2011, ApJ, 730, L33
Palla, F., Brand, J., Comoretto, G., Felli, M., & Cesaroni, R. 1991, A&A, 246, 249
Palla, F., Cesaroni, R., Brand, J., et al. 1993, A&A, 280, 599
Palla, F., & Stahler, S. W. 1993, ApJ, 418, 414
Panagia, N. 1973, AJ, 78, 929
Panagia, N., & Walmsley, C. M. 1978, A&A, 70, 411
Price, S. D., Egan, M. P., Mizuno, D. R., Kuchar, T. A., & Carey, S. J. 1999, Bulletin of the American Astronomical Society, 31, 1515
Reid, M. J., Argon, A. L., Masson, C. R., Menten, K. M., & Moran, J. M. 1995, ApJ, 443, 238
Richards, P. J., Little, L. T., Heaton, B. D., & Toriseva, M. 1987, MNRAS, 228, 43
Rubin, R. H. 1968, ApJ, 154, 391
Sánchez-Monge, Á., Palau, A., Estalella, R., Beltrán, M. T., & Girart, J. M. 2008, A&A, 485, 497
Sault, R. J., Teuben, P. J., & Wright, M. C. H. 1995, Astronomical Data Analysis Software and Systems IV, 77, 433
Schaerer, D., & de Koter, A. 1997, A&A, 322, 598
Sridharan, T. K., Beuther, H., Schilke, P., Menten, K. M., & Wyrowski, F. 2002, ApJ, 566, 931
Thompson, R. I. 1984, ApJ, 283, 165
Urquhart, J. S., Hoare, M. G., Lumsden, S. L., et al. 2012, MNRAS, 420, 1656
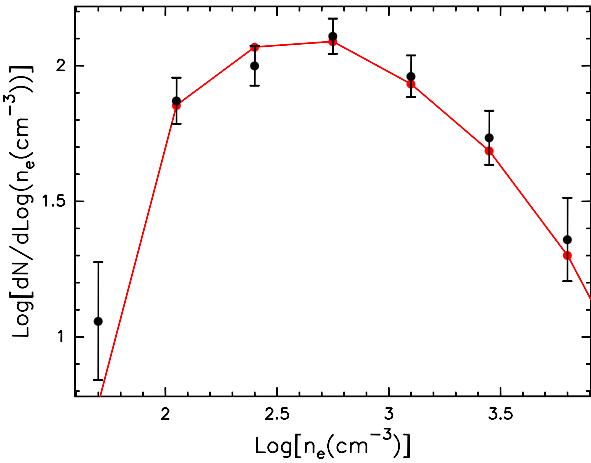
Fig. A.1: Electron density function obtained from the data (points with error bars) and best fit from the model (solid line) for $\alpha=-0.15$ and $N_{\mathrm{HII}}=15000$.
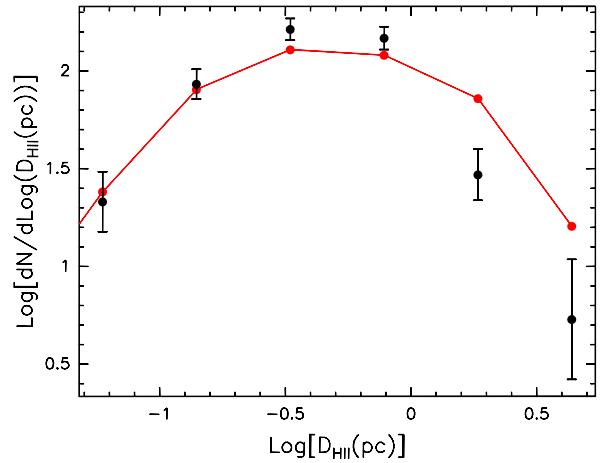
Fig. A.3: H II region diameter function obtained from the data (points with error bars) and from the same model fit (solid line) as in Fig. A.1.
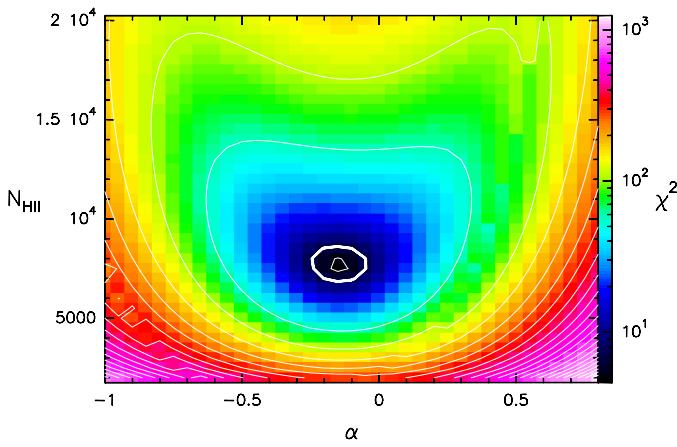
Fig. A.2: χ^2 obtained by comparing the n_{e} function from the model to that obtained from the data (see Fig. A.1), as a function of the two free parameters, α and N_{HII}. The minimum value (4.64) is obtained for $\alpha=-0.15$ and $N_{\mathrm{HII}}=15000$. The thick contour corresponds to χ^2 exceeding the minimum value by 2.3, as recommended by Lampton et al. (1976) to estimate the 1σ confidence level.

Urquhart, J. S., Hoare, M. G., Lumsden, S. L., Oudmaijer, R. D., & Moore, T. J. T. 2008, Massive Star Formation: Observations Confront Theory, 387, 381

Vacca, W. D., Garmany, C. D., & Shull, J. M. 1996, ApJ, 460, 914

Wilson, W. E., Ferris, R. H., Axtens, P., et al. 2011, MNRAS, 416, 832

Wood, D. O. S., & Churchwell, E. 1989, ApJS, 69, 831

Zhang, Q., Hunter, T. R., Brand, J., et al. 2001, ApJ, 552, L167

Zhang, Q., Hunter, T. R., Brand, J., et al. 2005, ApJ, 625, 864

Zinnecker, H., & Yorke, H. W. 2007, ARA&A, 45, 481

Appendix A: Model description

The purpose of this appendix is to give an estimate of the number of H II regions that can be detected in our survey. This obviously depends on the physical parameters of the H II regions, their distances, and the sensitivity of our observations. We make the following assumptions:

– the H II regions are spatially distributed across the Galaxy according to the equation

$$\frac{dN}{dV} = \frac{\exp\left[-\frac{|z|}{z_{\mathrm{d}}}\right]}{2z_{\mathrm{d}}} \frac{\exp\left[-\left(\frac{R-R_{\mathrm{o}}}{R_{\mathrm{d}}}\right)^2\right] - \exp\left[-\left(\frac{R-R_{\mathrm{o}}}{R_{\mathrm{h}}}\right)^2\right]}{\pi\left[R_{\mathrm{d}}\left(R_{\mathrm{d}} + \sqrt{\pi}R_{\mathrm{o}}\right) - R_{\mathrm{h}}\left(R_{\mathrm{h}} + \sqrt{\pi}R_{\mathrm{o}}\right)\right]}$$

$$\Leftrightarrow R \geq R_{\mathrm{o}}$$

$$\frac{dN}{dV} = 0 \quad \Leftrightarrow \quad R < R_{\mathrm{o}}$$

which is the same as Eq. (1) of Mottram et al. (2011), normalized in such a way that $\int_{-\infty}^{+\infty} dz \int_{R_{\mathrm{o}}}^{+\infty} \frac{dN}{dV} 2\pi R\, dR = 1$; here R is the galactocentric distance, z the height on the Galactic plane, $R_{\mathrm{o}}=2.2$ kpc, $R_{\mathrm{d}}=6.99$ kpc, $R_{\mathrm{h}}=1.71$ kpc, and $z_{\mathrm{d}}=0.039$ kpc (from Mottram et al. 2011);

– the H II regions are homogeneous Strömgren spheres ionized by stars with luminosities in the range 10^3–10^6 $L_{\odot}$;

– the normalized luminosity function ($\int_{\mathrm{Log}L_1}^{\mathrm{Log}L_2} \frac{dN}{d\mathrm{Log}L} d\mathrm{Log}L = 1$) of the ionizing star(s) is described by the power law

$$\frac{dN}{d\mathrm{Log}L} = \frac{\beta \ln 10\, L^{\beta}}{L_2^{\beta} - L_1^{\beta}}$$

with $L_1=10^3$ $L_{\odot}$, $L_2=10^6$ $L_{\odot}$, and $\beta=-0.9$, as found by Mottram et al. (2011);

– the normalized electron density distribution ($\int_{\mathrm{Log}n_{\mathrm{e}1}}^{\mathrm{Log}n_{\mathrm{e}2}} \frac{dN}{d\mathrm{Log}n_{\mathrm{e}}} d\mathrm{Log}n_{\mathrm{e}} = 1$) is also described by a power law, i. e.,

$$\frac{dN}{d\mathrm{Log}n_{\mathrm{e}}} = \frac{\alpha \ln 10\, n_{\mathrm{e}}^{\alpha}}{n_{\mathrm{e}2}^{\alpha} - n_{\mathrm{e}1}^{\alpha}} \quad \Leftrightarrow \quad \alpha \neq 0$$

$$\frac{dN}{d\mathrm{Log}n_{\mathrm{e}}} = \frac{\ln 10}{\ln(n_{\mathrm{e}2}/n_{\mathrm{e}1})} \quad \Leftrightarrow \quad \alpha = 0$$

with $n_{\mathrm{e}1}=30$ cm^{-3} and $n_{\mathrm{e}2}=2\times10^4$ cm^{-3} to span the range of n_{e} in Fig. 5.

Under these assumptions, the number of Galactic H II regions per unit volume, dex in luminosity, and dex in electron density is given by the expression

$$\mathcal{N}(R, z, \mathrm{Log}L, \mathrm{Log}n_{\mathrm{e}}) = N_{\mathrm{HII}} \frac{dN}{dV} \frac{dN}{d\mathrm{Log}L} \frac{dN}{d\mathrm{Log}n_{\mathrm{e}}}, \qquad (A.1)$$

where N_{HII} is the total number of H II regions. There are only two free parameters in this model: the index α and N_{HII}. In order to find the corresponding values, we can fit the electron density function obtained from our data and represented by the points with error bars in Fig. A.1. The number of H II regions in each n_{e} bin of this figure can be calculated from the model in the following way. The volume of the Galaxy is divided in a suitable number of cells in cylindrical coordinates and for each of these, Equation (A.1) is used to calculate the number of H II regions contained in that cell, spanning all luminosities in the range L_1-L_2, and with density falling in the chosen bin. In this process, only cells falling in the region surveyed by us (i. e., those with $254<l<360°$ and $|b|<10°$) were counted. Moreover, for each L the corresponding Lyman continuum, N_{Ly}, was computed assuming the relationship for a cluster rather than that for a single star (see Section 5.1), as it seems unlikely that H II regions with linear diameters up to 3 pc may be ionized by only one star. From n_{e} and N_{Ly}, one can calculate the diameter of the Strömgren H II region, D_{HII}, and the corresponding angular diameter and radio flux measured in the instrumental beam.

In order to take into account the bias due to the source selection criteria, as well as those introduced by the limited sensitivity of the observations, we took into account only the sources that satisfy the following requirements:

- $L/(4\pi d^2)>1.6\,L_{\odot}\,\mathrm{kpc}^{-2}$, the minimum bolometric flux of the IRAS sources selected by Palla et al. (1991) and Fontani et al. (2005);
- radio flux above 0.9 mJy beam^{-1}, the mean 3σ sensitivity of our maps;
- angular diameter below 60″, the maximum size imaged in our interferometric observations.

Finally, to construct the functions in Fig. A.1, we rejected all objects (both in the model and the data) with diameter $\leq 7″$, as these are basically unresolved and the corresponding value of n_{e} in Table 5 is a lower limit.

The best fit to the electron density function is compared to the data in Fig. A.1. Such a fit has been obtained with χ^2 minimization by varying the two free parameters of the models over a sufficiently large range of values. This is illustrated in Fig. A.2, where the χ^2 is plotted as a function of α and N_{HII}. The thick contour corresponds to the minimum χ^2 value (4.64) plus 2.3, which gives the 1σ confidence level according to Table 1 of Lampton et al. (1976). We conclude that the best fit is obtained for $N_{\mathrm{HII}}=15000^{+2000}_{-1300}$ and $\alpha=-0.15\pm0.1$

As previously explained, for given n_{e} and N_{Ly}, the H II region size is univocally determined. This means that knowledge of the density function $\frac{\mathrm{d}N}{\mathrm{d}\mathrm{Log}n_{\mathrm{e}}}$ provides us also with the analogous function for the linear diameter, $\frac{\mathrm{d}N}{\mathrm{d}\mathrm{Log}D_{\mathrm{HII}}}$. The latter is shown in Fig. A.3 and compared to the observed distribution. Clearly the two are quite consistent for all diameters, with some discrepancy for the largest D_{HII}, where the model appears to overestimate the measured value. However, the largest H II regions are also the most difficult to image with an interferometer, and this may explain such a small discrepancy.

Table 1: Target fields observed by ATCA at 18.0 GHz and 22.8 GHz

Region[a]	Type[b]	Dist.[c] (kpc)	α(J2000) (h m s)	δ(J2000) (° ′ ″)	l (°)	b (°)	18.0 GHz Beam (″×″)	P.A. (°)	Rms (Jy beam^{-1})	22.8 GHz Beam (″×″)	P.A. (°)	Rms (Jy beam^{-1})	Date[d]
08140−3559 0	H	3.8	08 15 59.00	−36 08 18.0	254.05	−0.56	29.1 × 18.7	−74	2.8×10^{-4}	21.9 × 14.8	−73	2.5×10^{-4}	25J
08211−4158 0	L	1.7	08 22 52.30	−42 07 57.0	259.76	−2.84	26.8 × 19.2	−76	2.0×10^{-4}	20.8 × 15.3	−75	1.0×10^{-4}	090
08438−4340 0	H	1.3	08 45 36.00	−43 51 01.0	263.62	−0.53	26.9 × 19.4	−79	2.5×10^{-3}	20.4 × 18.6	+86	1.5×10^{-3}	090
08470−4243 0	H	2.2	08 48 47.90	−42 54 22.0	263.25	+0.51	26.6 × 19.4	−76	1.7×10^{-4}	20.3 × 15.4	−77	2.5×10^{-4}	25J
08477−4359 0	L	1.8	08 49 32.90	−44 10 47.0	264.32	−0.18	26.4 × 19.3	−77	2.0×10^{-4}	20.2 × 15.3	−75	1.0×10^{-4}	090
08477−4359 1	L	1.8	08 49 35.13	−44 11 59.0	264.34	−0.19	26.6 × 19.3	−76	2.7×10^{-4}	20.1 × 15.5	−76	2.4×10^{-4}	25J
08563−4225 0	L	1.7	08 58 12.50	−42 37 34.0	264.14	+2.02	27.3 × 19.2	−76	5.0×10^{-5}	20.2 × 18.0	+89	7.0×10^{-5}	090
08589−4714 0	H	1.5	09 00 40.50	−47 25 55.0	268.06	−0.80	26.2 × 20.1	−76	2.0×10^{-4}	20.2 × 18.1	−83	8.0×10^{-5}	090
09014−4736 0	L	1.3	09 03 09.80	−47 48 28.0	268.62	−0.74	26.3 × 20.4	−77	2.0×10^{-4}	19.7 × 16.1	−78	2.0×10^{-4}	090
09026−4842 0	L	1.9	09 04 22.20	−48 54 21.0	269.57	−1.32	25.8 × 20.4	−77	1.3×10^{-4}	19.9 × 15.9	−78	1.5×10^{-4}	090
09131−4723 0	L	1.7	09 14 55.50	−47 36 13.0	269.81	+0.85	25.9 × 19.9	−75	5.0×10^{-5}	19.4 × 17.2	−77	3.0×10^{-5}	090
09166−4813 1	L	2.3	09 18 18.57	−48 26 49.0	270.81	+0.67	25.6 × 20.1	−77	7.0×10^{-5}	19.3 × 17.9	−56	3.0×10^{-5}	090
09209−5143 0	L	6.4	09 22 34.60	−51 56 23.0	273.77	−1.31	25.6 × 20.6	−73	2.9×10^{-4}	19.2 × 16.4	−75	3.3×10^{-4}	25J
09566−5607 0	H	6.8	09 58 23.30	−56 22 09.0	280.62	−1.19	25.0 × 21.0	−64	3.8×10^{-4}	19.3 × 16.5	−59	4.2×10^{-4}	25J
09578−5649 0	H	1.7	09 59 31.00	−57 03 45.0	281.16	−1.64	28.3 × 22.4	+89	4.0×10^{-3}	21.1 × 17.6	+89	4.0×10^{-3}	090
10019−5712 0	H	1.8	10 03 40.50	−57 26 39.0	281.84	−1.61	27.8 × 22.4	+87	7.0×10^{-4}	22.7 × 18.9	+52	1.0×10^{-4}	090
10038−5705 0	H	6.0	10 05 31.90	−57 19 54.0	281.98	−1.37	24.6 × 21.6	−66	2.7×10^{-4}	19.1 × 16.5	−63	3.3×10^{-4}	25J
10088−5730 2	L	1.8	10 10 41.72	−57 44 36.0	282.78	−1.30	27.3 × 22.7	+87	1.0×10^{-4}	21.1 × 17.3	+87	3.0×10^{-5}	090
10095−5843 0	L	1.1	10 11 15.80	−58 58 15.0	283.55	−2.27	25.7 × 23.1	−89	6.0×10^{-5}	19.5 × 17.8	+88	1.0×10^{-4}	100
10123−5728 0	L	0.9[f]	10 14 08.80	−57 42 12.0	283.14	−1.01	27.2 × 22.7	+86	1.5×10^{-3}	21.2 × 17.3	+86	8.0×10^{-4}	090
10184−5748 0	H	5.4	10 20 14.70	−58 03 38.0	284.01	−0.85	26.6 × 22.9	+87	4.4×10^{-3}	20.1 × 18.0	+85	2.5×10^{-2}	25J
10276−5711 0	H	5.9	10 29 30.10	−57 26 40.0	284.73	+0.32	25.6 × 20.9	−66	2.0×10^{-3}	19.9 × 16.4	−62	1.8×10^{-3}	26J
10277−5730 0	L	5.8	10 29 35.40	−57 45 34.0	284.90	+0.06	26.4 × 22.3	+88	6.0×10^{-4}	19.9 × 17.6	+88	5.8×10^{-4}	25J
10286−5838 0	H	5.9	10 30 31.50	−58 53 30.0	285.59	−0.85	24.8 × 20.7	−59	2.6×10^{-4}	19.4 × 16.3	−55	3.2×10^{-4}	26J
10295−5802 0	H	5.0	10 31 28.30	−58 02 07.0	285.26	−0.05	26.9 × 22.5	+86	2.0×10^{-2}	20.2 × 17.6	+87	1.5×10^{-2}	26J
10317−5936 0	L	8.9	10 33 38.10	−59 51 54.0	286.43	−1.48	24.8 × 20.8	−48	7.0×10^{-4}	19.3 × 16.4	−49	4.0×10^{-4}	26J
10320−5928 0	H	9.1	10 33 56.40	−59 43 53.0	286.40	−1.35	26.5 × 23.4	+88	3.1×10^{-3}	19.7 × 17.9	+87	3.4×10^{-3}	25J
10337−5710 0	H	0.4	10 35 40.70	−57 26 15.0	285.44	+0.75	25.4 × 22.3	−79	3.0×10^{-4}	19.0 × 17.6	−73	4.0×10^{-4}	100
10439−5941 0	L	2.6	10 45 54.00	−59 57 03.0	287.81	−0.82	25.5 × 21.2	−54	3.0×10^{-4}	19.4 × 16.2	−52	1.3×10^{-3}	26J
10501−5556 0	H	2.5	10 52 11.00	−56 12 26.0	286.86	+2.90	25.9 × 22.2	−84	2.2×10^{-4}	21.0 × 18.7	+45	4.5×10^{-5}	090
10521−6031 0	L	8.1	10 54 11.00	−60 47 30.0	289.11	−1.11	25.5 × 23.5	+76	4.1×10^{-4}	19.5 × 18.1	+81	3.7×10^{-4}	25J
10537−5930 0	L	7.2	10 55 49.00	−59 46 47.0	288.85	−0.11	26.1 × 21.4	−57	3.4×10^{-4}	19.7 × 16.2	−55	4.8×10^{-4}	26J
10548−5929 0	L	7.6	10 56 51.90	−59 45 14.0	288.96	−0.03	25.8 × 23.4	+80	2.7×10^{-4}	19.5 × 18.2	+89	3.2×10^{-4}	25J
10555−6242 0	H	3.0	10 57 33.40	−62 58 55.0	290.41	−2.91	25.5 × 23.9	+72	7.0×10^{-5}	21.6 × 19.6	+58	3.0×10^{-5}	090
10545−6244 1	L	2.0	10 57 32.74	−62 59 22.0	290.41	−2.92	24.5 × 24.1	−15	7.0×10^{-5}	18.8 × 18.3	−34	1.0×10^{-4}	100
10559−5914 0	H	6.4	10 57 58.20	−59 30 24.0	288.99	+0.26	25.1 × 20.9	−55	1.4×10^{-4}	20.0 × 16.5	−59	1.6×10^{-4}	26J
10572−6018 0	L	7.2	10 59 19.30	−60 34 10.0	289.58	−0.64	25.8 × 23.4	+83	3.9×10^{-4}	19.7 × 18.1	+88	3.2×10^{-4}	25J
10575−5844 0	L	—	10 59 40.30	−59 01 05.0	288.97	+0.79	25.5 × 23.3	+84	8.0×10^{-5}	19.8 × 17.7	+81	8.0×10^{-5}	090
10589−6034 0	H	8.0	11 00 59.80	−60 50 27.0	289.88	−0.80	25.3 × 21.0	−51	2.3×10^{-3}	19.9 × 16.8	−56	5.9×10^{-3}	26J
10591−5934 0	L	2.8	11 01 15.80	−59 51 01.0	289.50	+0.12	25.5 × 23.5	+77	2.9×10^{-4}	19.6 × 18.1	+85	4.4×10^{-4}	25J
11079−6101 0	H	8.2	11 10 01.40	−61 18 15.0	291.07	−0.79	25.9 × 21.1	−59	5.0×10^{-3}	19.8 × 16.5	−53	3.5×10^{-3}	26J
11220−6147 0	H	7.8	11 24 18.20	−62 04 04.0	292.92	−0.90	25.0 × 23.7	+76	2.9×10^{-4}	19.1 × 18.6	+70	4.1×10^{-4}	25J
11265−6158 0	L	3.4	11 28 50.90	−62 15 01.0	293.48	−0.90	25.1 × 22.8	−59	3.0×10^{-4}	19.1 × 17.8	−46	9.0×10^{-5}	100
11354−6234 0	H	9.6	11 37 47.90	−62 51 33.0	294.65	−1.18	26.8 × 21.1	−53	2.5×10^{-4}	20.4 × 16.5	−50	3.3×10^{-4}	26J
11380−6311 0	L	1.3	11 40 27.60	−63 27 56.0	295.10	−1.68	24.6 × 24.2	−11	3.0×10^{-4}	20.7 × 19.5	+10	5.0×10^{-4}	090
11404−6215 0	L	11.0	11 42 48.00	−62 32 20.0	295.11	−0.71	24.8 × 22.3	−41	5.0×10^{-4}	19.4 × 17.5	−38	2.0×10^{-4}	100
12063−6259 0	H	10.1	12 09 01.30	−63 15 57.0	298.18	−0.79	24.5 × 23.6	−47	2.0×10^{-2}	19.0 × 18.2	−15	2.0×10^{-2}	090
12102−6133 1	L	4.0	12 12 51.09	−61 49 53.0	298.39	+0.70	24.4 × 23.3	−45	1.0×10^{-4}	19.9 × 18.0	+01	4.0×10^{-5}	090
12127−6244 0	H	10.8	12 15 23.90	−63 01 20.0	298.86	−0.44	24.6 × 23.2	−24	2.5×10^{-2}	18.9 × 18.1	−31	3.5×10^{-2}	090
12132−6211 0	H	10.2	12 15 54.20	−62 27 50.0	298.84	+0.13	24.8 × 23.2	−65	1.0×10^{-3}	18.9 × 17.9	−28	2.0×10^{-3}	090
12157−6220 0	H	8.5	12 18 28.20	−62 37 13.0	299.15	+0.01	28.3 × 20.5	−61	3.1×10^{-4}	21.3 × 16.1	−58	5.0×10^{-4}	26J
12268−6156 0	H	4.3	12 29 42.10	−62 13 08.0	300.40	+0.55	30.1 × 23.1	+80	5.0×10^{-4}	22.5 × 19.4	+87	6.0×10^{-5}	090
12272−6244 0	H	11.2	12 30 04.00	−62 56 56.0	300.50	−0.18	29.4 × 23.4	+78	1.0×10^{-3}	24.2 × 19.2	+64	3.0×10^{-4}	090
12295−6224 0	L	4.4	12 32 22.70	−62 41 25.0	300.75	+0.10	30.1 × 23.1	+77	1.0×10^{-4}	22.5 × 18.0	+78	1.0×10^{-4}	090
12300−6119 0	H	4.3	12 32 52.10	−61 35 42.0	300.72	+1.20	29.9 × 23.1	+80	2.5×10^{-4}	22.6 × 17.9	+80	2.5×10^{-4}	090
13023−6213 0	L	4.8	13 05 30.70	−62 29 58.0	304.56	+0.33	26.5 × 23.8	+59	4.8×10^{-4}	20.6 × 18.2	+65	4.6×10^{-4}	25J
13024−6158 0	H	2.1	13 05 37.50	−62 14 39.0	304.58	+0.58	26.6 × 21.1	−57	1.5×10^{-4}	20.7 × 16.4	−52	9.0×10^{-5}	100
13039−6108 0	L	2.4	13 07 07.00	−61 24 47.0	304.81	+1.40	28.2 × 23.2	+78	1.0×10^{-4}	21.5 × 17.8	+77	5.0×10^{-5}	090
13039−6108 6	L	2.4	13 07 14.80	−61 22 55.0	304.82	+1.43	25.5 × 21.9	−55	2.5×10^{-4}	19.6 × 17.0	−52	2.0×10^{-4}	25J
13039−6331 0	H	12.1	13 07 09.40	−63 47 12.0	304.67	−0.97	26.9 × 21.1	−54	4.0×10^{-4}	20.6 × 16.6	−53	2.4×10^{-4}	100
13054−6159 0	H	3.6	13 08 34.90	−62 15 08.0	304.93	+0.55	26.2 × 22.0	−53	1.1×10^{-3}	19.6 × 16.8	−48	8.2×10^{-4}	25J
13106−6050 0	L	5.0	13 13 50.50	−61 06 44.0	305.64	+1.64	25.9 × 23.5	+68	4.9×10^{-4}	20.1 × 18.2	+64	3.5×10^{-4}	25J
13107−6244 0	H	3.6	13 13 56.80	−62 24 35.0	305.53	+0.35	25.7 × 21.8	−49	5.5×10^{-4}	19.7 × 17.0	−49	5.1×10^{-3}	25J
13333−6234 0	L	0.9	13 36 45.70	−62 49 36.0	308.08	−0.41	28.6 × 20.7	−56	2.5×10^{-3}	21.6 × 16.1	−61	1.0×10^{-3}	100
13395−6153 0	L	5.3	13 42 59.50	−62 08 43.0	308.91	+0.13	26.4 × 21.4	−55	5.0×10^{-4}	20.2 × 16.6	−53	6.0×10^{-4}	25J
13438−6203 0	L	5.4	13 47 21.90	−62 18 41.0	309.38	−0.14	24.4 × 24.2	+49	1.4×10^{-4}	19.0 × 18.5	+41	1.2×10^{-4}	25J
13481−6124 0	L	3.6[f]	13 51 37.80	−61 39 08.0	310.01	+0.39	26.3 × 21.0	−52	3.6×10^{-4}	20.4 × 16.5	−54	3.0×10^{-4}	25J
13534−6152 0	H	13.1	13 57 01.80	−62 07 11.0	310.52	−0.22	28.9 × 20.7	−63	1.5×10^{-3}	21.9 × 16.0	−61	2.0×10^{-3}	100
13560−6133 2	L	5.6	13 59 33.04	−61 49 13.0	310.88	−0.00	24.5 × 24.0	+77	3.0×10^{-4}	18.6 × 18.5	+10	3.3×10^{-4}	25J
13563−6109 0	H	5.6	13 59 55.50	−61 24 25.0	311.03	+0.38	24.4 × 23.6	−81	2.8×10^{-4}	18.6 × 18.5	+88	3.0×10^{-4}	25J
13585−6133 0	H	3.2	14 02 10.20	−61 48 22.0	311.18	−0.07	24.7 × 23.8	+54	3.5×10^{-4}	18.8 × 18.2	+56	2.2×10^{-4}	25J
13590−6051 0	H	6.7[f]	14 02 34.80	−61 05 40.0	311.42	+0.60	24.2 × 24.0	+84	5.2×10^{-4}	18.9 × 18.4	+65	4.7×10^{-4}	25J
13592−6153 0	H	4.2	14 02 53.90	−62 07 26.0	311.18	−0.40	28.9 × 20.6	−63	1.0×10^{-4}	21.8 × 15.9	−62	1.0×10^{-4}	100
14000−6104 0	L	5.6	14 03 36.60	−61 18 28.0	311.48	+0.36	24.6 × 23.7	+58	1.5×10^{-3}	19.2 × 18.4	+55	1.0×10^{-3}	25J
14039−6113 0	H	4.6	14 07 35.20	−61 27 17.0	311.90	+0.08	24.7 × 23.7	+56	3.5×10^{-3}	19.2 × 18.3	+70	5.0×10^{-3}	25J
14057−6032 0	H	0.8	14 09 23.50	−60 46 55.0	312.30	+0.66	25.5 × 23.2	+87	4.0×10^{-4}	19.1 × 18.4	+85	6.0×10^{-4}	090
14090−6132 0	H	2.0	14 12 42.40	−61 47 01.0	312.38	−0.41	28.8 × 20.3	−66	1.5×10^{-4}	21.5 × 15.9	−62	2.0×10^{-4}	100
14166−6118 0	L	3.3	14 20 19.50	−61 31 53.0	313.32	−0.47	28.7 × 20.5	−66	2.0×10^{-4}	22.0 × 15.9	−66	3.5×10^{-4}	100

Table 1: continued.

Region[a]	Type[b]	Dist.[c] (kpc)	α(J2000) (h m s)	δ(J2000) (° ′ ″)	l (°)	b (°)	18.0 GHz Beam (″ × ″)	P.A. (°)	Rms (Jy beam^{-1})	22.8 GHz Beam (″ × ″)	P.A. (°)	Rms (Jy beam^{-1})	Date[d]
14183−6050 0	L	3.4	14 22 02.80	−61 04 18.0	313.67	−0.10	24.9 × 23.1	−87	4.0×10^{-4}	19.0 × 18.4	−84	3.0×10^{-4}	090
14183−6050 3	L	3.4	14 22 21.54	−61 06 42.0	313.69	−0.15	29.8 × 20.3	−68	2.5×10^{-4}	22.5 × 15.7	−67	2.5×10^{-4}	26J
14188−6054 0	H	3.3	14 22 32.00	−61 08 18.0	313.70	−0.19	28.3 × 20.4	−67	2.0×10^{-4}	22.0 × 15.9	−65	1.8×10^{-4}	100
14201−6044 0	L	4.1	14 23 54.20	−60 57 45.0	313.92	−0.08	24.5 × 23.6	−88	1.0×10^{-4}	19.2 × 18.4	+86	8.0×10^{-5}	090
14201−6044 1	L	4.1	14 24 29.36	−60 56 33.0	313.99	−0.08	25.0 × 23.5	+90	1.0×10^{-4}	22.5 × 19.7	+44	1.0×10^{-4}	090
14212−6009 0	H	5.9	14 24 57.50	−60 22 50.0	314.24	+0.42	29.7 × 20.0	−70	2.5×10^{-3}	22.4 × 16.6	−66	4.4×10^{-3}	26J
14214−6017 0	H	5.9	14 25 08.80	−60 31 31.0	314.21	+0.28	29.4 × 20.0	−68	1.1×10^{-4}	22.1 × 15.8	−67	2.0×10^{-4}	26J
14394−6004 0	H	12.2[e]	14 43 15.20	−60 17 16.0	316.37	−0.37	30.8 × 19.8	−72	8.0×10^{-4}	23.0 × 15.4	−69	1.0×10^{-3}	26J
14425−6023 0	L	3.4[f]	14 46 23.50	−60 35 45.0	316.59	−0.81	25.9 × 21.1	−59	2.0×10^{-4}	19.9 × 16.7	−51	1.0×10^{-4}	100
14557−5849 0	H	2.7[f]	14 59 34.90	−59 01 23.0	318.78	−0.15	24.8 × 22.6	−72	1.0×10^{-3}	20.8 × 19.3	+19	4.5×10^{-4}	090
15015−5720 0	L	10.4[f]	15 05 19.20	−57 31 48.0	320.16	+0.79	31.6 × 19.6	−75	4.1×10^{-3}	23.5 × 15.4	−75	3.0×10^{-3}	26J
15038−5828 1	L	5.0	15 07 32.52	−58 40 33.0	319.84	−0.35	24.9 × 22.0	−71	2.0×10^{-4}	19.2 × 17.1	−75	2.5×10^{-4}	090
15061−5806 0	H	0.8	15 10 01.20	−58 17 41.0	320.32	−0.18	25.1 × 22.1	−67	3.0×10^{-3}	20.3 × 19.1	+27	1.0×10^{-3}	090
15068−5733 0	H	4.2	15 10 43.20	−57 44 46.0	320.67	+0.25	31.7 × 19.5	−77	5.9×10^{-4}	23.4 × 15.3	−75	4.5×10^{-4}	26J
15072−5855 0	L	3.0	15 11 07.90	−59 06 30.0	320.03	−0.95	26.0 × 20.9	−60	5.0×10^{-4}	19.8 × 16.4	−57	3.0×10^{-4}	100
15100−5613 0	H	2.9	15 13 49.40	−56 24 54.0	321.72	+1.17	31.4 × 19.5	−77	6.2×10^{-4}	23.4 × 15.2	−75	2.1×10^{-2}	26J
15100−5903 0	L	3.7	15 14 00.00	−59 15 09.0	320.27	−1.27	24.9 × 22.1	−68	1.5×10^{-4}	19.1 × 17.4	−69	1.0×10^{-4}	090
15178−5641 0	L	2.1	15 21 45.40	−56 52 42.0	322.40	+0.20	25.8 × 20.7	−65	1.2×10^{-3}	19.7 × 15.7	−60	1.2×10^{-3}	100
15219−5658 0	L	1.2	15 25 48.70	−57 09 11.0	322.71	−0.33	24.4 × 21.9	−68	7.0×10^{-4}	20.1 × 18.0	+86	1.5×10^{-4}	090
15239−5638 0	L	3.3	15 27 49.30	−55 48 42.0	323.69	+0.63	32.3 × 19.5	−79	3.2×10^{-4}	24.2 × 15.3	−77	5.3×10^{-4}	26J
15246−5612 0	L	4.5	15 28 32.60	−56 23 00.0	323.45	+0.10	26.2 × 20.2	−68	3.0×10^{-4}	20.2 × 15.9	−67	6.6×10^{-4}	26J
15262−5541 1	L	3.7	15 30 06.46	−55 52 40.0	323.91	+0.39	29.1 × 22.0	−90	2.0×10^{-4}	22.2 × 17.2	−90	1.0×10^{-4}	090
15278−5620 0	H	3.4[f]	15 31 43.20	−56 30 24.0	323.74	−0.25	29.3 × 22.2	+89	4.0×10^{-4}	22.1 × 17.2	+88	4.0×10^{-4}	090
15278−5620 2	H	3.4[f]	15 31 44.17	−56 32 08.0	323.73	−0.28	26.3 × 20.4	−66	1.5×10^{-4}	20.0 × 15.9	−65	1.2×10^{-4}	26J
15347−5518 0	L	4.2	15 38 36.00	−55 28 07.0	325.13	+0.03	26.4 × 20.2	−70	3.4×10^{-4}	20.2 × 15.7	−69	7.0×10^{-4}	26J
15371−5458 0	L	17.6	15 40 58.60	−55 08 20.0	325.60	+0.09	26.5 × 19.9	−69	7.5×10^{-4}	20.2 × 15.8	−67	2.0×10^{-3}	26J
15454−5335 0	H	5.2	15 49 16.00	−53 44 59.0	327.40	+0.45	26.7 × 19.8	−73	6.3×10^{-4}	20.2 × 15.6	−69	1.5×10^{-3}	26J
15454−5507 0	H	4.4	15 49 19.00	−55 16 52.0	326.45	−0.75	25.9 × 20.3	−68	1.8×10^{-4}	20.0 × 15.8	−68	4.2×10^{-4}	26J
15464−5445 0	H	3.9	15 50 17.80	−54 54 55.0	326.79	−0.55	28.3 × 21.7	−87	7.0×10^{-4}	21.3 × 17.2	−88	8.0×10^{-4}	090
15470−5419 0	L	4.1	15 50 55.20	−54 28 22.0	327.13	−0.26	26.3 × 19.9	−70	4.1×10^{-4}	20.2 × 15.7	−70	1.0×10^{-3}	26J
15470−5419 4	L	4.1	15 50 56.10	−54 30 38.0	327.11	−0.29	26.0 × 20.2	−70	2.6×10^{-4}	20.0 × 15.9	−66	3.2×10^{-4}	26J
15470−5419 3	L	4.1	15 51 01.62	−54 26 46.0	327.16	−0.25	26.2 × 20.1	−72	3.2×10^{-4}	20.0 × 15.7	−68	1.4×10^{-4}	26J
15470−5419 1	L	4.1	15 51 28.24	−54 31 42.0	327.16	−0.36	26.2 × 20.2	−68	2.4×10^{-4}	19.9 × 15.8	−69	1.4×10^{-4}	26J
15506−5325 0	L	4.7[e]	15 54 32.20	−53 33 53.0	328.12	+0.10	28.4 × 21.7	−88	1.0×10^{-3}	21.7 × 17.0	−86	5.0×10^{-4}	090
15507−5359 0	H	5.0[f]	15 54 36.50	−54 08 40.0	327.76	−0.35	26.1 × 20.1	−70	2.8×10^{-4}	19.9 × 15.7	−69	1.0×10^{-2}	26J
15519−5430 0	L	2.7	15 55 50.40	−54 38 58.0	327.57	−0.85	25.7 × 20.3	−69	3.5×10^{-4}	19.8 × 15.8	−70	3.4×10^{-4}	26J
15530−5231 0	H	6.0	15 56 49.40	−52 40 26.0	328.95	+0.57	25.8 × 20.1	−72	1.0×10^{-3}	19.9 × 15.5	−71	1.3×10^{-3}	26J
15557−5215 0	H	10.2[f]	15 59 36.20	−52 23 46.0	329.46	+0.51	26.0 × 19.8	−72	1.3×10^{-4}	19.9 × 15.5	−68	2.3×10^{-4}	26J
15557−5337 0	L	11.2[f]	15 59 38.20	−53 45 32.0	328.57	−0.53	25.5 × 20.2	−71	9.0×10^{-3}	19.5 × 15.8	−66	2.5×10^{-2}	26J
15579−5303 0	L	3.5[f]	16 01 46.60	−53 11 41.0	329.18	−0.31	25.6 × 20.1	−73	2.7×10^{-4}	19.9 × 15.9	−69	3.0×10^{-4}	26J
15579−5347 0	L	3.3[e]	16 01 52.60	−53 56 21.0	328.70	−0.88	28.0 × 21.7	−88	1.5×10^{-4}	21.2 × 17.2	−86	1.5×10^{-4}	090
15583−5314 0	L	5.0	16 02 10.10	−53 22 35.0	329.11	−0.49	25.8 × 20.3	−70	2.9×10^{-4}	19.7 × 15.9	−66	3.1×10^{-4}	26J
16056−5125 0	H	4.8	16 09 24.40	−51 33 08.0	331.15	+0.13	25.6 × 19.8	−71	4.4×10^{-4}	20.0 × 15.6	−71	2.5×10^{-3}	26J
16061−5048 0	L	3.6[f]	16 09 57.30	−50 56 45.0	331.62	+0.52	28.5 × 21.2	−81	2.0×10^{-4}	21.8 × 16.1	−82	1.5×10^{-4}	090
16061−5048 5	L	3.6[f]	16 09 57.30	−50 49 09.0	331.71	+0.62	26.6 × 20.9	−81	1.4×10^{-4}	20.1 × 16.4	−77	8.8×10^{-5}	25J
16061−5048 1	L	3.6[f]	16 10 06.61	−50 50 29.0	331.71	+0.58	26.5 × 20.8	−77	6.0×10^{-5}	19.7 × 16.5	−80	6.0×10^{-5}	25J
16061−5048 4	L	3.6[f]	16 10 06.61	−50 57 09.0	331.63	+0.50	25.8 × 20.6	−78	1.3×10^{-4}	20.1 × 16.1	−81	1.3×10^{-4}	25J
16069−4858 0	H	1.9	16 10 38.40	−49 05 52.0	332.96	+1.80	27.4 × 19.0	−77	2.5×10^{-4}	20.7 × 15.1	−74	3.0×10^{-4}	100
16085−5138 0	H	4.3	16 12 22.00	−51 46 18.0	331.33	−0.34	26.5 × 21.1	−81	2.5×10^{-4}	20.2 × 16.5	−80	2.0×10^{-3}	25J
16093−5128 8	L	6.1[f]	16 12 49.63	−51 36 34.0	331.50	−0.27	26.5 × 21.1	−80	3.0×10^{-4}	20.3 × 16.6	−79	2.2×10^{-4}	25J
16093−5128 2	L	6.1[f]	16 12 55.46	−51 43 22.0	331.43	−0.36	26.6 × 20.9	−80	6.7×10^{-4}	20.2 × 16.6	−80	6.1×10^{-4}	25J
16093−5128 0	L	6.1[f]	16 13 09.20	−51 36 26.0	331.53	−0.30	25.8 × 21.2	−78	5.1×10^{-4}	20.1 × 16.3	−78	4.5×10^{-4}	25J
16093−5128 0	L	11.9[f]	16 13 05.20	−50 23 05.0	332.37	+0.59	28.1 × 21.1	−83	1.5×10^{-4}	23.0 × 18.7	+79	3.5×10^{-5}	090
16106−5048 0	L	5.5	16 14 26.80	−50 56 12.0	332.14	+0.05	26.9 × 21.1	−80	3.1×10^{-4}	20.2 × 16.5	−79	2.5×10^{-4}	26J
16107−4956 0	L	5.2	16 14 29.40	−50 03 51.0	332.75	+0.67	26.8 × 20.9	−79	3.1×10^{-4}	20.5 × 16.4	−80	3.0×10^{-4}	25J
16112−4943 0	H	3.3	16 15 01.30	−49 50 37.0	332.96	+0.77	27.6 × 20.7	−82	4.5×10^{-3}	20.6 × 16.5	−81	2.5×10^{-3}	25J
16148−5011 0	L	3.3	16 18 35.20	−50 18 53.0	333.05	+0.04	27.1 × 21.1	−81	6.8×10^{-4}	20.8 × 16.2	−86	5.3×10^{-4}	25J
16153−5016 1	L	3.1[f]	16 18 56.56	−50 23 58.0	333.03	−0.06	27.5 × 19.2	−75	5.0×10^{-4}	20.7 × 15.1	−75	4.0×10^{-4}	100
16164−4929 0	H	2.6	16 20 09.70	−49 36 14.0	333.73	+0.37	26.9 × 21.1	−80	1.1×10^{-3}	20.6 × 16.5	−81	7.6×10^{-4}	26J
16164−4929 3	H	2.6	16 20 24.51	−49 35 34.0	333.76	+0.35	27.4 × 20.7	−79	2.5×10^{-4}	20.9 × 16.4	−79	3.0×10^{-4}	25J
16164−4837 0	H	3.6	16 20 12.20	−48 45 06.0	334.33	+0.97	27.2 × 19.1	−78	1.3×10^{-4}	20.5 × 15.1	−75	8.0×10^{-5}	100
16170−5053 0	L	11.4[f]	16 20 53.20	−51 00 14.0	332.82	−0.71	27.6 × 21.0	−81	8.0×10^{-4}	21.0 × 16.4	−83	4.4×10^{-4}	25J
16194−4934 0	L	5.3	16 23 13.20	−49 40 59.0	334.02	−0.04	28.3 × 20.6	−80	3.0×10^{-4}	21.2 × 16.4	−81	3.3×10^{-4}	26J
16204−4916 0	L	4.6	16 24 12.30	−49 23 34.0	334.34	+0.05	27.5 × 20.7	−79	5.0×10^{-4}	20.7 × 16.2	−78	3.0×10^{-3}	26J
16218−4931 0	L	2.9	16 25 37.90	−49 38 20.0	334.33	−0.29	27.3 × 19.3	−78	2.5×10^{-4}	20.7 × 15.0	−76	2.5×10^{-4}	100
16252−4853 0	L	3.4	16 29 01.60	−48 59 48.0	335.17	−0.24	27.4 × 20.4	−81	2.7×10^{-4}	20.8 × 16.3	−79	3.4×10^{-4}	26J
16254−4844 1	L	3.4	16 29 00.89	−48 50 31.0	335.28	−0.13	27.8 × 20.4	−79	1.6×10^{-4}	20.8 × 16.3	−79	1.0×10^{-4}	26J
16344−4605 0	L	4.4[f]	16 38 08.60	−46 11 10.0	338.28	+0.54	28.3 × 18.8	−80	2.0×10^{-4}	21.3 × 14.7	−79	1.0×10^{-4}	100
16363−4645 0	L	4.5[f]	16 40 00.50	−46 51 32.0	337.99	−0.15	27.9 × 20.2	−78	1.5×10^{-3}	21.0 × 15.8	−77	1.0×10^{-3}	26J
16396−4429 0	H	5.0	16 43 16.10	−44 35 19.0	340.07	+0.93	28.1 × 20.0	−77	4.6×10^{-4}	21.1 × 15.8	−76	1.5×10^{-3}	26J
16419−4602 0	L	3.2	16 45 37.90	−46 07 49.0	339.18	−0.40	27.7 × 20.3	−78	6.0×10^{-4}	21.1 × 15.8	−79	7.0×10^{-4}	26J
16428−4109 2	L	2.7	16 46 46.80	−41 14 22.0	343.03	+2.62	28.7 × 19.6	−76	8.5×10^{-5}	21.8 × 15.3	−76	8.0×10^{-5}	090
16428−4109 1	L	2.7	16 47 01.70	−41 15 18.0	343.05	+2.58	28.4 × 19.6	−76	2.0×10^{-4}	21.5 × 15.2	−76	8.0×10^{-5}	090
16435−4515 0	H	4.0	16 47 09.60	−45 21 15.0	339.94	−0.09	27.6 × 20.2	−76	2.6×10^{-4}	21.2 × 15.7	−76	3.2×10^{-4}	26J
16435−4515 3	H	4.0	16 47 33.13	−45 22 51.0	339.96	−0.16	28.4 × 20.0	−77	3.0×10^{-4}	21.2 × 16.0	−77	3.1×10^{-4}	26J
16464−4359 0	L	5.3	16 50 01.00	−44 05 03.0	341.24	+0.33	28.2 × 20.1	−77	1.5×10^{-4}	21.7 × 15.6	−76	2.0×10^{-4}	26J
16482−4443 0	H	3.7	16 51 49.10	−44 48 50.0	340.88	−0.38	28.1 × 20.2	−77	1.7×10^{-4}	21.4 × 15.8	−75	1.0×10^{-4}	26J
16501−4314 0	L	9.5[f]	16 53 41.10	−43 19 23.0	342.25	+0.31	27.3 × 19.6	−77	6.0×10^{-4}	21.9 × 15.4	−77	5.3×10^{-4}	26J
16535−4300 0	L	6.8	16 57 05.50	−43 05 20.0	342.82	−0.03	28.8 × 20.0	−78	2.8×10^{-4}	21.9 × 15.5	−76	3.1×10^{-4}	26J

Table 1: continued.

Region[a]	Type[b]	Dist.[c] (kpc)	α(J2000) (h m s)	δ(J2000) (° ′ ″)	l (°)	b (°)	18.0 GHz Beam (″ × ″)	P.A. (°)	Rms (Jy beam^{-1})	22.8 GHz Beam (″ × ″)	P.A. (°)	Rms (Jy beam^{-1})	Date[d]
16573−4214 2	L	2.6	17 00 33.38	−42 25 18.0	343.74	−0.11	29.0 × 19.5	−77	1.4×10^{-4}	22.0 × 15.3	−77	1.2×10^{-4}	26J
16573−4214 0	L	2.6	17 00 54.30	−42 19 10.0	343.86	−0.10	27.6 × 19.7	−76	2.0×10^{-4}	21.5 × 15.2	−77	4.0×10^{-4}	090
16574−4225 0	H	2.8	17 00 57.90	−42 29 54.0	343.72	−0.22	28.8 × 18.3	−85	2.5×10^{-4}	21.9 × 14.4	−84	2.0×10^{-4}	100
16579−4245 0	H	3.3	17 01 29.00	−42 50 06.0	343.52	−0.50	29.4 × 19.7	−77	2.5×10^{-4}	22.1 × 15.3	−77	2.5×10^{-4}	26J
17033−4035 0	L	9.8[f]	17 06 49.30	−40 39 51.0	345.84	+0.03	34.6 × 19.8	−75	8.0×10^{-4}	26.2 × 15.3	−75	9.0×10^{-4}	25J
17036−4033 0	L	5.7	17 07 08.90	−40 37 08.0	345.92	+0.00	35.4 × 19.6	−74	3.1×10^{-4}	26.2 × 15.2	−75	3.1×10^{-4}	25J
17040−3959 0	L	16.5[e]	17 07 33.70	−40 03 04.0	346.42	+0.28	26.4 × 18.7	−72	2.0×10^{-4}	19.9 × 14.9	−76	2.5×10^{-4}	100
17040−3959 1	L	16.5[e]	17 07 58.78	−40 02 24.0	346.48	+0.22	26.8 × 18.6	−77	3.5×10^{-4}	20.6 × 14.5	−75	3.0×10^{-4}	100
17082−4114 0	L	2.5	17 11 46.20	−41 18 03.0	345.89	−1.10	26.2 × 19.4	−72	2.0×10^{-4}	20.4 × 15.1	−75	2.0×10^{-4}	100
17095−3837 0	H	5.6	17 12 58.60	−38 40 33.0	348.15	+0.26	35.9 × 19.0	−73	7.0×10^{-4}	26.9 × 15.0	−75	5.0×10^{-4}	25J
17118−3909 0	H	6.4	17 15 19.10	−39 13 21.0	347.97	−0.43	33.1 × 18.8	−76	2.0×10^{-4}	24.9 × 14.8	−76	1.0×10^{-3}	00J
17141−3606 0	L	0.9	17 17 28.20	−36 09 38.0	350.71	+1.00	26.6 × 18.5	−75	2.0×10^{-4}	20.5 × 14.5	−76	8.0×10^{-5}	100
17149−3916 0	H	2.1	17 18 23.80	−39 19 10.0	348.24	−0.98	33.1 × 19.2	−77	1.2×10^{-2}	25.1 × 15.1	−76	1.2×10^{-2}	00J
17184−3638 0	H	27.1	17 21 51.30	−36 41 18.0	350.78	−0.03	27.0 × 18.6	−77	1.8×10^{-3}	20.6 × 14.6	−74	3.5×10^{-3}	100
17195−3811 2	H	3.6	17 23 00.30	−38 14 58.0	349.63	−1.10	33.5 × 19.3	−76	2.5×10^{-4}	24.8 × 15.1	−76	2.8×10^{-4}	00J
17200−3658 0	H	3.1[f]	17 23 29.30	−37 01 37.0	350.69	−0.49	27.3 × 18.5	−75	1.0×10^{-3}	21.0 × 14.5	−75	8.0×10^{-3}	100
17210−3646 0	H	2.6	17 24 27.90	−36 48 54.0	350.98	−0.53	27.2 × 18.3	−75	1.5×10^{-4}	20.9 × 14.4	−76	1.5×10^{-4}	100
17211−3537 0	L	6.2	17 24 28.50	−35 40 13.0	351.92	+0.11	34.0 × 18.8	−75	3.0×10^{-4}	25.9 × 14.8	−75	4.5×10^{-4}	00J
17218−3704 0	L	3.3	17 25 14.00	−37 07 29.0	350.81	−0.83	34.2 × 19.1	−76	3.5×10^{-4}	25.6 × 14.9	−75	3.0×10^{-4}	00J
17221−3619 1	H	3.6	17 25 31.42	−36 22 05.0	351.46	−0.46	27.8 × 18.4	−78	4.0×10^{-3}	20.9 × 14.8	−77	4.5×10^{-3}	100
17225−3426 0	L	1.1	17 25 50.30	−34 29 21.0	353.06	+0.54	34.6 × 18.8	−75	1.5×10^{-3}	26.6 × 14.5	−74	9.0×10^{-4}	00J
17230−3531 0	L	—	17 26 26.30	−35 33 35.0	352.24	−0.16	27.6 × 18.2	−77	3.5×10^{-4}	21.0 × 14.3	−76	1.0×10^{-4}	100
17242−3513 0	H	—	17 27 32.50	−35 16 06.0	352.60	−0.18	27.4 × 18.5	−77	2.0×10^{-3}	21.2 × 14.4	−77	1.5×10^{-3}	100
17249−3501 0	H	10.9[f]	17 28 19.00	−35 04 07.0	352.86	−0.20	37.3 × 19.0	−72	3.0×10^{-3}	28.1 × 14.8	−72	4.0×10^{-3}	26J[g]
17249−3501 5	H	10.9[f]	17 28 30.10	−35 01 51.0	352.91	−0.21	27.8 × 18.5	−77	5.5×10^{-4}	20.9 × 14.4	−74	2.0×10^{-4}	100
17256−3631 0	L	2.0	17 29 01.10	−36 33 38.0	351.70	−1.15	37.6 × 18.9	−72	1.4×10^{-2}	28.5 × 14.7	−73	6.0×10^{-3}	26J[g]
17279−3350 0	H	5.2	17 31 17.90	−33 52 50.0	354.19	−0.06	38.2 × 18.8	−72	5.0×10^{-3}	29.1 × 14.7	−72	3.5×10^{-3}	26J[g]
17296−3236 0	H	6.0	17 32 52.10	−32 38 28.0	355.41	+0.34	37.4 × 18.9	−70	3.8×10^{-4}	29.0 × 14.6	−72	3.2×10^{-4}	26J
17352−3153 0	H	6.6[e]	17 38 30.60	−31 54 41.0	356.66	−0.27	28.8 × 18.0	−77	2.0×10^{-4}	21.4 × 14.4	−74	1.5×10^{-4}	100
17355−3241 0	L	1.7	17 38 50.50	−32 43 35.0	356.01	−0.76	28.3 × 17.8	−76	4.0×10^{-4}	21.8 × 14.5	−77	2.5×10^{-4}	100
17377−3109 0	L	0.8	17 40 57.20	−31 11 00.0	357.56	−0.32	28.2 × 17.9	−76	2.0×10^{-4}	21.7 × 14.2	−76	1.5×10^{-4}	100
17425−3017 0	L	8.0[e]	17 45 45.10	−30 18 51.0	358.84	−0.74	28.2 × 17.7	−75	1.0×10^{-4}	21.8 × 14.5	−75	1.0×10^{-4}	100
18018−2426 9	L	3.1	18 04 53.85	−24 26 43.0	006.05	−1.45	60.3 × 18.1	−69	1.0×10^{-3}	46.2 × 13.7	−71	8.0×10^{-4}	100
18144−1723 0	L	4.4	18 17 24.40	−17 22 13.0	013.66	−0.60	46.6 × 17.7	−68	2.0×10^{-4}	35.8 × 13.7	−69	2.0×10^{-4}	100
18198−1429 0	H	4.3	18 22 41.60	−14 27 34.0	016.82	−0.35	49.3 × 17.6	−68	3.0×10^{-4}	36.9 × 13.6	−69	1.0×10^{-4}	100

Notes. [a] First number correspond to the IRAS source name. The second number if equal to 0: phase center corresponding to the IRAS source; if different of 0: phase center corresponding to the millimeter clump detected by Beltrán et al. (2006), the number corresponds to the number of the millimeter clump. [b] H (High) or L (Low) according to the classification of Palla et al. (1991). [c] Kinematic distance from Beltrán et al. (2006). The near/far ambiguity has been solved where indicated, if not, the near distance has been adopted. [d] Day of observation. 25J: 25 July 2009, 26J: 26 July 2009, 090: 9 October 2009, and 100: 10 October 2009. [e] Distance not available in Beltrán et al. (2006), obtained from different works: 14394−600, 17040−3959 and 17352−3153 from Green & McClure-Griffiths (2011); 15506−5325 and 15507−5347 from Grave & Kumar 2009; 17425−3017 from Molinari et al. (2008). [f] Near/far ambiguity solved. Refs: Green & McClure-Griffiths (2011); Urquhart et al. (2012). [g] Also observed on 10 October 2009.

Table 3: ATCA centimeter continuum sources at 18.0 GHz and 22.8 GHz

Region[a]	#[b]	α_{J2000} (h m s)	δ_{J2000} (° ′ ″)	18.0 GHz I_{peak} (Jy beam^{-1})	Flux[c] (Jy)	FWHP[d] (arcsec)	Deconv[d] (arcsec)	22.8 GHz I_{peak}[c] (Jy beam^{-1})	Flux[c] (Jy)	FWHP[d] (arcsec)	Deconv[d] (arcsec)	H$_2$O maser[e]
08140−3559 0	1	08 16 00.4	−36 08 27.8	0.0090	0.0107	25.9	11.1	0.0065	0.0107	23.8	15.5	−
08211−4158 0	1	08 22 52.2	−42 07 57.4	0.0021	0.0029	32.1	22.6	0.0021	0.0033	23.5	15.2	−
	2	08 22 52.7	−42 07 32.2	<0.0010				0.0021	0.0021	20.8	10.6	−
08438−4340 0	1	08 45 34.5	−43 50 31.2	0.0728	0.1407	41.0	34.0	0.0336	0.0713	32.2	25.6	−
	2	08 45 36.9	−43 51 20.3	0.0871	0.3917	54.7	49.7	0.0729	0.1829	32.1	25.5	−
	3	08 45 37.3	−43 50 36.0	0.0441	0.0441	21.7	<7.0	0.0482	0.0774	25.7	16.7	−
08470−4243 0	1	08 48 47.9	−42 54 16.7	0.0072	0.0131	32.0	22.5	0.0082	0.0148	23.2	14.9	Y
08477−4359 0	1	08 49 32.8	−44 10 46.3	0.0102	0.0106	23.2	<7.0	0.0093	0.0174	22.2	13.5	−
08477−4359 1[f]		no detection		<0.0014				<0.0012				−
08563−4225 0	1	08 58 12.0	−42 37 30.0	0.0041	0.0058	25.8	11.8	0.0052	0.0079	22.3	11.4	Y
08589−4714 0		no detection		<0.0010				<0.0004				−
09014−4736 0	1	09 03 09.2	−47 48 27.8	0.0287	0.0377	25.2	10.0	0.0269	0.0409	20.1	9.3	−
09026−4842 0	1	09 04 22.7	−48 54 26.0	0.0017	0.0028	32.0	22.3	0.0018	0.0050	24.4	16.6	−
09131−4723 0	1	09 14 53.5	−47 35 53.3	0.0023	0.0060	38.8	31.4	0.0035	0.0082	28.4	21.7	−
09166−4813 1	1	09 18 22.1	−48 26 55.3	0.0023	0.0045	32.8	23.7	0.0025	0.0031	20.9	9.4	−
09209−5143 0	1	09 22 35.6	−51 56 33.7	0.0052	0.0059	24.2	7.5	0.0052	0.0052	18.0	<7.0	−
09566−5607 0	1	09 58 23.6	−56 22 12.9	0.0756	0.0931	24.6	9.0	0.0707	0.0960	20.1	9.2	−
09578−5649 0	1	09 59 31.5	−57 03 49.2	0.5096	1.6230	40.3	31.4	0.3362	0.9360	27.8	20.0	−
10019−5712 0	1	10 03 41.1	−57 26 39.4	0.1545	0.2050	27.0	10.3	0.1453	0.2093	23.4	10.8	Y
10038−5705 0	1	10 05 29.0[g]	−57 19 52.9[g]	0.0021	0.0039	39.8	32.5	0.0016	0.0016	32.8	27.5	−
10088−5730 2		no detection		<0.0005				<0.0002				−
10095−5843 0	1	10 11 15.2	−58 58 15.0	0.0031	0.0037	27.2	12.0	0.0031	0.0042	23.0	13.4	Y
	2	10 11 17.0	−58 59 39.8	0.0055	0.0062	27.0	11.6	0.0049	0.0056	21.3	10.2	−
10123−5727 0	1	10 14 07.5	−57 41 42.2	0.0775	0.5431	76.6	72.5	0.0756	0.2718	21.7	10.0	−
10184−5748 0	1	10 20 15.3	−58 03 12.5	0.5100	0.8272	32.6	21.2	0.1868	0.1868	22.5	11.9	−
	2	10 20 15.6	−58 03 55.4	0.7119	0.8548	26.9	10.7	0.4986	0.4986	20.1	<7.0	−
10276−5711 0	1	10 29 31.3	−57 26 38.0	0.3707	1.1840	41.0	33.9	0.2465	0.9024	34.4	29.2	−
10277−5730 0	1	10 29 34.0	−57 45 56.4	0.0109	0.0160	26.1	9.5	0.0124	0.0159	21.7	10.9	−
	2	10 29 36.4	−57 45 13.6	0.0458	0.0868	32.5	21.6	0.0316	0.0871	33.5	27.8	−
10286−5838 0	1	10 30 26.4	−58 53 40.6	0.0021	0.0031	28.3	16.9	0.0025	0.0025	23.4	15.2	−
	2	10 30 33.9	−58 53 50.7	0.0064	0.0107	26.2	13.1	0.0078	0.0107	19.6	8.1	−
10295−5746 0	1	10 31 28.6	−58 02 26.0	1.4940	3.9360	41.1	32.9	0.8995	2.4340	31.1	24.7	Y
10317−5936 0	1	10 33 35.9	−59 51 17.6	0.0110	0.0186	32.7	23.6	0.0037	0.0039	23.4	15.2	Y
	2	10 33 39.4	−59 52 18.9	0.0316	0.0473	27.4	15.3	0.0289	0.0591	25.2	17.9	−
10320−5928 0	1	10 33 56.2	−59 43 58.6	0.7513	1.2480	27.9	12.6	0.7473	1.0940	19.3	<7.0	−
10337−5710 0	1	10 35 40.0	−57 26 09.8	0.0470	0.0480	23.6	<7.0	0.0502	0.0518	18.2	<7.0	Y
10439−5941 0	1	10 45 53.9	−59 57 03.6	0.1986	0.4219	28.4	16.4	0.1466	0.3314	22.4	13.7	−
10501−5556 0	1	10 52 10.3	−56 12 25.8	0.0188	0.0302	27.1	12.7	0.0113	0.0118	20.0	<7.0	Y
10521−6031 0	1	10 54 10.8	−60 47 29.7	0.0823	0.1209	28.3	14.1	0.0673	0.1337	25.3	16.9	−
10537−5930 0	1	10 55 49.2	−59 47 07.7	0.0422	0.1350	43.9	36.9	0.0233	0.0760	35.4	30.5	−
10548−5929 0	1	10 56 52.2	−59 45 16.3	0.0153	0.0166	26.0	8.6	0.0133	0.0193	22.9	13.0	−
10555−6242 0	1	10 57 32.6	−62 58 55.0	0.0015	0.0034	41.1	32.9	0.0010	0.0010	12.0	<7.0	−
10545−6244 1	1	10 57 33.4	−62 58 51.6	0.0013	0.0024	33.1	22.5	0.0023	0.0055	28.6	21.7	Y
10559−5914 0	1	10 58 00.7	−59 30 43.9	0.0032	0.0032	22.9	<7.0	0.0033	0.0033	17.2	<7.0	Y
10572−6018 0	1	10 59 20.1	−60 33 58.0	0.0610	0.1505	37.1	27.8	0.0416	0.1427	36.0	30.7	−
10575−5844 0	1	10 59 40.2	−59 01 05.0	0.0031	0.0040	24.9	<7.0	0.0031	0.0047	21.0	9.4	−
10589−6034 0	1	11 00 59.8	−60 50 23.4	1.0694	1.3820	24.5	8.2	0.8991	1.3460	21.0	10.3	−
10591−5934 0	1	11 01 15.3	−59 50 41.4	0.0198	0.0830	53.4	47.5	0.0111	0.0539	47.8	43.9	−
11079−6101 0	1	11 10 01.3	−61 18 29.0	0.0436	0.0436	21.6	<7.0	0.0393	0.0393	18.4	<7.0	−
11220−6147 0	1	11 24 17.3	−62 04 04.6	0.0031	0.0037	31.0	19.2	0.0030	0.0030	22.5	12.3	−
11265−6158 0	1	11 28 50.8	−62 14 26.2	0.0045	0.0103	45.0	38.1	0.0046	0.0103	25.0	16.9	−
	2	11 28 51.6	−62 15 10.9	0.0022	0.0039	37.1	28.3	0.0034	0.0043	18.3	<7.0	Y
11354−6234 0	1	11 37 45.7	−62 51 58.0	0.0010	0.0113	35.9	26.9	0.0031	0.0049	22.3	12.6	−
	2	11 37 47.8	−62 51 33.6	0.0209	0.0216	25.4	9.0	0.0166	0.0205	20.4	8.9	−
11380−6311 0	1	11 40 26.8	−63 27 24.9	0.0203	0.1027	56.4	50.8	0.0136	0.0745	52.4	48.4	−
11404−6232 0	1	11 42 47.8	−62 32 08.5	0.0137	0.0716	61.6	56.9	0.0088	0.0496	51.9	48.5	−
12063−6259 0	1	12 09 01.3	−63 15 57.0	2.0718	2.7180	26.2	10.3	1.8797	2.6850	20.6	8.7	−
12102−6133 1		no detection		<0.0005				<0.0002				−
12127−6244 0	1	12 15 23.8	−63 01 24.8	3.1886	6.9410	30.5	18.9	2.2643	4.7010	25.6	17.6	−
12132−6211 0	1	12 15 52.0	−62 27 41.0	0.1391	0.1819	27.2	12.8	0.1320	0.1752	20.0	7.8	−
	2	12 15 57.4	−62 28 01.8	0.1819	0.2521	27.7	13.7	0.1430	0.2449	23.7	14.9	−
12157−6220 0	1	12 18 28.8	−62 37 17.8	0.0265	0.0275	25.0	<7.0	0.0256	0.0270	18.9	<7.0	−
12268−6156 0	1	12 29 41.5	−62 13 08.0	0.0429	0.0451	27.1	<7.0	0.0421	0.0495	22.1	7.2	−
12272−6240 0	1	12 30 02.5	−62 57 15.9	0.0509	0.1824	54.3	47.6	0.0410	0.1149	35.6	28.3	−
	2	12 30 04.0	−62 56 40.1	0.0937	0.0985	28.7	11.7	0.0868	0.1161	23.1	8.1	−
12295−6224 0	1	12 32 28.6	−62 42 00.0	0.0047	0.0163	54.2	47.4	0.0026	0.0120	48.1	43.6	−
12300−6119 0		no detection		<0.0013				<0.0013				−
13023−6213 0	1	13 05 30.7	−62 29 58.6	0.1122	0.1188	25.8	<7.0	0.1121	0.1257	20.5	<7.0	−
13024−6158 0	1	13 05 39.1	−62 14 43.8	0.0051	0.0061	26.7	12.2	0.0072	0.0084	19.6	<7.0	−
13039−6108 0	1	13 07 07.0	−61 24 43.0	0.0041	0.0073	35.0	23.8	0.0031	0.0044	23.3	12.6	−
	2	13 07 18.2	−61 25 06.9	0.0012	0.0124	59.2	53.4	0.0057	0.0094	25.3	16.0	−
13039−6108 6		no detection		<0.0013				<0.0010				−
13039−6331 0		no detection		<0.0020				<0.0012				−
13054−6159 0	1	13 08 36.2	−62 15 13.6	0.2316	0.5406	34.7	25.1	0.1698	0.4735	30.0	23.8	−
13106−6050 0	1	13 13 48.6	−61 06 23.6	0.0064	0.0064	25.7	7.1	0.0222	0.0610	27.0	19.0	−
	2	13 14 00.2	−61 06 58.8	0.0661	0.2094	37.7	28.5	0.0084	0.0084	53.8	50.3	−
13107−6208 0	1	13 13 56.1	−62 24 39.8	0.1870	0.7472	48.9	42.8	0.1556	0.7650	42.0	37.8	−
13333−6234 0	1	13 36 32.4	−62 49 05.5	0.2196	0.2196	24.5	<7.0	0.2157	0.2157	18.9	<7.0	−
	2	13 36 46.5	−62 49 45.2	0.2033	0.5330	37.8	28.8	0.1521	0.4805	32.1	26.1	−
13395−6153 0	1	13 42 53.8	−62 08 43.1	0.0040	0.0040	26.3	11.1	0.0038	0.0038	16.8	<7.0	−
	2	13 43 01.7	−62 08 57.8	0.4589	0.5183	24.6	<7.0	0.4544	0.5357	19.1	<7.0	Y

Table 3: continued.

Region[a]	#[b]	α_{J2000} (h m s)	δ_{J2000} (° ′ ″)	I_{peak}[c] (Jy beam^{-1})	Flux[c] (Jy)	FWHP[d] (arcsec)	Deconv[d] (arcsec)	I_{peak} (Jy beam^{-1})	Flux[c] (Jy)	FWHP[d] (arcsec)	Deconv[d] (arcsec)	H_2O maser[e]
					18.0 GHz				22.8 GHz			
13438−6203 0	1	13 47 20.4	−62 19 01.2	0.0032	0.0060	37.0	27.9	0.0022	0.0098	30.4	23.9	−
	2	13 47 24.0	−62 18 11.2	0.0043	0.0105	42.1	34.3	0.0044	0.0046	26.1	18.1	Y
13481−6124 0	1	13 51 37.7	−61 39 07.7	0.0030	0.0030	20.0	<7.0	0.0040	0.0040	18.5	<7.0	−
13534−6152 0	1	13 57 01.0	−62 07 11.0	0.3919	0.5485	26.9	11.2	0.3515	0.5709	21.9	11.3	−
13560−6133 2	1	13 59 35.7	−61 48 19.8	0.1008	0.1766	31.0	19.3	0.0776	0.1746	28.6	21.6	−
13563−6109 0	1	13 59 56.2	−61 24 36.5	<0.0014				0.0021	0.0021	21.6	11.0	−
13585−6133 0	1	14 02 08.1	−61 48 26.8	0.0041	0.0041	24.7	<7.0	0.0063	0.0063	19.3	<7.0	−
	2	14 02 14.9[g]	−61 48 10.8[g]	0.0045	0.0061	30.0	17.6	0.0020	0.0021	18.4	<7.0	−
13590−6051 0	1	14 02 36.0	−61 05 44.8	0.1239	0.1617	26.4	10.7	0.1248	0.1699	19.8	<7.0	−
13592−6153 0	1	14 02 50.4[g]	−62 07 26.0[g]	0.0034	0.0050	32.3	21.1	0.0023	0.0032	23.4	14.1	−
	2	14 02 49.7[g]	−62 07 56.0[g]	0.0023	0.0024	27.7	13.0	<0.0005				−
14000−6104 0	1	14 03 35.5	−61 18 35.3	0.1777	0.3934	35.5	26.1	0.1053	0.3469	37.9	32.9	Y
14039−6113 0	1	14 07 35.7	−61 27 24.3	0.4761	1.4360	35.8	26.4	0.3024	0.9669	29.1	22.3	−
14057−6032 0	1	14 09 24.7	−60 46 59.8	0.0506	0.0541	25.2	<7.0	0.0530	0.0567	19.4	<7.0	−
14090−6132 0	1	14 12 32.4	−61 46 31.8	0.0038	0.0038	25.2	<7.0	0.0031	0.0031	18.1	<7.0	−
	2	14 12 44.5	−61 47 10.2	0.0240	0.0268	25.4	7.5	0.0232	0.0295	20.6	9.1	−
14166−6118 0	1	14 20 18.7	−61 31 53.0	0.0566	0.0831	28.3	14.5	0.0505	0.0877	24.3	15.4	−
14183−6050 0	1	14 22 02.0	−61 04 07.1	0.0249	0.0991	48.6	42.3	0.0211	0.0716	34.3	28.6	−
	2	14 22 11.6	−61 04 27.8	0.0415	0.0422	25.2	7.6	0.0316	0.0452	19.8	<7.0	−
14183−6050 3		no detection		<0.0013				<0.0013				−
14188−6054 0	1	14 22 31.8	−61 08 27.9	0.0042	0.0072	33.8	23.8	0.0032	0.0073	31.2	24.9	−
14201−6044 0	1	14 23 52.1	−60 57 35.3	0.0021	0.0035	34.0	24.0	0.0014	0.0037	35.3	29.9	−
14201−6044 1		no detection		<0.0005				<0.0005				−
14212−6009 0	1	14 24 57.8	−60 22 57.3	0.4133	1.5160	44.5	37.2	0.2715	1.0260	35.0	29.6	−
14214−6017 0	1	14 25 03.3	−60 31 06.2	0.0704	0.2525	49.8	43.5	0.0318	0.0789	31.5	25.3	−
	2	14 25 04.0	−60 31 51.1	0.0349	0.0525	32.4	21.5	0.0303	0.0339	20.9	9.3	−
	3	14 25 10.1	−60 32 16.0	0.0684	0.0684	26.0	9.4	0.0491	0.0823	25.7	17.7	−
	4	14 25 11.5	−60 31 46.0	0.0400	0.0400	24.4	<7.0	0.0108	0.0108	16.6	<7.0	−
14394−6004 0	1	14 43 12.9	−60 17 12.4	0.1175	0.2575	34.4	23.9	0.0732	0.1871	30.4	23.9	−
14425−6023 0	1	14 46 22.8	−60 35 39.1	0.0020	0.0026	31.4	21.0	0.0015	0.0027	27.3	20.2	−
14557−5849 0	1	14 59 34.3	−59 01 23.0	0.3286	0.4571	26.7	12.3	0.3108	0.4907	23.9	12.9	−
15015−5720 0	1	15 05 19.8	−57 31 48.0	0.3552	1.8171	64.9	59.9	0.1881	0.5223	37.5	32.3	−
	2	15 05 20.4	−57 30 38.0	0.2113	0.2619	1.9	<7.0	0.0761	0.8657	59.0	55.8	−
15038−5828 1		no detection		<0.0010				<0.0013				−
15061−5806 0	1	15 10 00.5	−58 17 30.7	1.2578	3.5506	38.6	30.6	1.0520	3.0840	31.7	24.9	Y
	2	15 10 06.9	−58 17 06.2	0.1626	0.3084	31.5	20.8	0.0268	3.0840	19.5	<7.0	−
15068−5733 0	1	15 10 43.4	−57 44 46.6	0.0176	0.0208	28.5	13.8	0.0217	0.0217	19.4	<7.0	−
	2	15 10 48.3	−57 45 03.4	0.0201	0.0387	34.5	23.9	0.0081	0.0294	40.5	35.8	−
15072−5855 0		no detection		<0.0025				<0.0015				−
15100−5613 0	1	15 13 49.9	−56 24 48.7	1.5495	2.1910	28.3	13.7	1.2748	1.9340	21.9	11.0	−
15100−5903 0	1	15 14 00.5	−59 15 03.7	0.0031	0.0048	27.6	14.4	0.0021	0.0064	35.9	30.9	−
15178−5641 0	1	15 21 44.1	−56 52 51.2	0.1044	0.4062	50.5	44.9	0.0647	0.2950	41.1	37.1	−
15219−5658 0	1	15 25 48.0	−57 09 05.7	0.1760	0.2624	26.7	13.2	0.1571	0.2727	23.6	14.0	Y
15239−5538 0	1	15 27 47.0	−55 48 51.8	0.0186	0.0582	49.9	43.1	0.0087	0.0235	37.5	32.1	−
15246−5612 0	1	15 28 32.4	−56 23 03.1	0.0415	0.0945	34.5	25.6	0.0259	0.0703	31.4	25.7	−
15262−5541 1	1	15 30 07.6	−55 52 20.3	0.0022	0.0032	37.2	27.2	0.0018	0.0044	33.8	27.6	−
15278−5620 0	1	15 31 43.7	−56 30 13.7	0.1155	0.1985	31.4	18.3	0.0829	0.1879	28.7	21.0	−
15278−5620 2[h]		no detection		<0.0007				<0.0006				−
15347−5518 0	1	15 38 35.6	−55 28 10.1	0.0411	0.0619	27.3	14.5	0.0257	0.0510	25.6	18.3	−
15371−5458 0	1	15 40 58.7	−55 08 20.6	0.1453	0.3354	34.1	25.2	0.1020	0.2698	28.7	22.4	−
15454−5335 0	1	15 49 19.2	−53 45 17.2	0.1563	0.1563	22.2	<7.0	0.1449	0.1672	19.0	<7.0	Y
15454−5507 0	1	15 49 18.7	−55 16 53.4	0.0123	0.0174	25.7	11.4	0.0102	0.0125	20.6	10.4	Y
15464−5445 0	1	15 50 17.1	−54 54 44.1	0.0888	0.3468	54.2	48.2	0.0560	0.2551	44.3	39.9	−
15470−5419 0	1	15 50 54.5	−54 28 33.5	0.0634	0.1344	30.0	19.4	0.0387	0.0975	26.7	19.8	−
15470−5419 4[i]		no detection		<0.0013				<0.0016				−
15470−5419 3[i]		no detection		<0.0016				<0.0007				−
15470−5419 1		no detection		<0.0012				<0.0007				−
15506−5325 0	1	15 54 31.6	−53 33 02.4	0.0349	0.1346	59.6	54.1	0.0187	0.0931	43.6	39.1	−
	2	15 54 35.0	−53 33 58.5	0.0303	0.0429	34.1	23.4	0.0137	0.0931	30.3	23.4	−
15507−5359 0	1	15 54 36.9	−54 08 49.8	0.5484	1.3900	32.6	23.1	0.3278	0.8359	27.2	20.7	−
15519−5430 0	1	15 55 46.6	−54 38 57.7	0.0317	0.1047	43.2	36.6	0.0192	0.0729	37.4	32.9	−
15530−5231 0	1	15 56 46.9	−52 40 35.0	0.1172	0.2443	35.8	27.6	0.0784	0.1820	27.3	20.9	−
	2	15 56 50.8	−52 40 25.7	0.1279	0.1526	29.1	18.0	0.1042	0.1333	20.5	10.4	Y
15557−5215 0	1	15 59 33.9	−52 23 45.7	0.0185	0.0443	35.9	27.8	0.0122	0.0355	33.0	27.9	−
15557−5337 0	1	15 59 36.5	−53 45 51.9	1.5710	2.1746	25.7	12.0	0.9028	1.3863	22.6	14.2	−
	2	15 59 38.1	−53 45 25.0	3.4038	4.4634	26.1	12.8	2.5461	4.2777	21.7	12.6	−
15579−5303 0	1	16 01 47.0	−53 11 45.8	0.0051	0.0052	24.9	10.2	0.0051	0.0058	20.8	10.7	Y
15579−5303 0	1	16 01 53.1	−53 56 15.1	0.0031	0.0059	37.5	28.2	0.0041	0.0074	25.5	16.8	−
15583−5314 0	1	16 02 11.2	−53 22 43.1	0.0020	0.0020	27.4	15.1	0.0021	0.0021	20.3	9.9	−
16056−5125 0	1	16 09 24.3	−51 33 10.3	0.1121	0.1266	22.8	<7.0	0.0885	0.1037	19.5	8.3	−
16061−5048 0	1	16 09 57.7	−50 56 49.2	0.0052	0.0083	32.0	20.5	0.0052	0.0093	20.9	9.2	−
16061−5048 5	1	16 10 01.1	−50 49 28.9	0.0037	0.0042	24.7	7.3	0.0027	0.0045	23.5	14.8	−
16061−5048 1[j]		no detection		<0.0003				<0.0003				−
	2	16 10 06.1	−50 50 28.7	0.0010	0.0010	22.1	<7.0	0.0012	0.0014	19.6	7.6	Y
16061−5048 4	1	16 10 06.9	−50 57 28.9	0.0046	0.0204	53.0	47.7	0.0034	0.0131	39.9	35.6	Y
16069−4858 0	1	16 10 34.8	−49 06 16.3	0.0099	0.0144	28.0	16.2	0.0091	0.0141	25.6	18.5	−
	2	16 10 36.3	−49 05 51.8	0.0188	0.0313	31.4	21.5	0.0137	0.0272	26.1	19.1	−
	3	16 10 38.3	−49 05 32.3	0.0265	0.0468	32.2	22.7	0.0182	0.0334	26.9	20.2	−
16085−5138 0	1	16 12 19.8	−51 46 06.8	0.3598	1.6460	52.4	46.7	0.2055	1.1390	43.2	39.1	−
16093−5128 8	1	16 12 42.1	−51 37 19.1	0.0075	0.0157	40.1	32.3	0.0044	0.0053	24.6	16.3	−
16093−5128 2	1	16 12 50.2	−51 43 31.0	0.2152	0.2322	23.9	<7.0	0.1981	0.2255	19.4	<7.0	−
16093−5128 0	1	16 13 11.2	−51 36 31.6	0.1284	0.1740	25.6	10.4	0.1099	0.1742	21.1	10.7	−

Table 3: continued.

Region[a]	#[b]	α_{J2000} (h m s)	δ_{J2000} (° ′ ″)	18.0 GHz				22.8 GHz				H$_2$O
				I_{peak}[c] (Jy beam^{-1})	Flux[c] (Jy)	FWHP[d] (arcsec)	Deconv[d] (arcsec)	I_{peak} (Jy beam^{-1})	Flux[c] (Jy)	FWHP[d] (arcsec)	Deconv[d] (arcsec)	maser[e]
16093−5015 0		no detection		<0.0007				<0.0002				−
16106−5048 0	1	16 14 27.3	−50 56 15.1	0.0112	0.0124	25.0	7.6	0.0092	0.0120	20.6	9.4	−
16107−4956 0	1	16 14 30.3	−50 04 00.8	0.0021	0.0021	32.0	21.5	0.0021	0.0026	27.8	20.9	−
16112−4943 0	1	16 15 00.9	−49 50 38.4	0.4438	1.3630	46.5	39.8	0.3029	1.2160	39.7	35.1	Y
16148−5011 0	1	16 18 37.5	−50 18 51.9	0.1613	0.2755	29.3	16.8	0.1218	0.2755	26.4	19.0	−
16153−5016 1	1	16 18 57.0	−50 23 52.2	0.0538	0.1067	25.7	11.5	0.0579	0.0829	18.3	<7.0	−
16164−4929 0	1	16 20 09.6	−49 36 17.1	0.2675	0.4001	27.8	14.3	0.2273	0.4026	23.2	14.0	−
16164−4929 3	1	16 20 19.3	−49 34 59.3	0.0068	0.0070	26.0	10.4	0.0099	0.0106	19.3	<7.0	−
16164−4837 0	1	16 20 13.1	−48 45 10.8	0.0041	0.0049	22.6	<7.0	0.0031	0.0057	23.6	15.6	−
16170−5053 0	1	16 20 50.3	−50 59 48.6	0.0251	0.0740	32.6	21.9	0.0129	0.0395	30.6	24.3	−
16194−4934 0	1	16 23 17.1	−49 41 11.3	0.0257	0.0298	26.2	10.1	0.0254	0.0312	20.6	8.7	−
16204−4916 0	1	16 24 14.3	−49 23 48.8	0.2671	0.4788	32.1	21.4	0.1960	0.4344	29.6	23.3	−
16218−4931 0	1	16 25 38.3	−49 38 14.1	0.0278	0.0374	26.4	13.1	0.0259	0.0417	21.7	12.5	Y
16252−4853 0	1	16 29 02.7	−48 59 50.2	0.0283	0.0572	32.5	22.2	0.0201	0.0449	28.6	21.9	−
16254−4844 1	1	16 28 58.8	−48 51 06.3	0.0014	0.0014	30.0	18.1	0.0012	0.0015	24.2	15.7	−
	2	16 29 00.9	−48 50 35.8	0.0012	0.0012	28.9	16.2	0.0012	0.0012	5.3	<7.0	Y
	3	16 29 03.4	−48 51 01.0	0.0011	0.0011	3.6	<7.0	0.0014	0.0014	23.6	14.7	−
16344−4605 0	1	16 38 09.1	−46 10 59.7	0.0021	0.0032	33.5	24.3	0.0018	0.0027	23.6	15.5	Y
16363−4645 0	1	16 39 58.5	−46 52 16.9	0.0264	0.0607	40.9	33.3	0.0056	0.0056	16.6	<7.0	−
	2	16 40 03.4	−46 51 07.1	0.0336	0.0597	35.0	25.6	0.0253	0.0462	27.3	20.3	−
16396−4429 0	1	16 43 15.7	−44 35 18.7	0.1122	0.1202	24.3	<7.0	0.1128	0.1228	18.2	<7.0	−
16419−4602 0	1	16 45 35.7	−46 07 44.5	0.0341	0.0787	31.4	20.5	0.0161	0.0374	25.6	17.9	−
16428−4109 2	1	16 46 47.1	−41 14 31.4	0.0010	0.0010	21.2	<7.0	0.0013	0.0024	29.6	23.2	−
16428−4109 1	1	16 47 03.9	−41 15 28.4	0.0022	0.0046	41.2	33.8	0.0021	0.0066	36.5	31.6	−
16435−4515 0	1	16 47 10.0	−45 21 04.7	0.0124	0.0140	25.5	9.3	0.0125	0.0155	20.5	9.2	−
16435−4515 3	1	16 47 31.7	−45 23 49.5	0.0055	0.0074	32.5	22.1	0.0034	0.0050	29.6	23.2	−
	2	16 47 33.1	−45 22 54.9	0.0020	0.0025	36.0	26.9	0.0020	0.0020	24.6	16.3	−
16464−4359 0	1	16 50 00.5	−44 05 02.7	0.0041	0.0077	34.4	24.8	0.0041	0.0076	26.8	19.4	Y
16482−4443 0	1	16 51 45.9	−44 48 12.8	0.0050	0.0076	31.1	20.0	0.0040	0.0047	19.6	<7.0	−
	2	16 51 47.1	−44 48 50.6	0.0025	0.0025	26.2	10.8	0.0024	0.0028	19.6	<7.0	Y
16501−4314 0	1	16 53 41.2	−43 19 08.5	0.0530	0.1964	42.3	35.4	0.0337	0.1332	35.1	29.9	−
16535−4300 0	1	16 57 06.4	−43 05 17.2	0.0020	0.0022	31.8	20.8	0.0021	0.0031	30.3	24.0	−
16573−4214 2		no detection		<0.0007				<0.0006				−
16573−4214 0	1	17 00 55.2	−42 19 05.4	0.0481	0.1647	42.0	34.8	0.0346	0.1270	29.3	23.1	−
16574−4225 0	1	17 00 58.3	−42 29 58.8	0.0248	0.0359	24.9	9.6	0.0237	0.0337	19.7	8.4	−
16579−4245 0		no detection		<0.0013				<0.0013				−
17033−4035 0		no detection		<0.0040				<0.0045				−
17036−4033 0	1	17 07 04.1	−40 37 12.8	0.0086	0.0086	27.9	9.1	0.0074	0.0074	20.1	<7.0	−
	2	17 07 04.9	−40 37 11.9	0.0017	0.0027	35.0	22.9	0.0012	0.0012	30.3	22.7	−
17040−3959 0	1	17 07 33.1	−40 03 05.0	0.0165	0.0274	26.6	14.5	0.0175	0.0265	18.4	<7.0	Y
17040−3959 1		no detection		<0.0018				<0.0015				−
17082−4114 0	1	17 11 40.8	−41 18 58.2	0.0025	0.0025	25.5	11.8	0.0033	0.0033	19.0	7.1	−
	2	17 11 45.7	−41 18 03.0	0.0143	0.0193	25.9	12.6	0.0093	0.0199	26.7	20.0	−
17095−3837 0	1	17 12 59.0	−38 40 28.5	0.0868	0.1187	29.6	13.9	0.0706	0.1217	25.1	15.0	−
17118−3909 0	1	17 15 17.8	−39 13 27.1	0.1475	0.3261	36.1	26.0	0.1154	0.2332	21.8	10.1	−
17141−3606 0	1	17 17 27.8	−36 09 47.2	0.0020	0.0030	32.5	23.8	0.0010	0.0011	19.3	8.5	−
17149−3916 0	1	17 18 22.6	−39 19 30.3	0.6413	2.4090	56.1	50.1	0.4024	1.0130	32.8	26.3	−
17184−3638 0	1	17 21 50.5	−36 41 13.4	1.6147	1.8440	23.3	<7.0	1.6008	1.8900	18.4	<7.0	Y
17195−3811 2		no detection		<0.0013				<0.0014				−
17200−3658 0	1	17 23 28.8	−37 01 42.5	0.0010	0.0020	36.9	29.1	0.0015	0.0028	24.5	17.1	Y
17211−3537 0	1	17 24 26.8	−35 40 07.6	0.0163	0.0300	34.3	23.2	0.0112	0.0247	31.9	25.1	−
17210−3646 0	1	17 24 29.9	−36 48 54.0	0.0143	0.0317	31.1	21.6	0.0102	0.0252	25.4	18.6	−
17218−3704 0	1	17 25 14.0	−37 07 30.4	0.0046	0.0109	46.4	38.7	0.0031	0.0047	24.7	15.0	−
17221−3619 1	1	17 25 31.4	−36 22 00.8	0.7122	2.4050	39.3	32.1	0.4795	1.7000	32.1	26.8	Y
17225−3426 0	1	17 25 53.3	−34 29 27.6	0.0619	0.1659	44.6	36.5	0.0406	0.0678	24.7	14.8	−
17230−3531 0	1	17 26 23.1	−35 33 54.3	0.0140	0.0273	34.9	26.7	0.0096	0.0179	25.1	18.1	−
	2	17 26 24.2	−35 34 20.1	0.0093	0.0097	22.5	<7.0	0.0060	0.0067	17.8	<7.0	−
	3	17 26 24.6	−35 33 34.2	0.0163	0.0325	36.4	28.6	0.0133	0.0270	25.5	18.6	−
17242−3513 0	1	17 27 29.2	−35 16 56.0	0.0875	0.2254	34.2	25.7	0.0390	0.0390	22.3	13.8	−
	2	17 27 30.0	−35 16 12.1	0.2031	0.6075	42.2	35.7	0.1208	0.2356	37.7	33.4	−
	3	17 27 33.3	−35 15 55.9	0.1272	0.2231	30.5	20.6	0.0598	0.3769	57.4	54.6	−
17249−3501 0	1	17 28 18.3	−35 04 16.0	0.4960	0.8296	29.4	17.3	0.3964	0.7902	25.7	17.6	Y
17249−3501 5		no detection		<0.0028				<0.0010				−
17256−3631 0	1	17 29 01.3	−36 33 31.9	0.8368	2.5020	43.1	35.8	0.5854	1.8710	35.5	30.2	−
17279−3350 0	1	17 31 17.4	−33 52 48.1	0.3439	0.6838	32.8	22.4	0.2706	0.5139	25.0	16.5	−
17296−3236 0	1	17 32 51.8	−32 38 35.3	0.0051	0.0051	27.2	<7.0	0.0051	0.0051	22.4	8.7	−
17352−3153 0	1	17 38 29.8	−31 54 35.1	0.0124	0.0155	25.9	12.3	0.0145	0.0161	18.6	<7.0	−
17355−3241 0		no detection		<0.0020				<0.0013				−
17377−3109 0	1	17 40 57.2	−31 11 00.0	0.0438	0.0474	23.1	<7.0	0.0610	0.0642	17.8	<7.0	Y
17425−3017 0	1	17 45 44.7	−30 18 45.7	0.0017	0.0033	34.4	26.2	0.0014	0.0034	31.1	25.5	−
18018−2426 9	1	18 04 52.7	−24 27 03.5	0.0378	0.0413	38.0	18.6	0.0152	0.0231	38.3	28.8	−
	2	18 04 53.1	−24 26 42.5	0.0341	0.0600	48.5	35.5	0.0175	0.0334	41.8	33.3	Y
	3	18 04 54.5	−24 26 18.0	0.0329	0.0329	36.6	15.6	0.0128	0.0181	37.0	27.0	−
18144−1723 0	1	18 17 21.6	−17 23 37.8	0.0172	0.0172	27.6	<7.0	0.0176	0.0262	24.5	10.4	−
18198−1429 0	1	18 22 42.0	−14 27 38.8	0.0030	0.0030	28.2	<7.0	0.0031	0.0043	27.8	16.3	−

Notes. [a] See Table 1. [b] ATCA source number (from this work). [c] Primary beam corrected. [d] FWHP: full width half power, and Deconv: deconvolved size (in arcsec). [e] Y: water maser associated with the centimeter source. [f] The source seen in the map is that associated with 08477−4359 0. [g] Coordinates from the 18.0 GHz map. [h] The source seen in the map is that associated with 15278−5620 0. [i] The source seen in the map is that associated with 15278−5620 0. [j] The source seen in the map is that associated with 15479−54190.

Table 4: Regions with water maser emission

#	Region	α_{J2000} (h m s)	δ_{J2000} (° ′ ″)	$\int S_\nu \, dv^a$ (Jy km s^{-1})	v_{peak} (km s^{-1})
1	08438−4340 0	08 45 33.718	−43 52 05.85	1.5891×10^{-1}	+9
2	08470−4243 0	08 48 47.887	−42 54 30.16	2.3593×10^{-1}	+17
3	08563−4225 0	08 58 11.630	−42 37 29.95	$1.2415 \times 10^{+0}$	+9
4	08589−4714 0	09 00 40.898	−47 26 04.88	$2.1442 \times 10^{+1}$	+7
5	09131−4723 0	09 14 51.711	−47 36 49.99	9.3873×10^{-1}	+7
6	09166−4813 1	09 17 54.507	−48 27 23.35	8.1421×10^{-2}	+7
7	09578−5649 0	09 59 31.319	−57 04 42.52	9.6140×10^{-2}	+3
8	10019−5712 0	10 03 40.288	−57 26 35.68	$6.0604 \times 10^{+0}$	−11
9	10088−5730 2	10 10 46.616	−57 43 56.77	1.2076×10^{-1}	−11
10	10095−5843 0	10 11 14.465	−58 58 11.68	1.1166×10^{-1}	−11
11	10276−5711 0	10 29 31.326	−57 26 49.26	2.3131×10^{-1}	+15
12	10295−5746 0	10 31 29.501	−58 02 17.06	$3.3319 \times 10^{+2}$	+15
13	10317−5936 0	10 33 36.712	−59 51 32.09	1.7312×10^{-1}	+29
14	10337−5710 0	10 35 40.044	−57 26 05.82	3.9008×10^{-1}	−11
15	10501−5556 0	10 52 12.860	−56 12 41.01	6.5700×10^{-2}	−11
16	10545−6244 1	10 57 33.437	−62 59 02.56	$2.4358 \times 10^{+1}$	+1
17	10555−6242 0	10 57 33.887	−62 59 01.95	$1.8009 \times 10^{+1}$	+0
18	10559−5914 0	10 58 00.455	−59 30 40.67	7.8435×10^{-2}	−66
19	11380−6311 0	11 40 29.273	−63 27 54.88	3.8797×10^{-1}	−0
20	12102−6133 1	12 12 56.019	−61 50 08.00	1.6179×10^{-1}	−27
21	11265−6158 0	11 28 50.655	−62 14 59.88	4.6810×10^{-1}	−26
22	12268−6156 0	12 29 44.423	−62 13 17.87	7.0320×10^{-2}	−28
23	12272−6240 0	12 30 03.434	−62 56 51.22	$6.0996 \times 10^{+1}$	+12
24	11404−6215 0	11 42 49.414	−62 32 40.87	1.5767×10^{-1}	+54
25	13333−6234 0	13 36 43.564	−62 49 45.14	6.5621×10^{-1}	−2
26	13395−6153 0	13 43 01.604	−62 08 53.06	9.9340×10^{-1}	−63
27	13438−6203 0	13 47 23.748	−62 18 10.40	8.5210×10^{-1}	−50
28	13534−6152 0	13 57 05.959	−62 07 52.40	5.9344×10^{-1}	+52
29	13560−6133 2	13 59 30.762	−61 48 40.12	4.7719×10^{-1}	−50
30	13585−6133 0	14 02 27.156	−61 45 13.05	3.5356×10^{-1}	+31
31	14000−6104 0	14 03 35.149	−61 18 26.87	1.6244×10^{-1}	−63
32	14201−6044 1	14 24 30.603	−60 56 36.28	4.3214×10^{-1}	−17
33	14214−6017 0	14 25 14.179	−60 32 21.79	$1.1790 \times 10^{+0}$	−62
34	14394−6004 0	14 43 11.057	−60 17 16.35	$1.9216 \times 10^{+0}$	+6
35	14557−5849 0	14 59 32.635	−59 00 33.53	$5.1293 \times 10^{+1}$	−138
36	15061−5806 0	15 10 00.528	−58 17 30.35	6.0789×10^{-1}	−4
37	15219−5658 0	15 25 47.784	−57 09 17.94	5.9701×10^{-2}	−18
38	15278−5620 0	15 31 45.509	−56 30 50.73	$1.4787 \times 10^{+0}$	−45
	15278−5620 2^b	...	...	...	...
39	15454−5335 0	15 49 19.409	−53 45 18.64	$4.2513 \times 10^{+0}$	−86
40	15454−5507 0	15 49 18.628	−55 16 53.84	2.6990×10^{-1}	−72
41		15 49 17.947	−55 16 51.61	1.4936×10^{-1}	−113
42	15470−5419 1	15 51 29.544	−54 31 23.06	1.3684×10^{-1}	−59
43	15470−5419 3	15 51 01.338	−54 26 37.45	8.5271×10^{-1}	−59
44	15519−5430 0	15 55 46.767	−54 39 17.64	2.2018×10^{-1}	−18
45	15530−5231 0	15 56 51.367	−52 40 24.87	8.6716×10^{-1}	−99
46	15557−5215 0	15 59 36.170	−52 22 55.17	$1.1532 \times 10^{+0}$	−99
47	15579−5303 0	16 01 46.569	−53 11 42.09	$1.3761 \times 10^{+1}$	−45
48	16061−5048 1	16 10 06.427	−50 50 28.61	$3.3032 \times 10^{+0}$	−71
49	16061−5048 4	16 10 05.966	−50 57 11.58	1.2589×10^{-1}	−31
	16061−5048 5^c	...	...	...	...
50	16069−4858 0	16 10 39.103	−49 05 56.75	9.5290×10^{-2}	−17
51	16093−5015 0	16 13 01.495	−50 22 36.76	2.0062×10^{-1}	−31
52	16112−4943 0	16 15 05.703	−49 50 26.96	5.3459×10^{-1}	−44
53		16 14 59.418	−49 50 41.30	3.2185×10^{-1}	−44
54		16 14 06.703	−49 46 09.56	1.9700×10^{-1}	−44
55	16153−5016 1	16 18 56.682	−50 23 51.12	2.7601×10^{-1}	−45
56	16204−4916 0	16 24 15.247	−49 22 24.62	3.0337×10^{-1}	−84
57	16218−4931 0	16 25 38.389	−49 38 13.02	3.2916×10^{-1}	−99
58	16252−4853 0	16 29 00.539	−48 58 57.91	1.1972×10^{-1}	−56
59	16254−4844 1	16 29 01.156	−48 50 32.09	2.3746×10^{-1}	−43
60	16344−4605 0	16 38 09.058	−46 11 02.29	$3.8671 \times 10^{+1}$	−58
61	16363−4645 0	16 39 59.623	−46 50 20.40	3.3537×10^{-1}	−69
62	16435−4515 0	16 47 02.887	−45 21 27.95	5.0995×10^{-1}	−55
63	16464−4359 0	16 50 01.312	−44 05 03.35	2.6794×10^{-1}	−81
64	16482−4443 0	16 51 46.752	−44 48 54.80	1.0681×10^{-1}	−27
65	16573−4214 2	17 00 32.633	−42 25 08.71	$8.6345 \times 10^{+0}$	−26
66	17033−4035 0	17 06 44.806	−40 39 29.09	3.1869×10^{-1}	−39
67	17040−3959 0	17 07 33.739	−40 03 08.75	1.7729×10^{-1}	−4
68	17082−4114 0	17 11 45.220	−41 17 49.42	2.6972×10^{-1}	−45
69	17118−3909 0	17 15 20.373	−39 13 41.13	2.0184×10^{-1}	−132
70	17149−3916 0	17 18 23.467	−39 18 40.29	5.8627×10^{-1}	+57
71	17184−3638 0	17 21 50.382	−36 41 13.95	8.2766×10^{-1}	+10
72	17195−3811 0	17 23 00.277	−38 14 58.11	8.4816×10^{-1}	−18
73	17195−3811 2	17 23 00.399	−38 14 55.42	$1.0467 \times 10^{+0}$	−50
74		17 23 01.191	−38 13 52.39	2.5878×10^{-1}	−37
75		17 22 57.048	−38 14 37.09	2.0529×10^{-1}	−24
76		17 23 00.216	−38 15 00.55	3.4993×10^{-1}	−10
77	17200−3658 0	17 23 28.498	−37 01 48.34	$3.1568 \times 10^{+0}$	−17
78	17221−3619 1	17 25 32.111	−36 22 05.75	1.4298×10^{-1}	−17

Table 4: continued.

#	Region	α_{J2000} (h m s)	δ_{J2000} ($^\circ$ $'$ $''$)	$\int S_\nu \, d\nu$ [a] (Jy km s^{-1})	v_{peak} (km s^{-1})
79	17230−3531 0	17 26 26.572	−35 33 44.14	1.8233×10^{-1}	−125
80		17 26 27.454	−35 34 42.03	9.5942×10^{-2}	−84
81	17249−3501 0	17 28 17.809	−35 04 12.48	2.4608×10^{-1}	−57
82	17279−3350 0	17 31 15.804	−33 51 51.72	5.8603×10^{-1}	−30
83	17377−3109 0	17 40 57.067	−31 11 00.35	$2.0537 \times 10^{+1}$	−3
84	18018−2426 9	18 04 53.462	−24 26 49.52	5.4888×10^{-1}	+11
85	18144−1723 0	18 17 23.980	−17 22 14.08	$5.2644 \times 10^{+0}$	+40

Notes. [a] Emission integrated over all the velocity range. In most of the cases the water maser emission is only detected in one channel of 13.5 km s^{-1}. [b] The maser emission seen in the map is that also detected in 15278−5620 0. [c] The maser emission seen in the map is that also detected in 16061−5048 1.

Table 5: Physical parameters of optically thin H II regions, and spectral indices

Region	#	Freq. (GHz)	Dist. (kpc)	radius (pc)	T_B (K)	n_e (cm^{-3})	EM (pc cm^{-6})	M_i ($M_\odot$)	log N_{Ly} (s^{-1})	Spectral type	Spectral index
08140−3559 0	1	18.0	3.8	0.102	3.28×10^{-1}	$6.00\times10^{+2}$	$4.91\times10^{+4}$	6.64×10^{-2}	46.26	B0.5	−0.0
08211−4158 0	1	18.0	1.7	0.093	2.11×10^{-2}	$1.59\times10^{+2}$	$3.16\times10^{+3}$	1.34×10^{-2}	44.99	B2	+0.5
	2	22.8	1.7	0.044	4.39×10^{-2}	$4.30\times10^{+2}$	$1.08\times10^{+4}$	3.74×10^{-3}	44.87	B2	+3.2
08438−4340 0	1	18.0	1.3	0.107	4.58×10^{-1}	$6.92\times10^{+2}$	$6.85\times10^{+4}$	8.82×10^{-2}	46.45	B0.5	−2.9
	2	18.0	1.3	0.157	5.98×10^{-1}	$6.54\times10^{+2}$	$8.94\times10^{+4}$	2.60×10^{-1}	46.89	B0.5	−3.2
	3	22.8	1.3	0.053	6.50×10^{-1}	$1.51\times10^{+3}$	$1.60\times10^{+5}$	2.29×10^{-2}	46.20	B0.5	+2.4
08470−4243 0	1	18.0	2.2	0.120	9.72×10^{-2}	$3.01\times10^{+2}$	$1.45\times10^{+4}$	5.40×10^{-2}	45.87	B0.5	+0.5
08477−4359 0	1	22.8	1.8	0.059	2.23×10^{-1}	$8.35\times10^{+2}$	$5.49\times10^{+4}$	1.78×10^{-2}	45.83	B0.5	+2.1
08477−4359 1			1.8								
08563−4225 0	1	18.0	1.7	0.049	1.57×10^{-1}	$6.02\times10^{+2}$	$2.35\times10^{+4}$	7.16×10^{-3}	45.30	B1	+1.3
08589−4714 0			1.5								
09014−4736 0	1	18.0	1.3	0.031	$1.42\times10^{+0}$	$2.25\times10^{+3}$	$2.13\times10^{+5}$	7.27×10^{-3}	45.88	B0.5	+0.4
09026−4842 0	1	18.0	1.9	0.103	2.15×10^{-2}	$1.53\times10^{+2}$	$3.22\times10^{+3}$	1.72×10^{-2}	45.09	B1	+2.4
09131−4723 0	1	18.0	1.7	0.129	2.31×10^{-2}	$1.42\times10^{+2}$	$3.46\times10^{+3}$	3.17×10^{-2}	45.31	B1	+1.3
09166−4813 1	1	18.0	2.3	0.132	3.04×10^{-1}	$4.55\times10^{+2}$	$3.83\times10^{+4}$	3.83×10^{-2}	45.45	B1	−1.6
09209−5143 0	1	18.0	6.4	0.117	3.88×10^{-1}	$6.10\times10^{+2}$	$5.81\times10^{+4}$	1.01×10^{-1}	46.45	B0.5	−0.5
09566−5607 0	1	18.0	6.8	0.148	$4.37\times10^{+0}$	$1.82\times10^{+3}$	$6.53\times10^{+5}$	6.08×10^{-1}	47.71	B0	+0.1
09578−5649 0	1	18.0	1.7	0.129	$6.20\times10^{+0}$	$2.32\times10^{+3}$	$9.27\times10^{+5}$	5.20×10^{-1}	47.74	B0	−2.3
10019−5712 0	1	18.0	1.8	0.045	$7.30\times10^{+0}$	$4.27\times10^{+3}$	$1.09\times10^{+6}$	4.00×10^{-2}	46.89	B0.5	+0.1
10038−5705 0	1	18.0	6.0	0.472	1.40×10^{-2}	$5.77\times10^{+1}$	$2.10\times10^{+3}$	6.29×10^{-1}	46.22	B0.5	−3.8
10088−5730 2			1.8								
10095−5843 0	1	18.0	1.1	0.032	9.75×10^{-2}	$5.85\times10^{+2}$	$1.46\times10^{+4}$	1.97×10^{-3}	44.73	B2	+0.6
	2	18.0	1.1	0.031	1.73×10^{-1}	$7.92\times10^{+2}$	$2.59\times10^{+4}$	2.43×10^{-3}	44.95	B2	−0.5
10123−5727 0	1	18.0	0.9	0.158	3.90×10^{-1}	$5.26\times10^{+2}$	$5.83\times10^{+4}$	2.15×10^{-1}	46.72	B0.5	−2.9
10184−5748 0	1	18.0	5.4	0.278	$6.92\times10^{+0}$	$1.67\times10^{+3}$	$1.03\times10^{+6}$	$3.71\times10^{+0}$	48.45	O7.5	−6.3
	2	18.0	5.4	0.140	$2.83\times10^{+1}$	$4.77\times10^{+3}$	$4.24\times10^{+6}$	$1.34\times10^{+0}$	48.47	O7.5	−2.3
10276−5711 0	1	18.0	5.9	0.484	$3.90\times10^{+0}$	$9.50\times10^{+2}$	$5.83\times10^{+5}$	$1.11\times10^{+1}$	48.69	O7	−1.1
10277−5730 0	1	18.0	5.8	0.133	6.72×10^{-1}	$7.53\times10^{+2}$	$1.01\times10^{+5}$	1.83×10^{-1}	46.80	B0.5	−0.0
	2	18.0	5.8	0.304	7.03×10^{-1}	$5.10\times10^{+2}$	$1.05\times10^{+5}$	$1.47\times10^{+0}$	47.54	B0	+0.0
10286−5838 0	1	18.0	5.9	0.241	4.12×10^{-2}	$1.38\times10^{+2}$	$6.17\times10^{+3}$	2.01×10^{-1}	46.11	B0.5	−0.9
	2	18.0	5.9	0.187	1.74×10^{-1}	$3.23\times10^{+2}$	$2.61\times10^{+4}$	2.19×10^{-1}	46.51	B0.5	+1.3
10295−5746 0	1	18.0	5.0	0.399	$1.37\times10^{+1}$	$1.97\times10^{+3}$	$2.05\times10^{+6}$	$1.29\times10^{+1}$	49.06	O6.5	−2.0
10317−5936 0	1	18.0	8.9	0.508	1.26×10^{-1}	$1.67\times10^{+2}$	$1.89\times10^{+4}$	$2.26\times10^{+0}$	47.24	B0	−6.6
	2	18.0	8.9	0.331	7.60×10^{-1}	$5.08\times10^{+2}$	$1.14\times10^{+5}$	$1.90\times10^{+0}$	47.65	B0	+0.9
10320−5928 0	1	18.0	9.1	0.278	$2.96\times10^{+1}$	$3.45\times10^{+3}$	$4.42\times10^{+6}$	$7.69\times10^{+0}$	49.09	O6	−0.6
10337−5710 0	1	18.0	0.4	<0.007	$>3.70\times10^{+0}$	$>7.82\times10^{+3}$	$>5.53\times10^{+5}$	$<2.53\times10^{-4}$	44.96	B2	+0.3
10439−5941 0	1	18.0	2.6	0.103	$5.94\times10^{+0}$	$2.54\times10^{+3}$	$8.88\times10^{+5}$	2.88×10^{-1}	47.53	B0	−1.0
10501−5556 0	1	18.0	2.5	0.077	7.10×10^{-1}	$1.02\times10^{+3}$	$1.06\times10^{+5}$	4.76×10^{-2}	46.35	B0.5	−4.0
10521−6031 0	1	18.0	8.1	0.276	2.30×10^{-1}	$9.67\times10^{+2}$	$3.45\times10^{+5}$	$2.11\times10^{+0}$	47.97	O9.5	+0.4
10537−5930 0	1	18.0	7.2	0.645	3.73×10^{-1}	$2.55\times10^{+2}$	$5.58\times10^{+4}$	$7.06\times10^{+0}$	47.92	O9.5	−2.4
10548−5929 0	1	18.0	7.6	0.158	8.53×10^{-1}	$7.79\times10^{+2}$	$1.28\times10^{+5}$	3.16×10^{-1}	47.05	B0	+0.6
10555−6242 0	1	18.0	3.0	0.239	1.17×10^{-2}	$7.42\times10^{+1}$	$1.75\times10^{+3}$	1.05×10^{-1}	45.55	B1	−5.0
10545−6244 1	1	18.0	2.0	0.109	1.82×10^{-2}	$1.37\times10^{+2}$	$2.73\times10^{+3}$	1.84×10^{-2}	45.06	B2	+3.4
10559−5914 0	1	18.0	6.4	<0.109	$>2.45\times10^{-1}$	$>5.03\times10^{+2}$	$>3.66\times10^{+4}$	$<6.66\times10^{-2}$	46.19	B0.5	+0.2
10572−6018 0	1	18.0	7.2	0.486	7.32×10^{-1}	$4.11\times10^{+2}$	$1.10\times10^{+5}$	$4.88\times10^{+0}$	47.96	O9.5	−0.2
10575−5844 0	1	22.8	—				$3.11\times10^{+4}$				+0.7
10589−6034 0	1	18.0	8.0	0.159	$7.76\times10^{+1}$	$7.40\times10^{+3}$	$1.16\times10^{+7}$	$3.07\times10^{+0}$	49.02	O6.5	−0.1
10591−5934 0	1	18.0	2.8	0.322	1.39×10^{-1}	$2.20\times10^{+2}$	$2.08\times10^{+4}$	7.61×10^{-1}	46.89	B0.5	−1.8
11079−6101 0	1	18.0	8.2	<0.139	$>3.36\times10^{+0}$	$>1.65\times10^{+3}$	$>5.02\times10^{+5}$	$<4.58\times10^{-1}$	47.54	B0	−0.4
11220−6147 0	1	18.0	7.8	0.362	3.77×10^{-2}	$1.08\times10^{+2}$	$5.63\times10^{+3}$	5.31×10^{-1}	46.42	B0.5	−0.8
11265−6158 0	1	18.0	3.4	0.314	2.68×10^{-2}	$9.78\times10^{+1}$	$4.00\times10^{+3}$	3.12×10^{-1}	46.15	B0.5	+0.0
	2	18.0	3.4	0.234	1.85×10^{-2}	$9.42\times10^{+1}$	$2.76\times10^{+3}$	1.24×10^{-1}	45.73	B1	+0.4
11354−6234 0	1	18.0	9.6	0.627	5.90×10^{-2}	$1.03\times10^{+2}$	$8.83\times10^{+3}$	$2.61\times10^{+0}$	47.09	B0	−3.6
	2	18.0	9.6	0.209	$1.01\times10^{+0}$	$7.37\times10^{+2}$	$1.51\times10^{+5}$	6.93×10^{-1}	47.37	B0	−0.2
11380−6311 0	1	18.0	1.3	0.160	1.50×10^{-1}	$3.24\times10^{+2}$	$2.24\times10^{+4}$	1.38×10^{-1}	46.31	B0.5	−1.4
11404−6215 0	1	18.0	11.0	1.517	8.35×10^{-2}	$7.86\times10^{+1}$	$1.25\times10^{+4}$	$2.83\times10^{+1}$	48.01	O9	−1.6
12063−6259 0	1	18.0	10.1	0.251	$9.76\times10^{+1}$	$6.60\times10^{+3}$	$1.46\times10^{+7}$	$1.08\times10^{+1}$	49.52	O5.5	−0.1
12102−6133 1			4.0								
12127−6244 0	1	18.0	10.8	0.495	$7.32\times10^{+1}$	$4.07\times10^{+3}$	$1.09\times10^{+7}$	$5.11\times10^{+1}$	49.98	O4	−1.6
12132−6211 0	1	18.0	10.2	0.316	$4.19\times10^{+0}$	$1.22\times10^{+3}$	$6.26\times10^{+5}$	$3.99\times10^{+0}$	48.35	O8	−0.2
	2	18.0	10.2	0.338	$5.07\times10^{+0}$	$1.30\times10^{+3}$	$7.59\times10^{+5}$	$5.20\times10^{+0}$	48.49	O7.5	−0.1
12157−6220 0	1	18.0	8.5	<0.144	$>2.12\times10^{+0}$	$>1.28\times10^{+3}$	$>3.17\times10^{+5}$	$<3.98\times10^{-1}$	47.37	B0	−0.1
12268−6156 0	1	22.8	4.3	0.075	$2.24\times10^{+0}$	$2.34\times10^{+3}$	$5.49\times10^{+5}$	1.03×10^{-1}	47.05	B0	+0.4
12272−6240 0	1	18.0	11.2	1.292	3.04×10^{-1}	$1.63\times10^{+2}$	$4.55\times10^{+4}$	$3.62\times10^{+1}$	48.43	O7.5	−2.0
	2	18.0	11.2	0.318	$2.71\times10^{+0}$	$9.78\times10^{+2}$	$4.05\times10^{+5}$	$3.25\times10^{+0}$	48.16	O8.5	+0.7
12295−6224 0	1	18.0	4.4	0.505	2.73×10^{-2}	$7.79\times10^{+1}$	$4.09\times10^{+3}$	$1.04\times10^{+0}$	46.57	B0.5	−1.3
12300−6119 0			4.3								
13023−6213 0	1	18.0	4.8	<0.081	$>9.14\times10^{+0}$	$>3.55\times10^{+3}$	$>1.37\times10^{+6}$	$<1.98\times10^{-1}$	47.51	B0	+0.2
13024−6158 0	1	18.0	2.1	0.062	1.55×10^{-1}	$5.30\times10^{+2}$	$2.31\times10^{+4}$	1.30×10^{-2}	45.50	B1	+1.4
13039−6108 0	1	18.0	2.4	0.138	4.84×10^{-2}	$1.98\times10^{+2}$	$7.24\times10^{+3}$	5.43×10^{-2}	45.69	B1	−2.2
	2	18.0	2.4	0.311	1.64×10^{-2}	$7.70\times10^{+1}$	$2.46\times10^{+3}$	2.39×10^{-1}	45.93	B0.5	−1.2
13039−6108 6			2.4								
13039−6331 0			12.1								
13054−6159 0	1	18.0	3.6	0.219	$3.24\times10^{+0}$	$1.29\times10^{+3}$	$4.84\times10^{+5}$	$1.40\times10^{+0}$	47.92	O9.5	−0.6
13106−6050 0	1	18.0	5.0	0.086	4.82×10^{-1}	$7.93\times10^{+2}$	$7.21\times10^{+4}$	5.21×10^{-2}	46.28	B0.5	+9.5
	2	18.0	5.0	0.345	9.72×10^{-1}	$5.62\times10^{+2}$	$1.45\times10^{+5}$	$2.39\times10^{+0}$	47.79	O9.5	−13.6
13107−6208 0	1	18.0	3.6	0.373	$1.54\times10^{+0}$	$6.81\times10^{+2}$	$2.31\times10^{+5}$	$3.66\times10^{+0}$	48.06	O9	+0.1
13333−6234 0	1	18.0	0.9	<0.015	$>1.69\times10^{+1}$	$>1.11\times10^{+4}$	$>2.53\times10^{+6}$	$<4.10\times10^{-3}$	46.32	B0.5	−0.1
	2	18.0	0.9	0.063	$2.42\times10^{+0}$	$2.08\times10^{+3}$	$3.61\times10^{+5}$	5.34×10^{-2}	46.71	B0.5	−0.4
13395−6153 0	1	18.0	5.3	0.143	1.21×10^{-1}	$3.08\times10^{+2}$	$1.81\times10^{+4}$	9.32×10^{-2}	46.12	B0.5	−0.2

Table 5: continued.

Region	#	Freq. (GHz)	Dist. (kpc)	radius (pc)	T_B (K)	n_e (cm^{-3})	EM (pc cm^{-6})	M_i ($M_\odot$)	log N_{Ly} (s^{-1})	Spectral type	Spectral index
	2	18.0	5.3	<0.090	>3.99 × 10^{+1}	>7.05 × 10^{+3}	>5.97 × 10^{+6}	<5.30 × 10^{-1}	48.24	O8.5	+0.1
13438−6203 0	1	18.0	5.4	0.365	2.93 × 10^{-2}	9.50 × 10^{+1}	4.38 × 10^{+3}	4.76 × 10^{-1}	46.32	B0.5	+2.1
	2	18.0	5.4	0.449	3.37 × 10^{-2}	9.17 × 10^{+1}	5.04 × 10^{+3}	8.59 × 10^{-1}	46.56	B0.5	−3.5
13481−6124 0	1	18.0	3.6	<0.061	>2.32 × 10^{-1}	>6.53 × 10^{+2}	>3.48 × 10^{+4}	<1.54 × 10^{-2}	45.67	B1	+1.2
13534−6152 0	1	18.0	13.1	0.356	1.64 × 10^{+1}	2.27 × 10^{+3}	2.46 × 10^{+6}	1.06 × 10^{+1}	49.05	O6.5	+0.2
13560−6133 2	1	18.0	5.6	0.262	1.79 × 10^{+0}	8.76 × 10^{+2}	2.68 × 10^{+5}	1.63 × 10^{+0}	47.82	O9.5	−0.0
13563−6109 0	1	22.8	5.6	0.149	4.00 × 10^{-2}	2.22 × 10^{+2}	9.83 × 10^{+3}	7.64 × 10^{-2}	45.89	B0.5	+1.6
13585−6133 0	1	18.0	3.2	<0.054	>3.16 × 10^{-1}	>8.09 × 10^{+2}	>4.73 × 10^{+4}	<1.34 × 10^{-2}	45.70	B1	+1.8
	2	18.0	3.2	0.137	7.34 × 10^{-2}	2.45 × 10^{+2}	1.10 × 10^{+4}	6.49 × 10^{-2}	45.86	B0.5	−4.4
13590−6051 0	1	18.0	6.7	0.174	5.30 × 10^{+0}	1.85 × 10^{+3}	7.92 × 10^{+5}	1.01 × 10^{+0}	47.93	O9.5	+0.2
13592−6153 0	1	18.0	4.2	0.215	4.27 × 10^{-2}	1.49 × 10^{+2}	6.39 × 10^{+3}	1.53 × 10^{-1}	46.02	B0.5	−1.9
	2	18.0	4.2	0.133	5.24 × 10^{-2}	2.11 × 10^{+2}	7.84 × 10^{+3}	5.08 × 10^{-2}	45.69	B1	−6.6
14000−6104 0	1	18.0	5.6	0.354	2.18 × 10^{+0}	8.31 × 10^{+2}	3.26 × 10^{+5}	3.82 × 10^{+0}	48.16	O8.5	−0.5
14039−6113 0	1	18.0	4.6	0.294	7.80 × 10^{+0}	1.72 × 10^{+3}	1.17 × 10^{+6}	4.53 × 10^{+0}	48.56	O7.5	−1.7
14057−6032 0	1	18.0	0.8	<0.014	>4.16 × 10^{+0}	>5.86 × 10^{+3}	>6.22 × 10^{+5}	<1.52 × 10^{-3}	45.61	B1	+0.2
14090−6132 0	1	18.0	2.0	<0.034	>2.90 × 10^{-1}	>9.80 × 10^{+2}	>4.34 × 10^{+4}	<3.96 × 10^{-3}	45.25	B1	−0.9
	2	18.0	2.0	0.036	1.82 × 10^{+0}	2.37 × 10^{+3}	2.72 × 10^{+5}	1.16 × 10^{-2}	46.10	B0.5	+0.4
14166−6118 0	1	18.0	3.3	0.116	1.49 × 10^{+0}	1.20 × 10^{+3}	2.22 × 10^{+5}	1.94 × 10^{-1}	47.03	B0.5	+0.2
14183−6050 0	1	18.0	3.4	0.348	2.09 × 10^{-1}	2.60 × 10^{+2}	3.13 × 10^{+4}	1.13 × 10^{+0}	47.13	B0	−1.4
	2	18.0	3.4	0.063	2.75 × 10^{+0}	2.22 × 10^{+3}	4.12 × 10^{+5}	5.64 × 10^{-2}	46.76	B0.5	+0.3
14183−6050 3			3.4								
14188−6054 0	1	18.0	3.3	0.190	4.83 × 10^{-2}	1.69 × 10^{+2}	7.22 × 10^{+3}	1.20 × 10^{-1}	45.97	B0.5	+0.1
14201−6044 0	1	18.0	4.1	0.239	2.27 × 10^{-2}	1.03 × 10^{+2}	3.39 × 10^{+3}	1.45 × 10^{-1}	45.84	B0.5	+0.2
14201−6044 1			4.1								
14212−6009 0	1	18.0	5.9	0.532	4.14 × 10^{+0}	9.35 × 10^{+2}	6.19 × 10^{+5}	1.45 × 10^{+1}	48.80	O7	−1.7
14214−6017 0	1	18.0	5.9	0.622	5.03 × 10^{-1}	3.01 × 10^{+2}	7.52 × 10^{+4}	7.50 × 10^{+0}	48.02	O9	−4.9
	2	18.0	5.9	0.307	4.30 × 10^{-1}	3.96 × 10^{+2}	6.42 × 10^{+4}	1.18 × 10^{+0}	47.33	B0	−1.8
	3	18.0	5.9	0.134	2.95 × 10^{+0}	1.57 × 10^{+3}	4.41 × 10^{+5}	3.90 × 10^{-1}	47.45	B0	+0.8
	4	18.0	5.9	<0.100	>3.08 × 10^{+0}	>1.86 × 10^{+3}	>4.61 × 10^{+5}	<1.93 × 10^{-1}	47.22	B0	−5.5
14394−6004 0	1	18.0	12.2	0.707	1.70 × 10^{+0}	5.19 × 10^{+2}	2.54 × 10^{+5}	1.90 × 10^{+1}	48.66	O7	−1.4
14425−6023 0	1	18.0	3.4	0.173	2.20 × 10^{-2}	1.19 × 10^{+2}	3.29 × 10^{+3}	6.40 × 10^{-2}	45.55	B1	+0.2
14557−5849 0	1	18.0	2.7	0.080	1.15 × 10^{+1}	4.01 × 10^{+3}	1.72 × 10^{+6}	2.14 × 10^{-1}	47.60	B0	+0.3
15015−5720 0	1	18.0	10.4	1.511	1.91 × 10^{+0}	3.77 × 10^{+2}	2.85 × 10^{+5}	1.34 × 10^{+2}	49.37	O5.5	−5.3
	2	22.8	10.4	1.408	6.53 × 10^{-1}	2.92 × 10^{+2}	1.60 × 10^{+5}	8.43 × 10^{+1}	49.05	O6.5	+5.1
15038−5828 1			5.0								
15061−5806 0	1	18.0	0.8	0.059	1.43 × 10^{+1}	5.21 × 10^{+3}	2.14 × 10^{+6}	1.12 × 10^{-1}	47.43	B0	−0.6
	2	18.0	0.8	0.040	2.69 × 10^{+0}	2.73 × 10^{+3}	4.02 × 10^{+5}	1.85 × 10^{-2}	46.37	B0.5	+9.7
15068−5733 0	1	18.0	4.2	0.140	4.13 × 10^{-1}	5.75 × 10^{+2}	6.18 × 10^{+4}	1.64 × 10^{-1}	46.64	B0.5	+0.2
	2	18.0	4.2	0.244	2.55 × 10^{-1}	3.43 × 10^{+2}	3.81 × 10^{+4}	5.13 × 10^{-1}	46.91	B0.5	−1.2
15072−5855 0			3.0								
15100−5613 0	1	18.0	2.9	0.096	4.39 × 10^{+1}	7.15 × 10^{+3}	6.57 × 10^{+6}	6.63 × 10^{-1}	48.34	O8	−0.5
15100−5903 0	1	18.0	3.7	0.129	8.82 × 10^{-2}	2.77 × 10^{+2}	1.32 × 10^{+4}	6.14 × 10^{-2}	45.89	B0.5	+1.2
15178−5641 0	1	18.0	2.1	0.229	7.60 × 10^{-1}	6.11 × 10^{+2}	1.14 × 10^{+5}	7.53 × 10^{-1}	47.33	B0	−1.4
15219−5658 0	1	18.0	1.2	0.038	5.65 × 10^{+0}	4.06 × 10^{+3}	8.46 × 10^{+5}	2.39 × 10^{-2}	46.65	B0.5	+0.2
15239−5538 0	1	18.0	3.3	0.345	1.18 × 10^{-1}	1.96 × 10^{+2}	1.77 × 10^{+4}	8.31 × 10^{-1}	46.87	B0.5	−3.8
15246−5612 0	1	18.0	4.5	0.279	5.43 × 10^{-1}	4.67 × 10^{+2}	8.12 × 10^{+4}	1.05 × 10^{+0}	47.35	B0	−1.3
15262−5541 1	1	18.0	3.7	0.244	1.64 × 10^{-2}	8.68 × 10^{+1}	2.45 × 10^{+3}	1.31 × 10^{-1}	45.72	B1	+1.3
15278−5620 0	1	18.0	3.4	0.150	2.25 × 10^{+0}	1.29 × 10^{+3}	3.36 × 10^{+5}	4.55 × 10^{-1}	47.43	B0	−0.2
15278−5620 2			3.4								
15347−5518 0	1	18.0	4.2	0.148	1.11 × 10^{+0}	9.18 × 10^{+2}	1.66 × 10^{+5}	3.06 × 10^{-1}	47.11	B0	−0.8
15371−5458 0	1	18.0	17.6	1.075	1.99 × 10^{+0}	4.56 × 10^{+2}	2.98 × 10^{+5}	5.85 × 10^{+1}	49.09	O6	−0.9
15454−5335 0	1	18.0	5.2	<0.088	>1.20 × 10^{+1}	>3.91 × 10^{+3}	>1.80 × 10^{+6}	<2.78 × 10^{-1}	47.70	B0	+0.3
15454−5507 0	1	18.0	4.4	0.122	5.03 × 10^{-1}	6.81 × 10^{+2}	7.52 × 10^{+4}	1.27 × 10^{-1}	46.60	B0.5	−1.4
15464−5445 0	1	18.0	3.9	0.456	5.62 × 10^{-1}	3.72 × 10^{+2}	8.41 × 10^{+4}	3.65 × 10^{+0}	47.79	O9.5	−1.3
15470−5419 0	1	18.0	4.1	0.193	1.35 × 10^{+0}	8.87 × 10^{+2}	2.02 × 10^{+5}	6.55 × 10^{-1}	47.43	B0	−1.4
15470−5419 4			4.1								
15470−5419 3			4.1								
15470−5419 1			4.1								
15506−5325 0	1	18.0	4.7	0.617	1.73 × 10^{-1}	1.77 × 10^{+2}	2.59 × 10^{+4}	4.31 × 10^{+0}	47.55	B0	−1.6
	2	18.0	4.7	0.266	2.96 × 10^{-1}	3.53 × 10^{+2}	4.43 × 10^{+4}	6.90 × 10^{-1}	47.05	B0	+3.3
15507−5359 0	1	18.0	5.0	0.280	9.80 × 10^{+0}	1.98 × 10^{+3}	1.47 × 10^{+6}	4.51 × 10^{+0}	48.61	O7	−2.2
15519−5430 0	1	18.0	2.7	0.240	2.95 × 10^{+0}	3.72 × 10^{+2}	4.41 × 10^{+4}	5.28 × 10^{-1}	46.96	B0.5	−1.5
15530−5231 0	1	18.0	6.0	0.401	1.21 × 10^{+0}	5.82 × 10^{+2}	1.81 × 10^{+5}	3.88 × 10^{+0}	48.02	O9	−1.2
	2	18.0	6.0	0.262	1.77 × 10^{+0}	8.72 × 10^{+2}	2.65 × 10^{+5}	1.62 × 10^{+0}	47.81	O9.5	−0.6
15557−5215 0	1	18.0	10.2	0.688	2.16 × 10^{-1}	1.88 × 10^{+2}	3.23 × 10^{+4}	6.31 × 10^{+0}	47.74	B0	−0.9
15557−5337 0	1	18.0	11.2	0.325	5.73 × 10^{+1}	4.45 × 10^{+3}	8.58 × 10^{+6}	1.57 × 10^{+1}	49.51	O5.5	−1.9
	2	18.0	11.2	0.346	1.03 × 10^{+2}	5.79 × 10^{+3}	1.55 × 10^{+7}	2.49 × 10^{+1}	49.82	O5	−0.2
15579−5303 0	1	18.0	3.5	0.086	1.92 × 10^{-1}	5.00 × 10^{+2}	2.87 × 10^{+4}	3.30 × 10^{-2}	45.88	B0.5	+0.5
15579−5347 0	1	18.0	3.3	0.226	2.80 × 10^{-2}	1.18 × 10^{+2}	4.18 × 10^{+3}	1.40 × 10^{-1}	45.88	B0.5	+0.9
15583−5314 0	1	18.0	5.0	0.183	3.39 × 10^{-2}	1.44 × 10^{+2}	5.07 × 10^{+3}	9.10 × 10^{-2}	45.78	B0.5	+0.0
16056−5125 0	1	22.8	4.8	0.096	3.58 × 10^{+0}	2.62 × 10^{+3}	8.80 × 10^{+5}	2.40 × 10^{-1}	47.46	B0	−0.8
16061−5048 0	1	18.0	3.6	0.179	7.45 × 10^{-2}	2.16 × 10^{+2}	1.11 × 10^{+4}	1.28 × 10^{-1}	46.10	B0.5	+0.5
16061−5048 5	1	18.0	3.6	0.064	2.99 × 10^{-1}	7.27 × 10^{+2}	4.48 × 10^{+4}	1.92 × 10^{-2}	45.81	B0.5	+0.3
16061−5048 1			3.6								
	2	22.8	3.6	0.066	5.58 × 10^{-2}	3.93 × 10^{+2}	1.37 × 10^{+4}	1.19 × 10^{-2}	45.33	B1	+1.3
16061−5048 4	1	18.0	3.6	0.417	3.37 × 10^{-2}	9.53 × 10^{+1}	5.04 × 10^{+3}	7.11 × 10^{-1}	46.49	B0.5	−1.9
16069−4858 0	1	18.0	1.9	0.075	2.06 × 10^{-1}	5.56 × 10^{+2}	3.08 × 10^{+4}	2.40 × 10^{-2}	45.79	B0.5	−0.1
	2	18.0	1.9	0.099	2.55 × 10^{-1}	5.37 × 10^{+2}	3.81 × 10^{+4}	5.41 × 10^{-2}	46.13	B0.5	−0.6
	3	18.0	1.9	0.104	3.44 × 10^{-1}	6.08 × 10^{+2}	5.14 × 10^{+4}	7.14 × 10^{-2}	46.30	B0.5	−1.4
16085−5138 0	1	18.0	4.3	0.487	2.85 × 10^{+0}	8.10 × 10^{+2}	4.26 × 10^{+5}	9.66 × 10^{+0}	48.56	O7.5	−1.6

Table 5: continued.

Region	#	Freq. (GHz)	Dist. (kpc)	radius (pc)	T_B (K)	n_e (cm^{-3})	EM (pc cm^{-6})	M_i ($M_\odot$)	$\log N_{Ly}$ (s^{-1})	Spectral type	Spectral index
16093−5128 8	1	18.0	6.1	0.478	5.65×10^{-2}	$8.46 \times 10^{+3}$	$1.15 \times 10^{+2}$	$1.30 \times 10^{+0}$	46.84	B0.5	−4.6
16093−5128 2	1	18.0	6.1	<0.104	$>1.79 \times 10^{+1}$	$>4.40 \times 10^{+3}$	$>2.67 \times 10^{+6}$	$<5.04 \times 10^{-1}$	48.01	O9	−0.1
16093−5128 0	1	18.0	6.1	0.154	$6.02 \times 10^{+0}$	$2.09 \times 10^{+3}$	$9.01 \times 10^{+5}$	7.95×10^{-1}	47.88	O9.5	+0.0
16093−5015 0			11.9								
16106−5048 0	1	18.0	5.5	0.101	8.10×10^{-1}	$9.47 \times 10^{+2}$	$1.21 \times 10^{+5}$	1.02×10^{-1}	46.65	B0.5	−0.1
16107−4956 0	1	18.0	5.2	0.271	1.68×10^{-2}	$8.33 \times 10^{+1}$	$2.51 \times 10^{+3}$	1.72×10^{-1}	45.82	B0.5	+0.9
16112−4943 0	1	18.0	3.3	0.319	$3.24 \times 10^{+0}$	$1.07 \times 10^{+3}$	$4.85 \times 10^{+5}$	$3.57 \times 10^{+0}$	48.24	O8.5	−0.5
16148−5011 0	1	18.0	3.3	0.134	$3.69 \times 10^{+0}$	$1.76 \times 10^{+3}$	$5.52 \times 10^{+5}$	4.39×10^{-1}	47.55	B0	+0.0
16153−5016 1	1	18.0	3.1	0.086	$3.05 \times 10^{+0}$	$1.99 \times 10^{+3}$	$4.57 \times 10^{+5}$	1.32×10^{-1}	47.08	B0	−1.1
16164−4929 0	1	18.0	2.6	0.090	$7.38 \times 10^{+0}$	$3.03 \times 10^{+3}$	$1.10 \times 10^{+6}$	2.29×10^{-1}	47.51	B0	+0.0
16164−4929 3	1	18.0	2.6	0.066	2.44×10^{-1}	$6.46 \times 10^{+2}$	$3.65 \times 10^{+4}$	1.88×10^{-2}	45.75	B1	+1.7
16164−4837 0	1	22.8	3.6	0.136	5.45×10^{-2}	$2.71 \times 10^{+2}$	$1.34 \times 10^{+4}$	7.10×10^{-2}	45.95	B0.5	+0.6
16170−5053 0	1	18.0	11.4	0.605	5.82×10^{-1}	$3.29 \times 10^{+2}$	$8.71 \times 10^{+4}$	$7.53 \times 10^{+0}$	48.06	O9	−2.7
16194−4934 0	1	18.0	5.3	0.129	$1.11 \times 10^{+0}$	$9.83 \times 10^{+2}$	$1.66 \times 10^{+5}$	2.19×10^{-1}	47.00	B0.5	+0.2
16204−4916 0	1	18.0	4.6	0.239	$3.93 \times 10^{+0}$	$1.36 \times 10^{+3}$	$5.88 \times 10^{+5}$	$1.92 \times 10^{+0}$	48.08	O9	−0.4
16218−4931 0	1	18.0	2.9	0.092	8.26×10^{-1}	$1.00 \times 10^{+3}$	$1.24 \times 10^{+5}$	8.05×10^{-2}	46.57	B0.5	+0.5
16252−4853 0	1	18.0	3.4	0.183	4.39×10^{-1}	$5.19 \times 10^{+2}$	$6.56 \times 10^{+4}$	3.27×10^{-1}	46.89	B0.5	−1.0
16254−4844 1	1	18.0	3.4	0.149	1.60×10^{-2}	$1.10 \times 10^{+2}$	$2.39 \times 10^{+3}$	3.77×10^{-2}	45.28	B1	+0.2
	2	18.0	3.4	0.134	1.69×10^{-2}	$1.19 \times 10^{+2}$	$2.53 \times 10^{+3}$	2.94×10^{-2}	45.21	B1	+0.2
	3	22.8	3.4	0.121	1.49×10^{-2}	$1.51 \times 10^{+2}$	$3.05 \times 10^{+3}$	2.75×10^{-2}	45.28	B1	+1.0
16344−4605 0	1	18.0	4.4	0.259	2.04×10^{-2}	$9.40 \times 10^{+1}$	$3.05 \times 10^{+3}$	1.69×10^{-1}	45.86	B0.5	−0.8
16363−4645 0	1	18.0	4.5	0.363	2.06×10^{-1}	$2.52 \times 10^{+2}$	$3.08 \times 10^{+4}$	$1.25 \times 10^{+0}$	47.16	B0	-10.1
	2	18.0	4.5	0.279	3.43×10^{-1}	$3.71 \times 10^{+2}$	$5.13 \times 10^{+4}$	8.37×10^{-1}	47.16	B0	−1.1
16396−4429 0	1	18.0	5.0	<0.085	$>9.25 \times 10^{+0}$	$>3.50 \times 10^{+3}$	$>1.38 \times 10^{+6}$	$<2.21 \times 10^{-1}$	47.55	B0	+0.1
16419−4602 0	1	18.0	3.2	0.159	7.05×10^{-1}	$7.05 \times 10^{+2}$	$1.05 \times 10^{+5}$	2.94×10^{-1}	46.98	B0.5	−3.1
16428−4109 2	1	22.8	2.7	0.152	1.06×10^{-2}	$1.13 \times 10^{+2}$	$2.61 \times 10^{+3}$	4.12×10^{-2}	45.33	B1	+3.6
16428−4109 1	1	18.0	2.7	0.221	1.53×10^{-2}	$8.80 \times 10^{+1}$	$2.28 \times 10^{+3}$	9.82×10^{-2}	45.60	B1	+1.5
16435−4515 0	1	18.0	4.0	0.090	6.09×10^{-1}	$8.69 \times 10^{+2}$	$9.10 \times 10^{+4}$	6.63×10^{-2}	46.42	B0.5	+0.4
16435−4515 3	1	18.0	4.0	0.214	5.71×10^{-2}	$1.73 \times 10^{+2}$	$8.53 \times 10^{+3}$	1.76×10^{-1}	46.15	B0.5	−1.7
	2	18.0	4.0	0.261	1.32×10^{-2}	$7.54 \times 10^{+1}$	$1.98 \times 10^{+3}$	1.39×10^{-1}	45.68	B1	−1.0
16464−4359 0	1	18.0	5.3	0.319	4.72×10^{-2}	$1.29 \times 10^{+2}$	$7.06 \times 10^{+3}$	4.32×10^{-1}	46.41	B0.5	−0.1
16482−4443 0	1	18.0	3.7	0.179	7.18×10^{-2}	$2.12 \times 10^{+2}$	$1.07 \times 10^{+4}$	1.26×10^{-1}	46.09	B0.5	−2.0
	2	18.0	3.7	0.097	8.12×10^{-2}	$3.07 \times 10^{+2}$	$1.21 \times 10^{+4}$	2.85×10^{-2}	45.61	B1	+0.5
16501−4314 0	1	18.0	9.5	0.816	5.90×10^{-1}	$2.85 \times 10^{+2}$	$8.83 \times 10^{+4}$	$1.60 \times 10^{+1}$	48.32	O8	−1.6
16535−4300 0	1	18.0	6.8	0.343	1.93×10^{-2}	$7.96 \times 10^{+1}$	$2.89 \times 10^{+3}$	3.31×10^{-1}	46.08	B0.5	+1.4
16573−4214 2			2.6								
16573−4214 0	1	18.0	2.6	0.220	5.12×10^{-1}	$5.12 \times 10^{+2}$	$7.66 \times 10^{+4}$	5.59×10^{-1}	47.12	B0	−1.1
16574−4225 0	1	18.0	2.8	0.065	$1.47 \times 10^{+0}$	$1.59 \times 10^{+3}$	$2.20 \times 10^{+5}$	4.54×10^{-2}	46.52	B0.5	−0.3
16579−4245 0			3.3								
17033−4035 0			9.8								
17036−4033 0	1	18.0	5.7	0.125	3.95×10^{-1}	$5.94 \times 10^{+2}$	$5.91 \times 10^{+4}$	1.21×10^{-1}	46.52	B0.5	−0.7
	2	18.0	5.7	0.317	1.93×10^{-2}	$8.27 \times 10^{+1}$	$2.89 \times 10^{+3}$	2.71×10^{-1}	46.01	B0.5	−3.4
17040−3959 0	1	18.0	16.5	0.581	4.89×10^{-1}	$3.07 \times 10^{+2}$	$7.32 \times 10^{+4}$	$6.23 \times 10^{+0}$	47.94	O9.5	−0.1
17040−3959 1			16.5								
17082−4114 0	1	18.0	2.5	0.072	6.85×10^{-2}	$3.28 \times 10^{+2}$	$1.02 \times 10^{+4}$	1.24×10^{-2}	45.27	B1	+1.1
	2	18.0	2.5	0.076	4.58×10^{-1}	$8.20 \times 10^{+2}$	$6.84 \times 10^{+4}$	3.78×10^{-2}	46.15	B0.5	+0.1
17095−3837 0	1	18.0	5.6	0.189	$2.32 \times 10^{+0}$	$1.18 \times 10^{+3}$	$3.47 \times 10^{+5}$	8.14×10^{-1}	47.64	B0	+0.1
17118−3909 0	1	18.0	6.4	0.403	$1.82 \times 10^{+0}$	$7.13 \times 10^{+2}$	$2.73 \times 10^{+5}$	$4.82 \times 10^{+0}$	48.20	O8.5	−1.4
17141−3606 0	1	18.0	0.9	0.052	1.98×10^{-2}	$2.07 \times 10^{+2}$	$2.96 \times 10^{+3}$	2.99×10^{-3}	44.45	B2	−4.2
17149−3916 0	1	18.0	2.1	0.255	$3.62 \times 10^{+0}$	$1.26 \times 10^{+3}$	$5.41 \times 10^{+5}$	$2.17 \times 10^{+0}$	48.10	O8.5	−3.7
17184−3638 0	1	18.0	27.1	<0.460	$>1.42 \times 10^{+2}$	$>5.88 \times 10^{+3}$	$>2.12 \times 10^{+7}$	$<5.91 \times 10^{+1}$	50.20	O4	+0.1
17195−3811 2			3.6								
17200−3658 0	1	18.0	3.1	0.219	8.89×10^{-3}	$6.75 \times 10^{+1}$	$1.33 \times 10^{+3}$	7.32×10^{-2}	45.36	B1	+1.4
17211−3537 0	1	18.0	6.2	0.348	2.11×10^{-1}	$2.61 \times 10^{+2}$	$3.15 \times 10^{+4}$	$1.14 \times 10^{+0}$	47.13	B0	−0.8
17210−3646 0	1	18.0	2.6	0.136	2.56×10^{-1}	$4.60 \times 10^{+2}$	$3.83 \times 10^{+4}$	1.20×10^{-1}	46.40	B0.5	−1.0
17218−3704 0	1	18.0	3.3	0.309	2.73×10^{-2}	$9.96 \times 10^{+1}$	$4.09 \times 10^{+3}$	3.05×10^{-1}	46.15	B0.5	−3.6
17221−3619 1	1	18.0	3.6	0.281	$8.78 \times 10^{+0}$	$1.87 \times 10^{+3}$	$1.31 \times 10^{+6}$	$4.28 \times 10^{+0}$	48.57	O7	−1.5
17225−3426 0	1	18.0	1.1	0.097	4.70×10^{-1}	$7.36 \times 10^{+2}$	$7.02 \times 10^{+4}$	7.01×10^{-2}	46.37	B0.5	−3.8
17230−3531 0	1	18.0	—				$2.15 \times 10^{+4}$				−1.8
	2	18.0	—				$1.12 \times 10^{+5}$				−1.6
	3	18.0	—				$2.24 \times 10^{+4}$				−0.8
17242−3513 0	1	18.0	—				$1.93 \times 10^{+5}$				−7.4
	2	18.0	—				$2.69 \times 10^{+5}$				−4.0
	3	18.0	—				$2.98 \times 10^{+5}$				+2.2
17249−3501 0	1	18.0	10.9	0.457	$1.04 \times 10^{+1}$	$1.60 \times 10^{+3}$	$1.56 \times 10^{+6}$	$1.58 \times 10^{+1}$	49.06	O6.5	−0.2
17249−3501 5			10.9								
17256−3631 0	1	18.0	2.0	0.173	$7.38 \times 10^{+0}$	$2.19 \times 10^{+3}$	$1.10 \times 10^{+6}$	$1.18 \times 10^{+0}$	48.07	O9	−1.2
17279−3350 0	1	18.0	5.2	0.282	$5.14 \times 10^{+0}$	$1.43 \times 10^{+3}$	$7.69 \times 10^{+5}$	$3.32 \times 10^{+0}$	48.34	O8	−1.2
17296−3236 0	1	22.8	6.0	0.126	1.61×10^{-1}	$4.84 \times 10^{+2}$	$3.94 \times 10^{+4}$	1.00×10^{-1}	46.35	B0.5	+0.0
17352−3153 0	1	18.0	6.6	0.196	3.88×10^{-1}	$4.71 \times 10^{+2}$	$5.81 \times 10^{+4}$	3.69×10^{-1}	46.90	B0.5	+0.2
17355−3241 0			1.7								
17377−3109 0	1	18.0	0.8	<0.014	$>3.65 \times 10^{+0}$	$>5.49 \times 10^{+3}$	$>5.46 \times 10^{+5}$	$<1.42 \times 10^{-3}$	45.56	B1	+1.3
17425−3017 0	1	18.0	8.0	0.508	1.80×10^{-2}	$6.31 \times 10^{+1}$	$2.69 \times 10^{+3}$	8.52×10^{-1}	46.39	B0.5	+0.1
18018−2426 9	1	18.0	3.1	0.140	4.50×10^{-1}	$6.01 \times 10^{+2}$	$6.72 \times 10^{+4}$	1.70×10^{-1}	46.67	B0.5	−2.5
	2	18.0	3.1	0.267	1.80×10^{-1}	$2.75 \times 10^{+2}$	$2.69 \times 10^{+4}$	5.39×10^{-1}	46.83	B0.5	−2.5
	3	18.0	3.1	0.117	5.12×10^{-1}	$7.01 \times 10^{+2}$	$7.66 \times 10^{+4}$	1.16×10^{-1}	46.57	B0.5	−2.5
18144−1723 0	1	22.8	4.4	0.111	5.72×10^{-1}	$9.76 \times 10^{+2}$	$1.41 \times 10^{+5}$	1.37×10^{-1}	46.79	B0.5	+1.8
18198−1429 0	1	22.8	4.3	0.170	3.79×10^{-2}	$2.03 \times 10^{+2}$	$9.31 \times 10^{+3}$	1.03×10^{-1}	45.98	B0.5	+1.4

Table 7: Sources classified as *type 1* objects: millimeter-only sources

millimeter[a]				centimeter[b]		H$_2$O maser[c]	
Region	#	α_{J2000}	δ_{J2000}	Region	#	Region	#
08438−4340	2	131.382	−43.839				
08438−4340	1	131.394	−43.868			08438−4340 0	1
08470−4243	1	132.197	−42.911				
08477−4359	3	132.378	−44.191				
08477−4359	2	132.378	−44.184				
08477−4359	1	132.396	−44.200				
08563−4225	4	134.540	−42.644				
09014−4736	2	135.784	−47.812				
09131−4723	4	138.708	−47.590				
09131−4723	2	138.715	−47.586				
09166−4813	1	139.577	−48.447				
09209−5143	2	140.659	−51.935				
09578−5649	2	149.871	−57.076			09578−5649 0	7
10088−5730	2	152.674	−57.743				
10276−5711	2	157.413	−57.438				
10277−5730	1	157.414	−57.762				
10295−5746	8	157.897	−58.038				
10295−5746	5	157.872	−58.022				
10295−5746	2	157.855	−58.051				
10317−5936	2	158.387	−59.878				
10317−5936	1	158.404	−59.858			10317−5936 0	13
10320−5928	3	158.516	−59.731				
10320−5928	2	158.450	−59.734				
10439−5941	3	161.484	−59.964				
10521−6031	1	163.541	−60.798				
10537−5930	1	163.954	−59.789				
10545−6244	1	164.387	−62.989				
10548−5929	2	164.216	−59.763				
10548−5929	1	164.207	−59.756				
10554−6237	1	164.388	−62.986				
10559−5914	2	164.493	−59.513				
10572−6018	1	164.808	−60.572				
10575−5844	1	164.922	−59.014				
10591−5934	3	165.272	−59.857				
10591−5934	2	165.298	−59.846				
10591−5934	1	165.294	−59.859				
11079−6101	2	167.473	−61.304				
11354−6234	1	174.440	−62.861				
11380−6311	7	175.160	−63.457				
11380−6311	3	175.125	−63.468			11380−6311 0	19
11404−6215	1	175.710	−62.546			11404−6215 0	24
12102−6133	1	183.213	−61.831				
12127−6244	4	183.889	−63.033				
12132−6211	1	183.961	−62.464				
12157−6220	1	184.613	−62.625				
12272−6240	3	187.512	−62.964				
12295−6224	3	188.099	−62.701	12295−6224 0	1		
12295−6224	2	188.114	−62.684				
12295−6224	1	188.099	−62.693				
13039−6108	7	196.826	−61.366				
13039−6108	6	196.812	−61.382				
13039−6108	5	196.784	−61.409	13039−6108 0	1		
13054−6159	5	197.117	−62.250				
13054−6159	3	197.131	−62.261				
13106−6050	5	198.451	−61.130				
13106−6050	4	198.456	−61.101				
13333−6234	4	204.190	−62.840				
13333−6234	3	204.224	−62.829				
13438−6203	1	206.851	−62.300	13438−6203 0	2	13438−6203 0	27
13481−6124	5	207.922	−61.670				
13481−6124	4	207.917	−61.637				
13560−6133	2	209.888	−61.820				
13560−6133	1	209.883	−61.811			13560−6133 2	29
13563−6109	6	210.018	−61.391				
13563−6109	5	209.967	−61.420				
13563−6109	3	210.004	−61.396				
14000−6104	4	210.865	−61.299				
14039−6113	6	211.878	−61.455				
14090−6132	4	213.163	−61.792				
14090−6132	3	213.134	−61.790				
14166−6118	2	215.091	−61.520				
14183−6050	4	215.498	−61.069	14183−6050 0	1		
14183−6050	3	215.590	−61.112				
14183−6050	2	215.649	−61.129				
14188−6054	2	215.647	−61.127				
14201−6044	2	215.948	−60.954				
14201−6044	1	216.122	−60.943			14201−6044 1	32
14212−6009	4	216.276	−60.383				
14212−6009	1	216.235	−60.387	14212−6009 0	1		
14214−6017	4	216.279	−60.503				
14394−6004	2	220.831	−60.292				
14394−6004	1	220.795	−60.288			14394−6004 0	34
14557−5849	1	224.887	−59.010			14557−5849 0	35

Table 7: continued.

millimeter[a]				centimeter[b]		H$_2$O maser[c]	
Region	#	α_{J2000}	δ_{J2000}	Region	#	Region	#
15015−5720	2	226.347	−57.539				
15038−5828	1	226.885	−58.676				
15061−5806	6	227.467	−58.306				
15061−5806	3	227.526	−58.275				
15072−5855	1	227.787	−59.113				
15100−5903	1	228.517	−59.250				
15178−5641	2	230.407	−56.878				
15262−5541	1	232.527	−55.878				
15278−5620	2	232.934	−56.536				
15371−5458	1	235.244	−55.139	15371−5458 0	1		
15454−5507	1	237.341	−55.281				
15464−5445	1	237.578	−54.909				
15470−5419	4	237.734	−54.511				
15470−5419	3	237.757	−54.446			15470−5419 3	43
15470−5419	1	237.868	−54.528				
15506−5325	3	238.615	−53.551				
15506−5325	1	238.619	−53.563				
15530−5231	4	239.191	−52.687				
15557−5215	4	239.872	−52.398				
15557−5215	2	239.901	−52.383			15557−5215 0	46
15557−5215	1	239.919	−52.392				
15579−5303	5	240.470	−53.199				
15579−5303	1	240.444	−53.195	15579−5303 0	1	15579−5303 0	47
16061−5048	5	242.489	−50.819				
16061−5048	4	242.528	−50.953	16061−5048 4	1	16061−5048 4	49
16061−5048	3	242.489	−50.939				
16061−5048	2	242.510	−50.826				
16061−5048	1	242.528	−50.841	16061−5048 1	2	16061−5048 1	48
16085−5138	10	243.246	−51.722				
16085−5138	4	243.070	−51.766				
16093−5015	2	243.286	−50.378				
16093−5015	1	243.258	−50.378			16093−5015 0	51
16093−5128	8	243.206	−51.609				
16093−5128	2	243.231	−51.723				
16106−5048	3	243.622	−50.930				
16107−4956	2	243.626	−50.057				
16107−4956	1	243.629	−50.066				
16112−4943	2	243.776	−49.841			16112−4943 0	52
16148−5011	3	244.647	−50.315				
16153−5016	9	244.666	−50.317				
16164−4929	6	245.133	−49.591				
16164−4929	4	245.092	−49.593				
16164−4929	3	245.102	−49.593				
16170−5053	1	245.197	−51.006				
16254−4844	1	247.254	−48.842	16254−4844 1	2	16254−4844 1	59
16363−4645	6	249.999	−46.863				
16419−4602	2	251.408	−46.126				
16419−4602	1	251.395	−46.130				
16428−4109	4	251.730	−41.248				
16428−4109	3	251.728	−41.237				
16428−4109	2	251.695	−41.239				
16428−4109	1	251.757	−41.255	16428−4109 1	1		
16435−4515	4	251.768	−45.341				
16435−4515	3	251.888	−45.381	16435−4515 3	2		
16464−4359	1	252.507	−44.084			16464−4359 0	63
16535−4300	1	254.279	−43.089				
16573−4214	5	255.217	−42.319				
16573−4214	4	255.244	−42.306				
16573−4214	3	255.232	−42.315				
16573−4214	2	255.139	−42.422				
16579−4245	3	255.383	−42.826				
17033−4035	4	256.711	−40.660				
17033−4035	2	256.682	−40.669				
17033−4035	1	256.673	−40.669				
17036−4033	6	256.805	−40.619				
17036−4033	4	256.808	−40.610				
17036−4033	2	256.799	−40.608				
17040−3959	2	256.888	−40.053	17040−3959 0	1	17040−3959 0	67
17040−3959	1	256.995	−40.040				
17082−4114	2	257.969	−41.294				
17082−4114	1	257.931	−41.305				
17095−3837	4	258.221	−38.682				
17095−3837	3	258.221	−38.674				
17095−3837	1	258.238	−38.674				
17141−3606	11	259.362	−36.141				
17141−3606	10	259.387	−36.156				
17141−3606	9	259.368	−36.154				
17141−3606	8	259.381	−36.152				
17149−3916	4	259.622	−39.317				
17149−3916	3	259.593	−39.311			17149−3916 0	70
17149−3916	2	259.579	−39.315				
17184−3638	2	260.472	−36.682				
17195−3811	3	260.754	−38.261				

Table 7: continued.

millimeter[a]				centimeter[b]		H$_2$O maser[c]	
Region	#	α_{J2000}	δ_{J2000}	Region	#	Region	#
17195−3811	2	260.751	−38.249			17195−3811 0	72
17210−3646	2	261.108	−36.806				
17211−3537	1	261.119	−35.672				
17218−3704	3	261.303	−37.136				
17218−3704	2	261.328	−37.120				
17218−3704	1	261.319	−37.123				
17221−3619	3	261.395	−36.359				
17230−3531	2	261.596	−35.562	17230−3531 0	1		
17230−3531	1	261.610	−35.562			17230−3531 0	79
17242−3513	4	261.894	−35.273	17242−3513 0	3		
17249−3501	5	262.125	−35.031				
17249−3501	3	262.095	−35.075				
17256−3631	8	262.252	−36.578				
17256−3631	6	262.255	−36.541				
17256−3631	3	262.241	−36.538				
17425−3017	1	266.438	−30.310				
18014−2428	15	271.228	−24.430				

Notes. [a] Millimeter source: Region indicates the IRAS name, # indicates the millimeter clump from Beltrán et al. (2006), α_{J2000} and δ_{J2000} are the right ascension (in degrees) and the declination (in degrees). [b] Centimeter source: Region indicates the name of the ATCA field (see Table 1), # indicates the number of the ATCA source detected in the observed field (see Table 3). [c] H$_2$O maser spot: Region indicates the name of the ATCA field (see Table 1), # indicates the number of the water maser component as listed in Table 4.

Table 8: Sources classified as *type 2* objects: millimeter and infrared sources

millimeter[a]				infrared[b]			centimeter[c]		H$_2$O maser[d]	
Region	#	α_{J2000}	δ_{J2000}	MSX name	α_{J2000}	δ_{J2000}	Region	#	Region	#
08140−3559	1	123.985	−36.134	G254.0491−00.5615	123.988	−36.136				
08211−4158	1	125.718	−42.135	G259.7592−02.8378	125.718	−42.132	08211−4158 0	1		
08563−4225	1	134.549	−42.628	G264.1444+02.0190	134.553	−42.627	08563−4225 0	1	08563−4225 0	3
08589−4714	1	135.165	−47.436	G268.0594−00.8040	135.171	−47.434			08589−4714 0	4
09014−4736	1	135.764	−47.808	G268.6056−00.7476	135.770	−47.806				
09026−4842	3	136.096	−48.910	G269.5703−01.3202	136.094	−48.907	09026−4842 0	1		
09131−4723	1	138.721	−47.597	G269.8017+00.8510	138.721	−47.599	09131−4723 0	1		
09209−5143	3	140.651	−51.944	G273.7699−01.3089	140.650	−51.943	09209−5143 0	1		
09566−5607	1	149.593	−56.371	G280.6208−01.1879	149.597	−56.371	09566−5607 0	1		
09578−5649	1	149.883	−57.063	G281.1641−01.6418	149.879	−57.061	09578−5649 0	1		
10019−5712	1	150.919	−57.446	G281.8449+01.6094	150.921	−57.444	10019−5712 0	1	10019−5712 0	8
10038−5705	1	151.379	−57.332	G281.9780+01.3712	151.381	−57.331				
10095−5843	1	152.812	−58.973	G283.5475−02.2655	152.815	−58.971	10095−5843 0	1	10095−5843 0	10
10123−5727	3	153.574	−57.690	G283.1465−00.9828	153.575	−57.688				
10123−5727	1	153.533	−57.697	G283.1277−01.0041	153.524	−57.695	10123−5727 0	1		
10184−5748	1	155.065	−58.067	G284.0155−00.8579	155.065	−58.066	10184−5748 0	2		
10276−5711	1	157.388	−57.447	G284.7336+00.3265	157.385	−57.443	10276−5711 0	1		
10286−5838	1	157.636	−58.898	G285.5970−00.8508	157.639	−58.897	10286−5838 0	2		
10295−5746	1	157.872	−58.040	G285.2611−00.0492	157.871	−58.037	10295−5746 0	1	10295−5746 0	12
10320−5928	1	158.485	−59.734	G286.3938−01.3514	158.485	−59.733	10320−5928 0	1		
10337−5710	1	158.915	−57.438	G285.4410+00.7510	158.918	−57.436	10337−5710 0	1	10337−5710 0	14
10439−5941	1	161.479	−59.949	G287.8134−00.8140	161.476	−59.949	10439−5941 0	1		
10501−5556	1	163.046	−56.212	G286.8574+02.8949	163.044	−56.209	10501−5556 0	1	10501−5556 0	15
10555−6242	1	164.389	−62.986	G290.4086−02.9130	164.389	−62.982	10545−6244 1	1	10545−6244 1	16
10559−5914	1	164.462	−59.493	G288.9606+00.2645	164.464	−59.490				
10589−6034	1	165.245	−60.841	G289.8794−00.7979	165.249	−60.840	10589−6034 0	1		
11079−6101	1	167.501	−61.309	G291.0670−00.7941	167.506	−61.308	11079−6101 0	1		
11220−6147	1	171.066	−62.068	G292.9183−00.9020	171.073	−62.068	11220−6147 0	1		
11265−6158	1	172.212	−62.252	G293.4823−00.9047	172.214	−62.252	11265−6158 0	2	11265−6158 0	21
12063−6259	1	182.250	−63.268	G298.1829−00.7860	182.255	−63.266	12063−6259 0	1		
12127−6244	5	183.864	−63.040	G298.8691−00.4515	183.869	−63.039				
12127−6244	1	183.845	−63.027	G298.8591−00.4372	183.852	−63.024	12127−6244 0	1		
12132−6211	2	183.990	−62.468	G298.8449+00.1221	183.990	−62.468	12132−6211 0	2		
12268−6156	1	187.425	−62.221	G300.4013+00.5458	187.424	−62.219	12268−6156 0	1		
12272−6240	1	187.517	−62.949	G300.5035−01.1804	187.513	−62.951			12272−6240 0	23
12300−6119	1	188.208	−61.593	G300.7221+01.2007	188.212	−61.591				
13023−6213	1	196.383	−62.499	G304.5572+00.3279	196.381	−62.499	13023−6213 0	1		
13024−6158	1	196.411	−62.246	G304.5848+00.5804	196.411	−62.246	13024−6158 0	1		
13039−6331	1	196.784	−63.787	G304.6668−00.9654	196.789	−63.784				
13054−6159	2	197.160	−62.259	G304.9323+00.5462	197.160	−62.259				
13106−6050	2	198.460	−61.110	G305.6327+01.6467	198.454	−61.108	13106−6050 0	1		
13107−6208	1	198.496	−62.416	G305.5393+00.3394	198.498	−62.418				
13333−6234	2	204.190	−62.831	G308.0813−00.4131	204.195	−62.831	13333−6234 0	2	13333−6234 0	25
13333−6234	1	204.142	−62.818	G308.0568−00.3960	204.136	−62.818	13333−6234 0	1		
13384−6152	2	205.757	−62.151	G308.9176+00.1231	205.757	−62.148	13395−6153 0	2	13395−6153 0	26
13395−6153	1	205.757	−62.145	G308.9176+00.1231	205.757	−62.148			13395−6153 0	26
13481−6124	2	207.907	−61.652	G310.0135−00.3892	207.908	−61.652	13481−6124 0	1		
13534−6152	1	209.257	−62.117	G310.5163−00.2179	209.254	−62.120	13534−6152 0	1		
13563−6109	1	209.991	−61.409	G311.0341+00.3791	209.988	−61.410	13563−6109 0	1		
13585−6133	1	210.533	−61.808	G311.1794−00.0720	210.535	−61.806	13585−6133 0	1		
13590−6051	2	210.654	−61.097	G311.4255+00.5964	210.652	−61.096	13590−6051 0	1		
13592−6153	1	210.720	−62.124	G311.1771−00.3998	210.720	−62.123	13592−6153 0	1		
14000−6104	3	210.903	−61.306	G311.4824+00.3602	210.899	−61.308	14000−6104 0	1	14000−6104 0	31
14039−6113	1	211.901	−61.455	G311.8998+00.0812	211.900	−61.457	14039−6113 0	1		
14057−6032	1	212.352	−60.784	G312.3070−00.6613	212.353	−60.783	14057−6032 0	1		
14090−6132	1	213.181	−61.788	G312.3825−00.4143	213.182	−61.785	14090−6132 0	2		
14166−6118	1	215.081	−61.531	G313.3153−00.4640	215.075	−61.531	14166−6118 0	1		
14183−6050	1	215.645	−61.143	G313.7051−00.1895	215.644	−61.141				
14188−6054	1	215.647	−61.143	G313.7051−00.1895	215.644	−61.141				
14214−6017	1	216.306	−60.528	G314.2204+00.2726	216.304	−60.527				
14425−6023	1	221.602	−60.598	G316.5871−00.8086	221.597	−60.596	14425−6023 0	1		
14557−5849	2	224.895	−59.025	G318.7748−00.1513	224.894	−59.024	14557−5849 0	1		
15061−5806	1	227.501	−58.292	G320.3150−00.1770	227.501	−58.293	15061−5806 0	1	15061−5806 0	36
15068−5733	1	227.684	−57.748	G320.6747+00.2452	227.682	−57.746	15068−5733 0	1		
15100−5613	2	228.432	−56.426	G321.7020+01.1747	228.427	−56.422				
15100−5613	1	228.452	−56.413	G321.7209+01.1711	228.460	−56.415	15100−5613 0	1		
15178−5641	3	230.443	−56.878	G322.3954+00.2031	230.434	−56.878	15178−5641 0	1		
15178−5641	1	230.423	−56.876	G322.3946+00.2093	230.426	−56.873				
15219−5658	1	231.449	−57.153	G322.7056−00.3283	231.446	−57.152	15219−5658 0	1	15219−5658 0	37
15239−5538	1	231.975	−55.814	G323.6920+00.6228	231.966	−55.812				
15246−5612	1	232.132	−56.386	G323.4468+00.0968	232.133	−56.385	15246−5612 0	1		
15278−5620	1	232.938	−56.513	G323.7399−00.2617	232.938	−56.513			15278−5620 0	38
15347−5518	1	234.642	−55.469	G325.1240+00.0312	234.643	−55.468	15347−5518 0	1		
15454−5335	1	237.332	−53.754	G327.4014+00.4454	237.329	−53.754	15454−5335 0	1	15454−5335 0	39
15470−5419	2	237.726	−54.484	G327.1309−00.2655	237.728	−54.477	15470−5419 0	1		
15507−5359	2	238.660	−54.138	G327.7726−00.3426	238.663	−54.131				
15519−5430	1	238.948	−54.654	G327.5646−00.8489	238.945	−54.653	15519−5430 0	1	15519−5430 0	44
15530−5231	1	239.213	−52.674	G328.9580+00.5671	239.211	−52.673	15530−5231 0	2	15530−5231 0	45
15557−5337	1	239.902	−53.766	G328.5669−00.5327	239.903	−53.764	15557−5337 0	1		
15579−5347	1	240.469	−53.941	G328.7050−00.8841	240.470	−53.939	15579−5347 0	1		
15583−5314	1	240.546	−53.376	G329.1087−00.4908	240.547	−53.378	15583−5314 0	1		
16056−5125	2	242.348	−51.552	G331.1465+00.1343	242.352	−51.552	16056−5125 0	1		
16069−4858	1	242.663	−49.102	G332.9565+01.8035	242.661	−49.098			16069−4858 0	50

Table 8: continued.

millimeter[a]				infrared[b]			centimeter[c]		H$_2$O maser[d]	
Region	#	α_{J2000}	δ_{J2000}	MSX name	α_{J2000}	δ_{J2000}	Region	#	Region	#
16085−5138	6	243.081	−51.766	G331.3312−00.3316	243.082	−51.768	16085−5138 0	1		
16085−5138	2	243.110	−51.771	G331.3402−00.3444	243.107	−51.771				
16085−5138	1	243.207	−51.729	G331.4181−00.3546	243.209	−51.725	16093−5128 2	1		
16093−5128	4	243.295	−51.607	G331.5383−00.3072	243.298	−51.608	16093−5128 0	1		
16093−5128	1	243.206	−51.725	G331.4181−00.3546	243.209	−51.725	16093−5128 2	1		
16112−4943	3	243.752	−49.846	G332.9639+00.7718	243.758	−49.844	16112−4943 0	1	16112−4943 0	53
16148−5011	2	244.661	−50.317	G333.0494+00.0324	244.655	−50.316	16148−5011 0	1		
16148−5011	1	244.737	−50.399	G333.0299−00.0645	244.739	−50.399			16153−5016 1	55
16153−5016	1	244.736	−50.399	G333.0299−00.0645	244.739	−50.399	16153−5016 1	1		
16164−4929	2	245.078	−49.582	G333.7595+00.3624	245.082	−49.583	16164−4929 3	1		
16164−4929	1	245.040	−49.606	G333.7261+00.3678	245.039	−49.603	16164−4929 0	1		
16164−4837	1	245.054	−48.754	G334.3321+00.9645	245.056	−48.752	16164−4837 0	1		
16194−4934	2	245.822	−49.685	G334.0256−00.0502	245.822	−49.687	16194−4934 0	1		
16204−4916	1	246.058	−49.395	G334.3417+00.0455	246.060	−49.395	16204−4916 0	1		
16218−4931	1	246.408	−49.639	G334.3272−00.2884	246.412	−49.639	16218−4931 0	1	16218−4931 0	57
16252−4853	2	247.263	−48.999	G335.1734−00.2428	247.262	−48.998	16252−4853 0	1		
16344−4605	2	249.552	−46.206	G338.2717+00.5211	249.553	−46.205				
16344−4605	1	249.539	−46.184	G338.2801+00.5419	249.538	−46.185	16344−4605 0	1	16344−4605 0	60
16363−4645	3	250.018	−46.854	G338.0008−00.1498	250.018	−46.854	16363−4645 0	2		
16396−4429	1	250.817	−44.589	G340.0708+00.9267	250.817	−44.588	16396−4429 0	1		
16435−4515	2	251.790	−45.350	G339.9426−00.0940	251.793	−45.351	16435−4515 0	1		
16435−4515	1	251.762	−45.359	G339.9267−00.0837	251.767	−45.356			16435−4515 0	62
16482−4443	1	252.942	−44.816	G340.8781−00.3752	252.949	−44.814	16482−4443 0	2	16482−4443 0	64
16501−4314	2	253.415	−43.321	G342.2495+00.3082	253.423	−43.320	16501−4314 0	1		
16501−4314	1	253.427	−43.325	G342.2477+00.3056	253.424	−43.323				
16574−4225	2	255.244	−42.503	G343.7217−00.2231	255.244	−42.500	16574−4225 0	1		
16579−4245	1	255.392	−42.837	G343.5213−00.5171	255.392	−42.839				
17036−4033	5	256.790	−40.619	G345.9184+00.0017	256.789	−40.619	17036−4033 0	2		
17118−3909	1	258.824	−39.225	G347.9676−00.4321	258.826	−39.223	17118−3909 0	1		
17149−3916	1	259.599	−39.322	G348.2362−00.9809	259.605	−39.322	17149−3916 0	1		
17184−3638	1	260.458	−36.686	G350.7833−00.0273	260.461	−36.687	17184−3638 0	1	17184−3638 0	71
17195−3811	1	260.754	−38.232	G349.6433−01.0957	260.756	−38.232			17195−3811 2	74
17200−3658	1	260.869	−37.027	G350.6879−00.4909	260.871	−37.029	17200−3658 0	1	17200−3658 0	77
17210−3646	1	261.122	−36.813	G350.9780−00.5384	261.125	−36.816	17210−3646 0	1		
17221−3619	2	261.381	−36.357	G351.4768−00.4525	261.385	−36.355				
17221−3619	1	261.381	−36.368	G351.4661−00.4582	261.383	−36.367	17221−3619 1	1	17221−3619 1	78
17225−3426	7	261.445	−34.497	G353.0473+00.5558	261.439	−34.489				
17242−3513	3	261.872	−35.268	G352.5975−00.1762	261.874	−35.271	17242−3513 0	2		
17242−3513	2	261.869	−35.288	G352.5844−00.1810	261.870	−35.284	17242−3513 0	1		
17249−3501	1	262.074	−35.069	G352.8577−00.2040	262.079	−35.070	17249−3501 0	1	17249−3501 0	81
17256−3631	1	262.257	−36.556	G351.6976−01.1477	262.255	−36.558	17256−3631 0	1		
17279−3350	2	262.822	−33.881	G354.1882−00.0598	262.823	−33.881	17279−3350 0	1		
17296−3236	1	263.217	−32.643	G355.4099+00.3419	263.217	−32.642	17296−3236 0	1		
17352−3153	1	264.620	−31.911	G356.6620−00.2638	264.623	−31.911	17352−3153 0	1		
17355−3241	1	264.708	−32.724	G356.0124−00.7616	264.710	−32.726				
17377−3109	1	265.238	−31.183	G357.5571−00.3208	265.238	−31.183	17377−3109 0	1	17377−3109 0	83
18014−2428	2	271.219	−24.445	G006.0485−01.4468	271.221	−24.445	18018−2426 9	2	18018−2426 9	84
18144−1723	1	274.349	−17.368	G013.6554−00.5949	274.347	−17.369				
18198−1429	1	275.673	−14.462	G016.8217−00.3484	275.674	−14.461	18198−1429 0	1		

Notes. [a] Millimeter source: columns as in Table 7. [b] Infrared source: MSX name as listed in the MSX Point Source Catalogue (Price et al. 1999), α_{J2000} and δ_{J2000} right ascension (in degrees) and declination (in degrees). [c] Centimeter source: columns as in Table 7. [d] H$_2$ maser spot: columns as in Table 7.

Á. Sánchez-Monge et al.: Different evolutionary stages in massive star formation

Table 9: Sources classified as *type 3* objects: infrared-only sources

MSX name	α_{J2000}	δ_{J2000}	Region	#	Region	#
	infrared[a]		centimeter[b]		H$_2$O maser[c]	
G254.0567−00.5580	123.997	−36.140				
G263.5994−00.5236	131.389	−43.831				
G263.6200−00.5308	131.399	−43.851				
G263.6385−00.5217	131.425	−43.860				
G263.2493+00.5153	132.200	−42.906	08470−4243 0	1	08470−4243 0	2
G264.3225−00.1857	132.386	−44.181	08477−4359 0	1		
G268.0519−00.8095	135.158	−47.432				
G268.0440−00.7994	135.161	−47.419				
G268.0640−00.8162	135.162	−47.445				
G268.0799−00.8067	135.188	−47.451				
G268.6162−00.7389	135.790	−47.808	09014−4736 0	1		
G268.6184−00.7302	135.802	−47.804				
G270.8164+00.6893	139.605	−48.440				
G281.1656−01.6451	149.878	−57.065				
G281.1782−01.6519	149.888	−57.078				
G281.1834−01.6414	149.908	−57.073				
G282.7848−01.2869	152.695	−57.732			10088−5730 2	9
G283.1263−00.9887	153.538	−57.681				
G284.0079−00.8485	155.063	−58.054	10184−5748 0	1		
G284.7306+00.3213	157.375	−57.446			10276−5711 0	11
G284.9025+00.0540	157.392	−57.764	10277−5730 0	1		
G284.9007+00.0653	157.400	−57.753	10277−5730 0	2		
G285.2504−00.0701	157.834	−58.049				
G285.2416−00.0505	157.839	−58.028				
G285.2412−00.0464	157.842	−58.024				
G285.2568−00.0430	157.870	−58.029				
G286.4203−01.4801	158.402	−59.858	10317−5936 0	1		
G286.4345−01.4907	158.416	−59.874	10317−5936 0	2		
G286.3931−01.3484	158.487	−59.730				
G287.8149−00.8332	161.460	−59.966				
G289.1062−01.1087	163.543	−60.793	10521−6031 0	1		
G288.8524−00.1088	163.955	−59.782	10537−5930 0	1		
G288.9583−00.0283	164.213	−59.755	10548−5929 0	1		
G288.9865+00.2533	164.501	−59.512	10559−5914 0	1	10559−5914 0	18
G289.5787−00.6388	164.825	−60.570				
G288.9744+00.7910	164.921	−59.019	10575−5844 0	1		
G289.8953−00.8074	165.271	−60.855				
G289.8981−00.8131	165.271	−60.861				
G289.8985−00.7986	165.284	−60.848				
G289.4993+00.1231	165.316	−59.844	10591−5934 0	1		
G289.5051+00.1161	165.321	−59.853				
G291.0511−00.7784	167.487	−61.287				
G291.0515−00.7748	167.491	−61.284				
G294.6466−01.1777	174.449	−62.859	11354−6234 0	2		
G295.1013−01.6833	175.107	−63.470				
G295.1026−01.6778	175.114	−63.465				
G295.1085−00.7120	175.694	−62.536	11404−6215 0	1		
G295.1172−00.7206	175.708	−62.547				
G298.1829−00.7789	182.258	−63.259				
G298.8559−00.4623	183.837	−63.048				
G298.8700−00.4335	183.877	−63.022				
G298.8720−00.4287	183.882	−63.017				
G298.8332+00.1279	183.967	−62.461	12132−6211 0	1		
G299.1531+00.0086	184.620	−62.621	12157−6220 0	1		
G300.4007+00.5401	187.422	−62.225				
G300.4005+00.5500	187.423	−62.215				
G300.5030−00.1905	187.510	−62.962				
G300.5027−00.1833	187.511	−62.954	12272−6240 0	1		
G300.5035−00.1698	187.515	−62.941				
G300.5047−00.1745	187.517	−62.946	12272−6240 0	2		
G300.7486+00.1016	188.097	−62.689				
G304.9184+00.5645	197.128	−62.241				
G304.9275+00.5585	197.148	−62.247				
G304.9289+00.5524	197.152	−62.253	13054−6159 0	1		
G304.9406+00.5557	197.176	−62.249				
G305.5190+00.3485	198.453	−62.411				
G305.5302+00.3662	198.473	−62.392				
G305.5313+00.3505	198.479	−62.408				
G305.5345+00.3499	198.486	−62.408	13107−6208 0	1		
G305.5389+00.3672	198.492	−62.391				
G305.5388+00.3604	198.493	−62.397				
G308.9323+00.1289	205.785	−62.139				
G309.3767−00.1377	206.837	−62.308				
G310.8902+00.0089	209.899	−61.805	13560−6133 2	1		
G311.1779−00.0960	210.546	−61.830				
G311.8742+00.0890	211.844	−61.457				
G311.8810+00.1002	211.851	−61.445				
G311.8772+00.0776	211.857	−61.467				
G311.8928+00.0931	211.879	−61.448				
G312.3063+00.6647	212.350	−60.780				
G313.6668−00.1023	215.508	−61.072				
G313.6833−00.1088	215.544	−61.072				
G313.6870−00.1996	215.616	−61.156				

35

Table 9: continued.

infrared[a]			centimeter[b]		H$_2$O maser[c]	
MSX name	α_{J2000}	δ_{J2000}	Region	#	Region	#
G313.7132−00.1766	215.651	−61.126				
G313.9140−00.0745	215.967	−60.960	14201−6044 0	1		
G313.9710−00.0741	216.076	−60.940				
G314.2269+00.4099	216.218	−60.397				
G314.2437+00.4231	216.240	−60.378				
G314.2495+00.4338	216.243	−60.366				
G314.2462+00.4174	216.249	−60.383				
G314.2004+00.2900	216.253	−60.518				
G314.2014+00.2864	216.258	−60.521	14214−6017 0	1		
G314.2015+00.2834	216.260	−60.524				
G314.2124+00.2939	216.273	−60.510				
G314.2605+00.4027	216.286	−60.392				
G314.2125+00.2632	216.295	−60.539				
G314.2161+00.2546	216.308	−60.546				
G314.2354+00.2913	216.319	−60.505				
G316.3627−00.3631	220.804	−60.287	14394−6004 0	1		
G320.1488+00.8145	226.300	−57.516				
G320.1515+00.8109	226.308	−57.518				
G320.1542+00.7976	226.324	−57.528	15015−5720 0	1		
G320.1524+00.7924	226.326	−57.533				
G320.1655+00.8126	226.329	−57.509				
G320.1697+00.8097	226.338	−57.510	15015−5720 0	2		
G320.1750+00.8001	226.356	−57.516				
G320.3144−00.1845	227.507	−58.300				
G320.3333−00.1790	227.533	−58.285	15061−5806 0	2		
G320.2698−01.2678	228.504	−59.253	15100−5903 0	1		
G322.3904+00.1957	230.433	−56.887				
G323.6814+00.6298	231.944	−55.812	15239−5538 0	1		
G323.6934+00.6328	231.958	−55.803				
G323.9169+00.3984	232.523	−55.870	15262−5541 1	1		
G323.7410−00.2552	232.933	−56.507				
G325.1158+00.0078	234.656	−55.492				
G325.5964+00.0912	235.246	−55.138				
G327.4012+00.4488	237.326	−53.751				
G326.4477−00.7485	237.327	−55.282	15454−5507 0	1	15454−5507 0	40
G326.7831−00.5548	237.573	−54.921				
G326.7899−00.5485	237.576	−54.912	15464−5445 0	1		
G326.7878−00.5526	237.577	−54.916				
G326.7896−00.5594	237.587	−54.920				
G326.7859−00.5644	237.588	−54.927				
G328.1202+00.1115	238.626	−53.559				
G327.7555−00.3324	238.630	−54.134				
G327.7579−00.3515	238.654	−54.147	15507−5359 0	1		
G327.5761−00.8497	238.961	−54.647				
G328.9480+00.5709	239.194	−52.676	15530−5231 0	1		
G328.9483+00.5520	239.215	−52.691				
G329.4506+00.5124	239.886	−52.395	15557−5215 0	1		
G329.4533+00.5034	239.899	−52.401				
G328.5759−00.5285	239.910	−53.755	15557−5337 0	2		
G329.4626+00.5037	239.911	−52.394				
G328.5739−00.5483	239.929	−53.771				
G331.6218+00.5208	242.493	−50.946	16061−5048 0	1		
G331.7095+00.6034	242.506	−50.825	16061−5048 5	1		
G331.3292−00.3350	243.083	−51.772				
G331.3334−00.3376	243.091	−51.771				
G332.1420+00.0431	243.613	−50.939	16106−5048 0	1		
G332.7506+00.6682	243.629	−50.066	16107−4956 0	1		
G332.9793+00.7771	243.769	−49.830				
G332.9623+00.7541	243.775	−49.858				
G332.9879+00.7693	243.788	−49.829				
G332.9872+00.7659	243.790	−49.832				
G333.0221−00.0377	244.701	−50.385				
G332.8014−00.7017	245.189	−51.013				
G332.8143−00.6977	245.199	−51.001				
G335.1572−00.2172	247.217	−48.992				
G337.9758−00.1370	249.979	−46.864				
G337.9662−00.1507	249.985	−46.880				
G337.9732−00.1458	249.986	−46.872	16363−4645 0	1		
G337.9858−00.1442	249.997	−46.861				
G337.9684−00.1599	249.997	−46.885				
G338.0012−00.1337	250.000	−46.843				
G339.1707−00.3880	251.396	−46.129	16419−4602 0	1		
G339.1704−00.3927	251.400	−46.132				
G343.0290+02.6199	251.695	−41.242	16428−4109 2	1		
G343.0500+02.6094	251.724	−41.233				
G343.0574+02.5615	251.778	−41.259				
G339.9429−00.1187	251.820	−45.367				
G339.9689−00.1507	251.879	−45.367				
G341.2366+00.3361	252.502	−44.084	16464−4359 0	1		
G340.8832−00.3663	252.943	−44.804	16482−4443 0	1		
G342.2464+00.2842	253.446	−43.337				
G342.8211−00.0307	254.277	−43.088	16535−4300 0	1		
G343.8354−00.1058	255.213	−42.338				

Table 9: continued.

infrared[a]			centimeter[b]		H$_2$O maser[c]	
MSX name	α_{J2000}	δ_{J2000}	Region	#	Region	#
G343.8569−00.0986	255.223	−42.317	16573−4214 0	1		
G345.8197+00.0341	256.677	−40.678				
G345.8486+00.0193	256.715	−40.664				
G345.8677−01.1011	257.923	−41.316	17082−4114 0	1		
G345.8869−01.1042	257.941	−41.303	17082−4114 0	2		
G348.1485+00.2549	258.246	−38.675	17095−3837 0	1		
G347.9779−00.4321	258.834	−39.215				
G347.9752−00.4364	258.836	−39.220				
G347.9706−00.4443	258.841	−39.228				
G347.9747−00.4435	258.844	−39.224				
G347.9742−00.4508	258.851	−39.229				
G347.9721−00.4591	258.858	−39.236				
G350.7082+00.9911	259.370	−36.165				
G350.8074−00.8267	261.303	−37.119				
G350.8040−00.8331	261.307	−37.125	17218−3704 0	1		
G351.4677−00.4512	261.377	−36.362				
G351.4880−00.4642	261.405	−36.352				
G351.4658−00.4812	261.407	−36.380				
G353.0587+00.5337	261.469	−34.492	17225−3426 0	1		
G352.2436−00.1617	261.617	−35.557				
G352.6006−00.1674	261.867	−35.263				
G352.6023−00.1983	261.899	−35.279				
G352.6159−00.1948	261.905	−35.266				
G351.6947−01.1490	262.255	−36.561				
G351.7052−01.1666	262.281	−36.563				
G354.2042−00.0419	262.816	−33.857				
G354.2041−00.0456	262.819	−33.859				
G354.2130−00.0524	262.832	−33.856				
G358.8387−00.7420	266.438	−30.314	17425−3017 0	1		
G013.6562−00.5997	274.351	−17.371			18144−1723 0	85
G016.8182−00.3308	275.657	−14.456				

Notes. [a] Infrared source: columns as in Table 8. [b] Centimeter source: columns as in Table 7. [c] H$_2$O maser spot: columns as in Table 7.

Appendix B: Figures
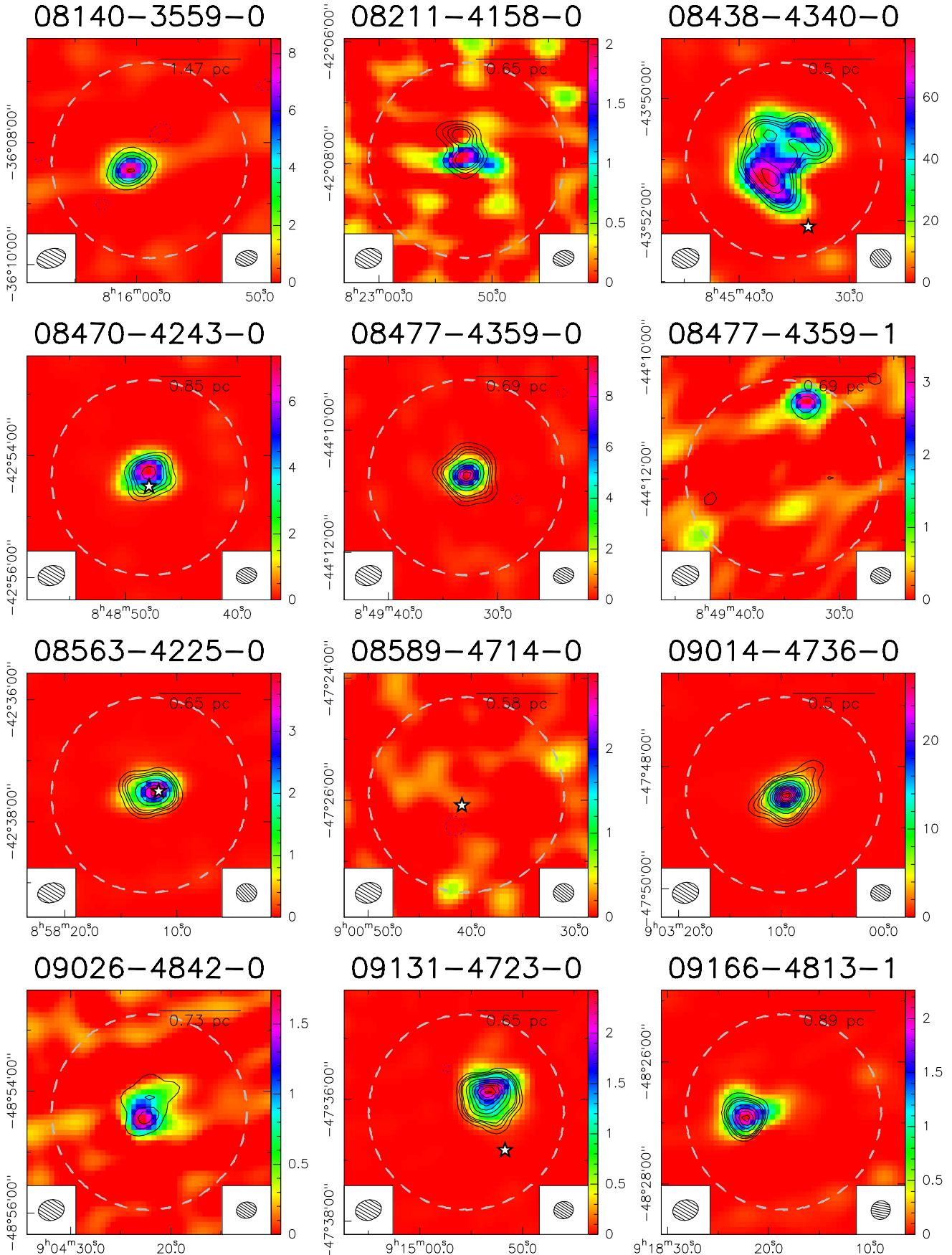
Fig. B.1: ATCA continuum images at 18.0 GHz (color scale, units mJy beam^{-1}) and 22.8 GHz (contours). Synthesized beams are indicated at the bottom left (18.0 GHz) and right (22.8 GHz) corners (see Table 1 for values). The primary beam at 22.8 GHz is indicated with the dashed grey circle. When a distance is available the spatial scale corresponding to 80″ is indicated at the top of the panel. White stars show the position of water masers (see Table 4).
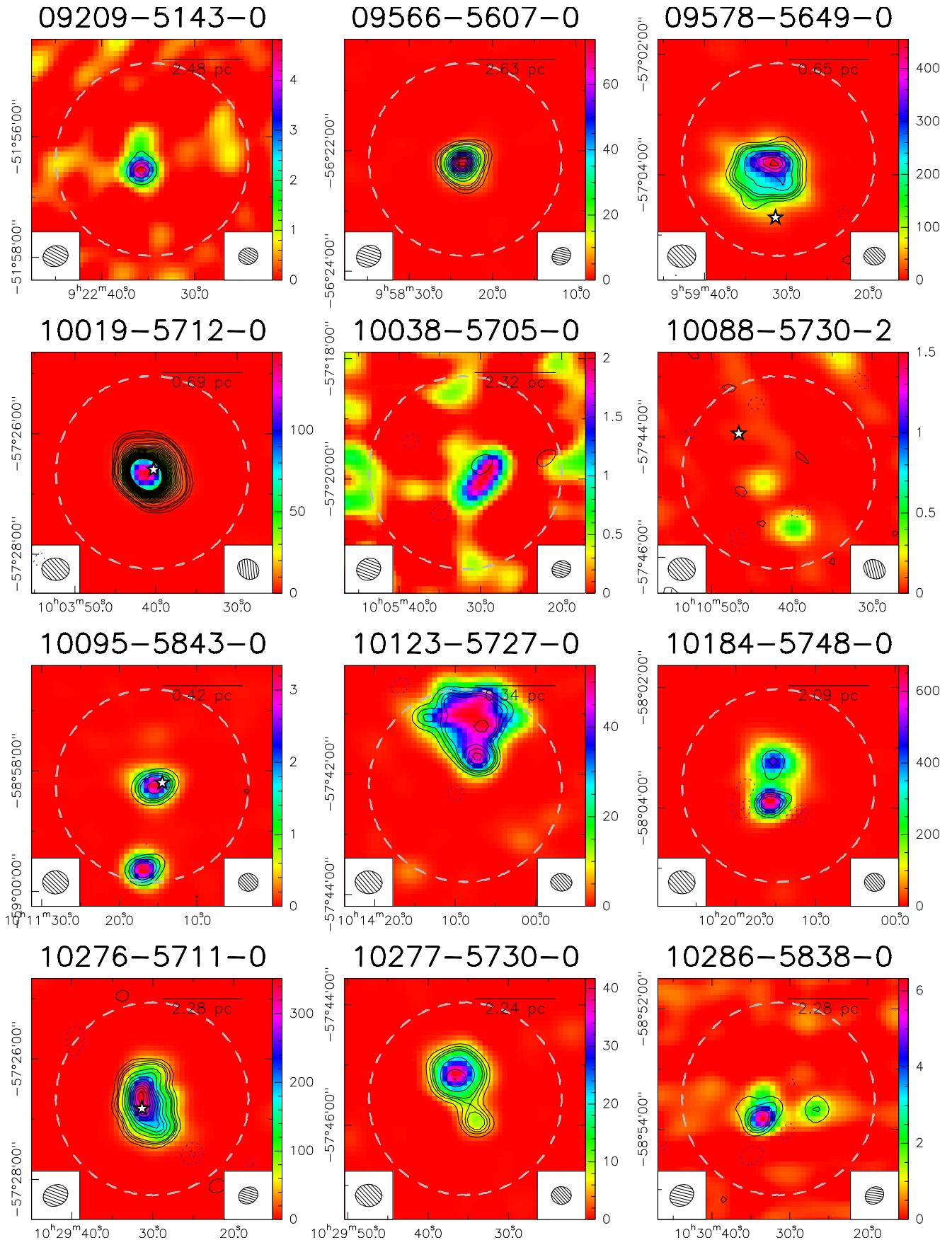
Fig. B.1: continued.
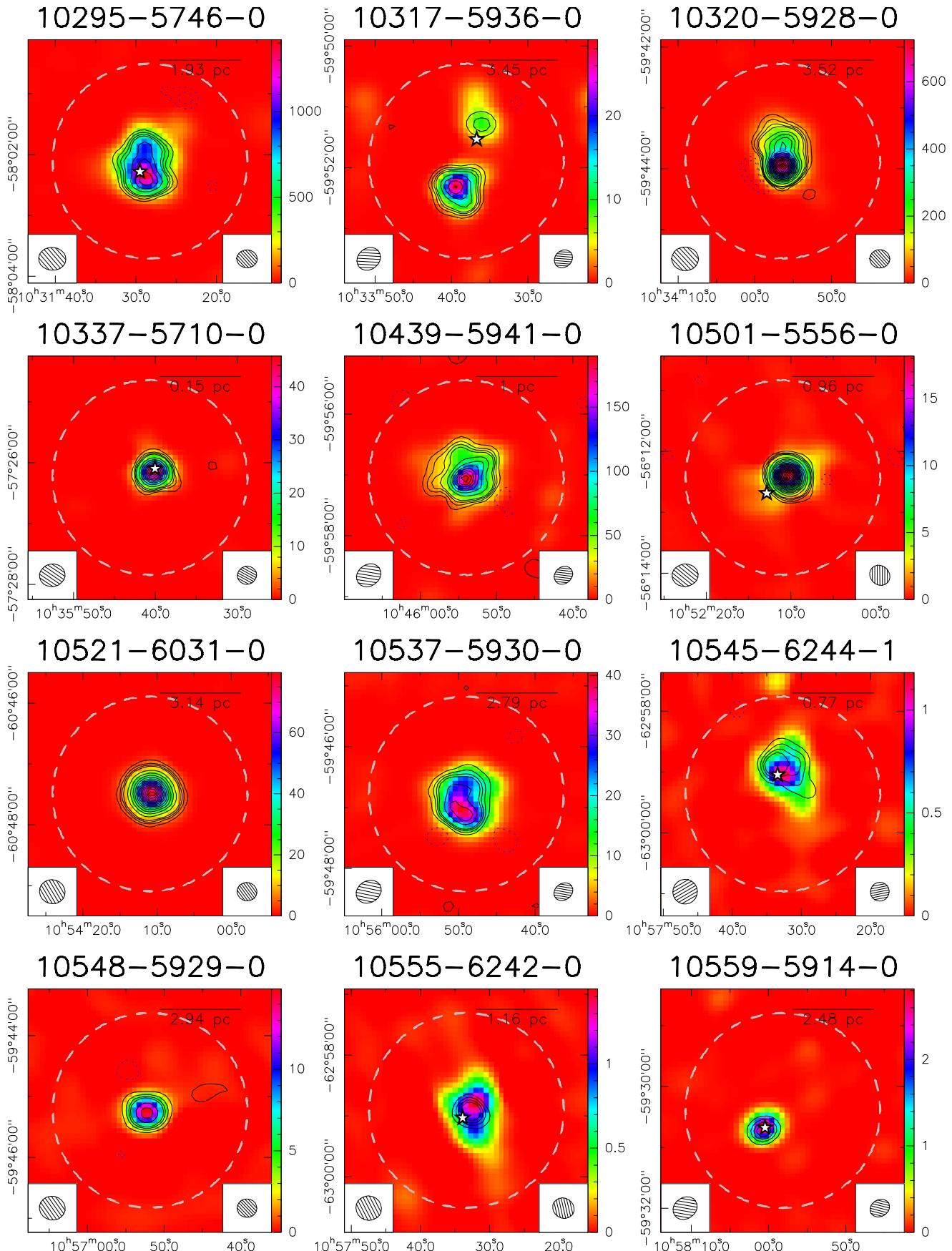
Fig. B.1: continued.
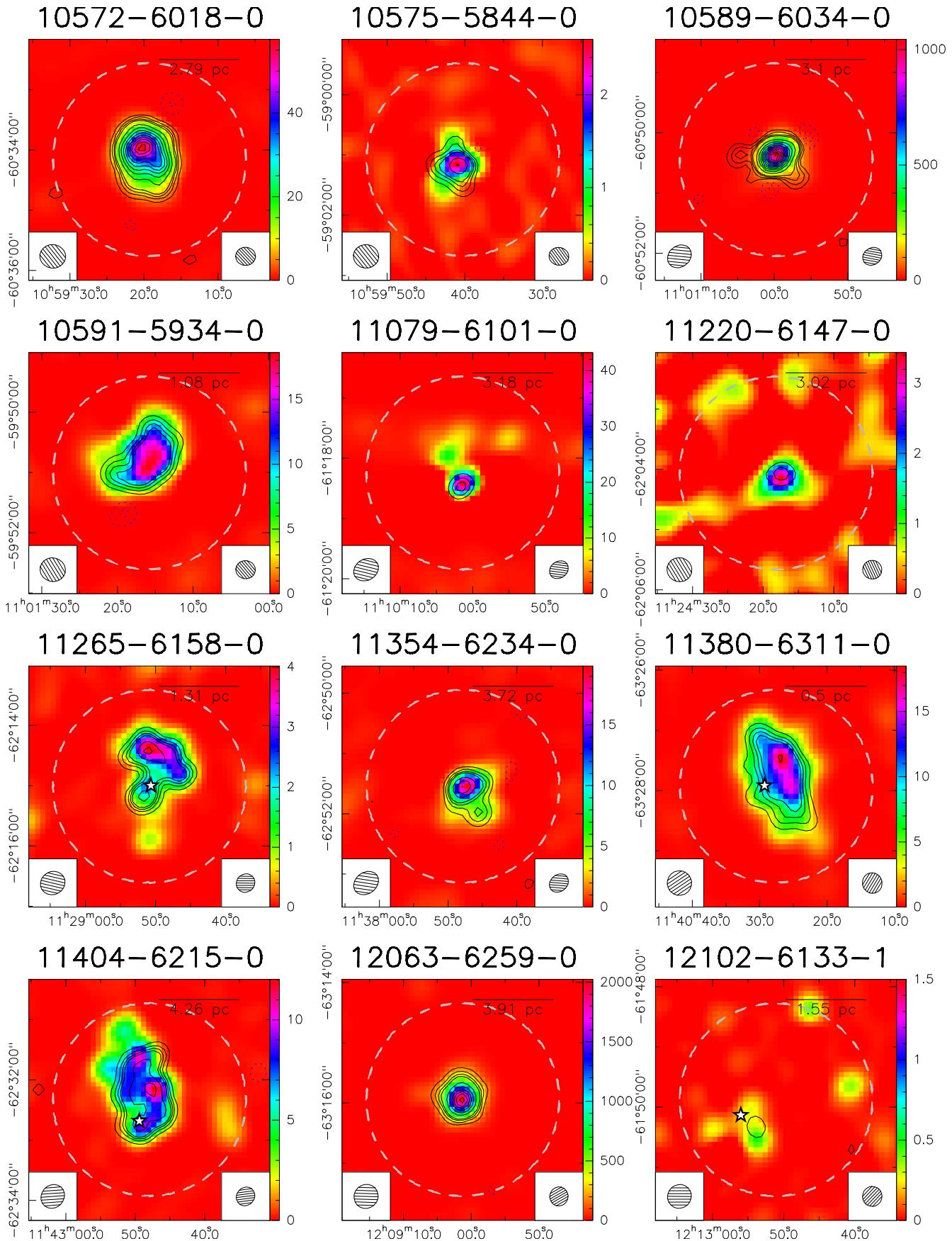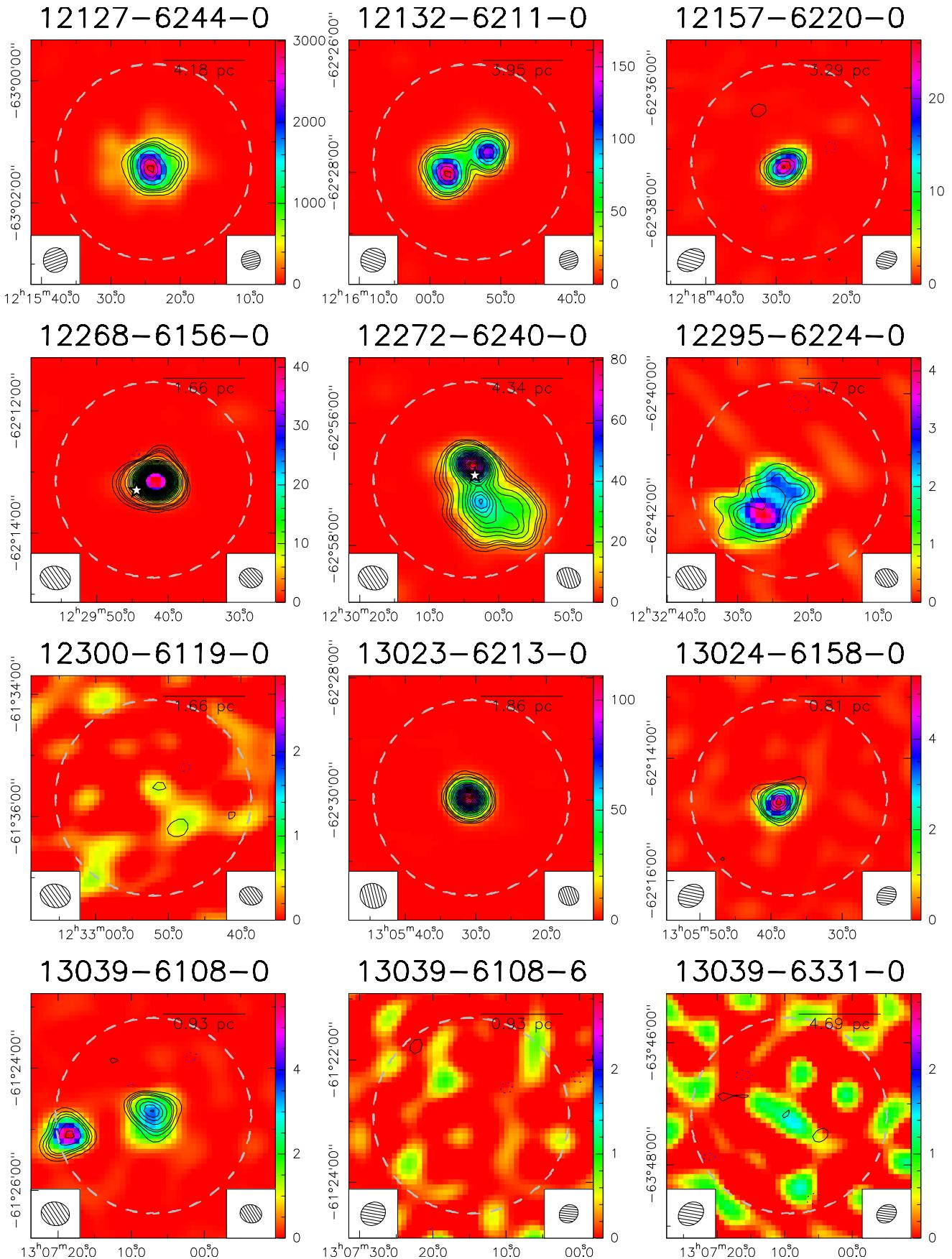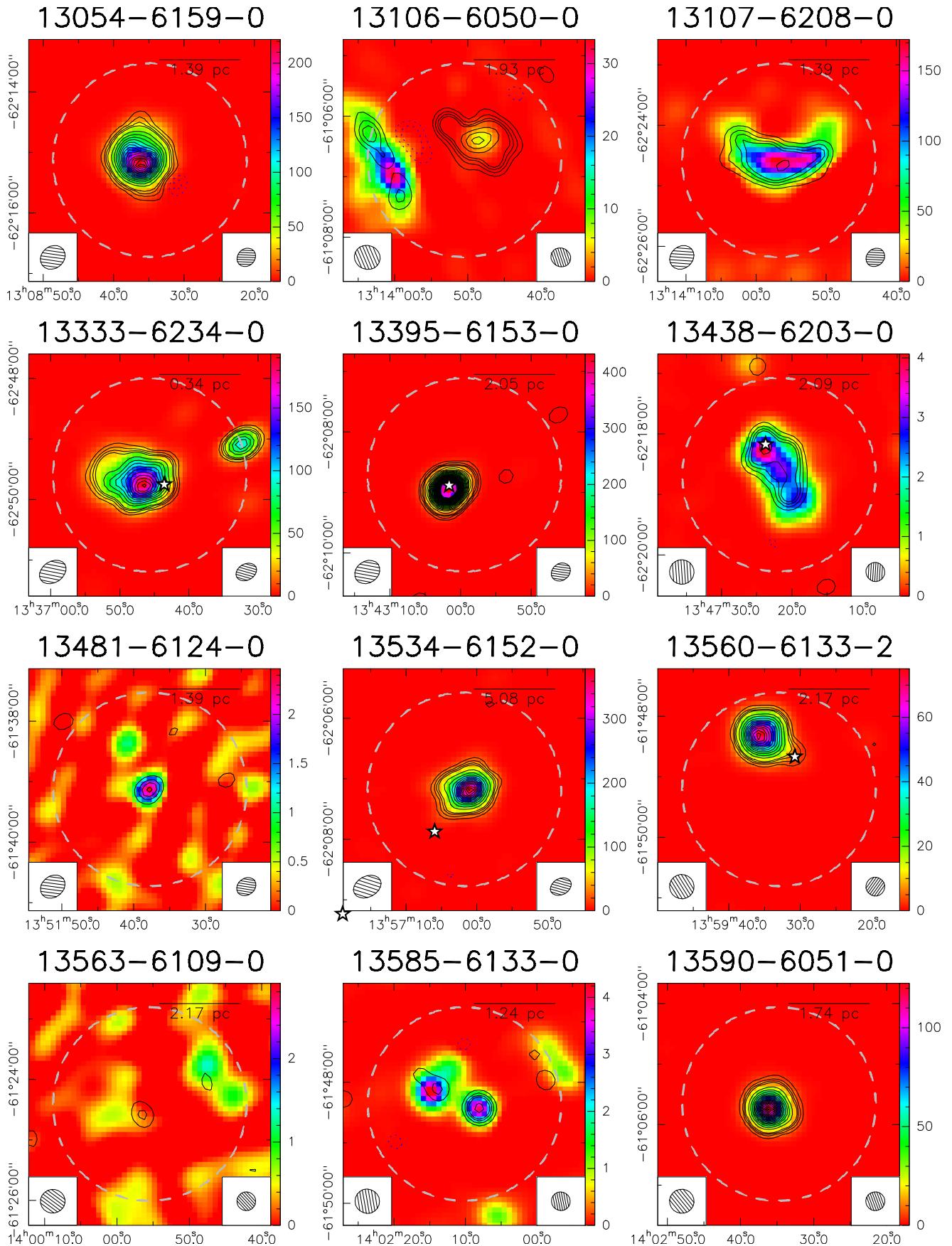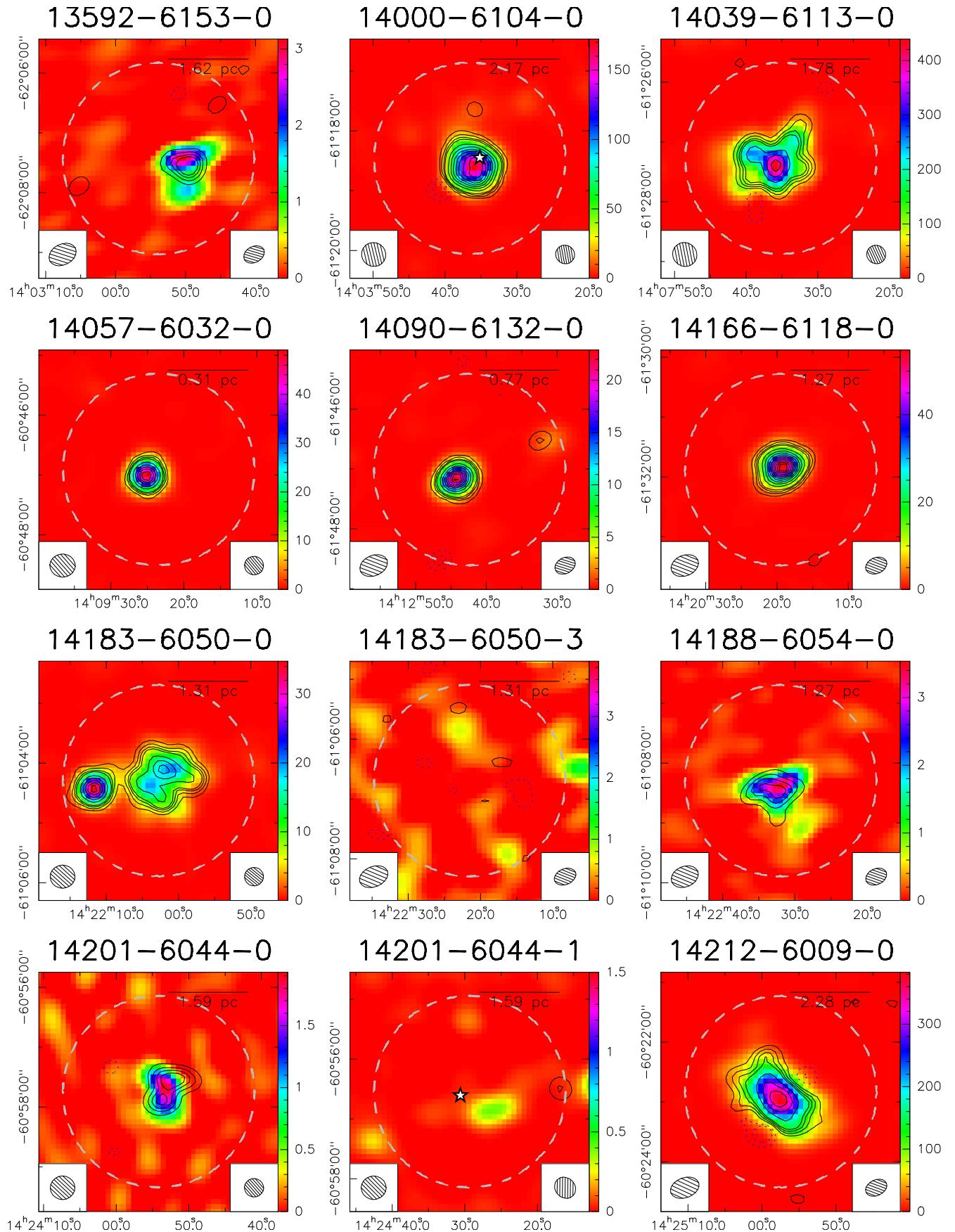
Fig. B.1: continued.

Fig. B.1: continued.

Fig. B.1: continued.
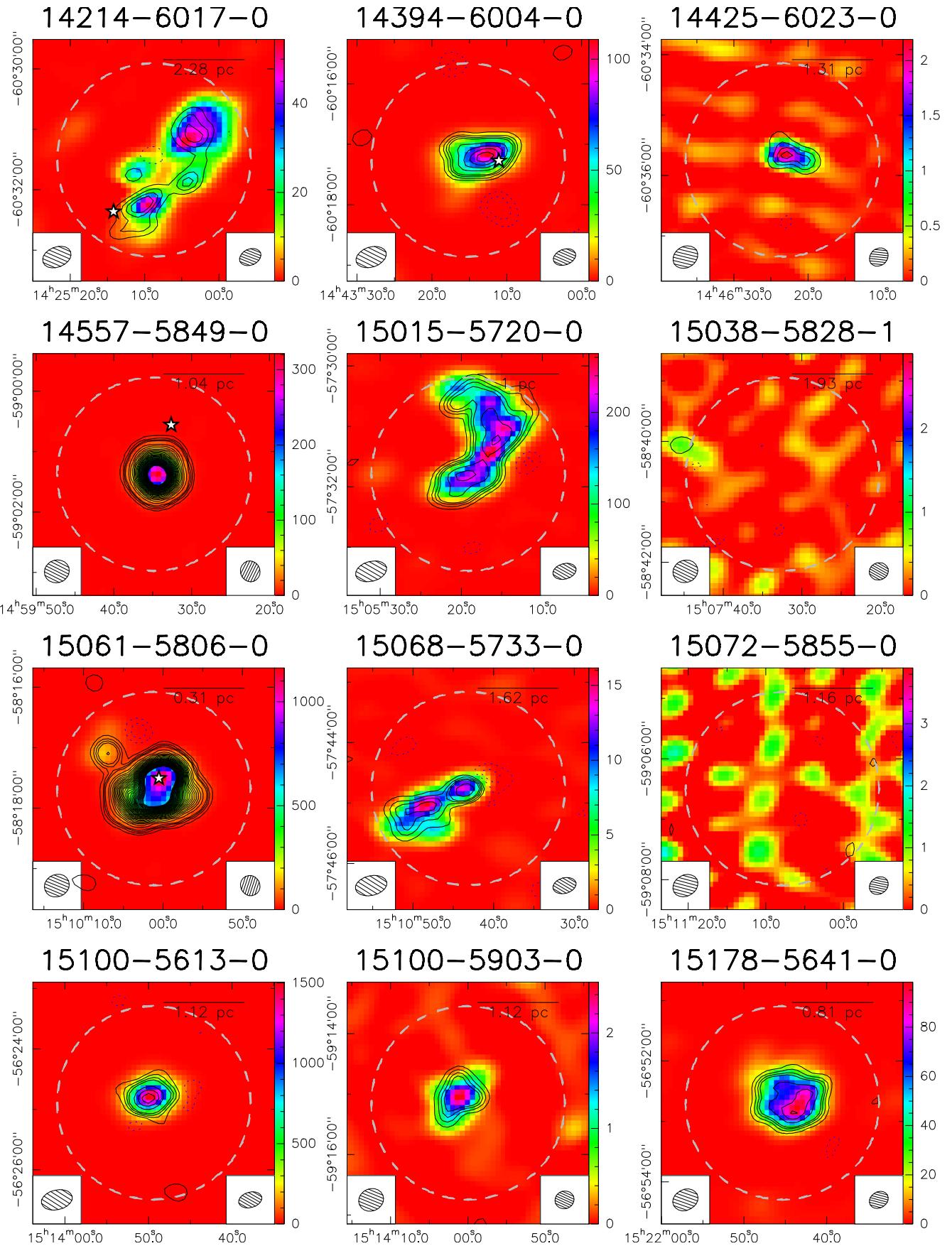
Fig. B.1: continued.
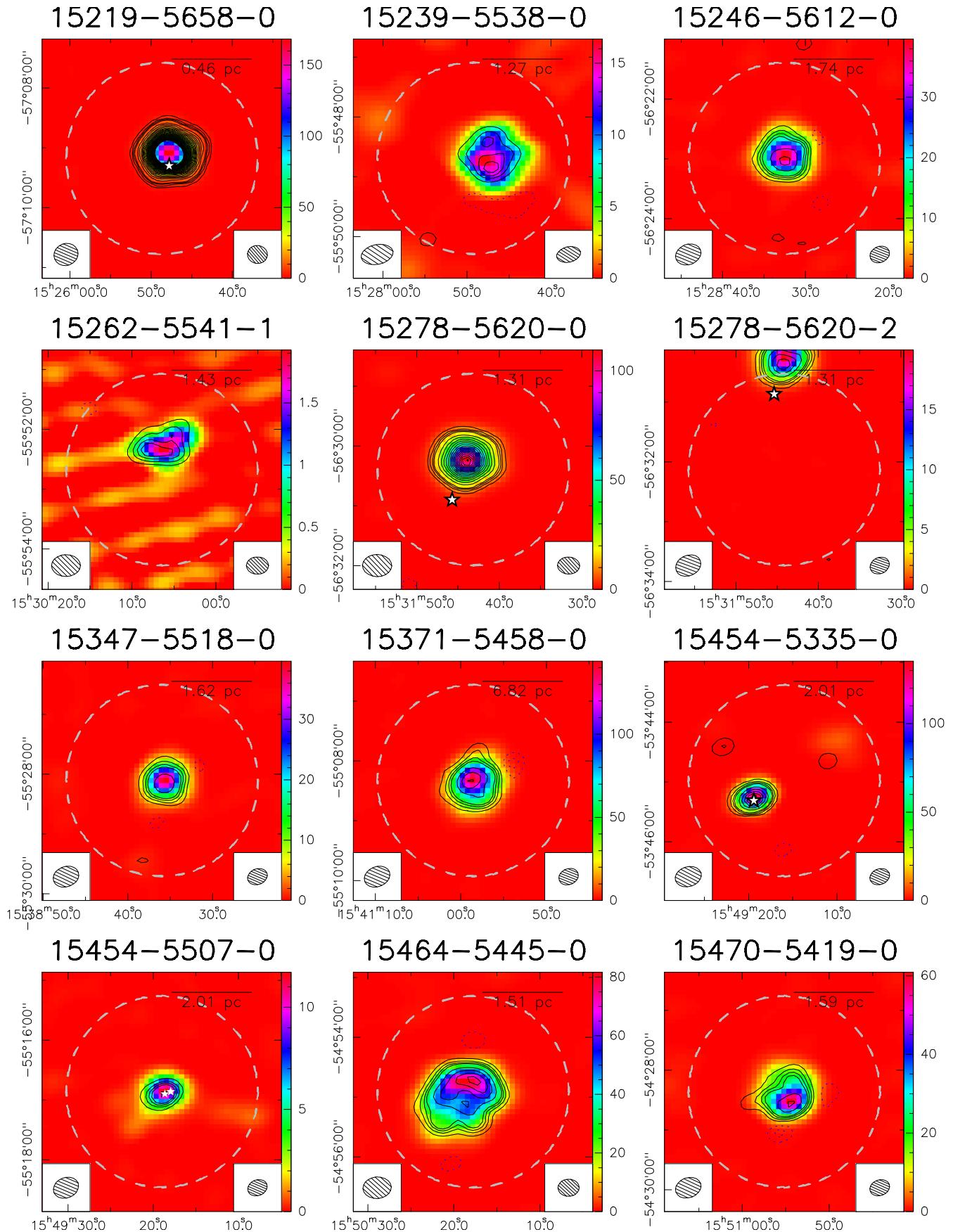
Fig. B.1: continued.
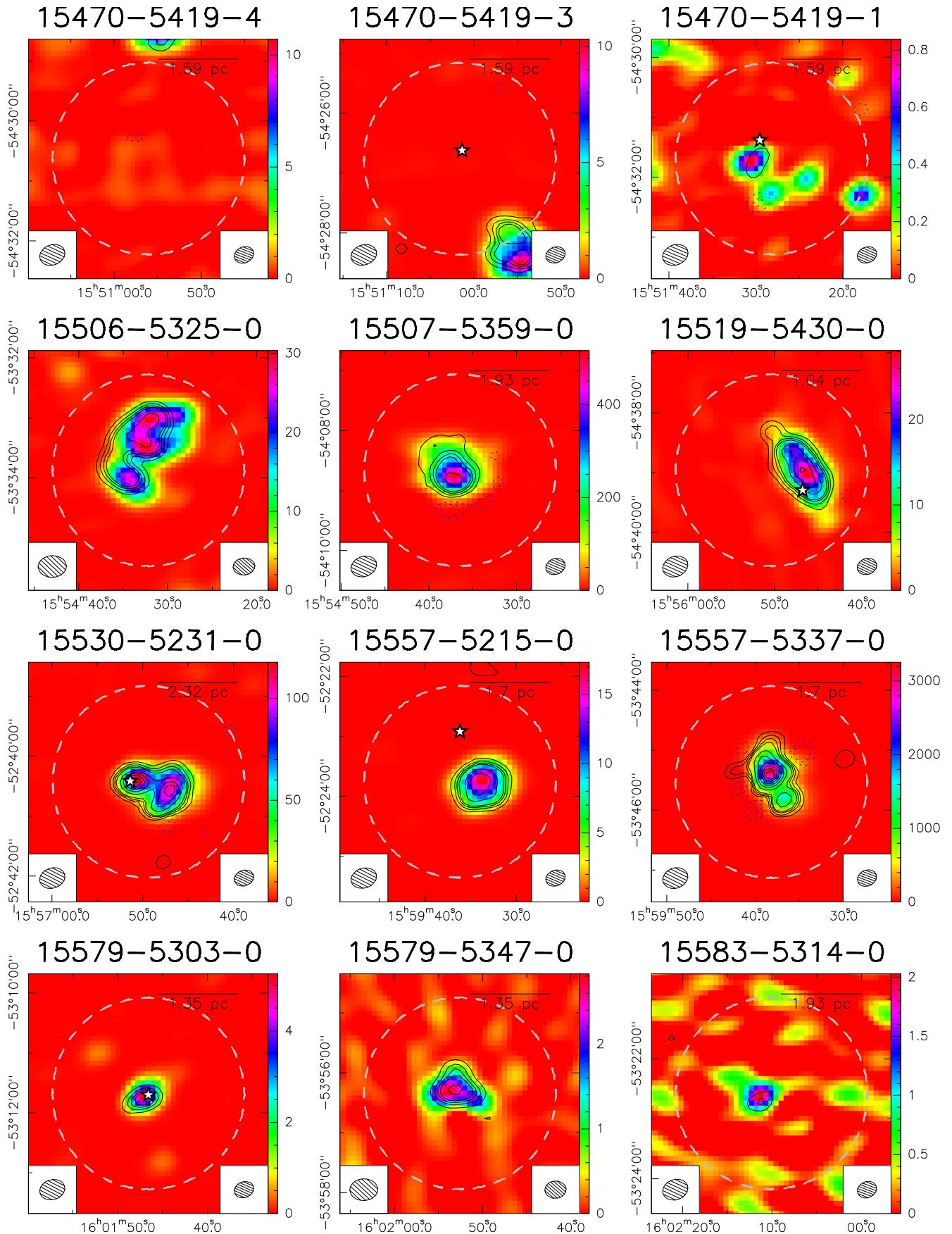
Fig. B.1: continued.
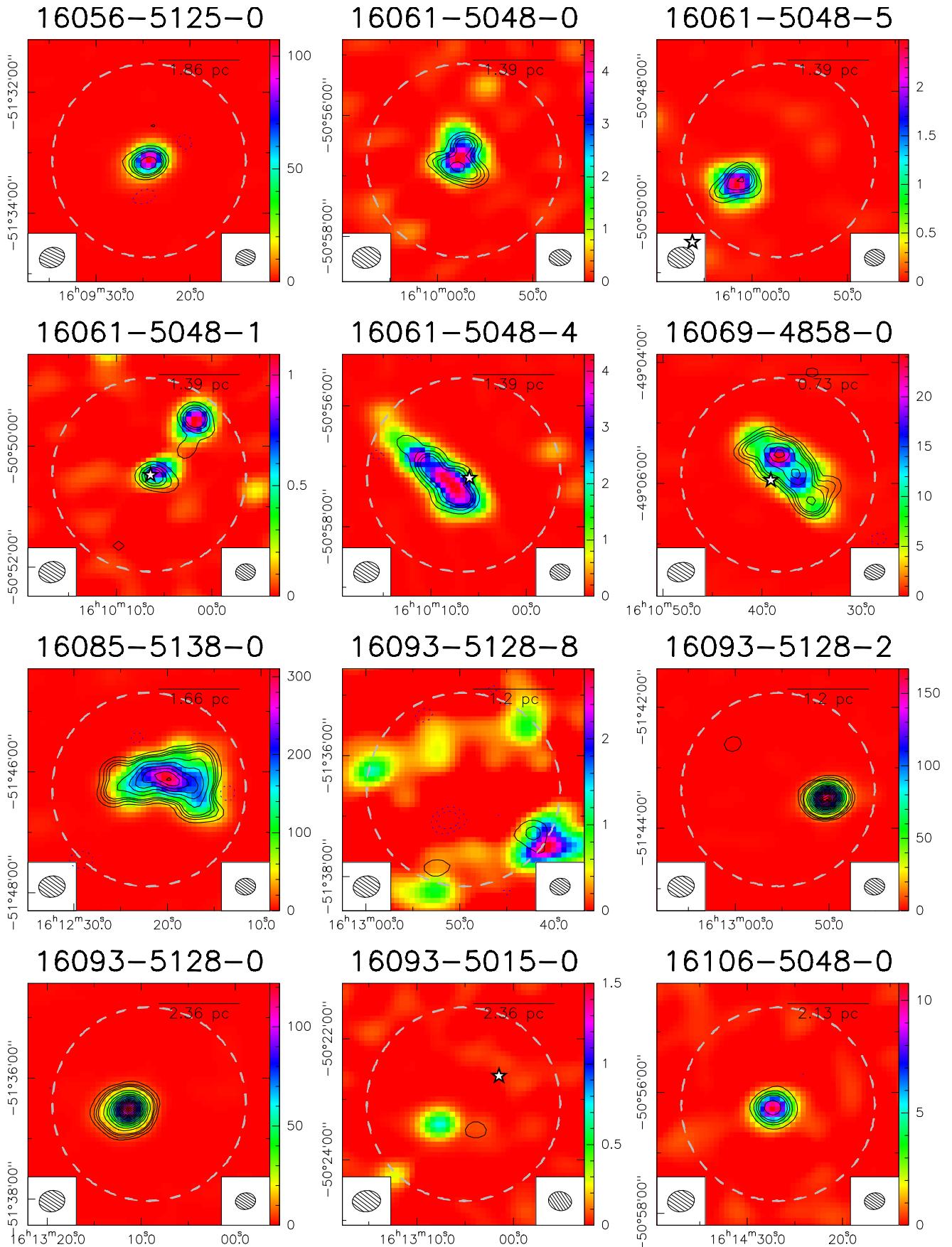
Fig. B.1: continued.
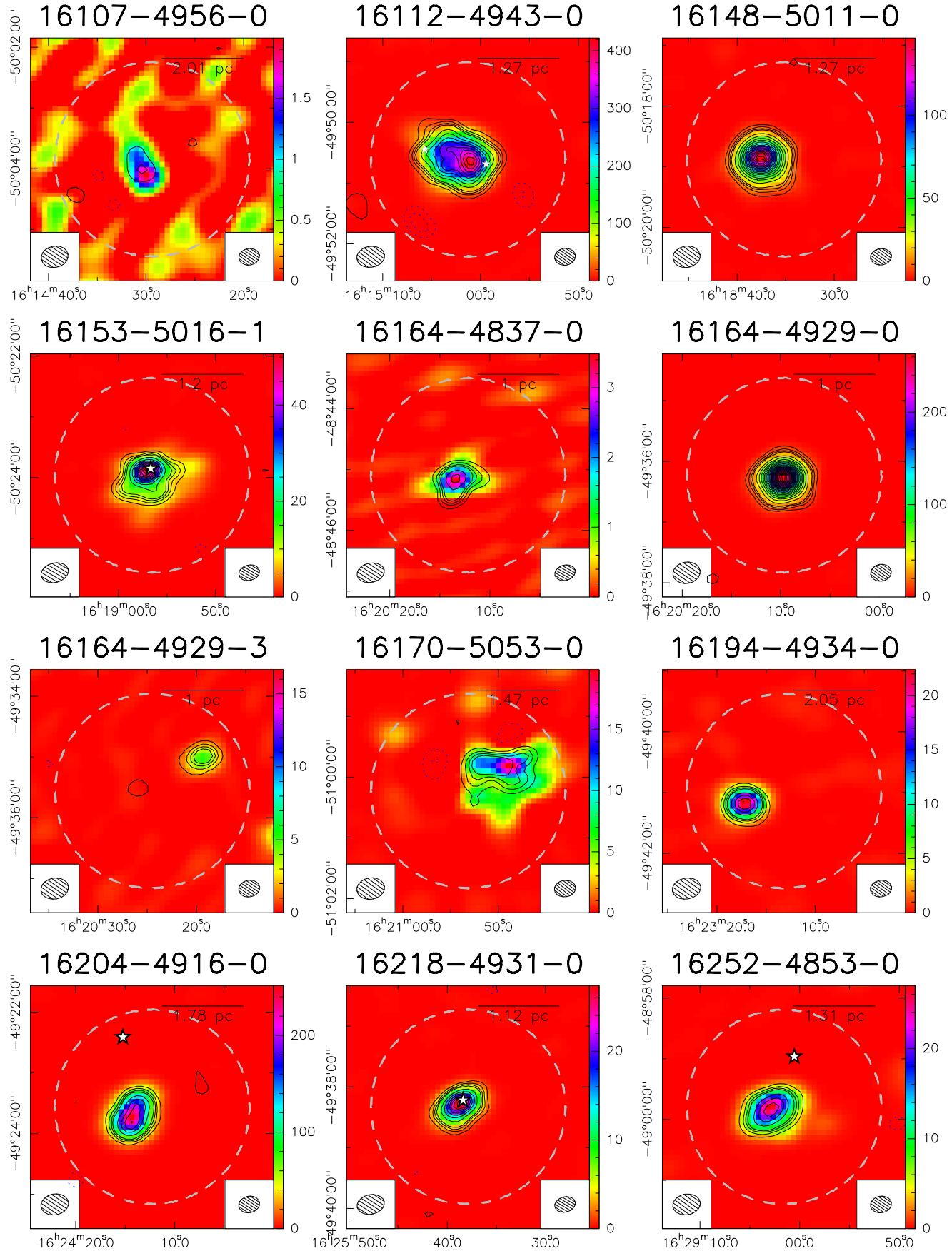
Fig. B.1: continued.
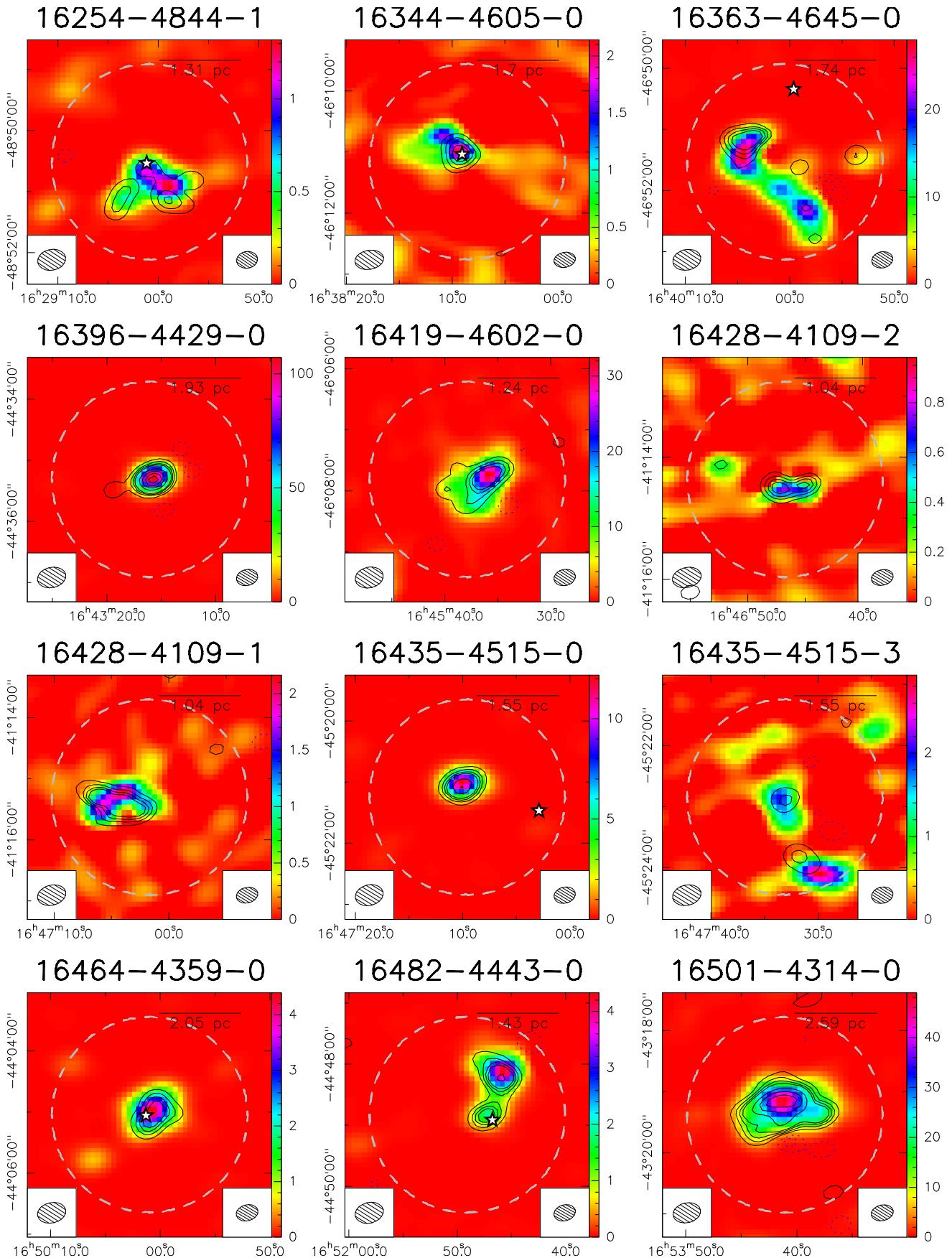
Fig. B.1: continued.
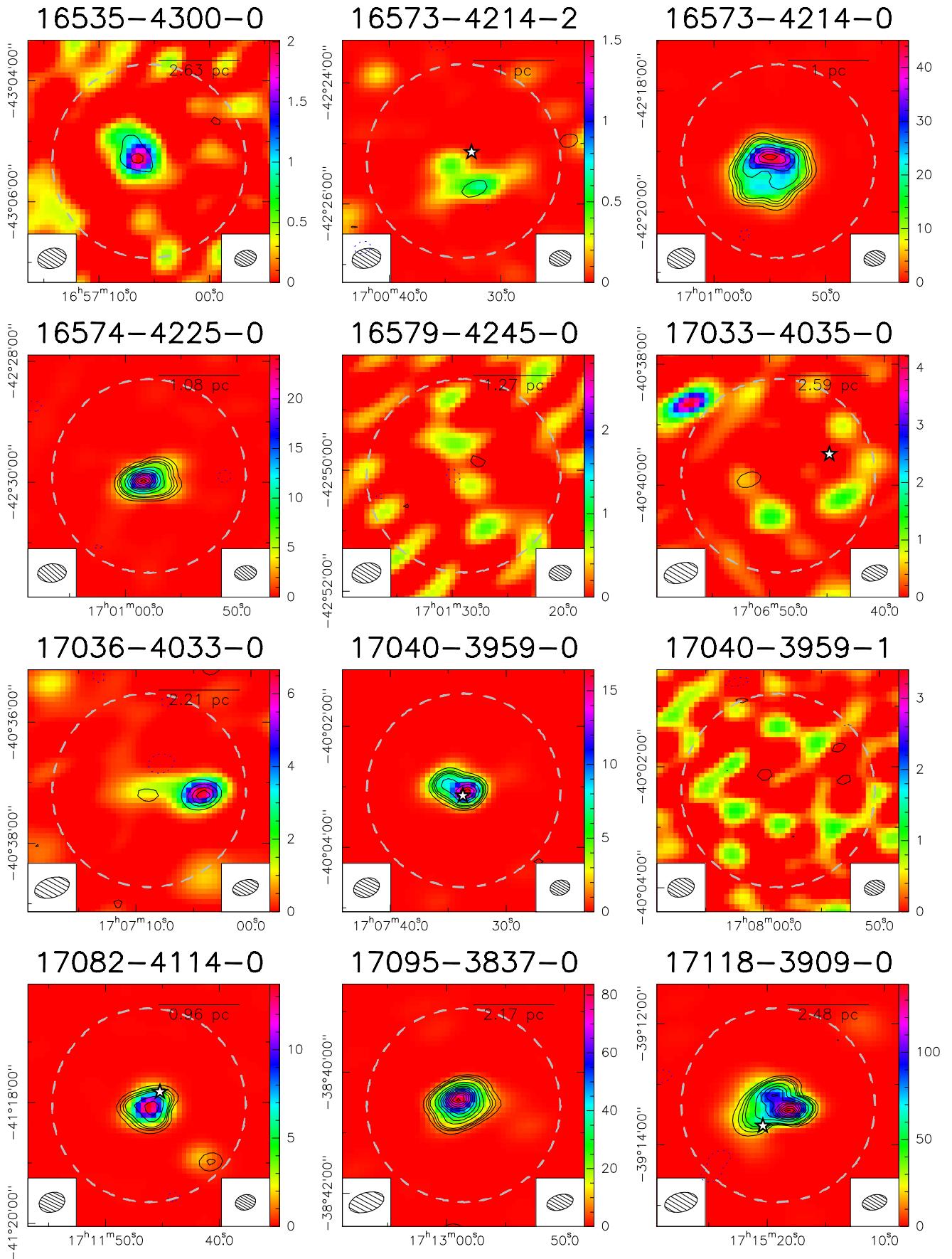
Fig. B.1: continued.
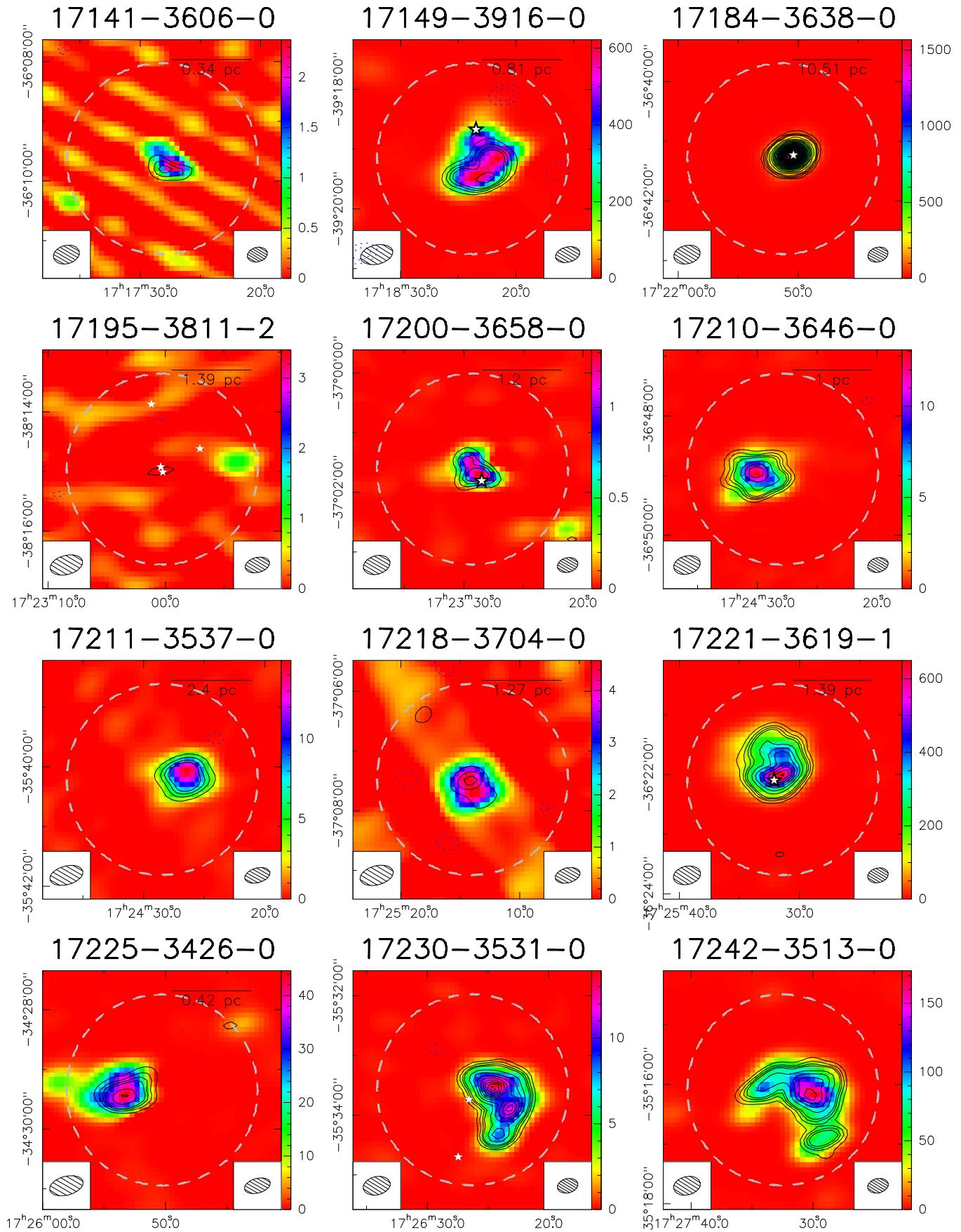
Fig. B.1: continued.
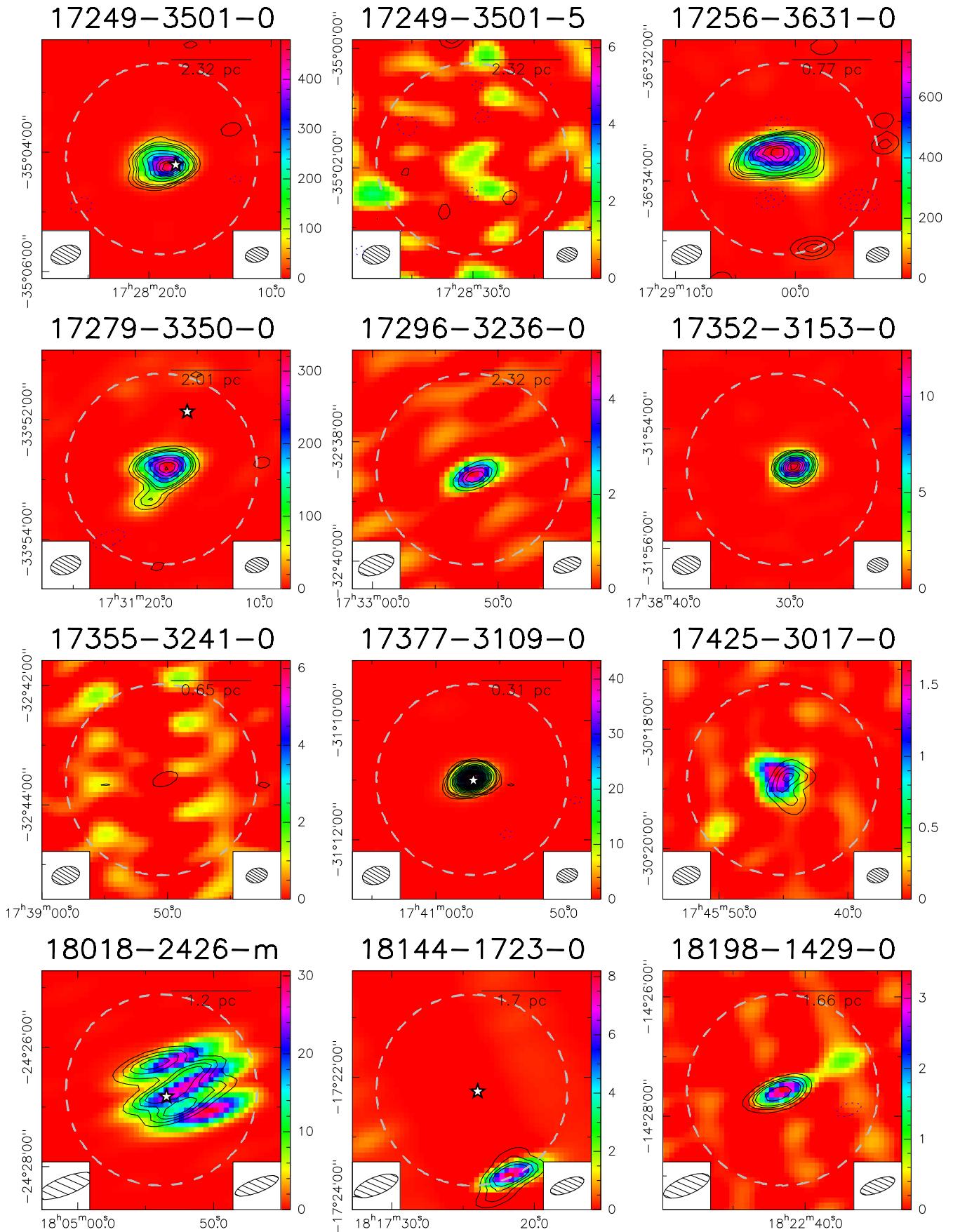
Fig. B.1: continued.

Fig. B.1: continued.
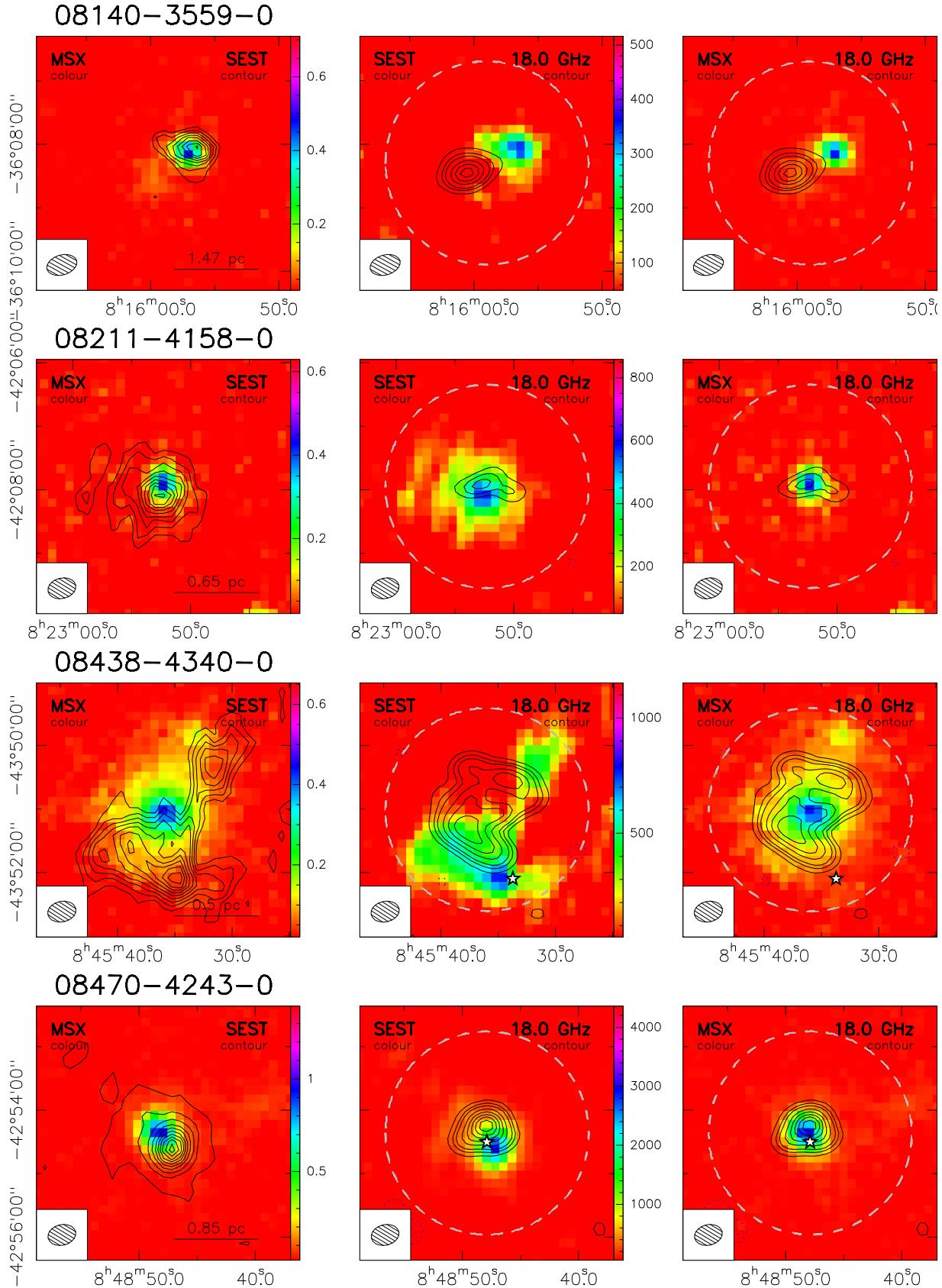
Fig. B.2: ATCA, SEST and MSX maps. For each source we show three panels: **left** 21 μm MSX image (color scale) and 1.2 mm SEST image (contours), **middle** 1.2 mm SEST image (color scale) and 18.0 GHz ATCA image (contours), and **right** 21 μm MSX image (color scale, as in left panel) and 18.0 GHz ATCA image (contours). The spatial scale is shown in sources with distance determination. The primary beam of the ATCA image is shown as a white dashed circle. Water masers are shown as star symbols.

08477−4359−0
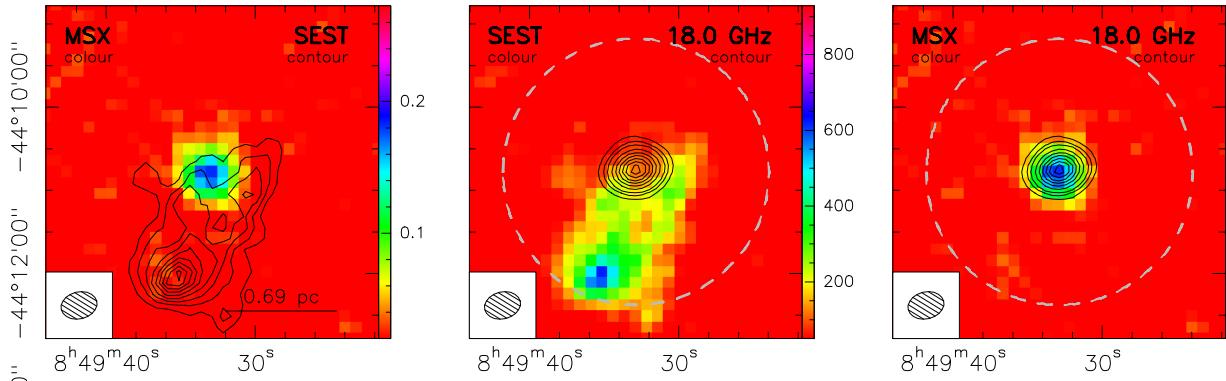
08477−4359−1
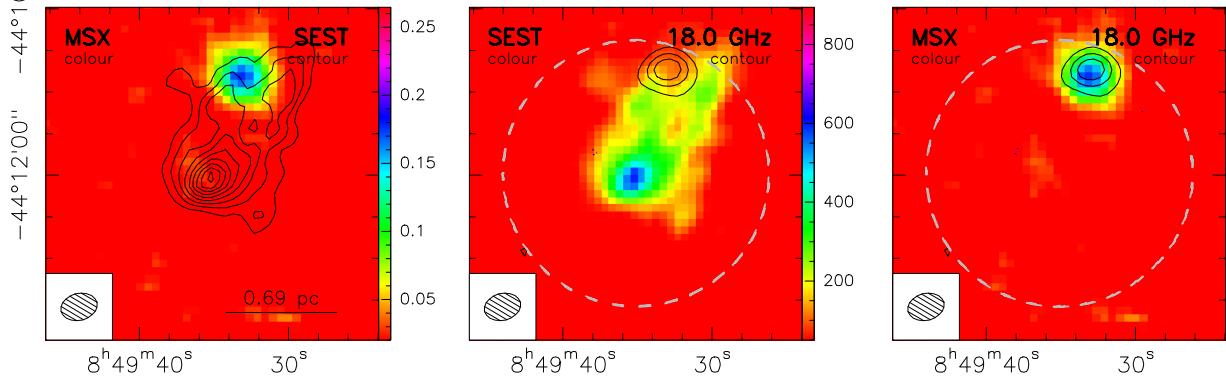
08563−4225−0
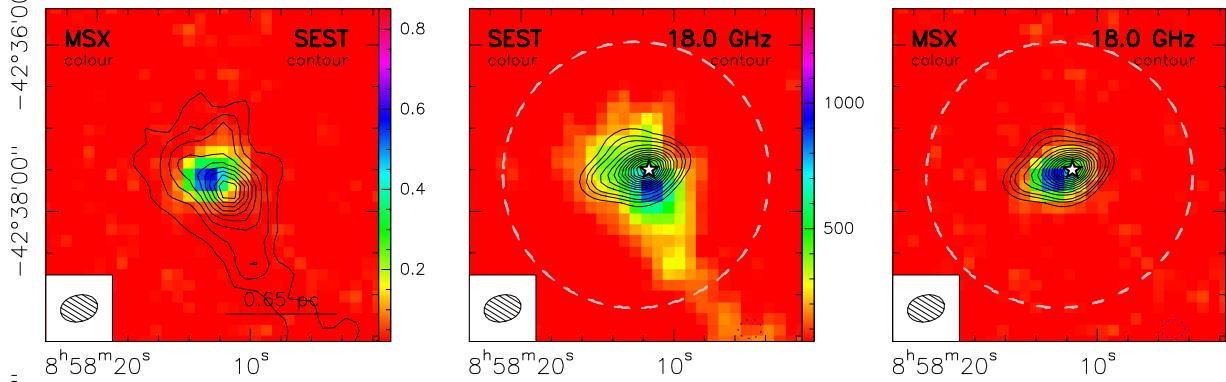
08589−4714−0
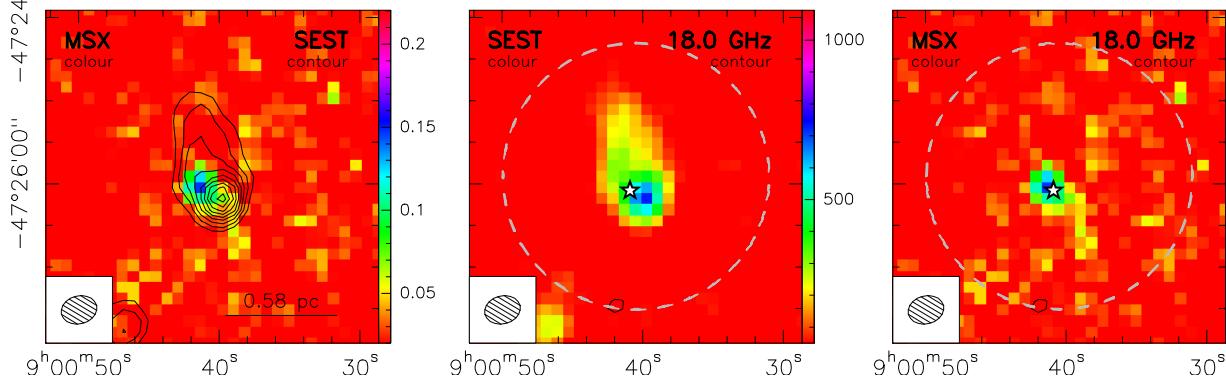
Fig. B.2: continued.

09014−4736−0
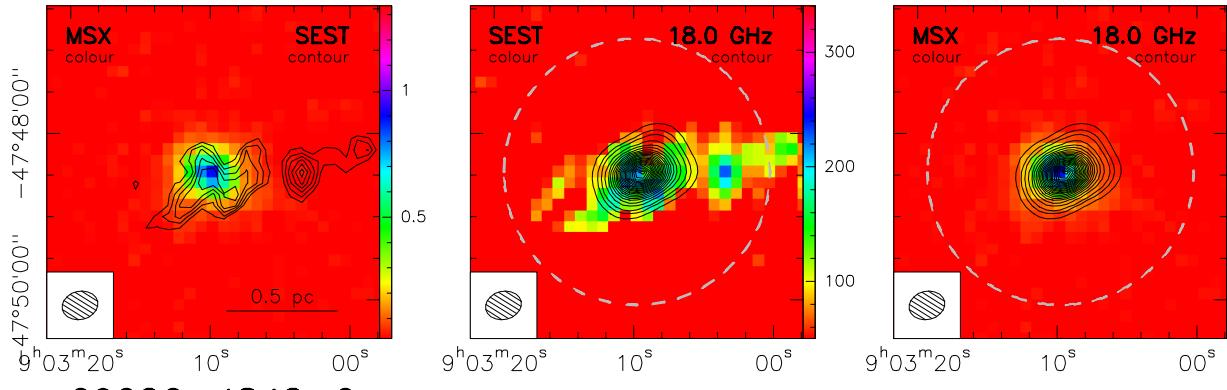
09026−4842−0
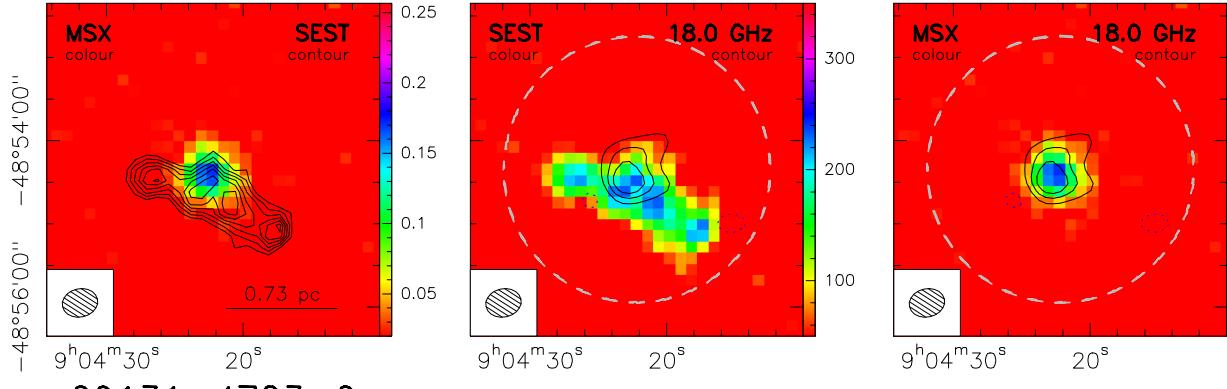
09131−4723−0
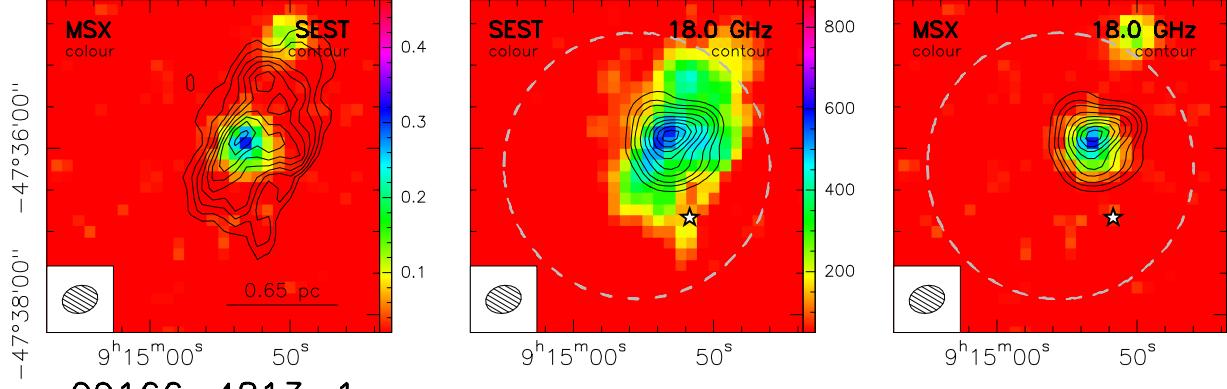
09166−4813−1


Fig. B.2: continued.
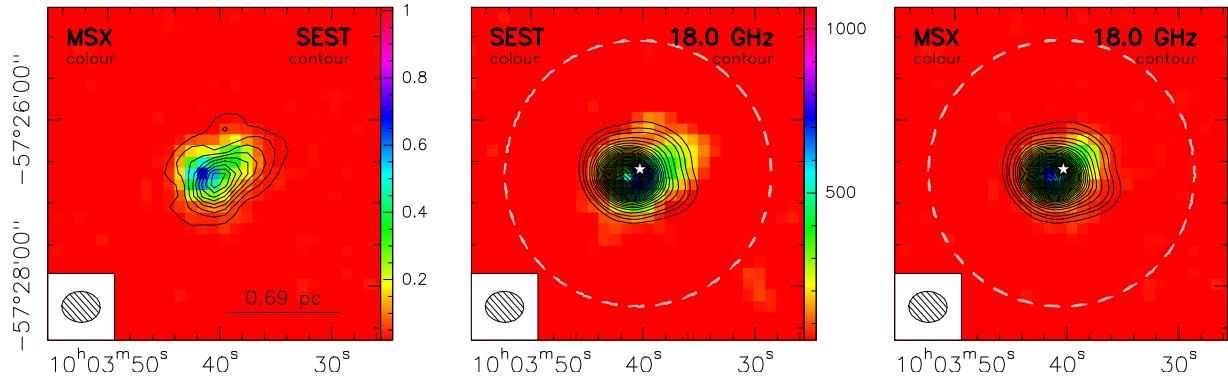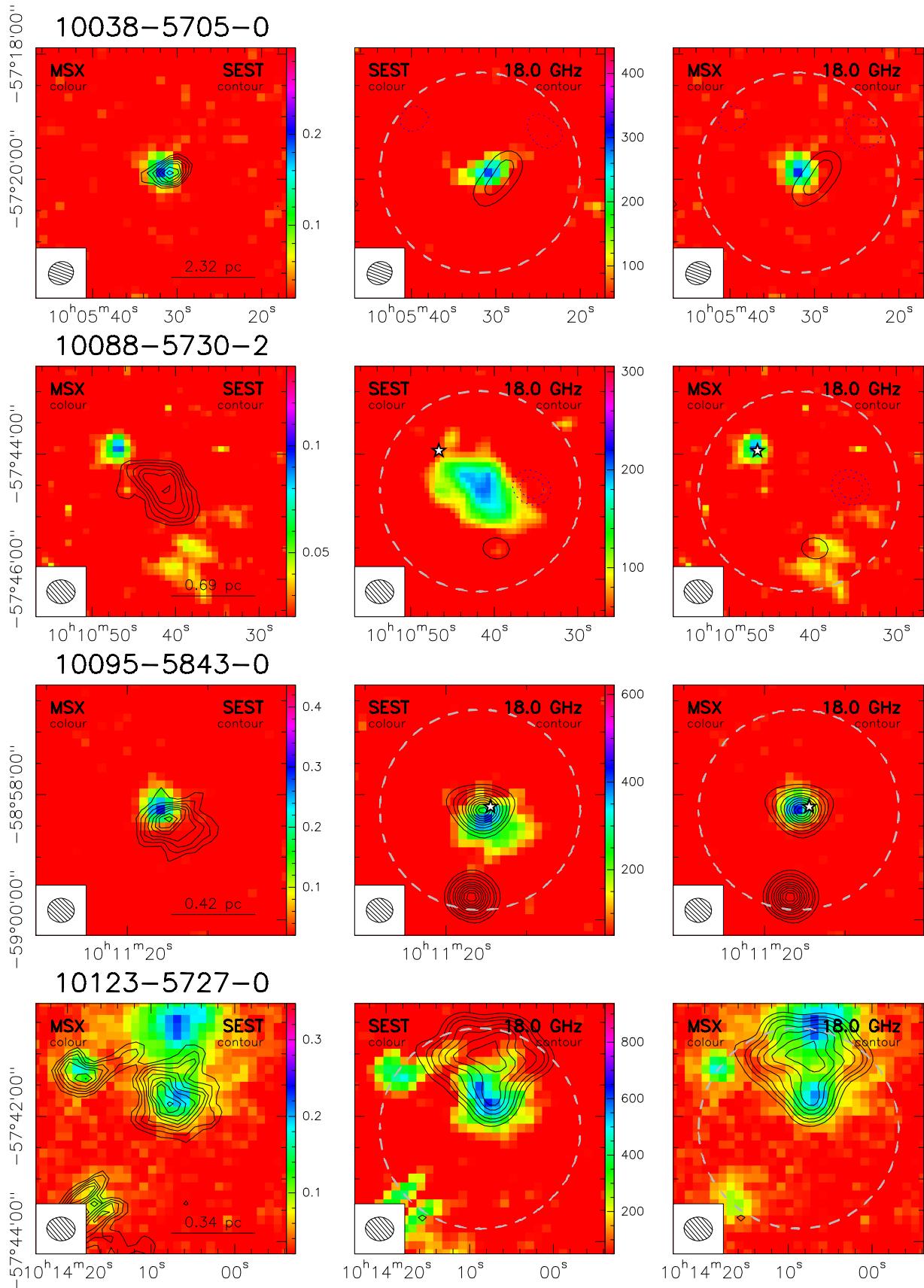
Fig. B.2: continued.

Fig. B.2: continued.

Fig. B.2: continued.

10295−5746−0

10317−5936−0

10320−5928−0

10337−5710−0

Fig. B.2: continued.

Fig. B.2: continued.

Fig. B.2: continued.

10572−6018−0

10575−5844−0

10589−6034−0

10591−5934−0

Fig. B.2: continued.

11079−6101−0

11220−6147−0

11265−6158−0

11354−6234−0

Fig. B.2: continued.

Fig. B.2: continued.

Fig. B.2: continued.

Fig. B.2: continued.

13024−6158−0

13039−6108−0

13039−6108−6

13039−6331−0

Fig. B.2: continued.

13054−6159−0

13106−6050−0

13107−6208−0

13333−6234−0

Fig. B.2: continued.

Fig. B.2: continued.

Fig. B.2: continued.

Fig. B.2: continued.

14090−6132−0

14166−6118−0

14183−6050−0

14183−6050−3

Fig. B.2: continued.

14188−6054−0

14201−6044−0

14201−6044−1

14212−6009−0

Fig. B.2: continued.

Fig. B.2: continued.

Fig. B.2: continued.

Fig. B.2: continued.

15219−5658−0

15239−5538−0

15246−5612−0

15262−5541−1
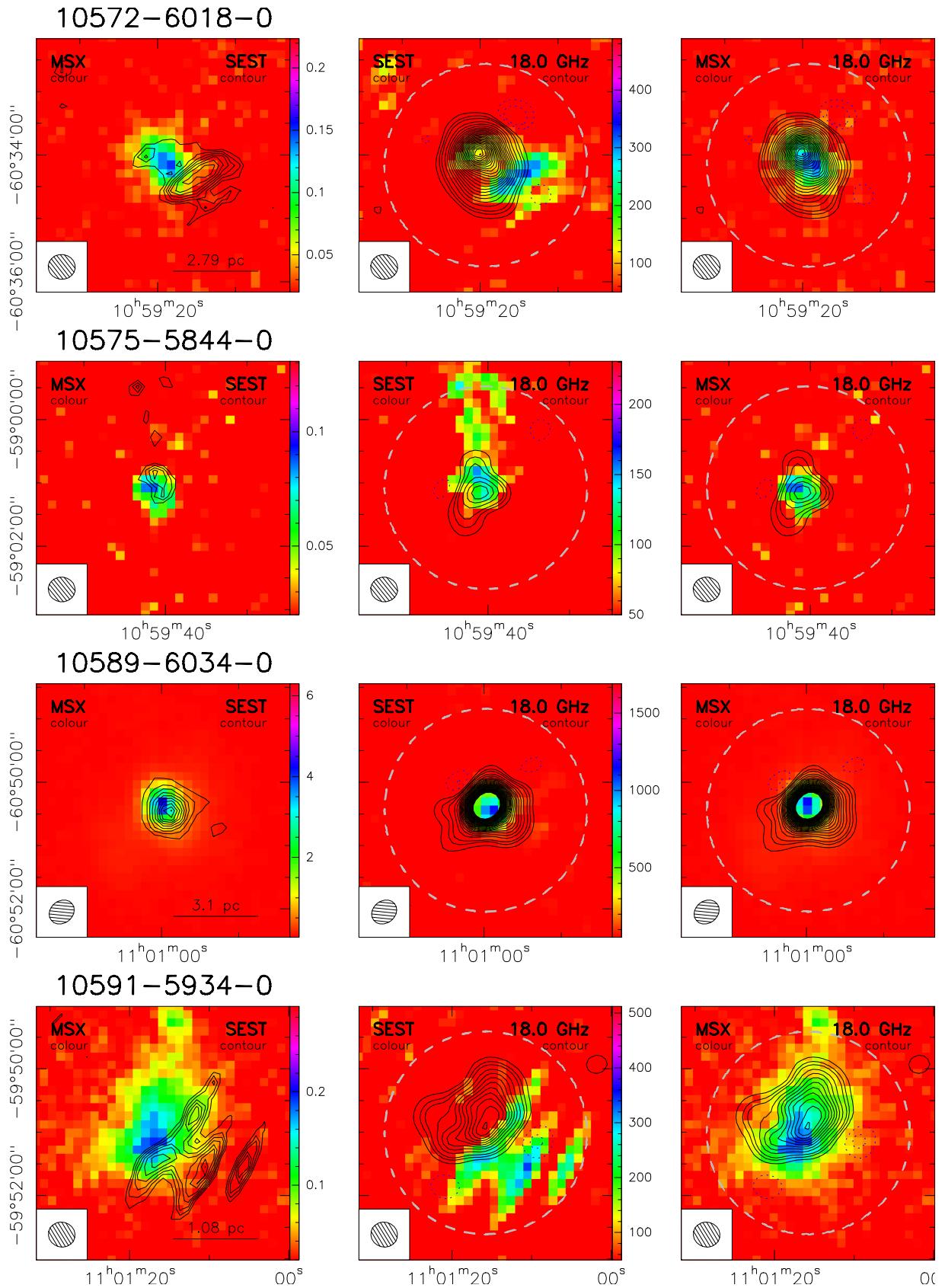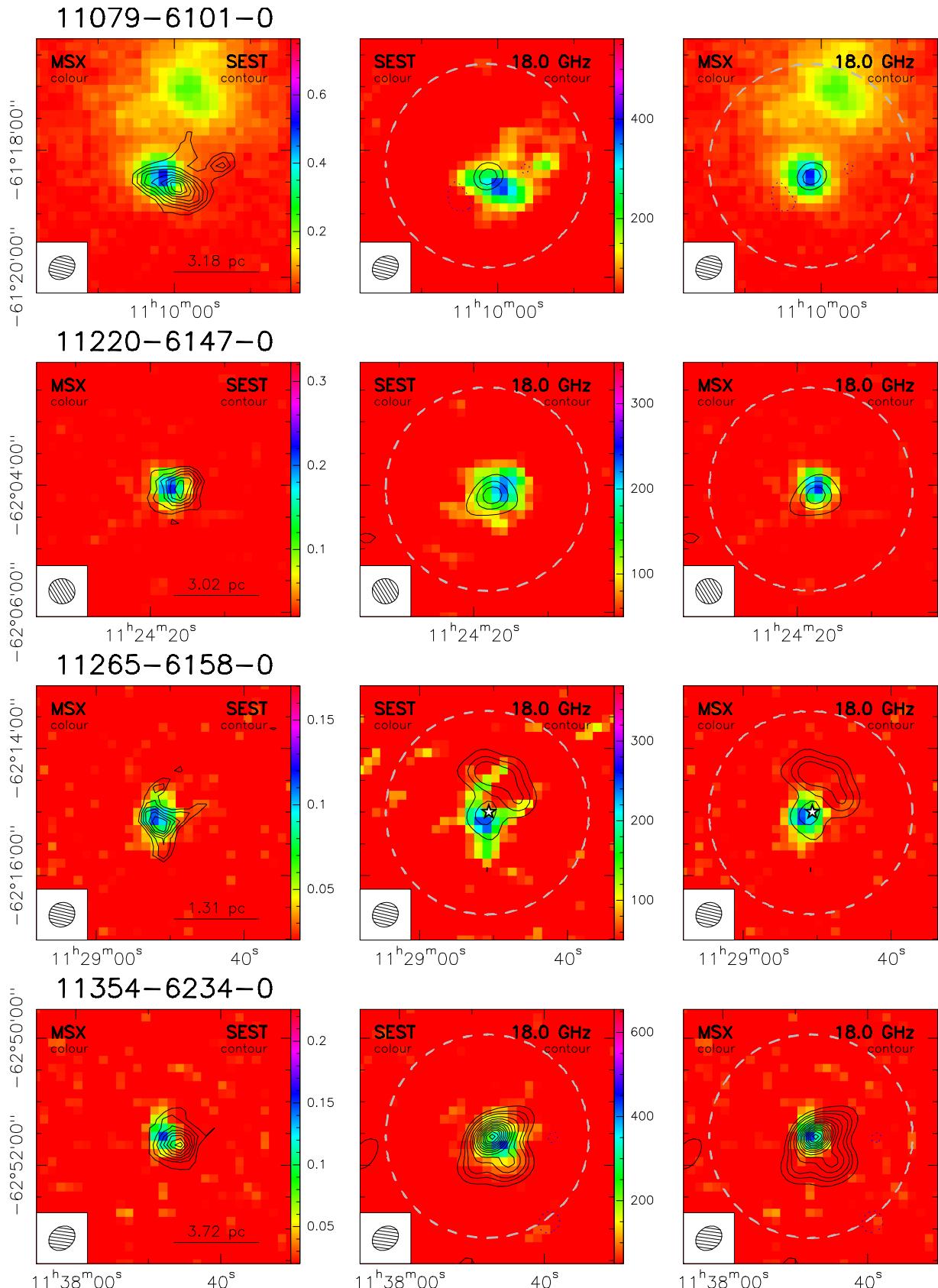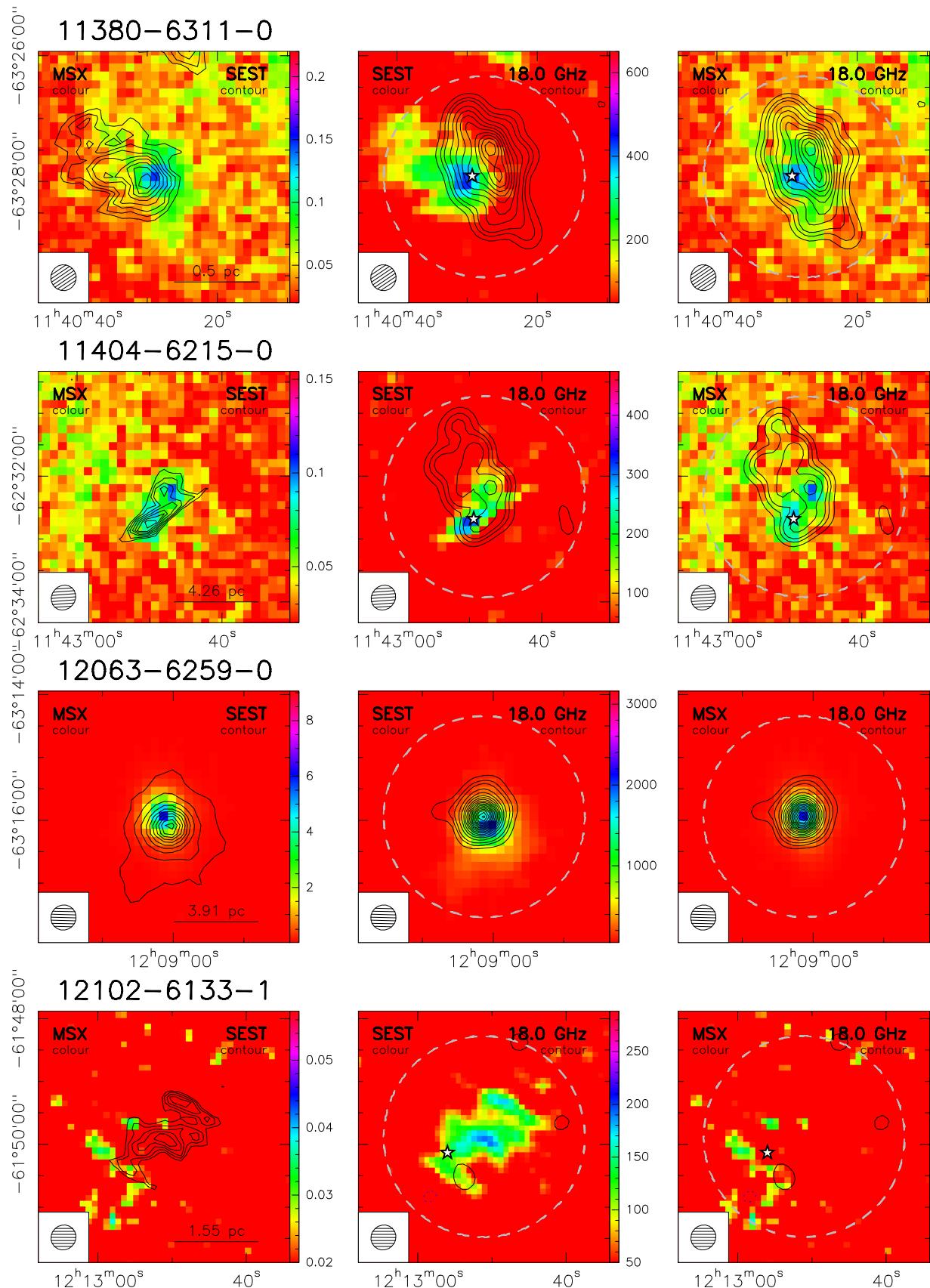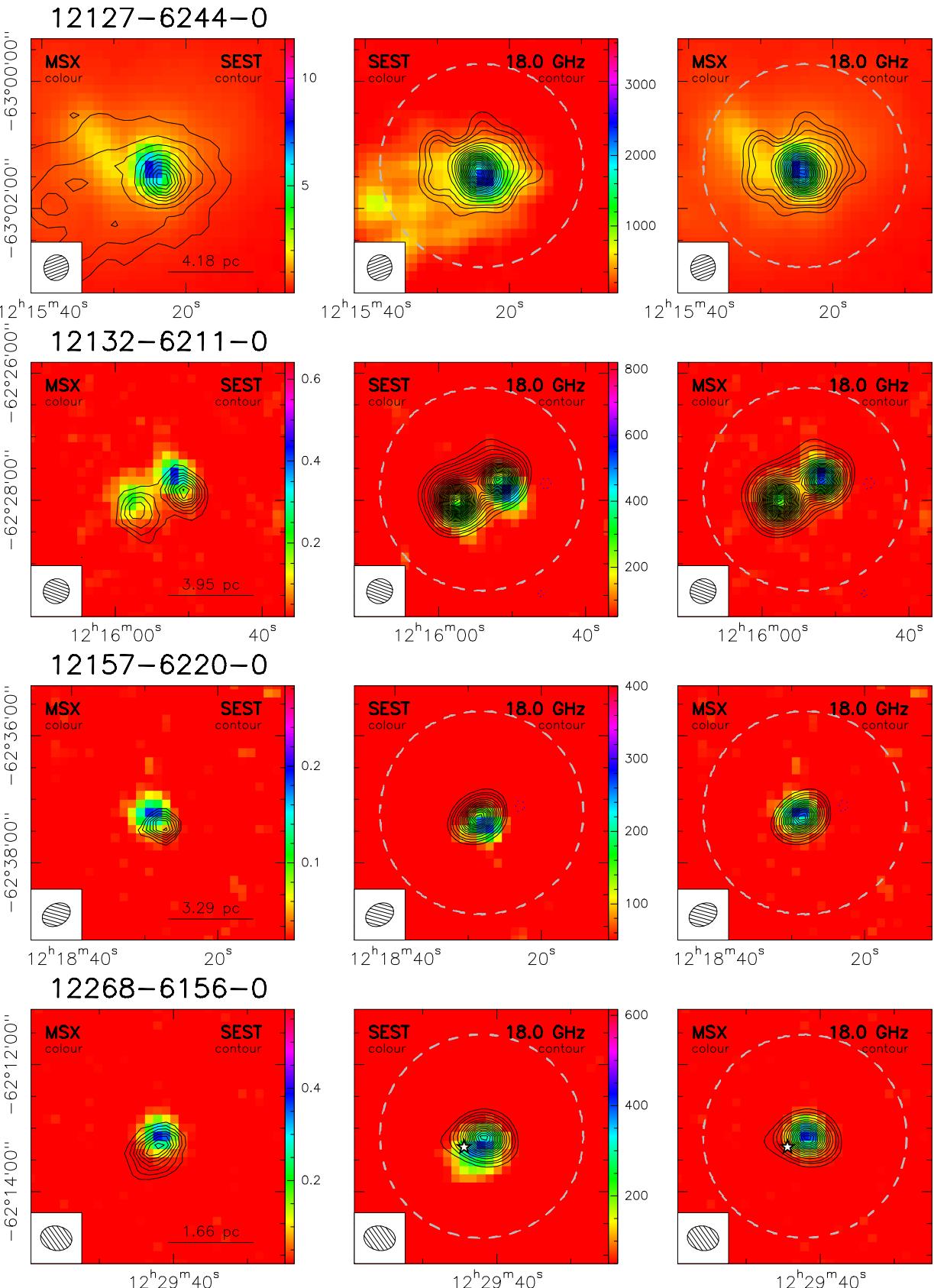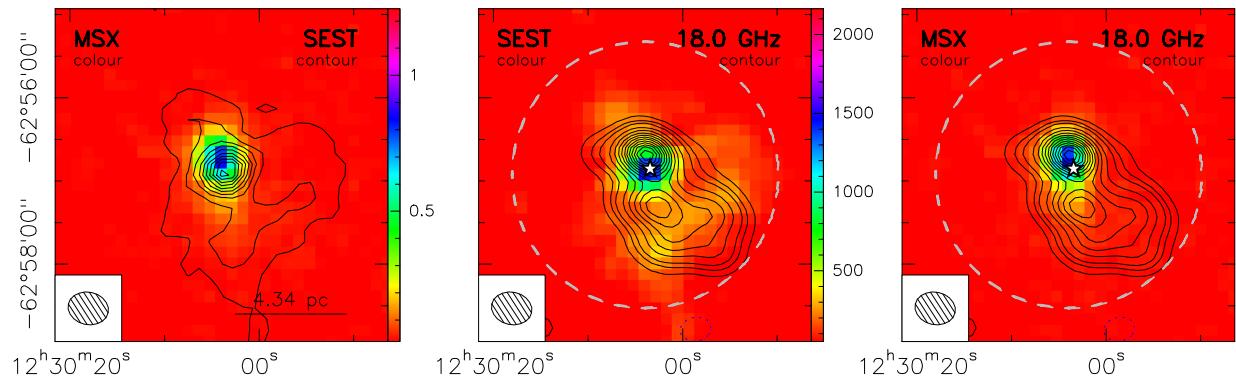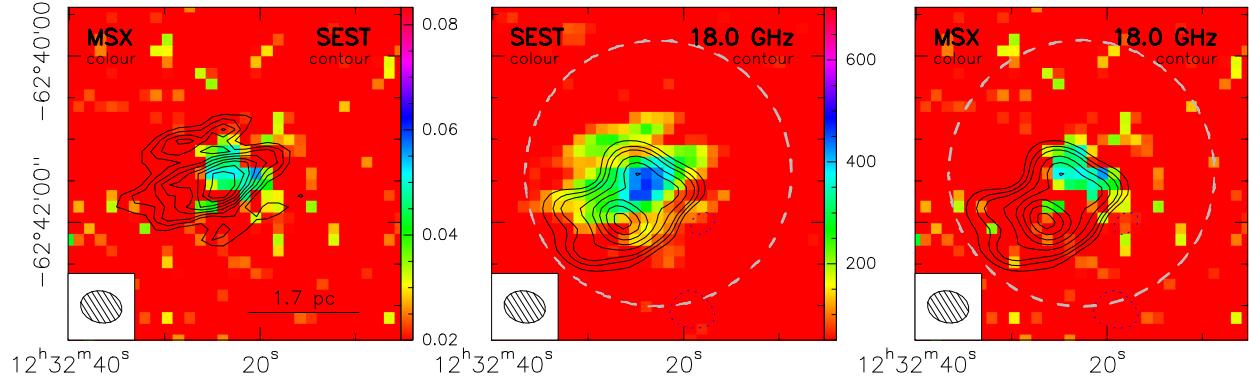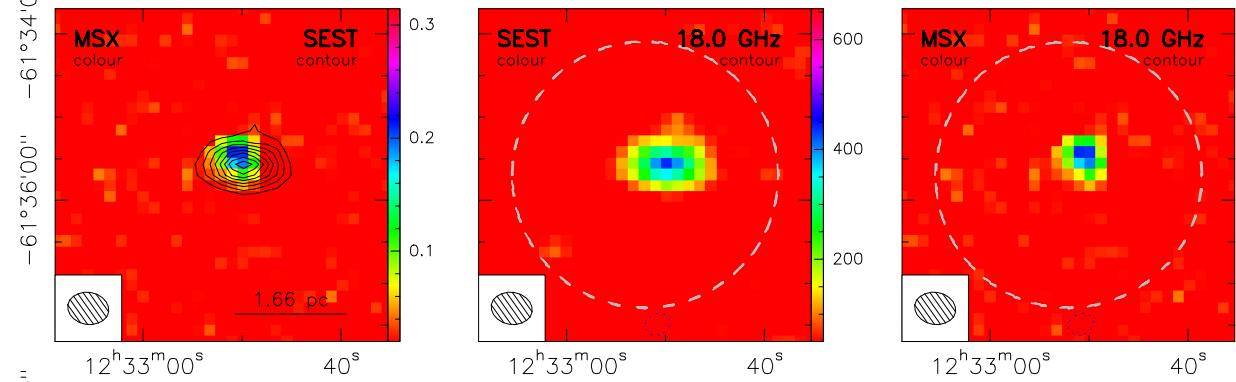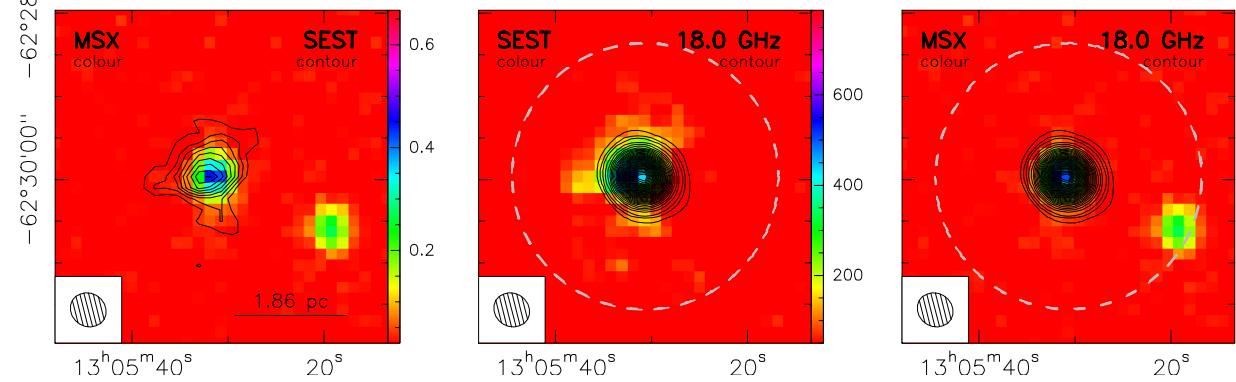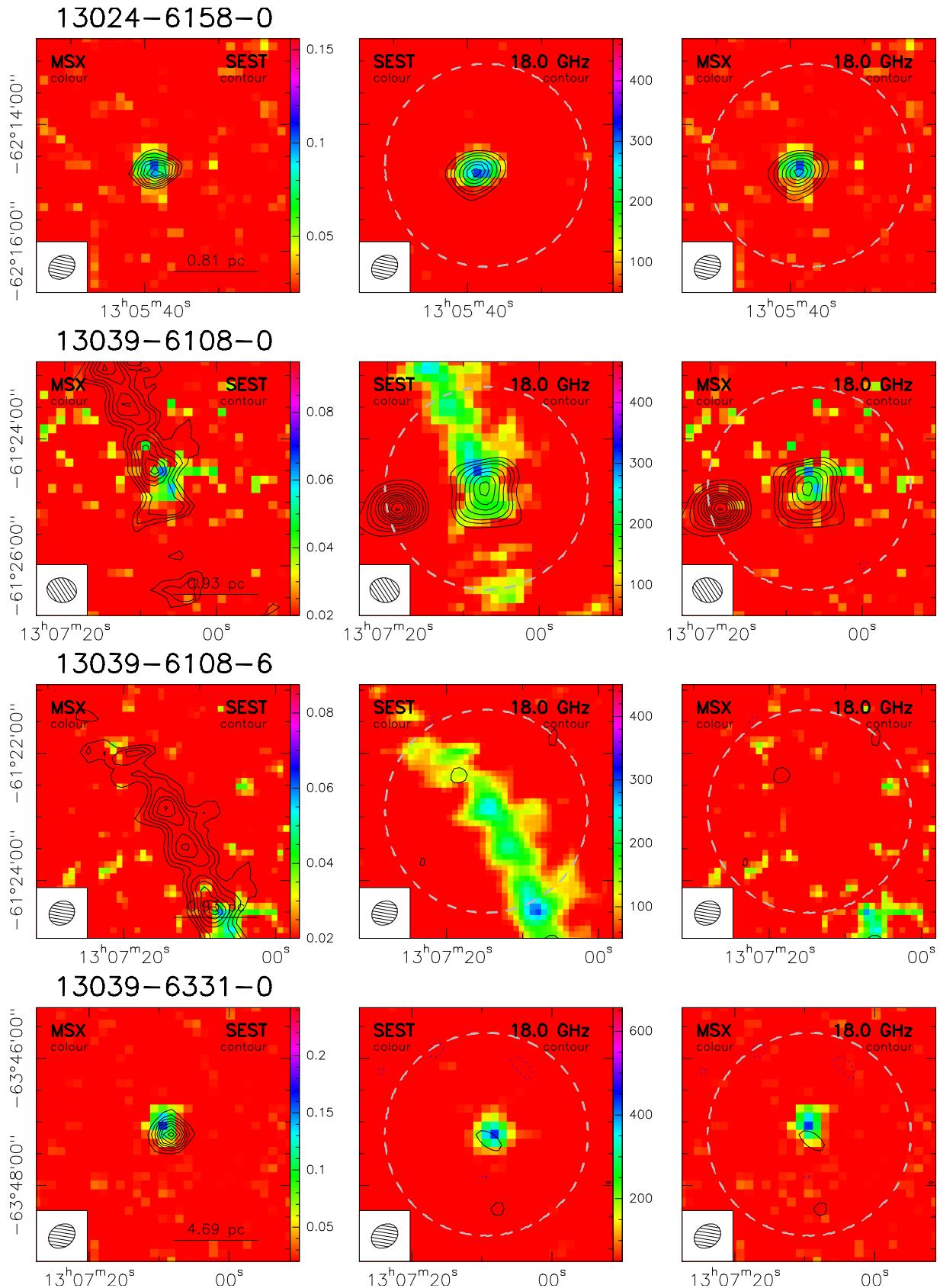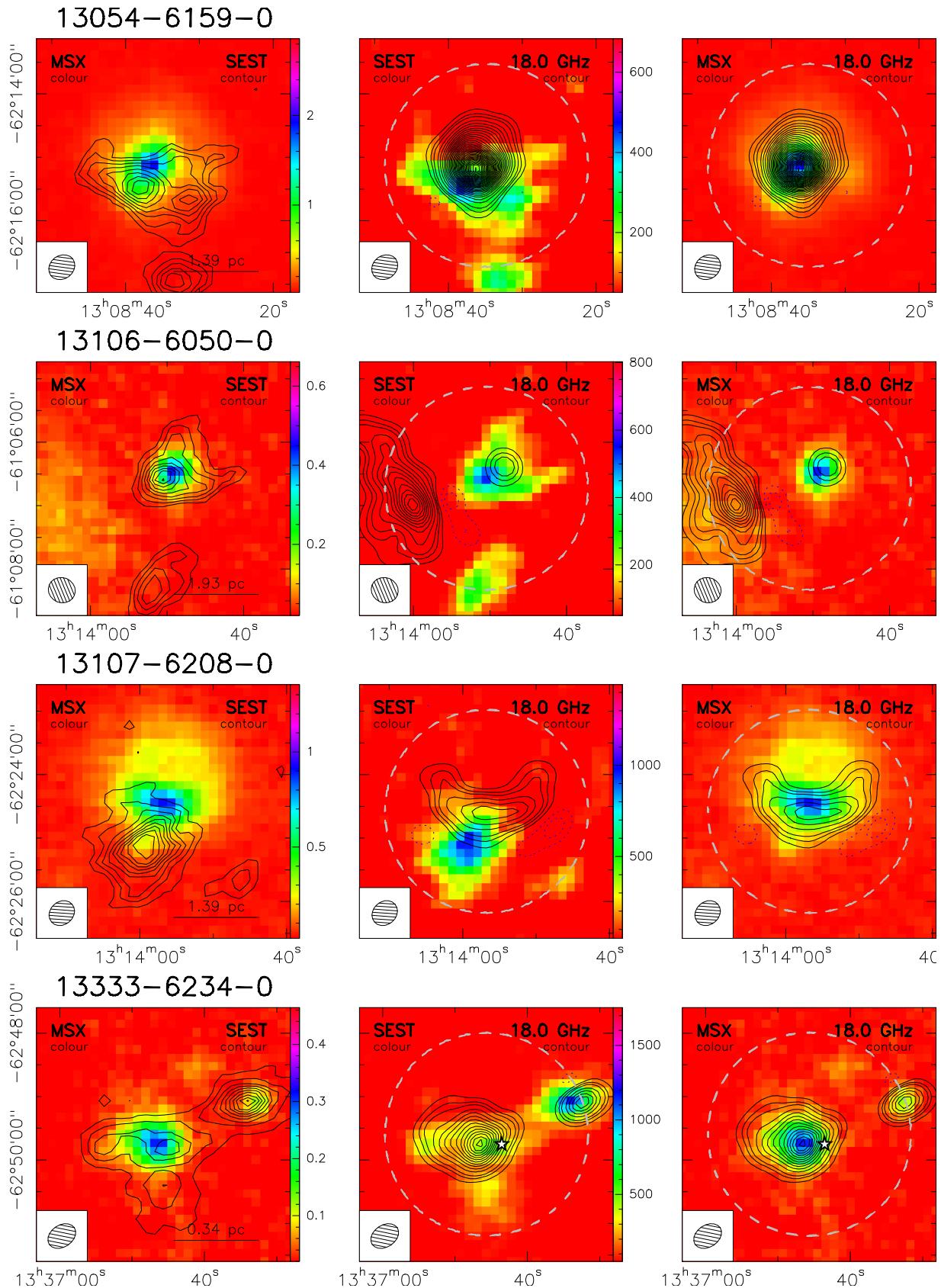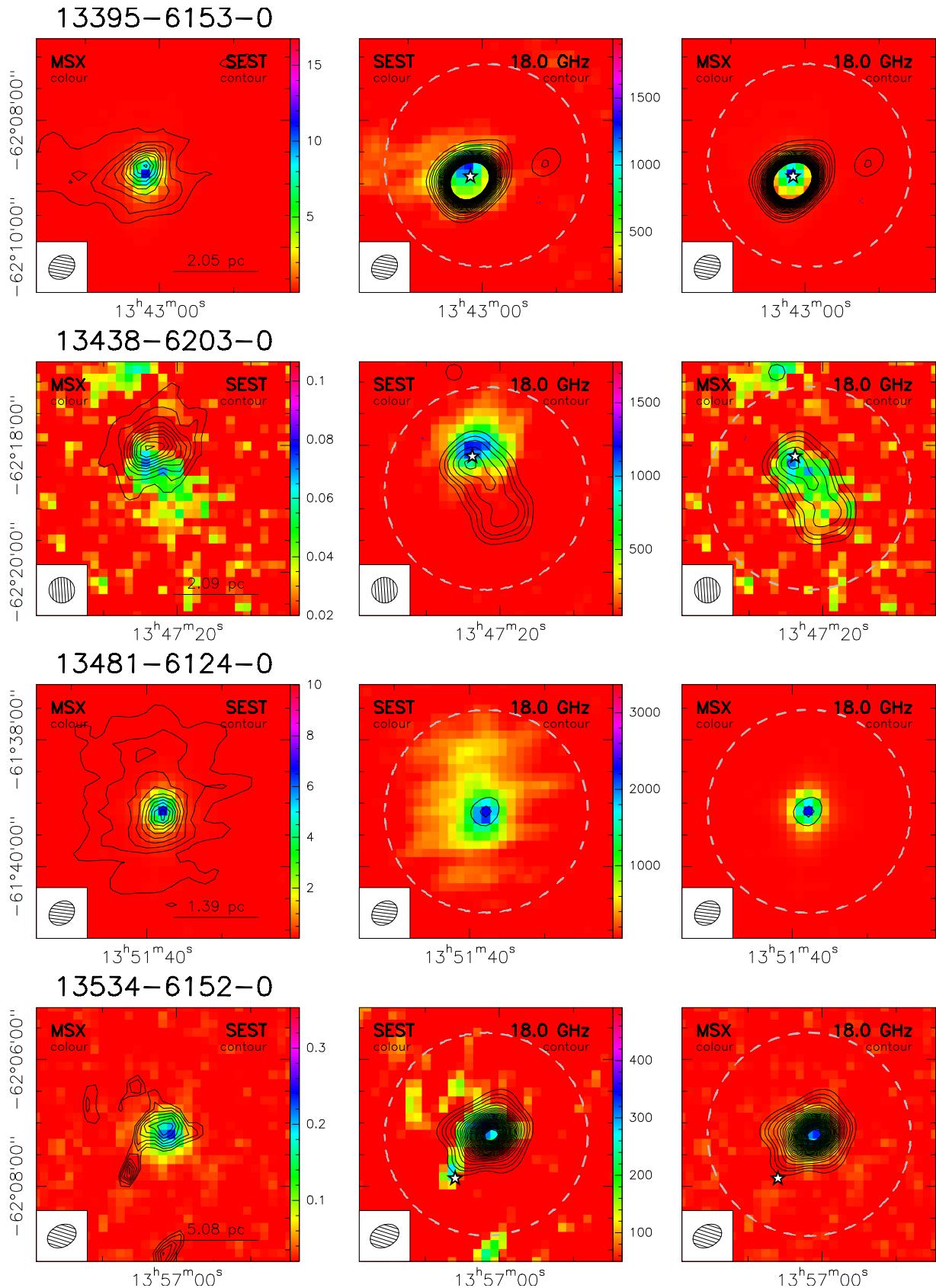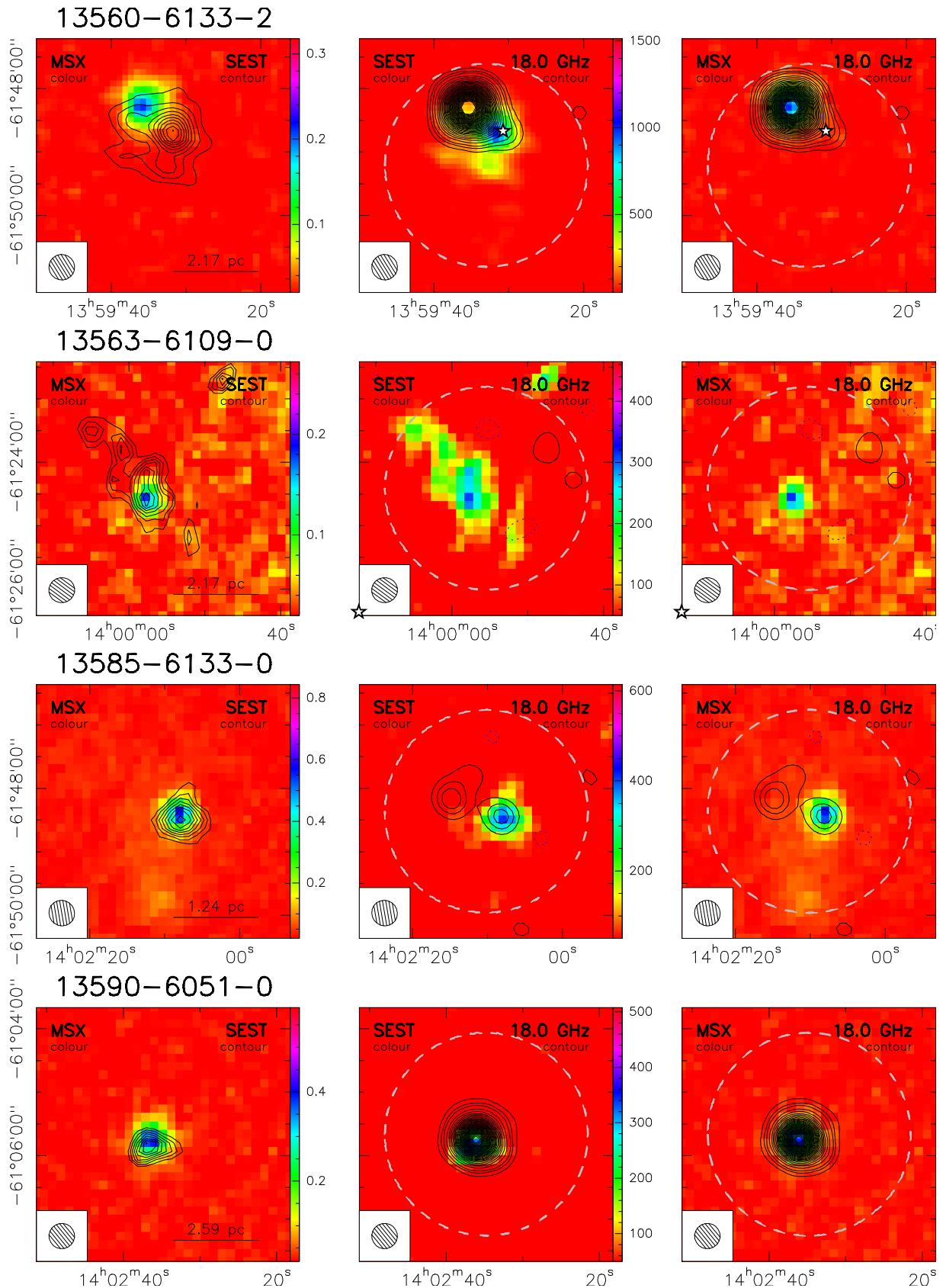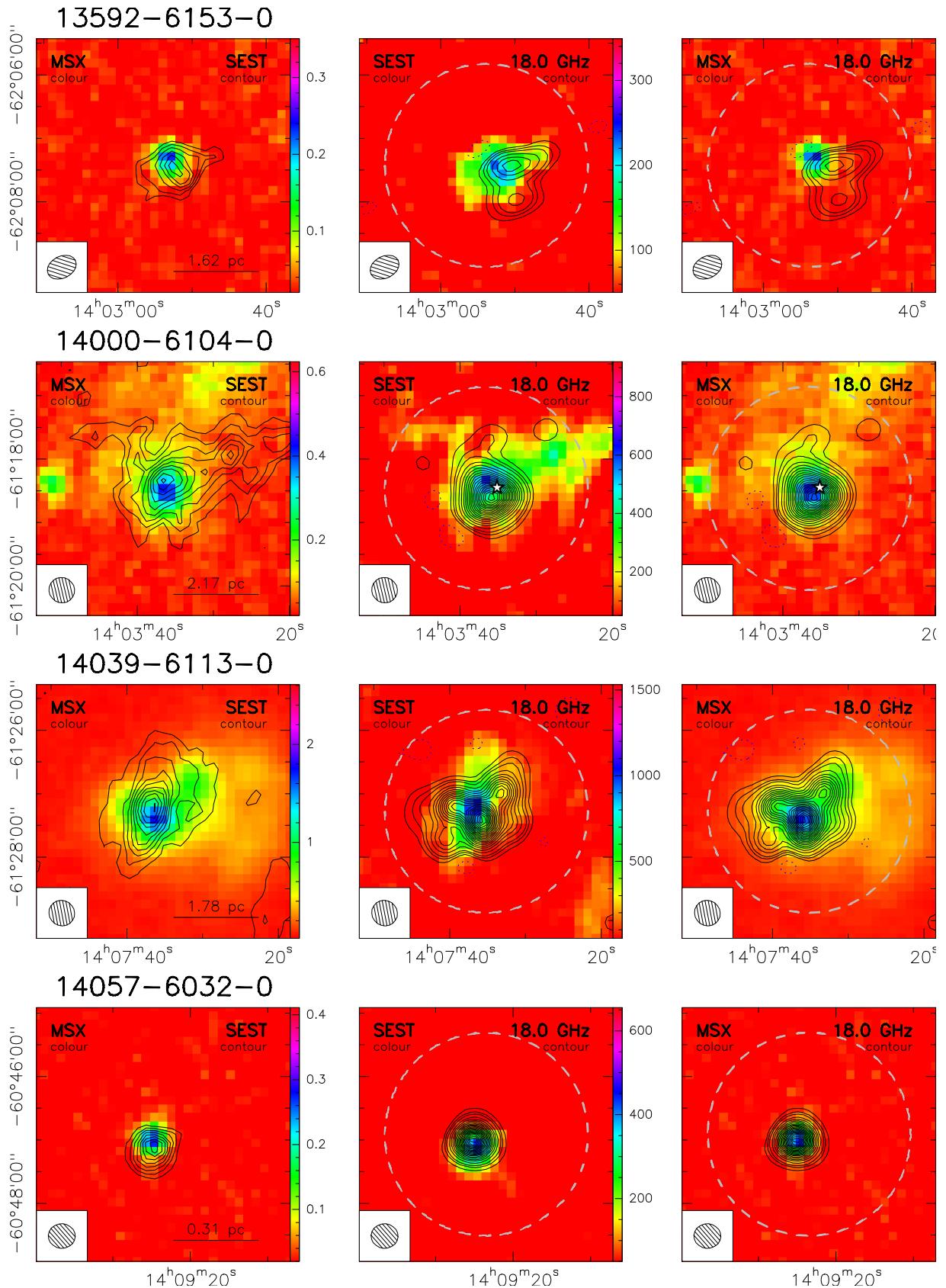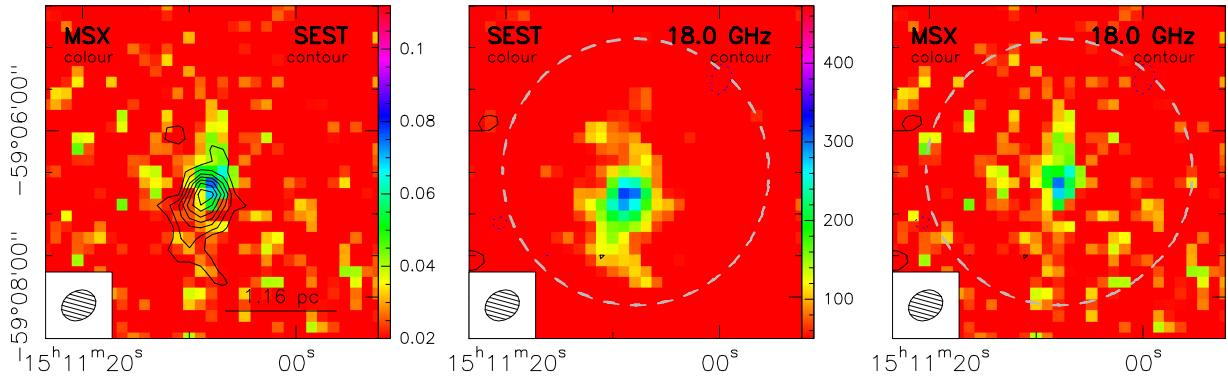
Fig. B.2: continued.

15278−5620−0
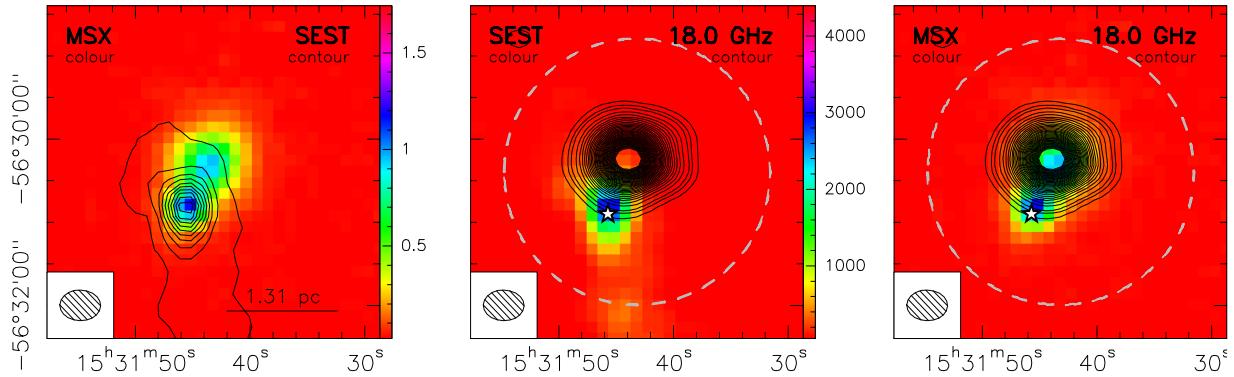
15278−5620−2
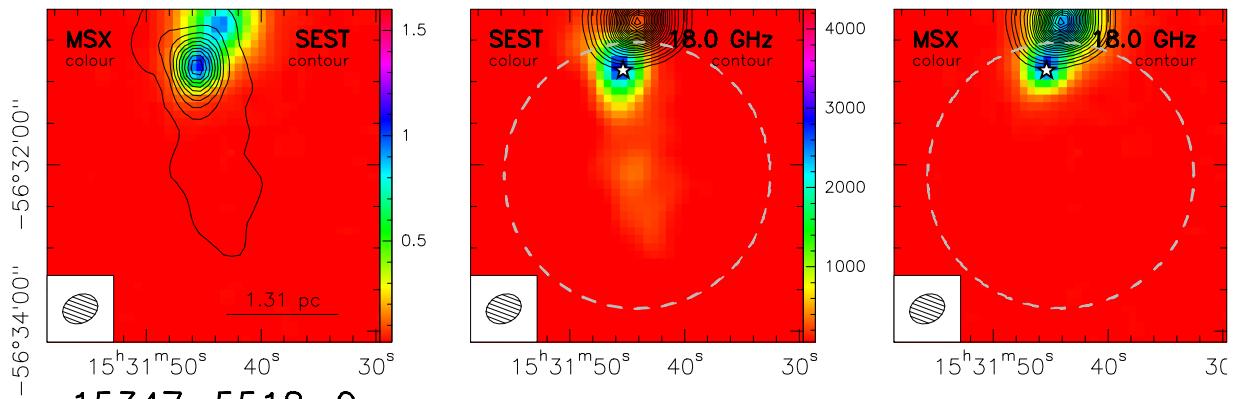
15347−5518−0
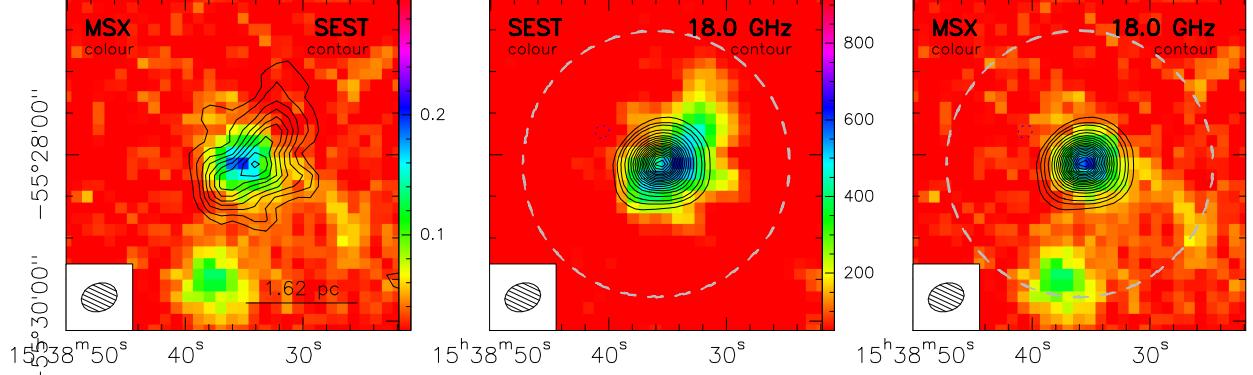
15371−5458−0
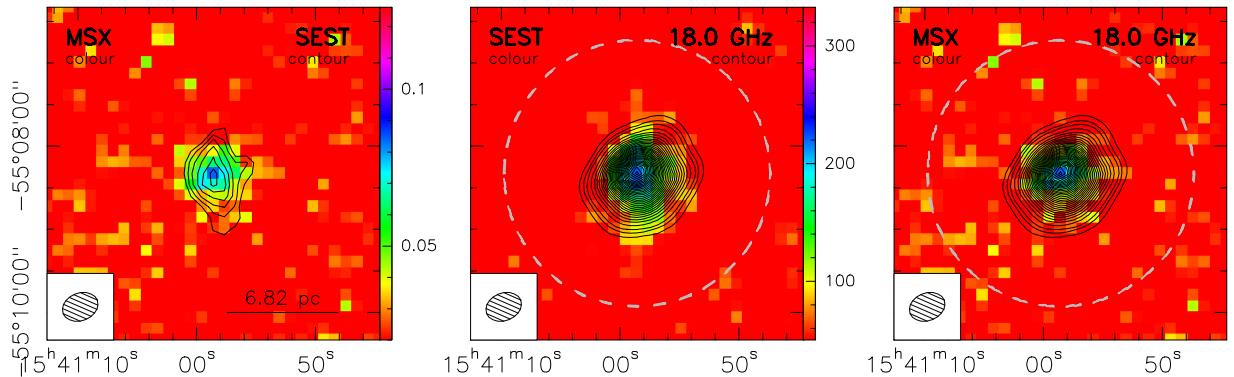
Fig. B.2: continued.
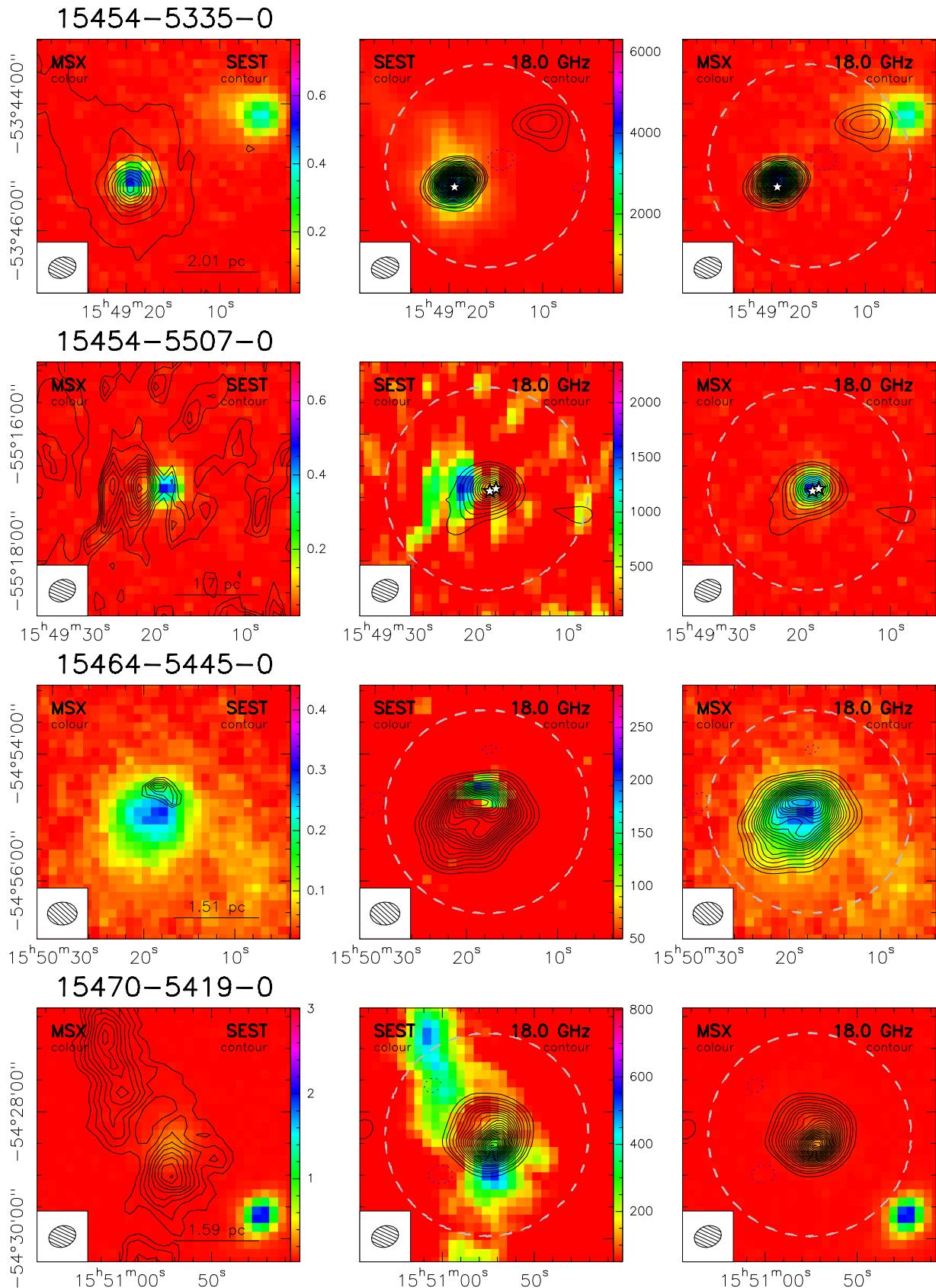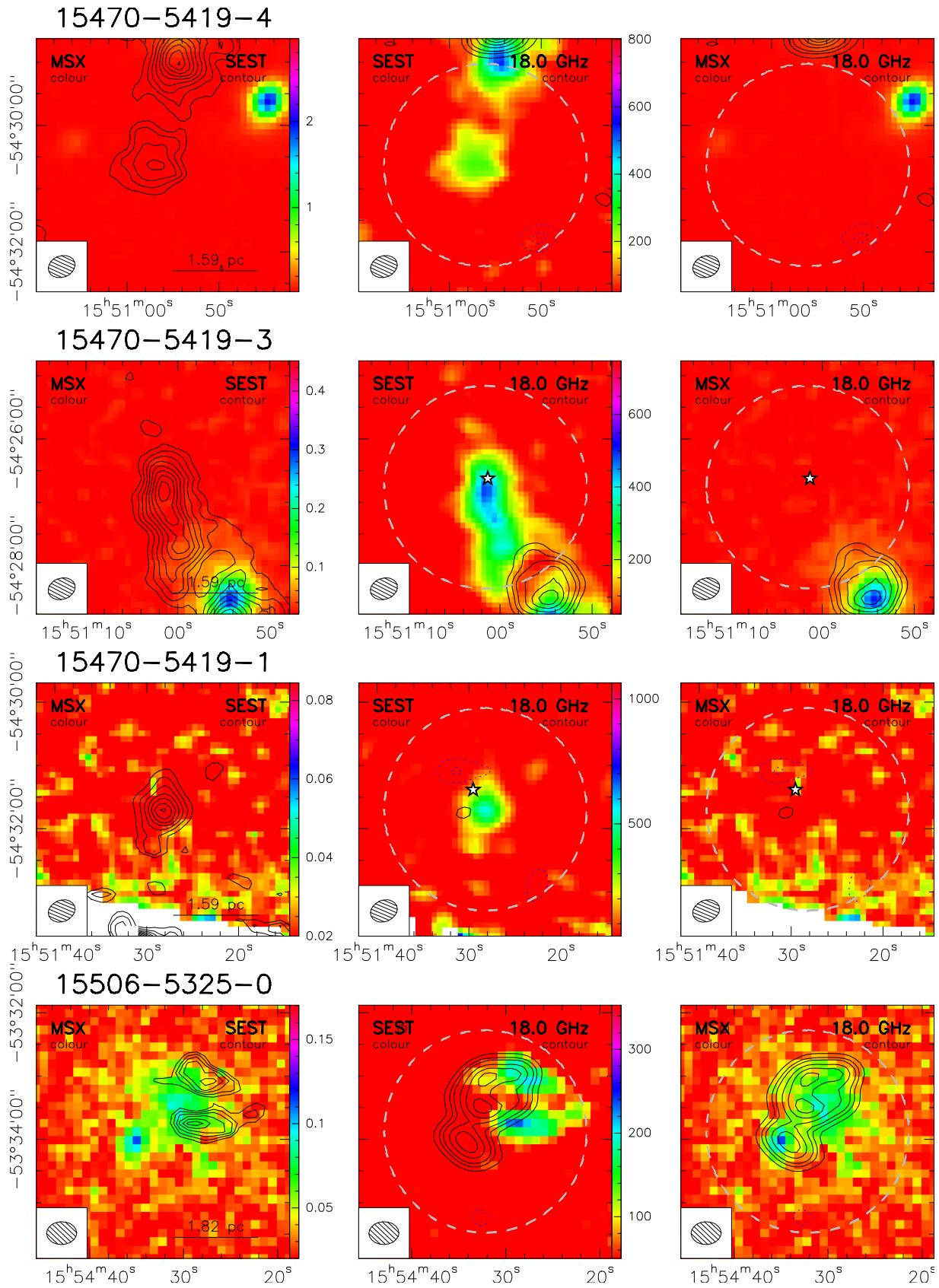
Fig. B.2: continued.

Fig. B.2: continued.

15507−5359−0
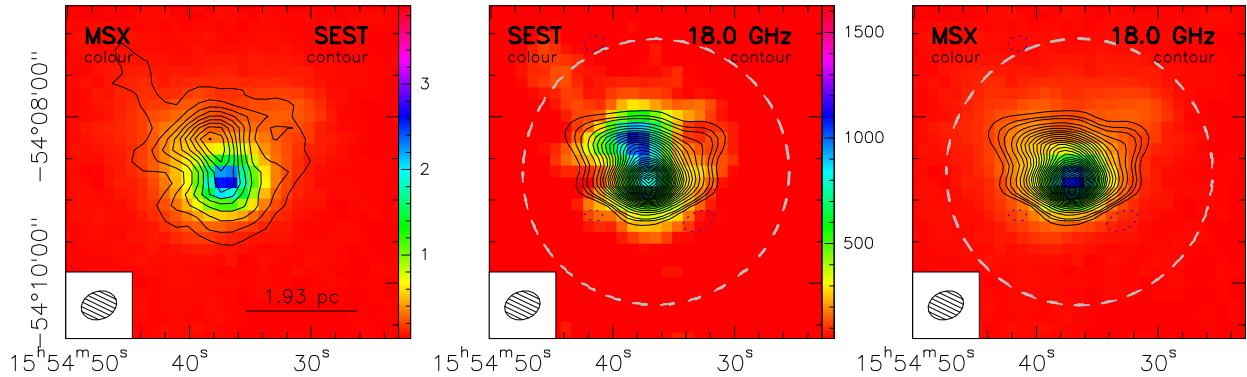
15519−5430−0
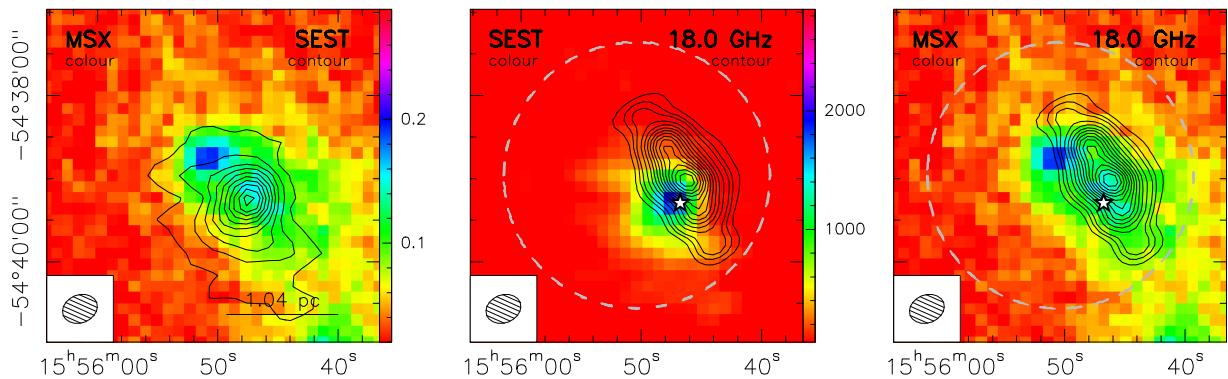
15530−5231−0
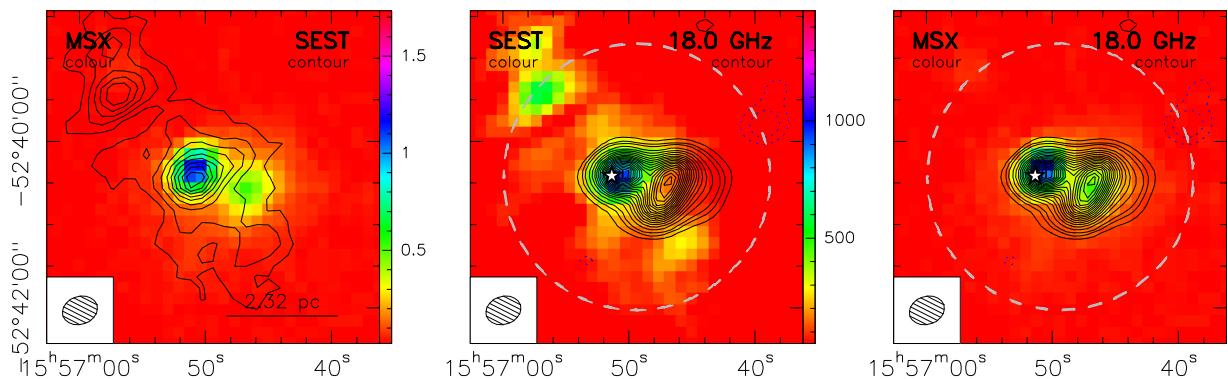
15557−5215−0
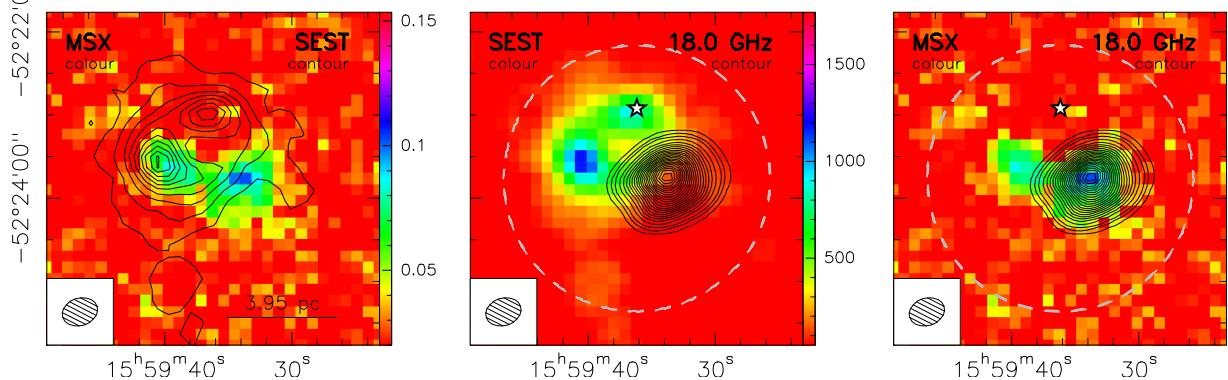
Fig. B.2: continued.
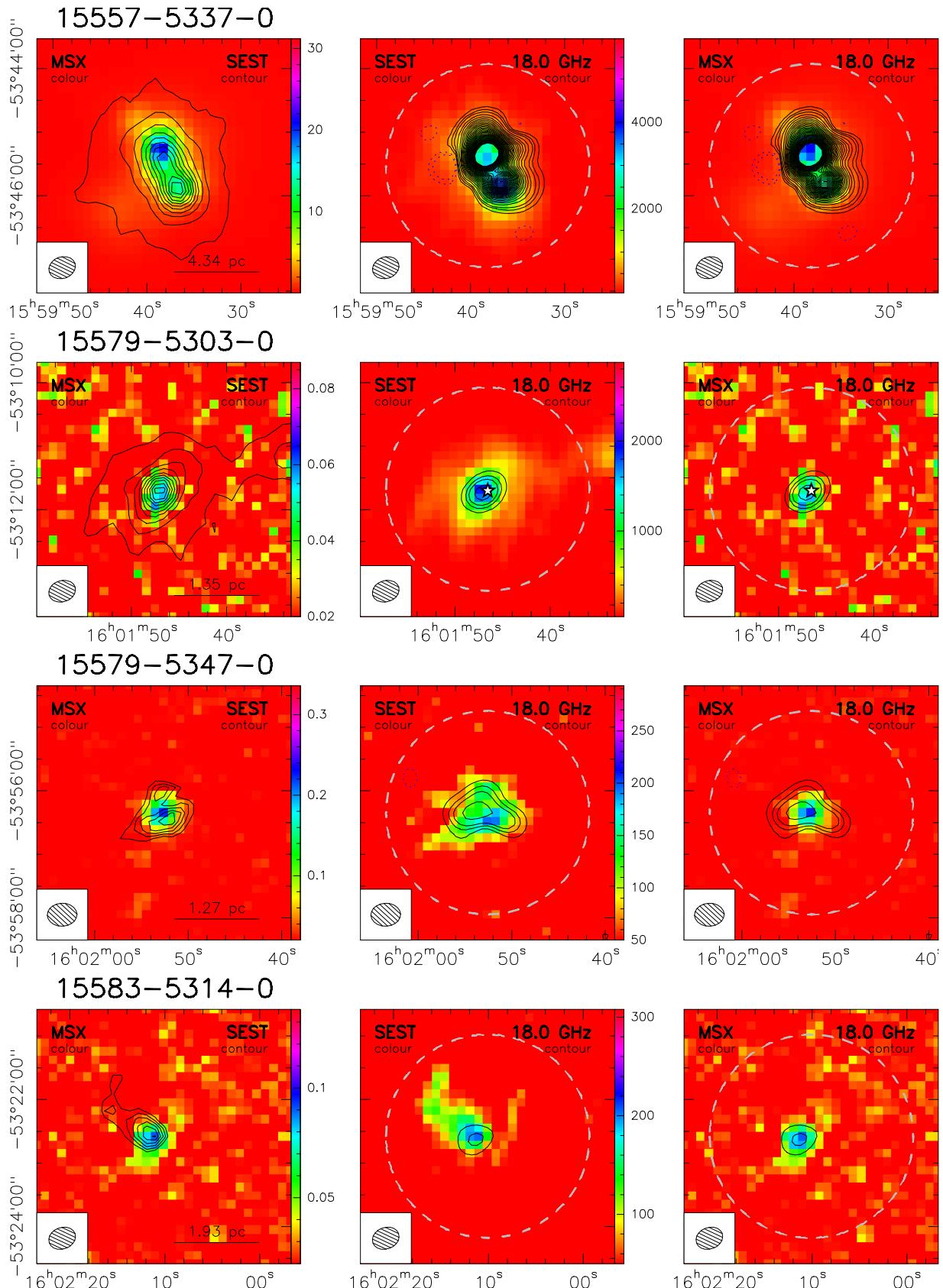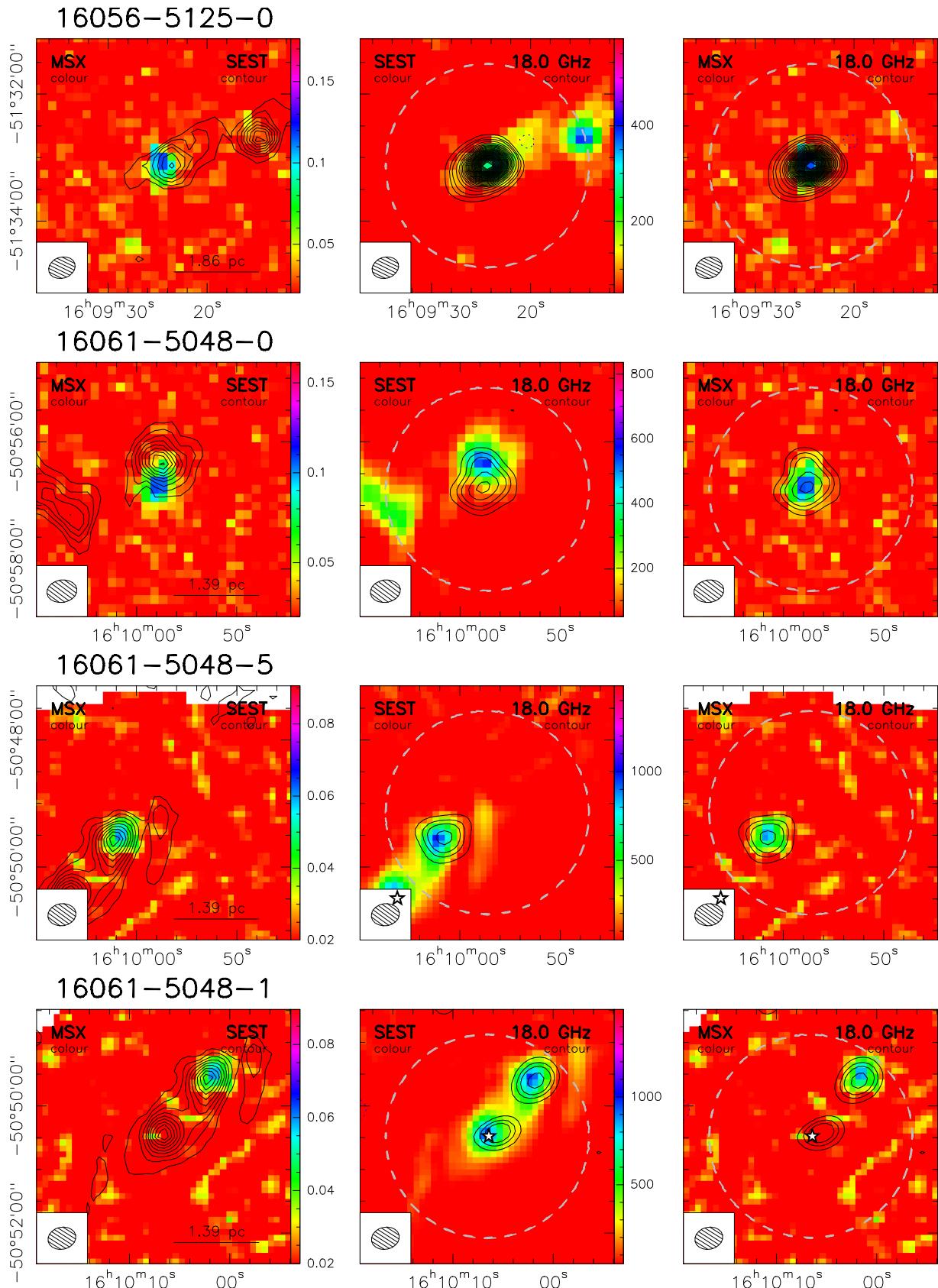
Fig. B.2: continued.

Fig. B.2: continued.

16061−5048−4
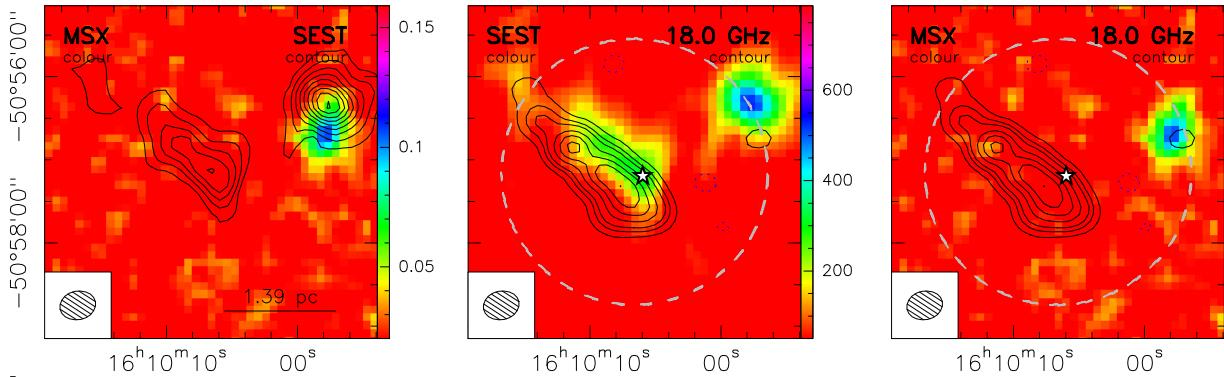
16069−4858−0
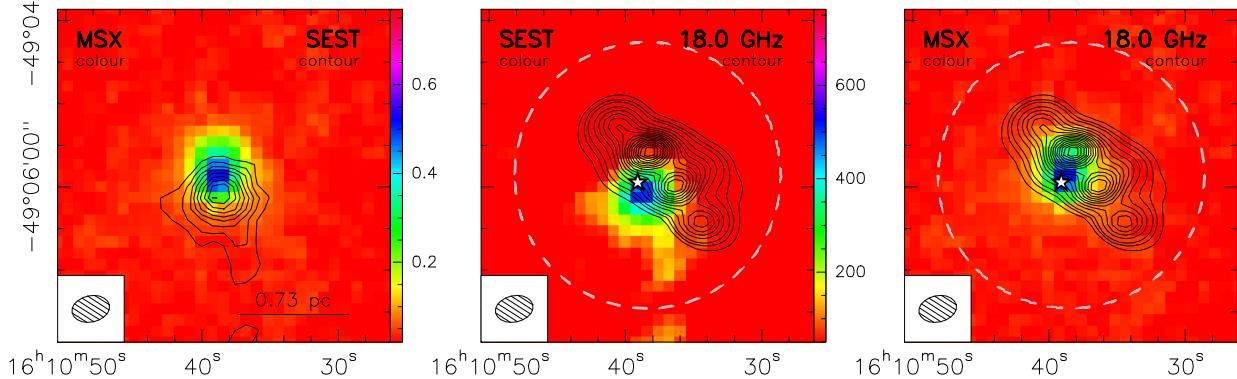
16085−5138−0
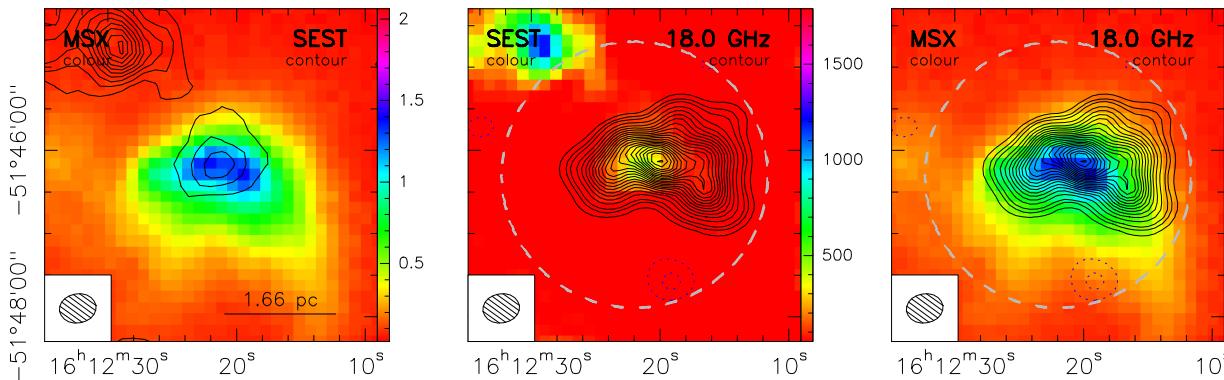
16093−5128−8
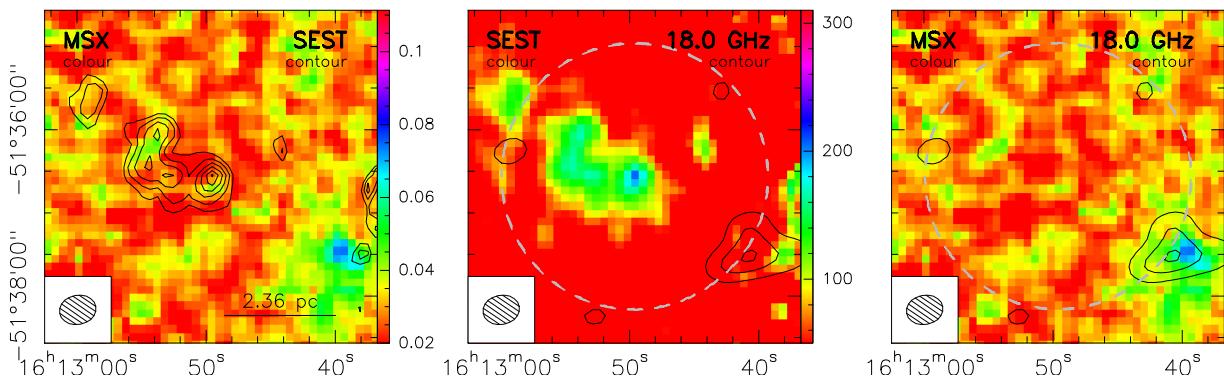
Fig. B.2: continued.
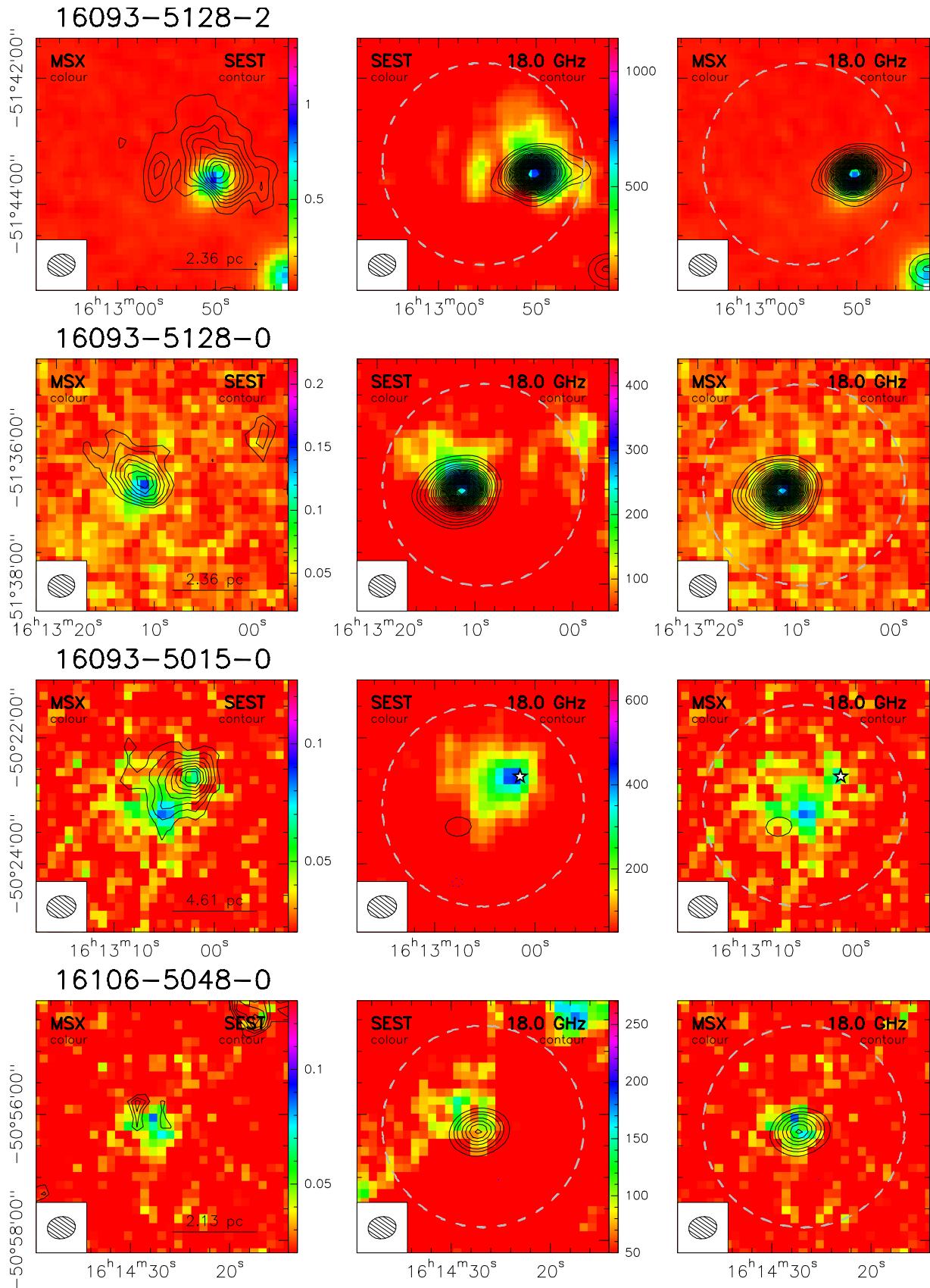
Fig. B.2: continued.
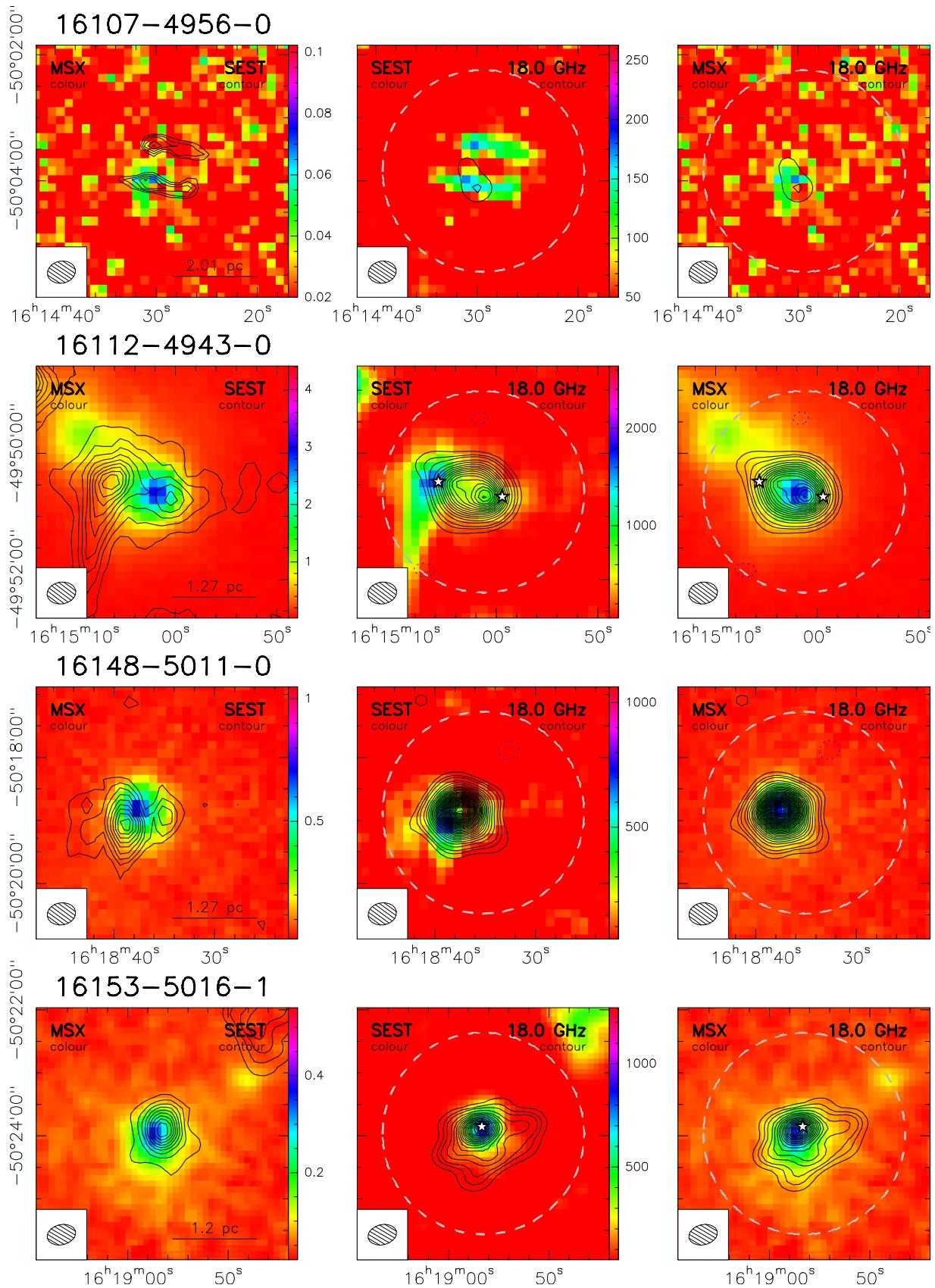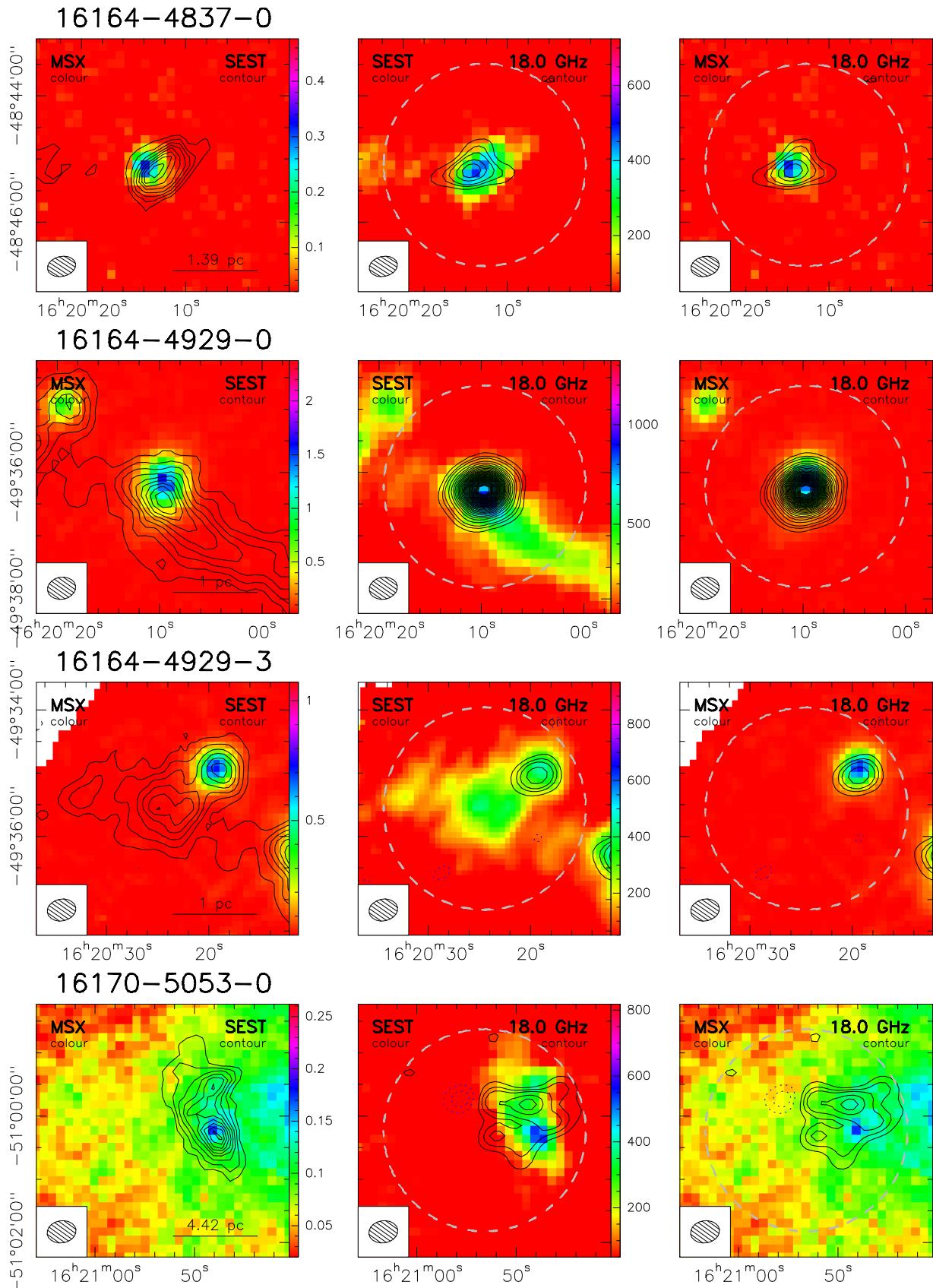
Fig. B.2: continued.

16164−4837−0

16164−4929−0

16164−4929−3
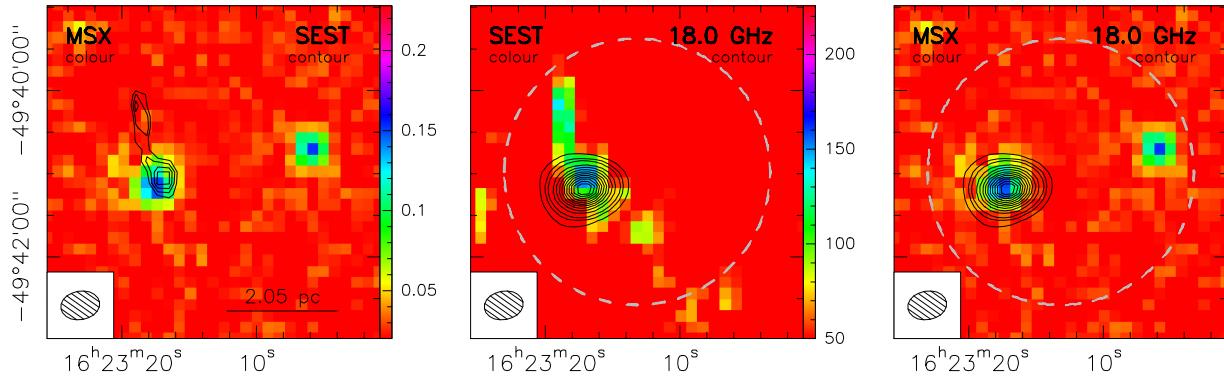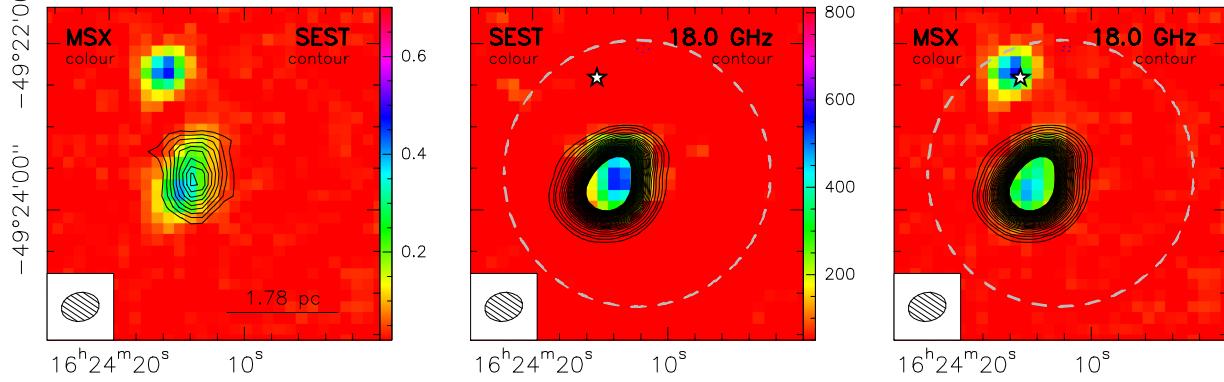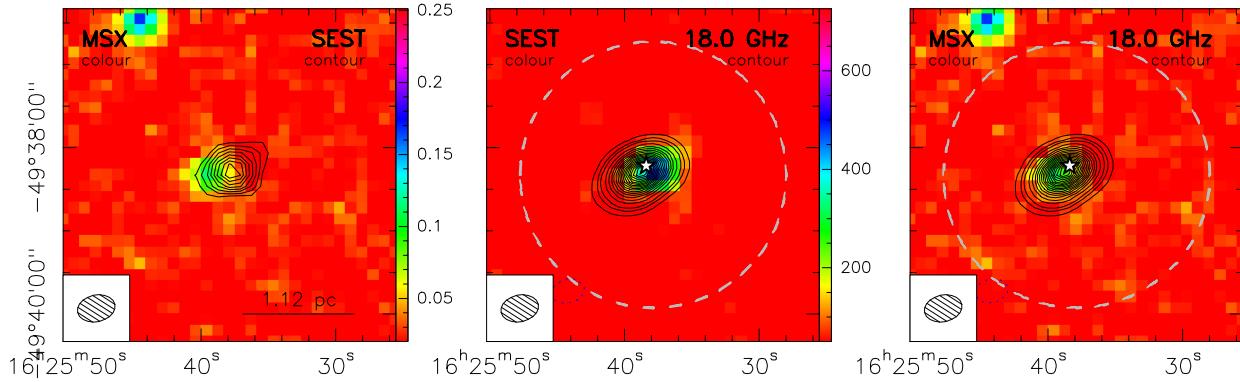
16170−5053−0

Fig. B.2: continued.
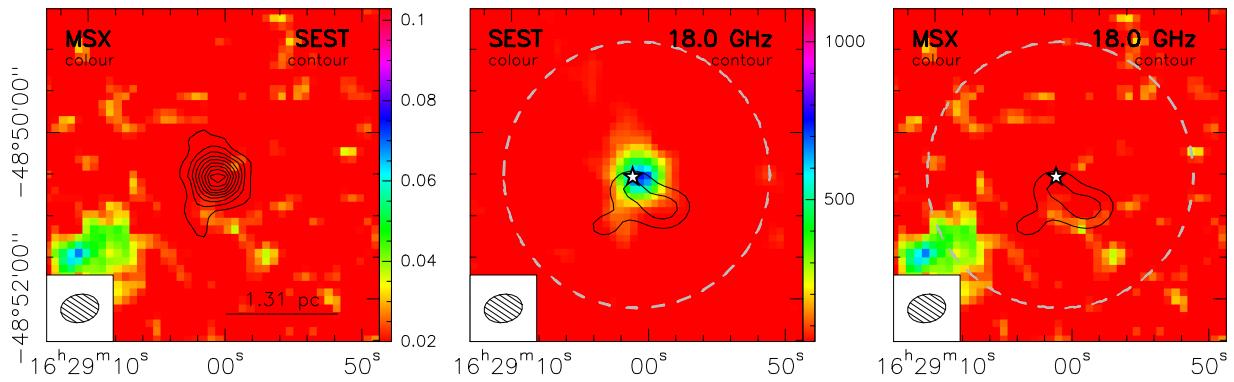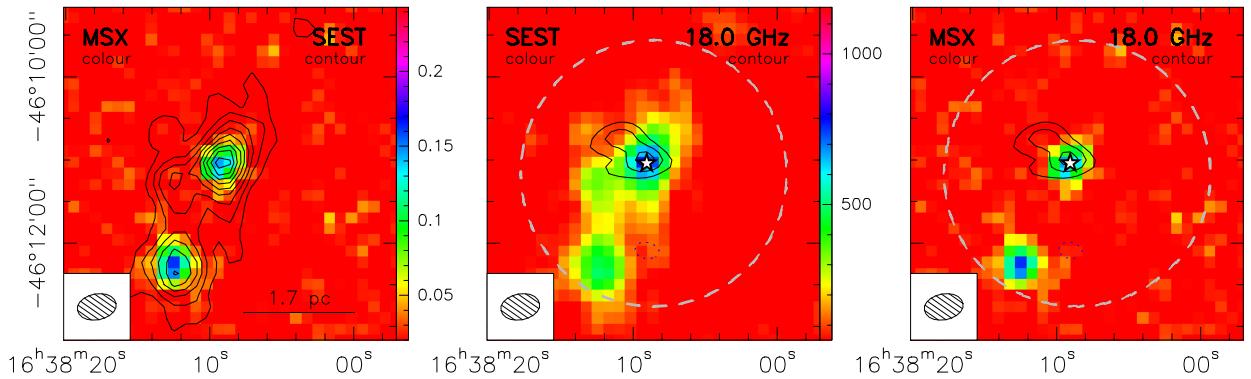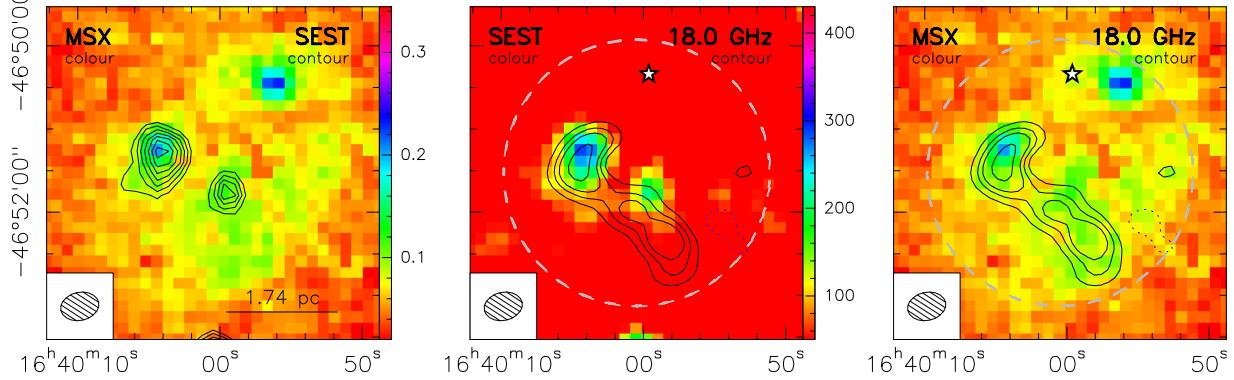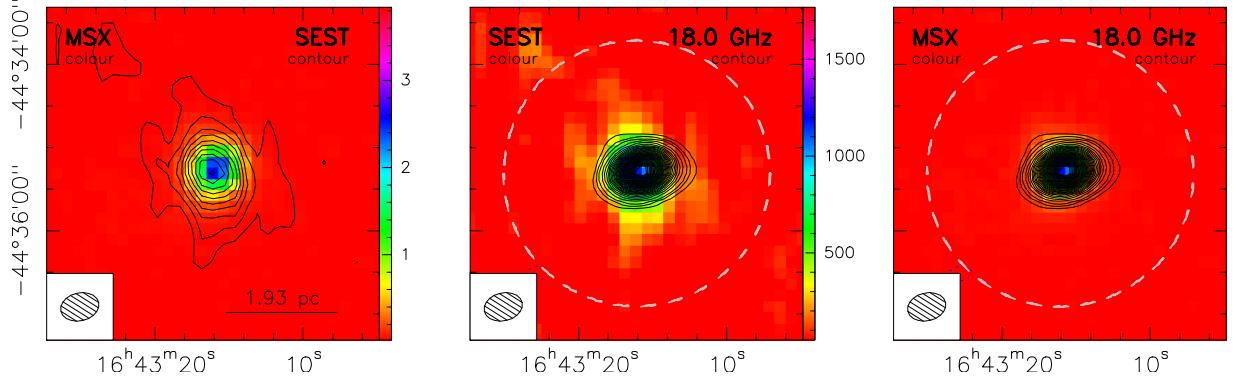
Fig. B.2: continued.
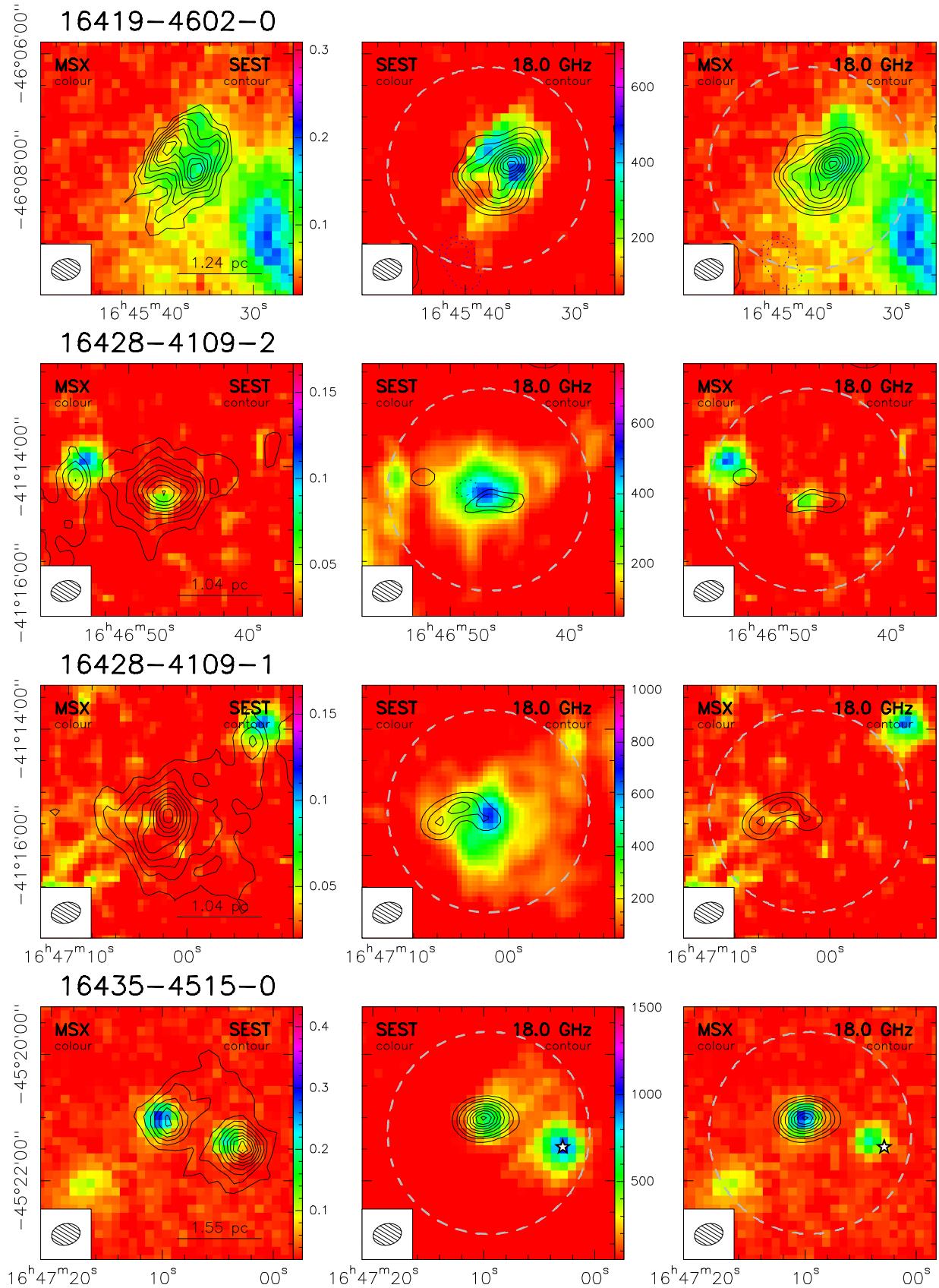
Fig. B.2: continued.

Fig. B.2: continued.

16435−4515−3
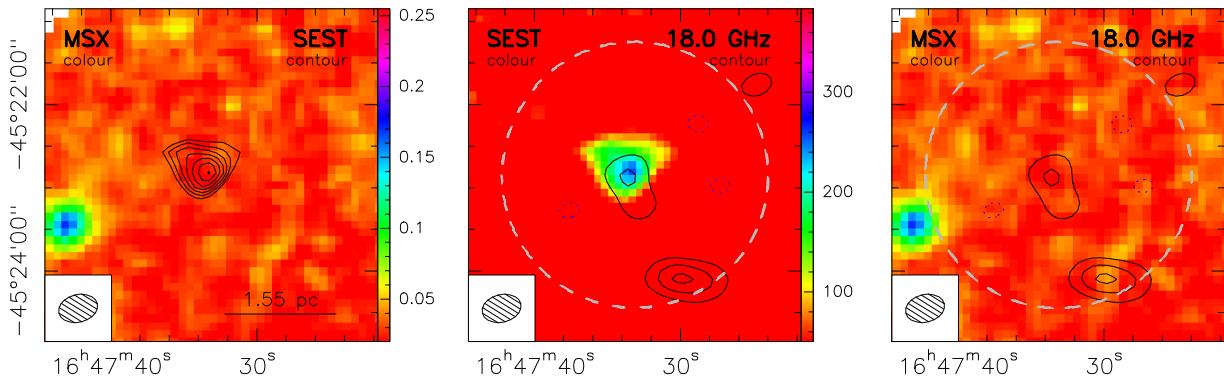
16464−4359−0
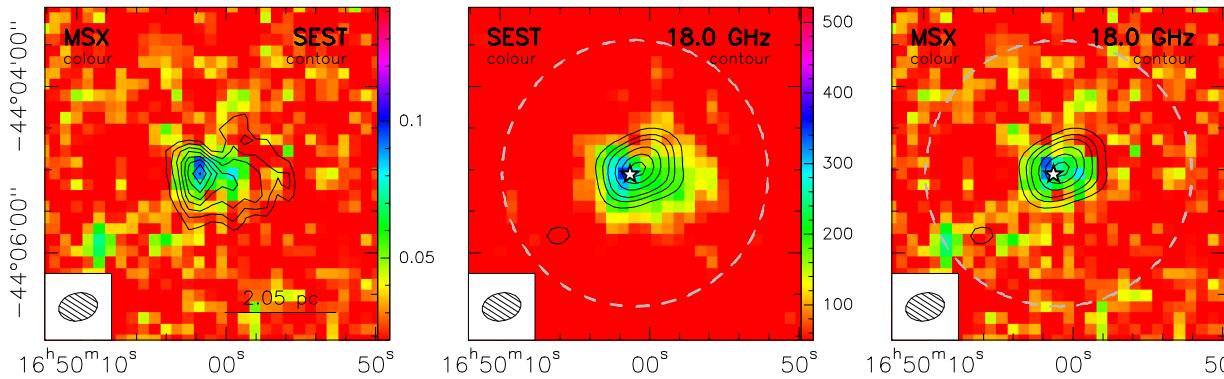
16482−4443−0
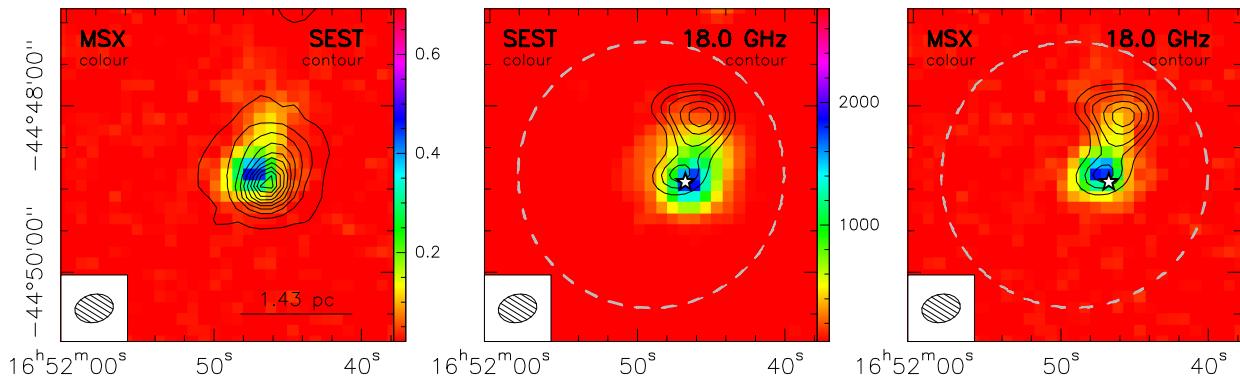

16501−4314−0
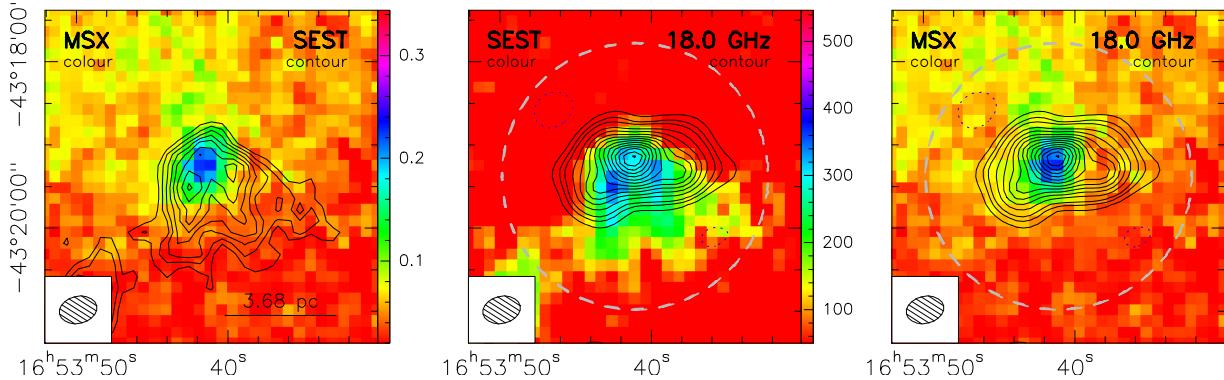
Fig. B.2: continued.

Fig. B.2: continued.

Fig. B.2: continued.

17141−3606−0

## 17149−3916−0

17184−3638−0

17195−3811−2
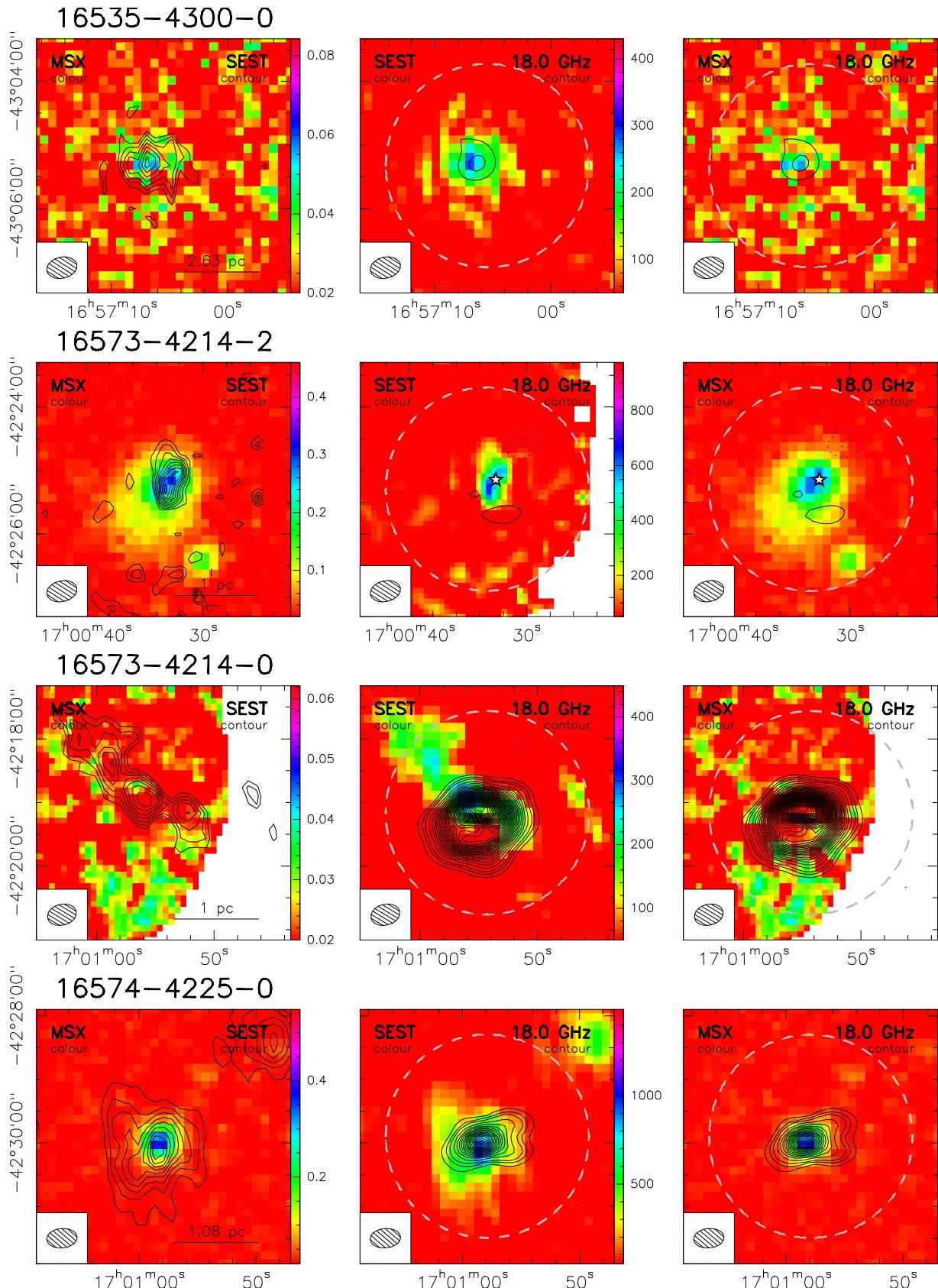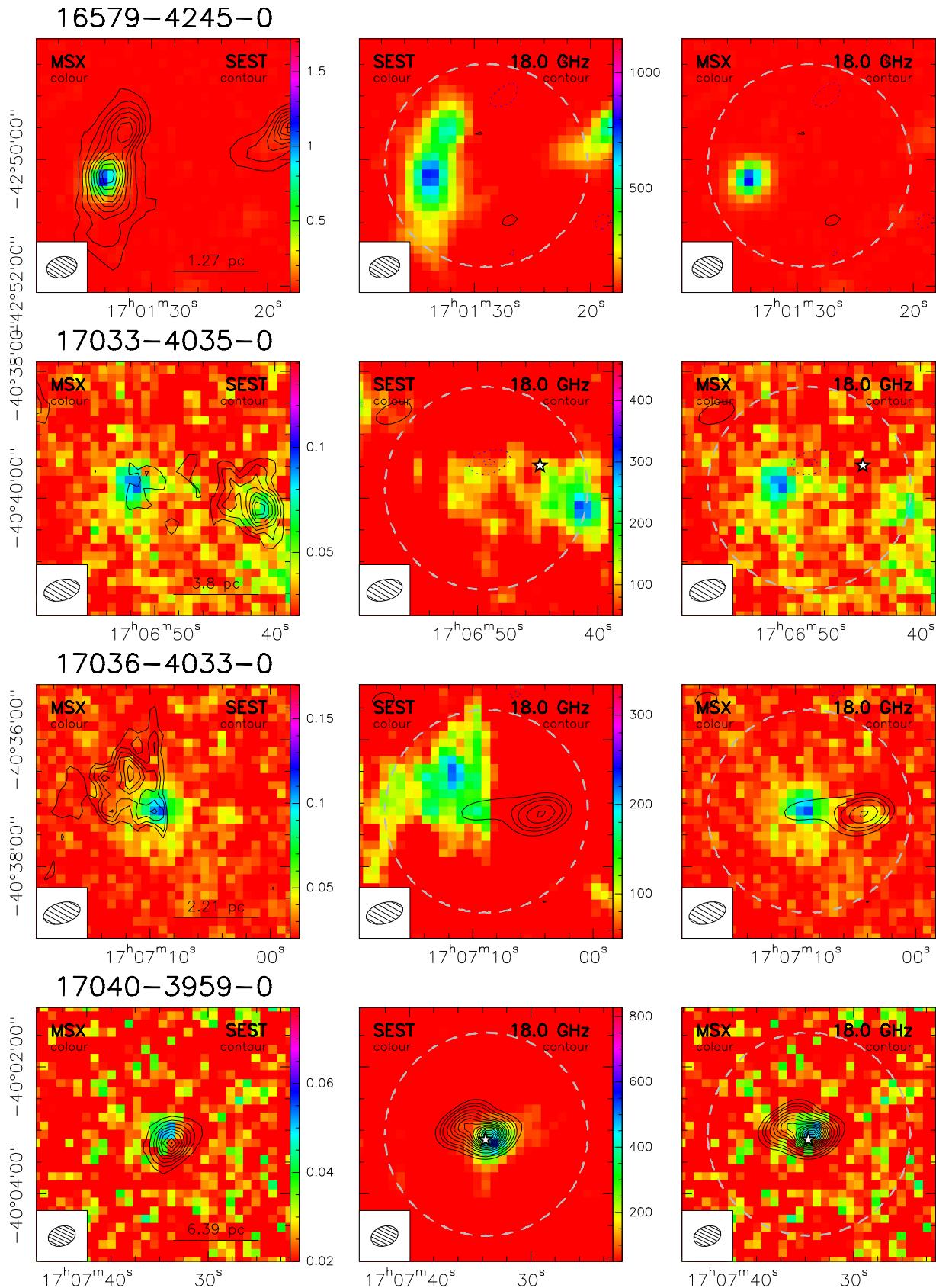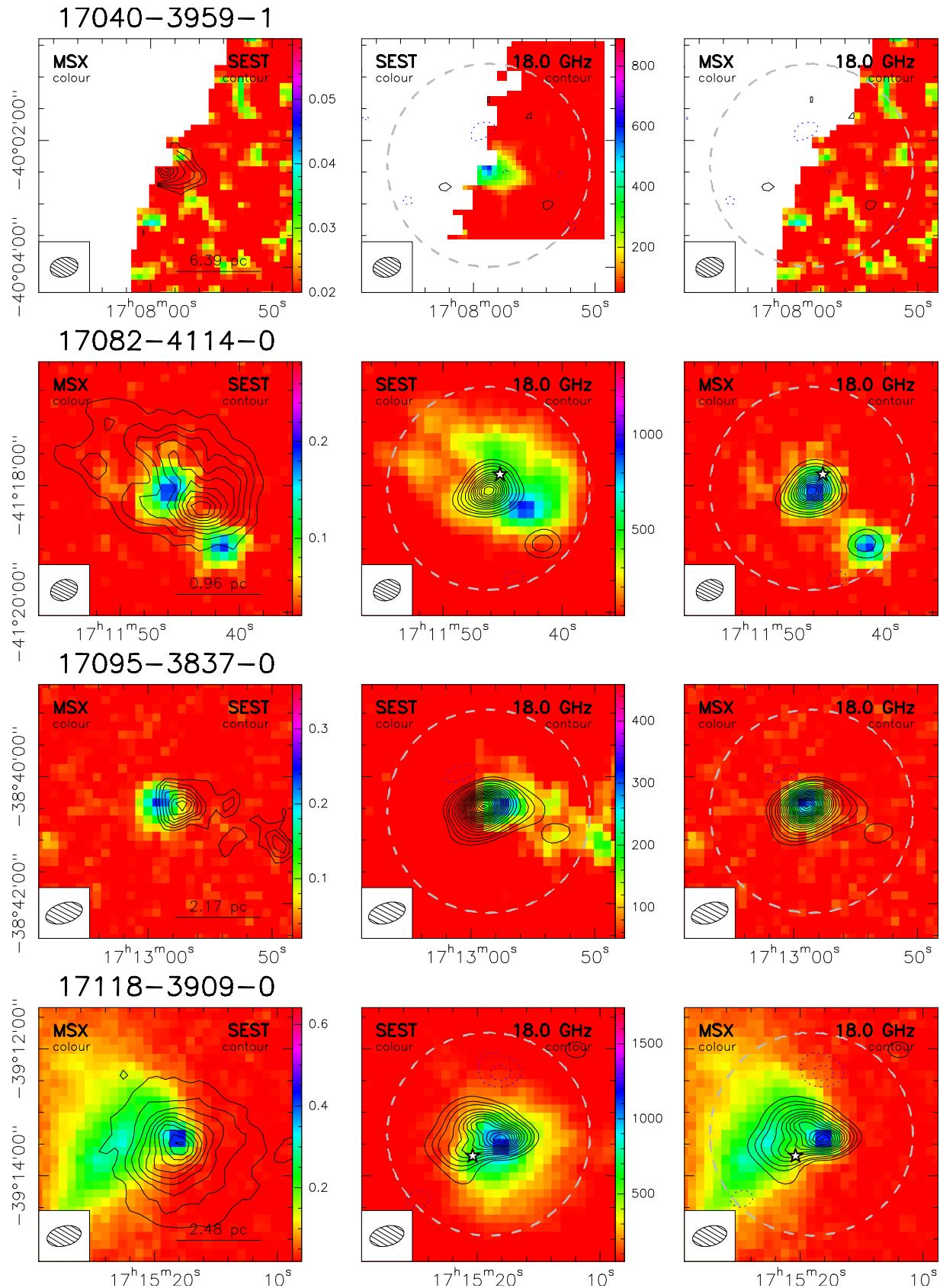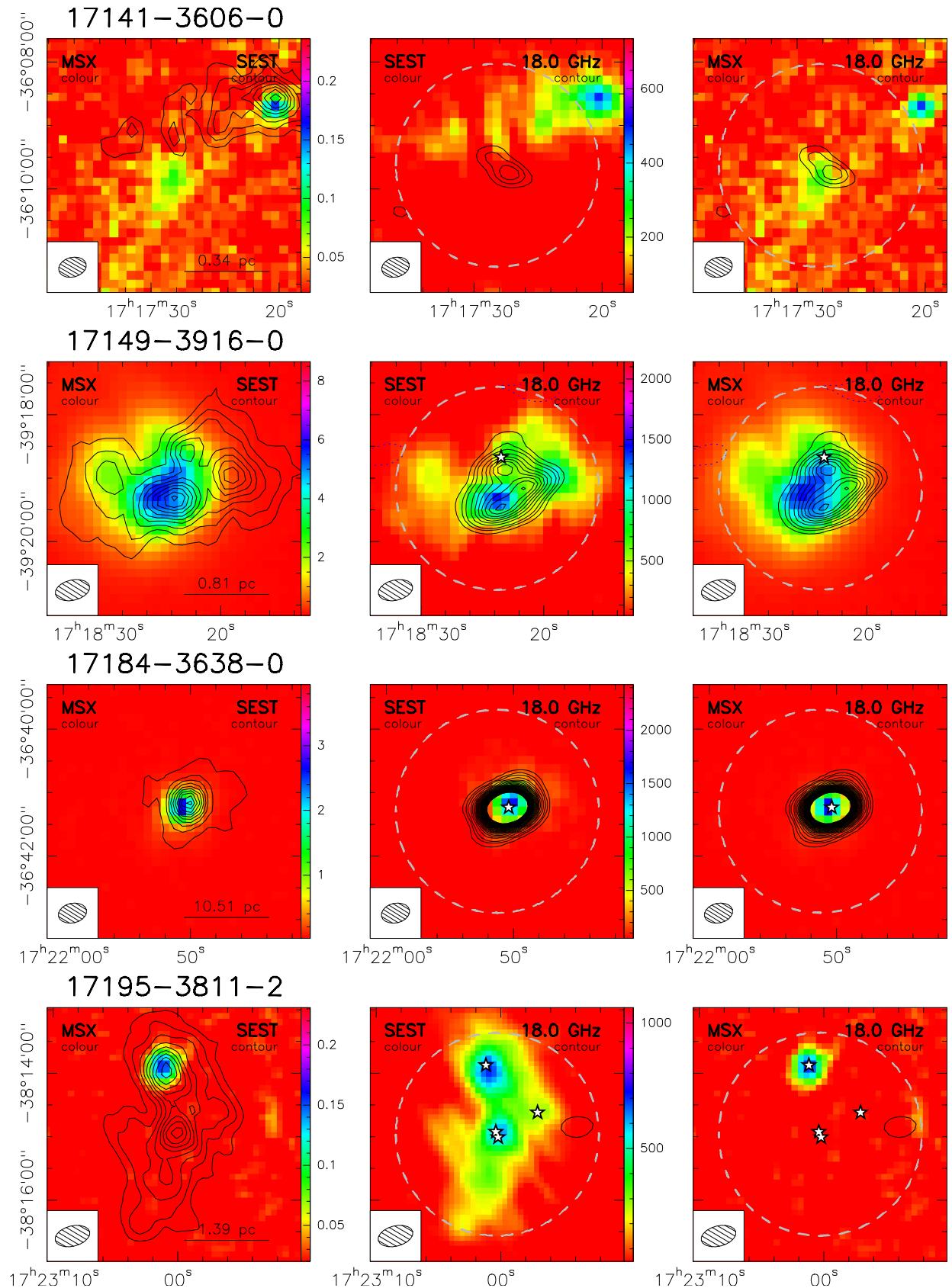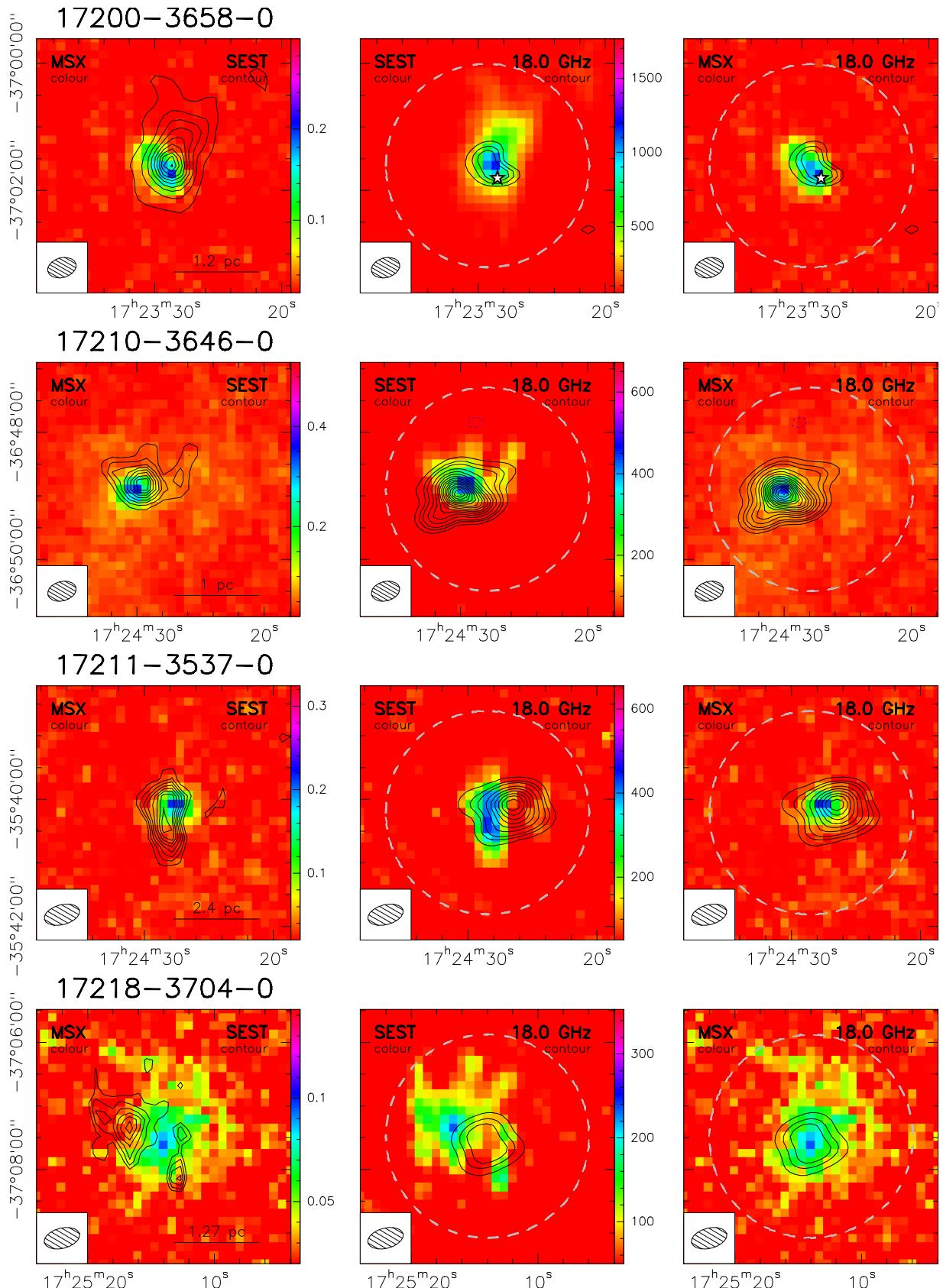
Fig. B.2: continued.

Fig. B.2: continued.

17221−3619−1
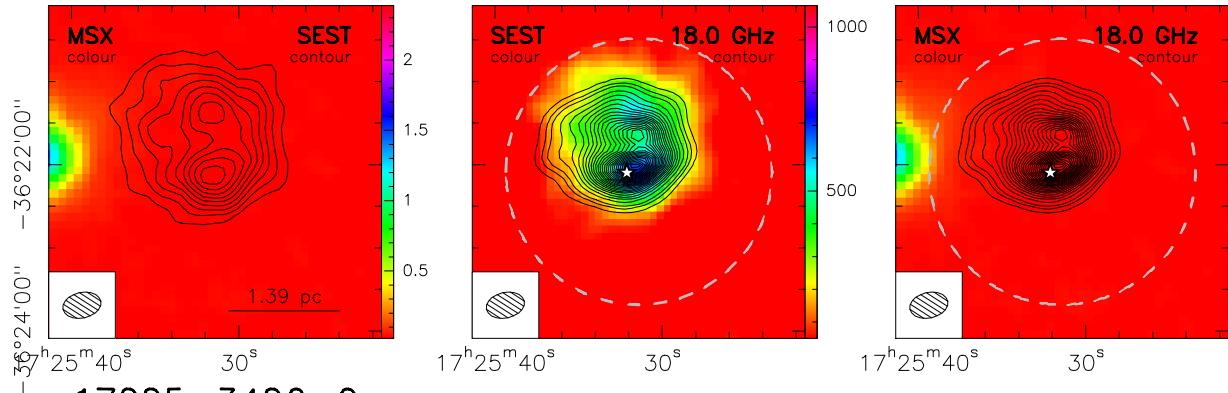
17225−3426−0
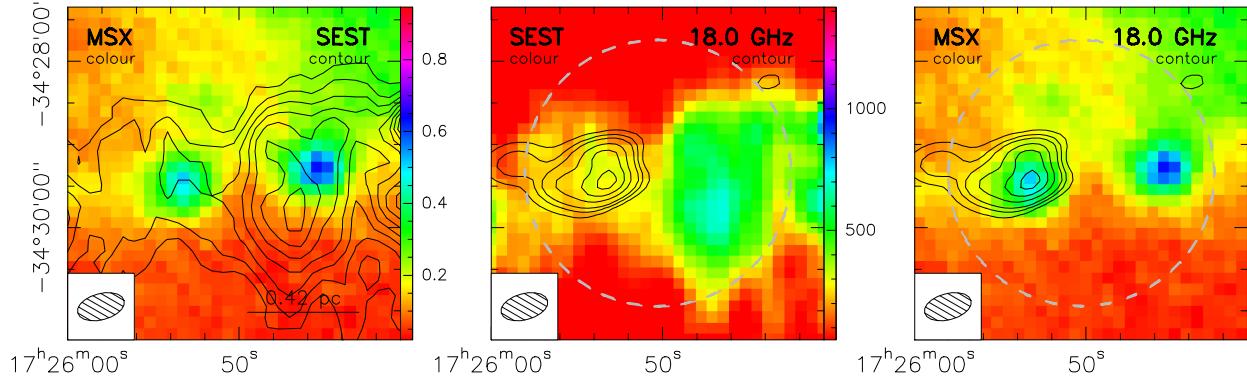
17230−3531−0
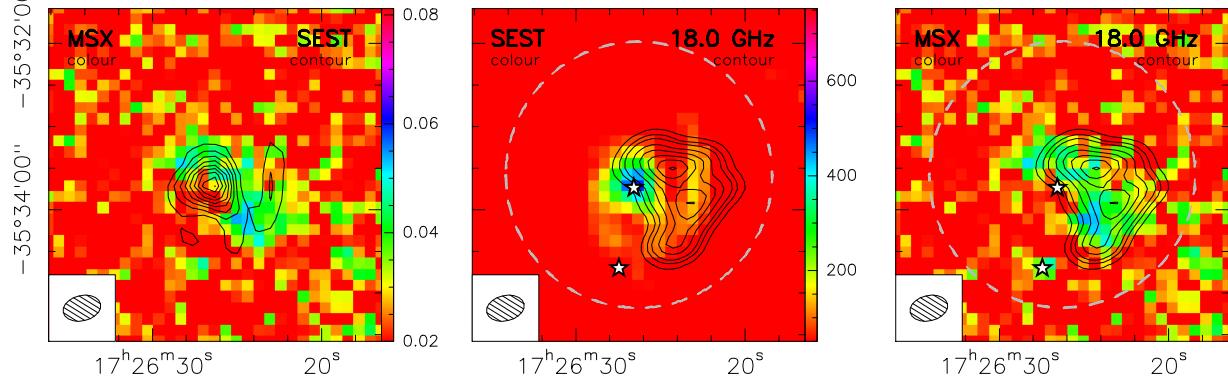
17242−3513−0
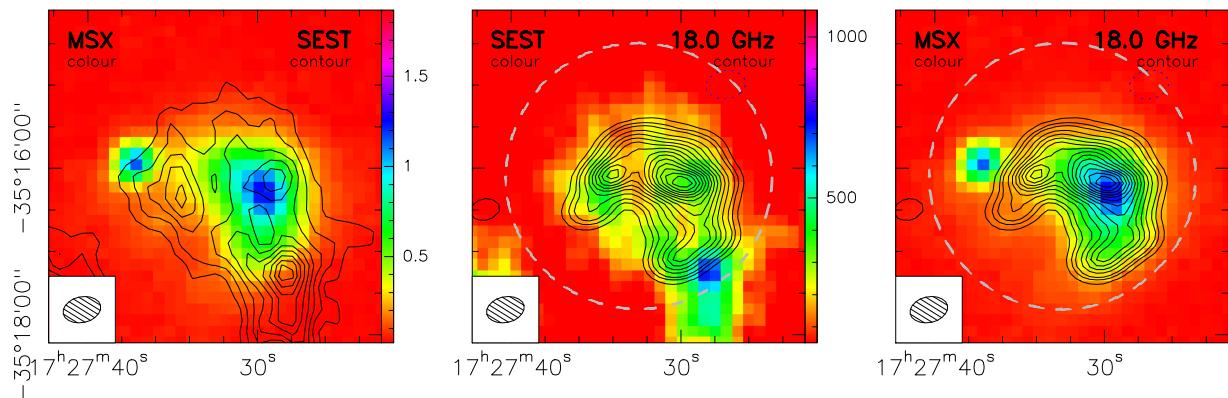
Fig. B.2: continued.

17249−3501−0
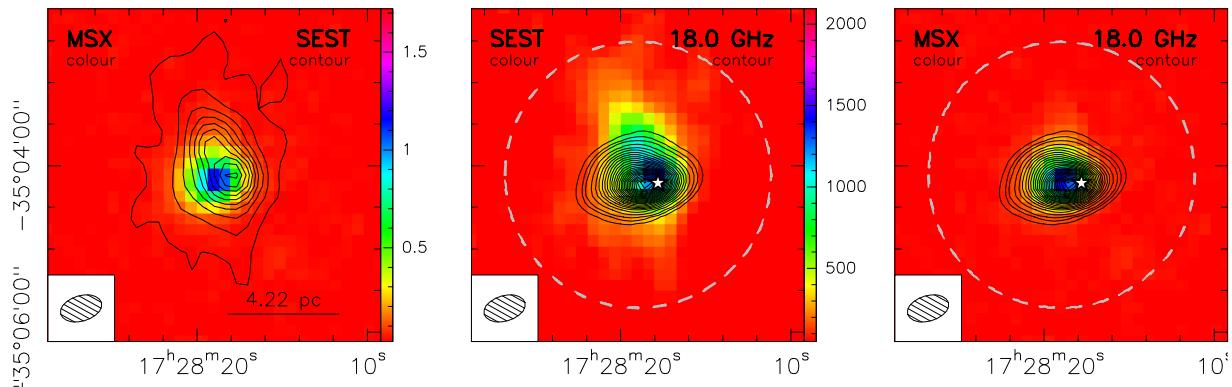
17249−3501−5
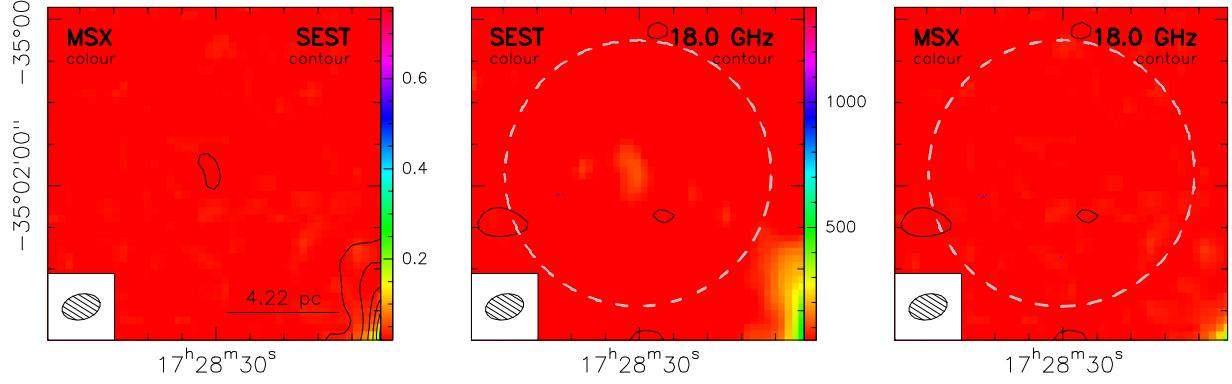
17256−3631−0
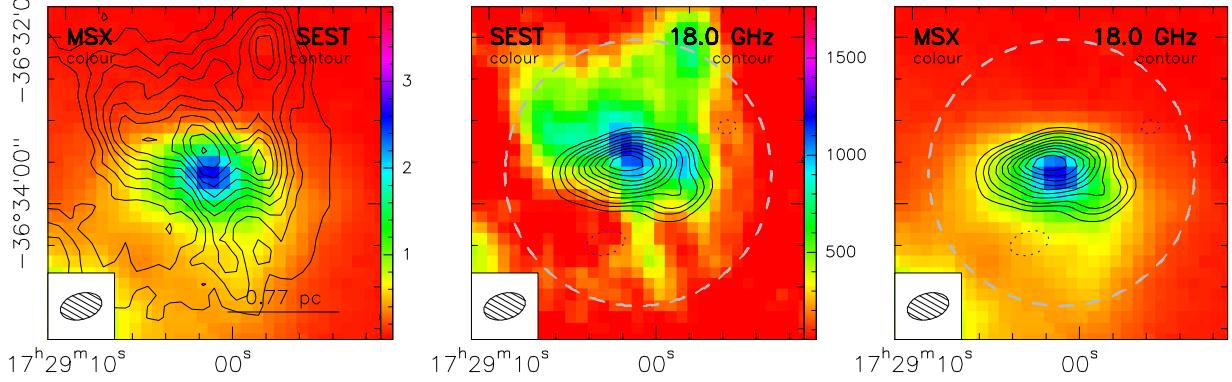
17279−3350−0
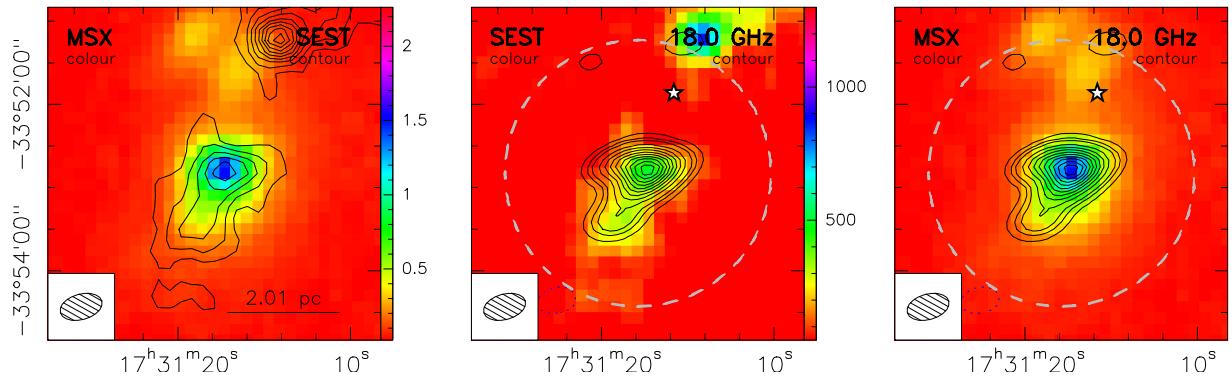
Fig. B.2: continued.

17296−3236−0
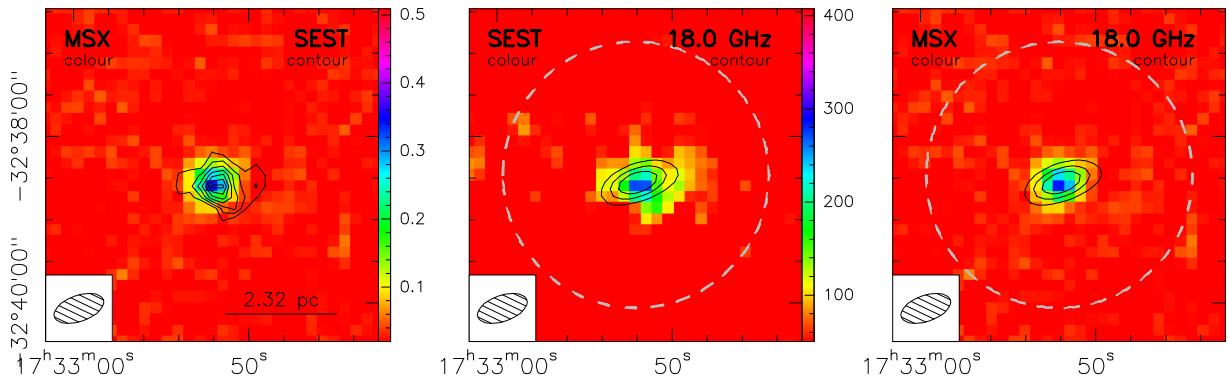
17352−3153−0
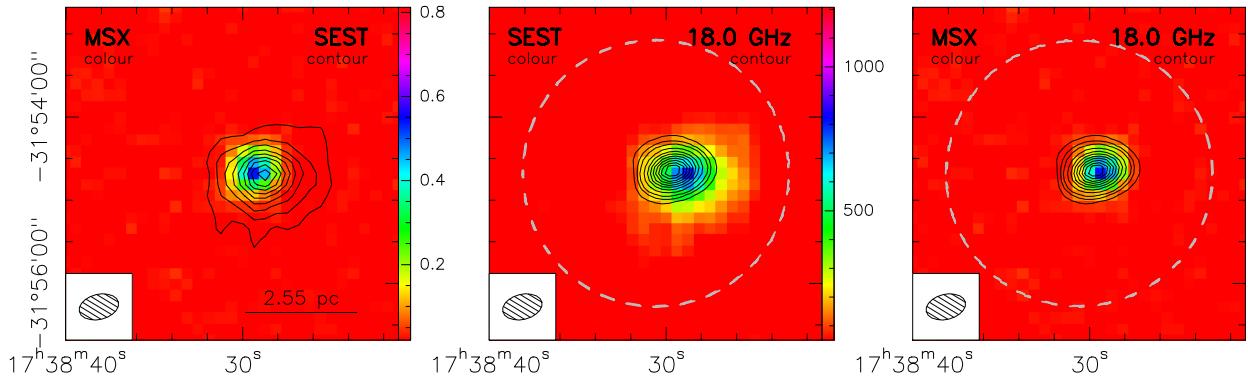
17355−3241−0
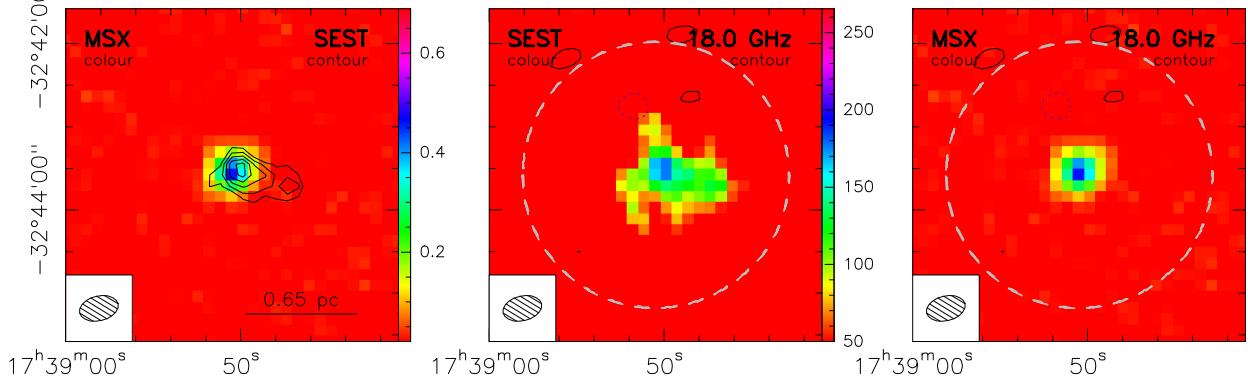
17377−3109−0

Fig. B.2: continued.

17425−3017−0

18018−2426−m

18144−1723−0

18198−1429−0

Fig. B.2: continued.